A Study of $K^+\Lambda$ Photoproduction in the CLAS *g11a* Dataset: Differential Cross Section, Recoil Polarization, and a Partial Wave Analysis

by

Michael Evan McCracken

A dissertation submitted in partial fulfillment of the requirements
for the degree of

Doctor of Philosophy

in the Department of Physics

Carnegie Mellon University

August 5, 2008

Abstract

In this work, we present measurements of $\gamma p \to K^+\Lambda$ differential cross section and Λ recoil polarization from the CLAS *g11a* dataset. The measurements cover the center-of-mass energy range from 1.62 GeV to 2.84 GeV, expanding the observed range of this reaction by roughly 300 MeV. We have analyzed this reaction via both the $K^+p\pi^-$ and $K^+p(\pi^-)$ final state topologies independently and found excellent agreement. The precision of these *g11a* measurements improves characterization of this reaction and displays very good agreement with previous CLAS measurements.

A mass-independent partial wave analysis has also been performed using binned χ^2 fits to *g11a* differential cross section and recoil polarization results as well as previous CLAS *g1c* beam-recoil polarization results. A model of non-resonant photoproduction has been assembled based upon the t-channel K^+, $K^*(892)$, and $K_1(1270)$ exchange diagrams. We have found evidence of contributions of the four-star $S_{11}(1650)$, $P_{13}(1720)$, and $F_{15}(1680)$ states to this reaction near threshold. In the $\sqrt{s}$ range 1.8 GeV to 2.0 GeV, the data shows evidence of the presence of multiple $\frac{3}{2}^+$ states and a single $\frac{1}{2}^-$ state at $\sqrt{s} \approx 1.92$ GeV.

Contents

List of Figures

Chapter 1

Introduction

The *strong interaction* is the term given to the physics which governs the dynamics of the fundamental constituents of most matter. Quantum Chromodynamics (QCD) is the theory that represents physicists' current understanding of the strong interaction as the attraction between *quarks* mediated by *gluons*. Among other phenomena, QCD dictates the binding of quarks into composite particles called *hadrons*, of which the proton and neutron are the most abundant.

As a physical theory, QCD is quite attractive. Its elegance and compactness are æsthetically and mathematically pleasing. More pleasing are the rich and complex physical phenomena which arise from its compact form. As a predictive tool, QCD has had much success with hadrons composed of higher-mass quarks and processes at very high energies. For such systems, perturbation theory or effective potentials can be used to approximate the full QCD theory. However, QCD presents enormous challenges when applied to more common hadrons and energies typical of nuclear physics (a few GeV). Direct QCD calculations for systems such as the proton are beyond our current computational ability. For this reason, specialized techniques and models have been developed which allow calculations in this energy regime.

The goal of this analysis is to further investigate strong interaction phenomena in the non-perturbative QCD regime. Specifically, we seek to characterize the physics by which a high-energy photon (γ) and a proton (p) combine to create two different hadrons, the K^+ meson and the Λ baryon. We refer to this full reaction as $\gamma p \to K^+\Lambda$. Using data from the CLAS experiment at Jefferson Laboratory, we have measured characteristic observables of this reaction in the center-of-mass energy range from 1.62 GeV to 2.84 GeV. We then use these measurements to interpret the physical process by which the γp initial state becomes the $K^+\Lambda$ final state.

In this chapter, we discuss the motivation for our study of the $\gamma p \to K^+\Lambda$ reaction. We discuss the theoretical efforts, namely the Constituent Quark Model, to which our analysis is directly relevant. We also discuss the results of past analyses, both experimental and theoretical, to demonstrate this analysis' contribution to the field of Nuclear Physics.

1.1 QCD and the Quark Model

Quantum Chromodynamics is a remarkable theory. It is elegant and powerful and gives rise to a wealth of strong interaction phenomena. It does, however, present significant challenges in computation at energies typical of nuclear processes. In this section, we describe the theory through a brief comparison to a more familiar theory, Quantum Electrodynamics. We review some of the tools that have been developed to allow for predictive calculations, namely the relativized Constituent Quark Model of Capstick and Roberts. These calculations present us with the Missing Baryons problem, to which this analysis is directly related.

Flavor	$I(J^P)$	Mass (MeV/c^2)	electric charge (e)
u - up	$\frac{1}{2}(\frac{1}{2}^+)$	1.5 to 3.0	2/3
d - down	$\frac{1}{2}(\frac{1}{2}^+)$	3 to 7	$-1/3$
s - strange	$0(\frac{1}{2}^+)$	95±25	$-1/3$
c - charm	$0(\frac{1}{2}^+)$	1250±90	2/3
b - bottom	$0(\frac{1}{2}^+)$	≈4500	$-1/3$
t - top	$0(\frac{1}{2}^+)$	≈175000	2/3

Table 1.1: Quantum numbers and masses of the six quark flavors are provided above. I, J, and P denote isospin, spin, and parity quantum numbers. Masses are given in units of MeV/c^2 and charge in units of the electron charge.

1.1.1 Quantum Chromodynamics by Comparison

In order to understand the difficulties associated with applying Quantum Chromodynamics to calculations at nuclear physics energies, we make comparison to a simpler and more familiar theory, Quantum Electrodynamics (QED). QED describes the electromagnetic interaction between particles which have electric charge. Interaction is mediated by a massless gauge particle, the *photon* (γ); *i.e.* for two charged particles to interact, a photon is exchanged between them. At the most fundamental scale, there are only two types of processes (called vertices) in QED: a charged particle can emit or absorb a photon (see Figure 1.1). The probability with which a charged particle emits or absorbs a photon, called the electromagnetic coupling for a given vertex, is small. From these two simple vertices, any electromagnetic phenomenon can be understood by constructing all possible ways the process can occur.

As an example, we consider the Coulomb interaction between two charged particles. Figure 1.1(b) shows the simplest (tree-level) diagram representing this, *i.e.* exchange of a single photon. This diagram is built of two vertices: e_1 emits a photon and e_2 absorbs the photon. The diagram in Figure 1.1(c) shows another, much more complicated way in which the interaction can proceed. Because this diagram contains many more vertices, each of which has a small coupling, the overall probability of this process is much smaller than the tree-level process. Because of this, QED calculations may omit more complicated diagrams, and perturbation theory may be used to any desired level of precision. QED is an amazing predictive tool, boasting agreement with experimental observation to an accuracy of more than ten significant figures [1]. The electromagnetic interaction is responsible for many composite systems in nature including atoms and molecules. Though the complexity of these systems scales with the number of particles involved, QED is readily applicable to simple systems, boasting predictive results such as the Lamb shift.

Similar to QED, Quantum Chromodynamics describes the strong interaction as the interaction between fundamental fermions, called *quarks*, mediated by a massless gauge particle called the *gluon*. There are six different *flavors* of quark, summarized in Table 1.1. In QCD, each quark and gluon possesses an additional degree of freedom called *color*, an analog of electric charge in QED. Just as in QED, QCD allows vertices in which a quark emits or absorbs a gluon. However, unlike the electrically neutral photon of QED, the gluon carries the color charge of QCD, allowing for vertices composed solely of gluons. Figure 1.1(d) shows the basic vertices of QCD.

Furthermore, the coupling at each QCD vertex is not necessarily a small constant; rather it is energy-dependent and comparable to unity at low energies. Figures 1.1(e,f) show basic diagrams which represent a strong interaction between two quarks. Figure (e) is the simplest process, whereas Figure (f) represents a calculational mess. As for QED, we wish to calculate the bound states allowed by the QCD theory. We know from experiment that quark-antiquark pair states, called mesons, exist and include species such as the π^- ($d\overline{u}$ quark structure) and the D^+ ($c\overline{d}$). We are perhaps more

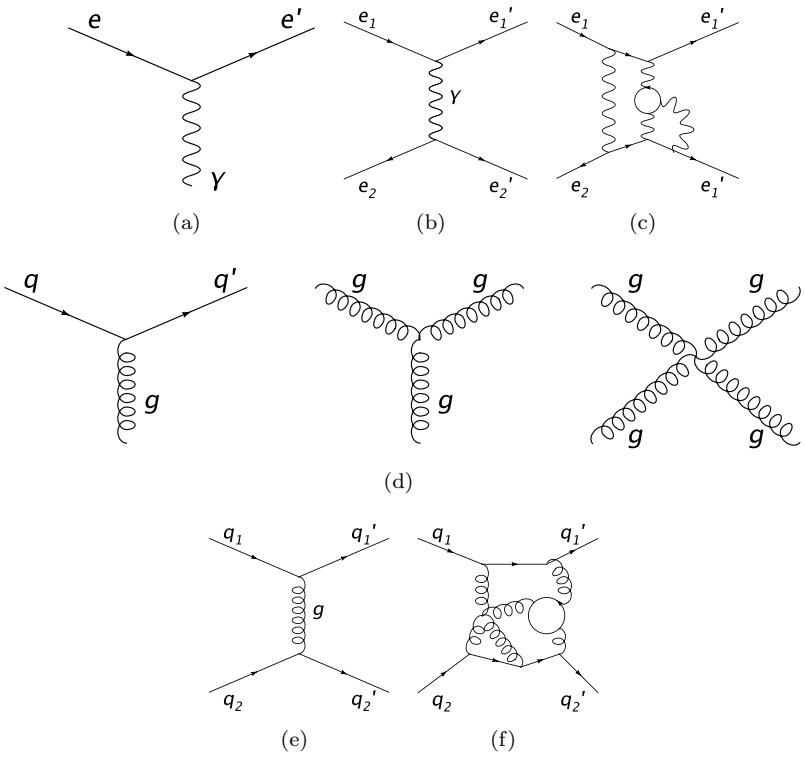

Figure 1.1: Figure (a) shows the possible QED vertex representing the emission or absorption of a photon (wavy line) by the charged particle e (straight line). Figures (b) and (c) both represent contributions to the Coulomb interaction between particles e_1 and e_2 composed of the vertex in (a). The figures in (d) are those allowed by QCD: emission or absorption of a gluon by a quark and the three- and four-gluon vertices. Figures (e) and (f) show diagrams representing strong interaction between two quarks.

familiar with three-quark states, called baryons, which include the proton (uud), neutron (udd), and more exotic states such as the Ξ^- (dss).

At high energies, where the QCD coupling is small, the more complicated diagram will have a small probability relative to the basic diagram and can be ignored. These energies are commonly referred to as the perturbative-QCD (pQCD) regime, as perturbation techniques can be applied. QCD is also manageable for meson states composed of heavy quarks (*e.g.* the Υ ($b\bar{b}$). Because the large quark masses account for the majority of the total mass (energy) of the system, the quarks can be seen as slow-moving, and a fully relativistic theory is unnecessary.

At lower energies, typically a few GeV, the QCD coupling is ≈ 1, and the more complicated diagrams may have contributions equal to that of the basic diagram. In this, the non-pQCD regime, perturbation techniques cannot be applied, and an infinite number of diagrams must be considered in any true QCD calculation. Note that the masses of the up and down quarks, the principle components of the proton, add to only $\approx$1% of the proton mass. This suggests the presence of additional phenomena in the proton or highly-relativistic quarks (or both), which preclude many model simplifications. Unfortunately, strongly-bound systems such as the proton and neutron fall within this regime.

1.1.2 The QCD Spectrum

Because we cannot use QCD for calculations at nuclear physics energies, calculational tools and models have been developed. In order to test these tools, however, specific features of the strong interaction must be isolated that are accessible to both these tools and experiment. Perhaps the most important of these features, the QCD spectrum, is the driving force behind this analysis and the baryon spectroscopy studies at Jefferson Lab and other facilities.

In the late 18^{th} and early 19^{th} centuries, several experimentally physical observed phenomena suggested the need for a new theoretical framework. Chief among these was the description of atomic spectra. It had been observed that the light emitted by atoms due to electronic de-excitation (transition from a higher-energy state to a lower-energy state) came only at certain wavelengths (energies) dependent upon the type of element. Classical theory could not provide justification for this, as it predicted a continuous spectrum of energy states corresponding to a continuous photon energy spectrum. Various theories were postulated, but no satisfying theory of the atom was given until Niels Bohr's 1913 introduction of the Bohr Model [3]. This model proposed that only discrete values of the orbital angular momentum of the atomic system (an thus the atomic energy states) were allowed, a model which described the hydrogen spectrum quite well. This and other phenomena showed the need for a theory describing the *quantized* nature of physics at the microscopic scale. In 1925, such a framework, Quantum Mechanics, was conceived.

A similar approach is taken with QCD in the non-perturbative regime. Analogous to the atomic spectrum created by the electromagnetic force, the strong interaction dictates the formation of a multitude of bound states. Whereas the nature of an excited atomic state is (in retrospect) fairly obvious, the highly-nonlinear nature of QCD obfuscates the nature of baryon excitation. It is believed that excitation could be the result of the dynamics of the three main quarks, gluons, or quark-antiquark pairs (or combinations of the three). With the laws of Quantum Mechanics in hand, we know that excited baryon states, called N^* states, should exist at discrete intervals. Indeed, observation confirms this. Figure 1.2 shows the baryon spectrum as revealed in the scattering of π mesons on the proton. It is important to note that these experiments considered only πN final states; that is they require that an N^* can decay to a pion and nucleon to be detected. From observation of these states, models have been created which attempt to approximate the full QCD theory.

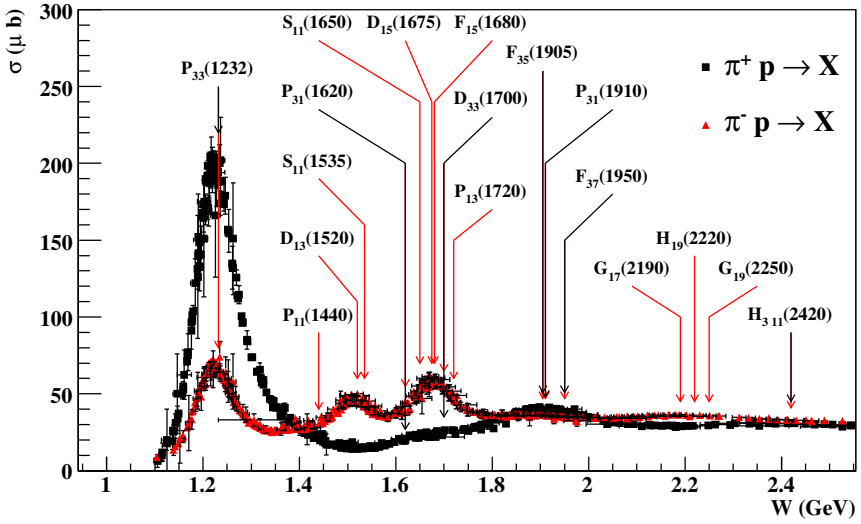

Figure 1.2: Shown above are the total cross sections from πp scattering experiments. The enhancements in σ are labeled with N^* states that are given a four-star ("existence is certain") rating by the PDG [5]. (Image source: [4].)

1.1.3 The Constituent Quark Model and the Missing Baryons Problem

One such model that has found some predictive success is the *Constituent Quark Model* (CQM). In this model, only the three main quarks, called the *valence* quarks, of a baryon state are considered. Excitations are the result of radial displacements or angular momentum of these quarks. In this simplified picture, calculations are possible. Table 1.2 lists the N^* states predicted by the CQM calculations of Capstick and Roberts [2], as well as the experimentally observed states. These particular calculations utilize relativized wavefunctions, though the calculations are not performed in a fully coviariant framework.

Note that the ratio of the number of states predicted by the CQM to the number of observed states is roughly 4:1. This disparity is called *The Missing Baryons Problem* and is the primary theoretical motivation for our analysis. Several possible explanations for this mismatch have been proposed. Central to this analysis is the hypothesis that, for reasons hidden to us by the complexity of QCD, not all N^* states can be created by (couple to) the πN system. Until recent years, the vast majority of data on N^* resonances has been from πN scattering and detection of πN final states. However, experiments have shown production of some N^* in γp scattering and decays to several other hadronic final states. By fully investigating the possible photoproduction and decay of N^* states to other channels, we test the CQM and learn more about the physics allowed by QCD.

1.2 The K^+ and Λ Hadrons

For this analysis, we have probed the structure of the proton using a high-energy beam of photons. In order to observe this physics, however, we must detect a useful set of final state particles. Our choice to examine the $K^+\Lambda$ final state is motivated by several factors. First, this final state is easily identifiable with the CLAS detector and allows for easy control of background. In addition, non-zero couplings of N^* states to $K^+\Lambda$ have been predicted [6] and observed in previous experiments [5].

J^P	M_{CQM}	M_{PDG}	Rating	J^P	M_{CQM}	M_{PDG}	Rating
$1/2^-$	1460	1535	****	$1/2^+$	1540	1440	****
$1/2^-$	1535	1650	****	$1/2^+$	1770	1710	***
$1/2^-$	1945	2090	*	$1/2^+$	1880		
$1/2^-$	2030			$1/2^+$	1975		
$1/2^-$	2070			$1/2^+$	2065	2100	*
$1/2^-$	2145			$1/2^+$	2210		
$1/2^-$	2195						
$3/2^-$	1495	1520	****	$3/2^+$	1795	1720	****
$3/2^-$	1625	1700	***	$3/2^+$	1870		
$3/2^-$	1960	2080	**	$3/2^+$	1910		
$3/2^-$	2055			$3/2^+$	1950		
$3/2^-$	2095			$3/2^+$	2030		
$3/2^-$	2165						
$3/2^-$	2180						
$5/2^-$	1630	1675	****	$5/2^+$	1770	1680	****
$5/2^-$	2080			$5/2^+$	1980	2000	**
$5/2^-$	2095	2200	**	$5/2^+$	1995		
$5/2^-$	2180						
$5/2^-$	2235						
$5/2^-$	2260						
$5/2^-$	2295						
$5/2^-$	2305						
$7/2^-$	2090	2190	****	$7/2^+$	2000	1990	**
$7/2^-$	2205			$7/2^+$	2390		
$7/2^-$	2255			$7/2^+$	2410		
$7/2^-$	2305			$7/2^+$	2455		
$7/2^-$	2355						
$9/2^-$	2215	2250	****	$9/2^+$	2345	2220	****
$11/2^-$	2600	2600	***				
$11/2^-$	2670						
$11/2^-$	2700						
$11/2^-$	2770						
$13/2^-$	2715						

Table 1.2: The table above gives predicted N^* states from the Constituent Quark Model calculations of Capstick and Roberts [2], as well as the associated observed states reported by the PDG. All masses are given in units of MeV/c^2.

Hadron	$I(J^P)$	Mass	Charge (e)	Valence quarks	Decay mode	$c\tau$
K^+	$\frac{1}{2}(0^-)$	493.677 MeV/c^2	+1	$u\bar{s}$	$\mu^+\nu_\mu$ (63%)	3.713 m
Λ	$0(\frac{1}{2}^+)$	1.115683 GeV/c^2	0	uds	$p\pi^-$ (63%)	7.89 cm

Table 1.3: Characteristics of K^+ and Λ hadrons [5]. Here, I, J, and P denote isospin, spin, and parity quantum numbers. Only the most prevalent decay modes are listed.

We gain access to the physics of excited nucleon photoproduction by analyzing events with a K^+ meson and Λ baryon in the final state. The K^+ is pseudo-scalar meson composed of $u\bar{s}$ valence quarks and has a mass of 493.677 MeV/c^2. The Λ is a electrically-neutral baryon composed of uds valance quarks and has a mass of 1.115683 GeV/c^2. The full quantum numbers of both particles are summarized in Table 1.3. It is important for the purposes of this analysis to note that the isospin quantum numbers of the K^+ and Λ are $\frac{1}{2}$ and 0, respectively. Thus, the $K^+\Lambda$ final state has a total isospin of $\frac{1}{2}$ and can not couple to the Δ resonances with $I = \frac{3}{2}$. Thus, we call the $K^+\Lambda$ final state an isospin-filter.

It is also worth commenting that K^+ and Λ are the lowest-mass meson and baryon with non-zero strangeness. As the strong interaction preserves strangeness conservation, the decays of these hadrons are mediated by the weak interaction. Thus, the particles are relatively long-lived on the scale of nuclear physics. The K^+ has $c\tau = 3.713$ m, making its direct observation with our detector possible. The Λ has $c\tau = 7.89$ cm, a scale smaller than most of our detector components. In light of this, our analysis detects the daughter particles of the Λ's main decay mode, $\Lambda \to p\pi^-$.

1.3 $\gamma p \to K^+\Lambda$ Observables

By considering spin states of the involved particles, we see that the $\gamma p \to K^+\Lambda$ reaction is fully described by $2 \times 2 \times 2 = 8$ complex helicity amplitudes. Parity invariance constraints reduce this number to 4 independent amplitudes. The pseudo-scalar nature of the K^+ meson simplifies study of this reaction: characterization of these amplitudes depends upon measurement of differential cross sections as well as seven single- and double-polarization observables. The single-polarization observables T, Σ, and P_Λ are the beam and target asymmetries and the Λ recoil polarization, respectively. The double-polarization observables are the beam-recoil polarization transfers denoted by C_x and C_z for circularly-polarized photons and O_x and O_z for linearly-polarized photons (subscripts represent the in-scattering-plane axes). Due to the self-analyzing nature of the predominant Λ decay mode, measurement of these polarization observables is simpler than in other reactions. As a result of this, world data on the $K^+\Lambda$ reaction are relatively extensive and are quickly becoming complete for energies in the resonance region.

For this analysis, we have used an unpolarized photon beam to catalyze the $\gamma p \to K^+\Lambda$ reaction, allowing observation of the differential cross section and Λ recoil polarization. We have observed the reaction in a large range of center-of-mass production angles at center-of-mass energies in the range 1.62 GeV to 2.84 GeV. Measurements of the differential cross section and P_Λ were produced at 2076 and 1715 $(\cos\theta_{CM}, \sqrt{s})$ points, respectively.

1.4 Previous Analyses of $\gamma p \to K^+\Lambda$

At the time of this analysis, the *g11a* dataset is by far the world's largest dataset for strangeness photoproduction in the resonance region. Several good measurements of the differential cross section and recoil polarization have been made in the past. In this section, we comment on these and show the necessity of our measurement.

1.4.1 Differential Cross Section Measurements

Experiments have produced measurements of the differential cross section for the $\gamma p \to K^+\Lambda$ reaction from as far in the past as 1957. We choose to separate these into three groups: studies performed before 1973, modern large-acceptance experiments, and modern limited-acceptance experiments. Below we examine each of these groups and comment on the contribution of our analysis to world data. The five sets of previous analyses considered in this section are plotted together in Figures 1.3-1.5.

Pre-1973 Studies

The experiments performed in the years prior to 1973 produced measurements at a total of 144 $(\cos\theta^K_{CM}, \sqrt{s})$ points. The results of these studies are summarized nicely in [7]. These measurements represent the center-of-mass energy range from threshold to $\sqrt{s} \approx 1.91$ GeV with a wide sampling of production angle. Figures 1.3-1.5 show these data present a large amount of scatter and generally large uncertainties. Relative to more modern, higher-statistics datasets, these results seem sparse. As little interpretation of the physics of $K^+\Lambda$ photoproduction can be done with these results alone, we include them here to demonstrate how far experimental technique has progressed in the past decades.

Modern Large-Acceptance Experiments: CLAS and SAPHIR

In recent years, measurements of the differential cross section have been made by the CLAS and SAPHIR collaborations. These measurements are very interesting as they provide the first characterization of the process over a wide $\sqrt{s}$ and angular range. More importantly, these results enabled several partial wave analyses of the reaction. At the time of this analysis, large discrepancies existed between results from the two experiments.

SAPHIR is a large-acceptance magnetic spectrometer at the Electron Stretcher Accelerator facility at the University of Bonn, Germany. The SAPHIR Collaboration published three separate studies of the differential cross section in 1994 (Bockhorst *et al.* [8]), 1998 (Tran *et al.* [9]), and most recently in 2004 (Glander *et al.* [10]). Here, we discuss only the most recent results as they are the most precise and represent the largest kinematic range. The 2004 results are formed from data taken in 1997-1998 representing a total of 51977 $K^+\Lambda$ data events. These results span the center-of-mass energy range from threshold to $\sqrt{s} \approx 2.4$ GeV. The data were separated into 50-MeV-wide bins in photon energy and 0.1-unit-wide bins in $\cos\theta_{CM}$. These results are plotted in Figures 1.3-1.5. Compared to the pre-1973 results, the SAPHIR results present an amazing gain in information. The results show trends of the differential cross section in production angle as well as $\sqrt{s}$. As such, these results were suitable for partial wave analyses of this reaction.

In 2005, the CLAS Collaboration published differential cross section results (Bradford *et al.* [11]) from two separate analyses, those of J. McNabb [12] and R. K. Bradford [13]. These results were from the CLAS *g1c* dataset collected in late 1999 from which $\approx 5.6 \times 10^5$ $K^+\Lambda$ events were selected. The data were separated into 10-MeV-wide bins in photon energy and give coverage in $\sqrt{s}$ from threshold to 2.53 GeV. Due to the increased statistics, the CLAS results provide a much smoother description of the reaction than the SAPHIR results, as well as an extension of the observed $\sqrt{s}$ range by roughly 100 MeV.

Agreement between the two results is quite good for center-of-mass energies below 1.8 GeV. However, several troubling discrepancies exist at higher $\sqrt{s}$ values. The most noticeable of these is the overall scale discrepancy; though the SAPHIR error bars are relatively large, the CLAS results are $\approx 20\%$ higher than those of SAPHIR for forward angles. The CLAS results also exhibit interesting shape at $\sqrt{s} \approx 1.9$ GeV, whereas the SAPHIR results do not. We see that for intermediate angles ($-0.15 \leq \cos\theta^K_{CM} < 0.15$), the CLAS results show a large enhancement in the differential cross section in the range 1.8 GeV$\leq \sqrt{s} <$1.95 GeV. This same feature is present in the CLAS data at

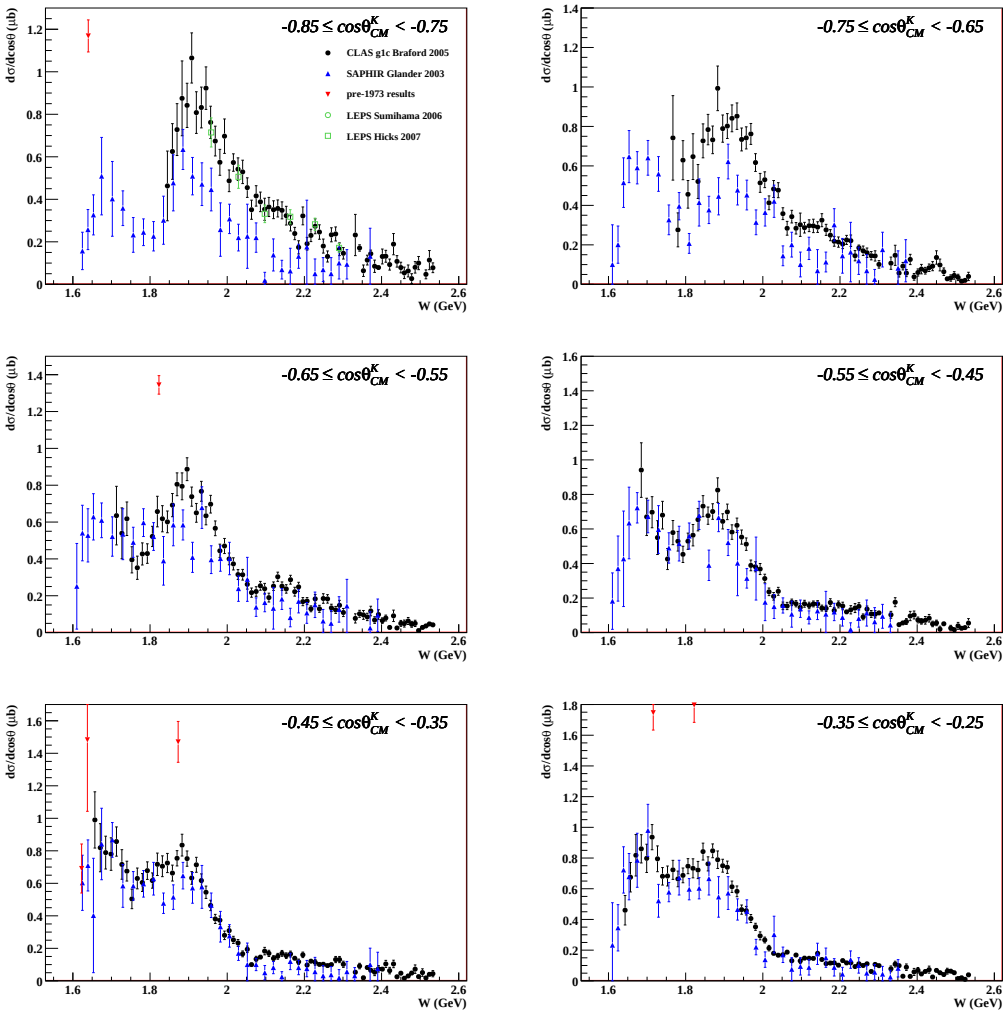

Figure 1.3: Shown above are previous measurements of the $\gamma p \to K^+\Lambda$ differential cross section at backward angles. Each plot displays data in a 0.1-unit-wide $\cos\theta_{CM}$ range versus $\sqrt{s}$. The legend at top left indicates the convention for all plots.

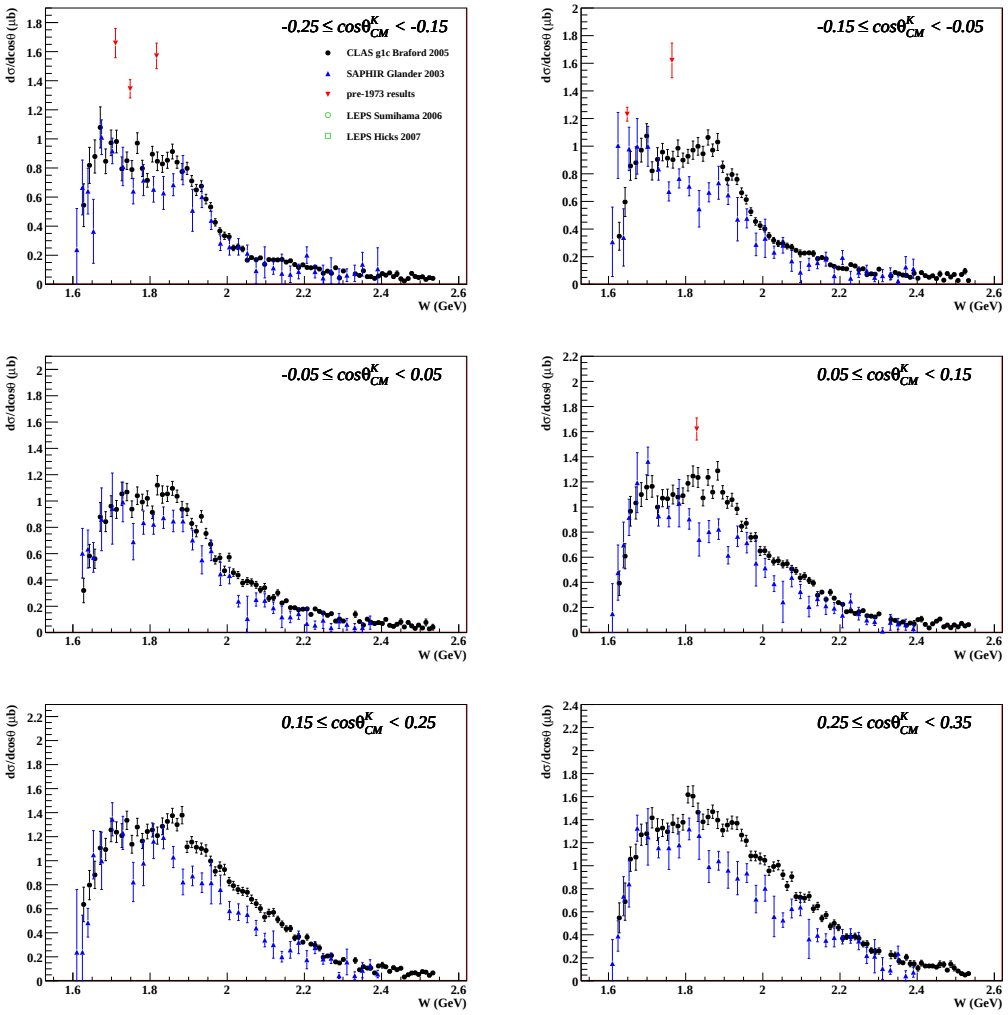

Figure 1.4: Shown above are previous measurements of the $\gamma p \to K^+\Lambda$ differential cross section at middle angles. Each plot displays data in a 0.1-unit-wide $\cos\theta_{CM}$ range versus $\sqrt{s}$. The legend at top left indicates the convention for all plots.

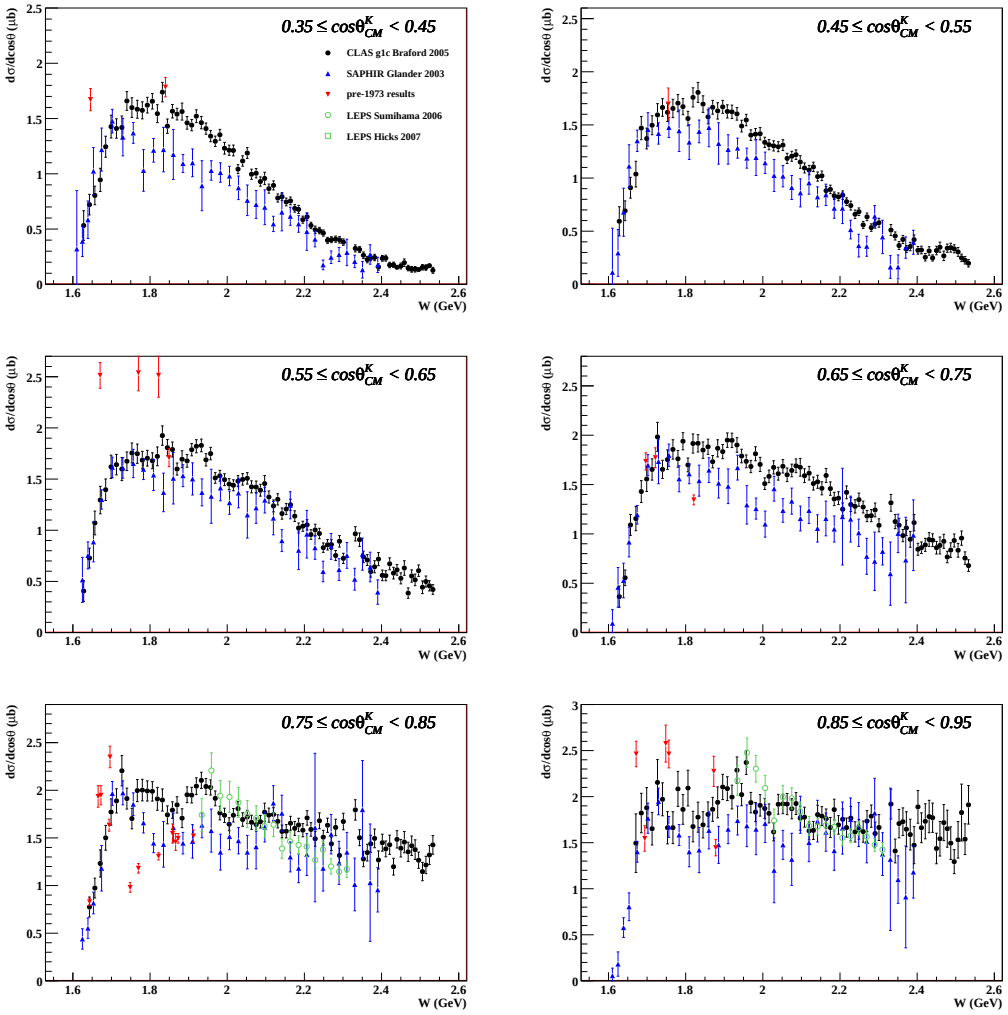

Figure 1.5: Shown above are previous measurements of the $\gamma p \to K^+\Lambda$ differential cross section at forward angles. Each plot displays data in a 0.1-unit-wide $\cos\theta_{CM}$ range versus $\sqrt{s}$. The legend at top left indicates the convention for all plots.

extreme forward and backward angles where the SAPHIR results once again do not show as much enhancement. Confirmation of this feature in the differential cross section is very important, as this type of structure is indicative of resonance production. As a result of the disparity between these measurements, previous partial wave analysis findings have been dependent upon the dataset used. Goals of our analysis include, but are not limited to, investigating the presence of the enhancement at $\sqrt{s} = 1.9$ GeV and resolving the scale discrepancy between these two experiments.

Modern Limited-Acceptance Measurements: LEPS

The LEPS experiment at the Spring-8 facility in Hyogo, Japan, has also produced measurements of the $\gamma p \to K^+\Lambda$ differential cross section at very forward (Sumihama *et al.*, 2006 [14]) and very backward (Hicks *et al.*, 2007 [15]) production angles. Though they add relatively few points to the world data on $\gamma p \to K^+\Lambda$, the LEPS measurements at forward and backward angles are important as the large-acceptance experiments (CLAS especially) cannot provide adequate acceptance at these angles. For the backward angle measurement, data were separated into two 0.1-unit-wide bins in $\cos\theta_{CM}$ in the range -1.0$\leq \cos\theta^K_{CM} <$-0.8 and six equal-width energy bins covering the $\sqrt{s}$ range from $\approx$1.92 GeV to $\approx$2.31 GeV. Of these measurements, only the more forward angular bins overlap with the previous CLAS and SAPHIR results. These results align very well with the previous CLAS measurements in this angular range, corroborating the scale of the CLAS measurement.

The forward-angle LEPS measurement represents three $\cos\theta^K_{CM}$ bins in the range $0.7 \leq \cos\theta^K_{CM} < 1.0$ and 18 bins in the energy range 1.92 GeV$\leq \sqrt{s} <$2.31 GeV. Here, comparison to the previous CLAS and SAPHIR results shows some discrepancy. The SAPHIR results show a more dramatic downward trend in $\sqrt{s}$ than the large-acceptance results. The LEPS results match the enhancement in the CLAS differential cross section at $\sqrt{s} = 1.95$ GeV, but for $\sqrt{s} >$2.15 GeV they show a steeper decrease with increasing $\sqrt{s}$. When comparing the *g11a* results in Chapter 6, we consider the the LEPS measurements where these discrepancies exist.

1.4.2 Λ Recoil Polarization

As discussed above, the self-analyzing nature of the $\Lambda \to p\pi^-$ decay allows for extraction of the Λ spin polarization. Figures 1.6 and 1.7 show these results in bins of center-of-mass production angle versus $\sqrt{s}$. Measurements of the single-polarization observable, P_Λ, have been made beginning in the early 1960's. As with the differential cross section data, experiments between 1960 and 1978 produced limited results; by 1978, the world data for the Λ recoil polarization included measurements at only 27 values of $(\sqrt{s}, \cos\theta_{CM})$, which can be found in [16, 17, 18, 19, 20, 21]. The majority of these points are for middle production angles and in the region $\sqrt{s} < 1.76$ GeV. We omit these points from Figures 1.6 and 1.7 as they present a considerable amount of scatter, and comparison with the more modern data is not particularly enlightening.

More recent measurements of P_Λ have been made with high-statistics datasets from the CLAS, SAPHIR, and GRAAL collaborations. In the same publication as their 2004 differential cross section measurements [10], the SAPHIR Collaboration published P_Λ measurements at 30 kinematic values. These measurements stretched the statistics to their limits, and consequently, the uncertainty in $\sqrt{s}$ associated with each point is sizable.

The CLAS Collaboration published measurements of the recoil polarization in 2004 [22] which were taken from the *g1c* dataset. These measurements considered only the lower-beam energy production run, limiting results to the range $\sqrt{s} < 2.3$ GeV. The roughly 3×10^5 data were separated into 0.2-unit-wide $\cos\theta_{CM}$ bins and, in most cases, 50-MeV-wide bins in photon energy. In some regions of phase-space, energy binning was coarser to bolster statistics for each point. At backward angles, the SAPHIR and CLAS results show fair agreement; error bars are large enough to account for discrepancies in most regions. At extreme forward angles, however, there is a notable discrepancy between the two results; the SAPHIR results show a more negative polarization than the CLAS

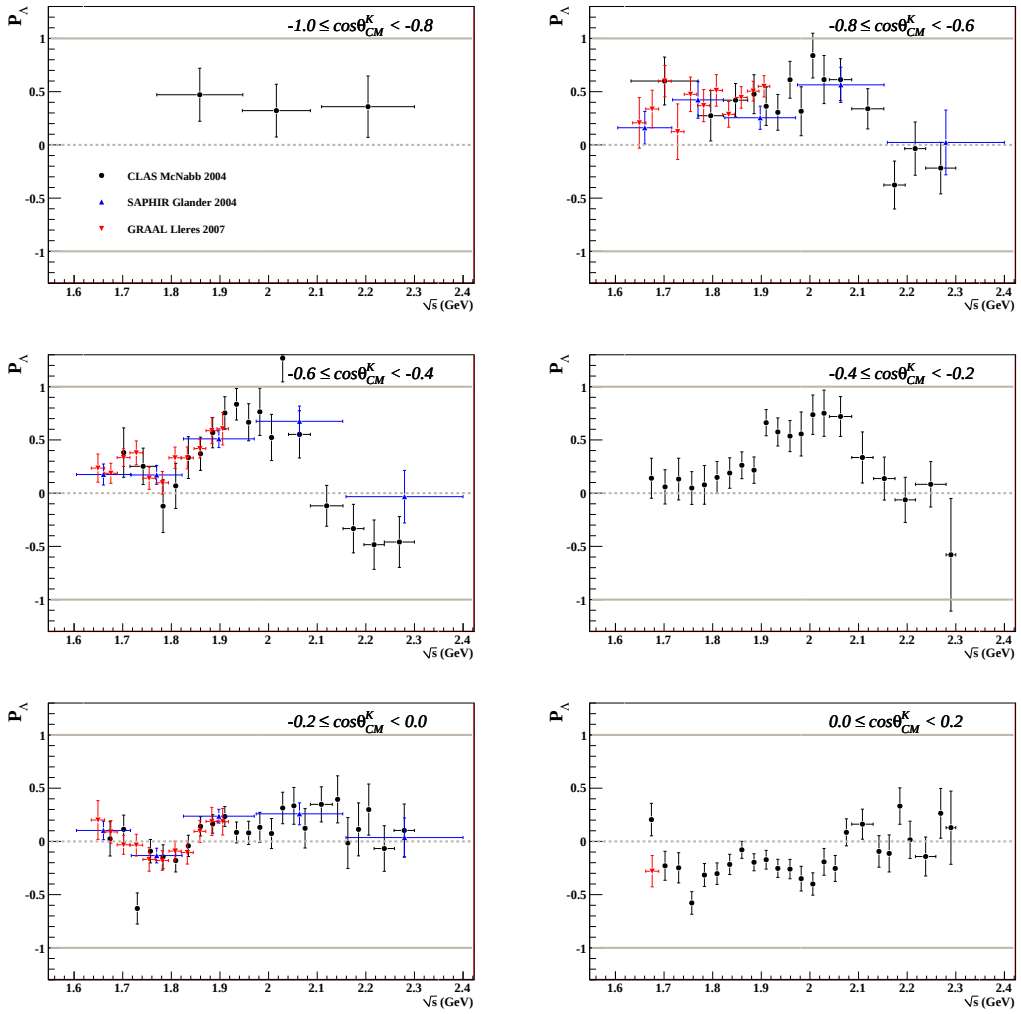

Figure 1.6: Shown above are P_Λ results from previous analyses of $\gamma p \rightarrow K^+\Lambda$ at backward and middle production angles. Each plot represents data in the 0.2-unit-wide $\cos\theta^K_{CM}$ range indicated. Marker convention is given at top left and is the same for all plots.

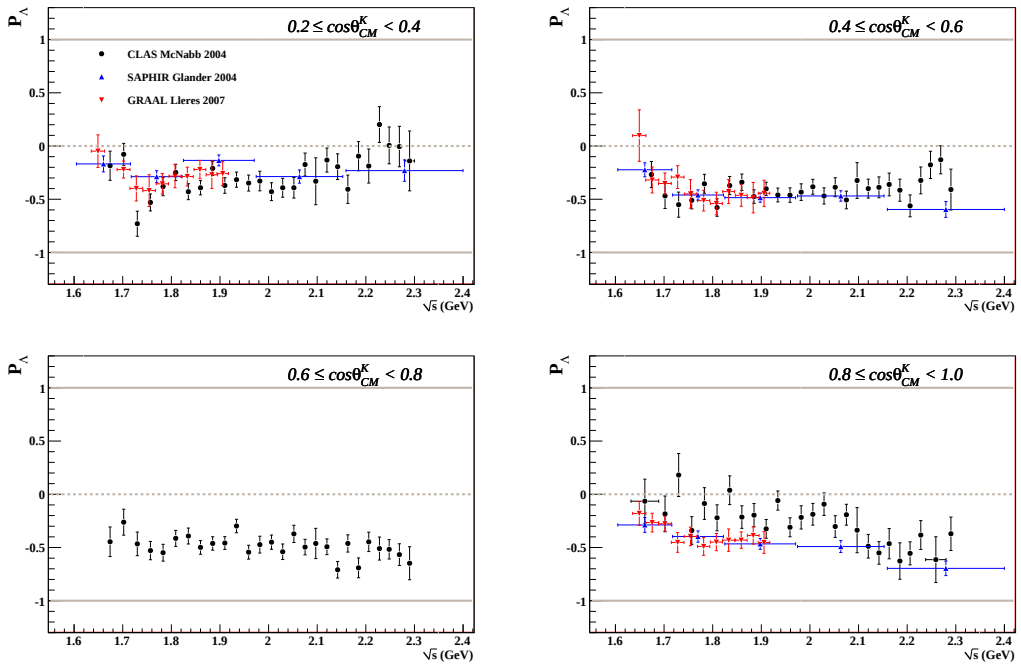

Figure 1.7: Shown above are P_Λ results from previous analyses of $\gamma p \to K^+\Lambda$ at forward production angles. Each plot represents data in the 0.2-unit-wide $\cos\theta^K_{CM}$ range indicated. Marker convention is given at top left and is the same for all plots.

results in the $\sqrt{s}$ range 1.8 GeV to 2.05 GeV. Because of the coarseness of the SAPHIR data, we cannot use comparison to discern whether interesting shapes in the CLAS results (*e.g.* $\sqrt{s}$ = 2.05 GeV and forward angles) are attributable to physics or statistical variance.

Very recently, the collaboration at the GRAAL facility in Grenoble, France, published recoil polarization measurements at 65 kinematic points [23]. Binning in energy is roughly equal to that of the CLAS result ($\approx$ 50 MeV in photon energy), and measurements were taken at six fixed lab production angles yielding center-of-mass angles of roughly 35°, 60°, 80°, 100°, 120°, and 140°. Though these results occupy a smaller range of $\sqrt{s}$ ($<$ 1.91 GeV) than the CLAS and SAPHIR data, they offer a satisfying amount of consistency. With comparisons to these data, we are able to scrutinize the CLAS measurements. We see that at forward production angles, where the CLAS data shows a significant amount of fluctuation, the GRAAL results are smooth and agree well with the SAPHIR data. Agreement between the three results is good in other kinematic regions.

1.5 The Call for a *g11a* Measurement

Of course, the mere existence of the *g11a* dataset does not warrant an additional study of $\gamma p \to K^+\Lambda$ reaction. However, in light of the discrepancies we have described above, our *g11a* measurements add much to the world data. Our measurement is the most precise to date, boasting the finest $\sqrt{s}$ binning and experimental uncertainties equal to, and in many regions smaller than, those of the previous CLAS measurements. This refinement of characterization of the reaction will lead to more accurate interpretation via partial wave analyses. There are also several specific issues which we seek to address with our measurements. The discrepancy in scale between the previous CLAS and SAPHIR differential cross section results is troubling. Though our analysis uses the same detector as the previous CLAS results, the run conditions and analysis methods are distinct enough that we may confirm the previous results. We also seek to investigate the enhancement of the differential cross section at $\sqrt{s} \approx 1.9$ GeV. The results of previous analyses of excited nucleon resonances in this reaction have depended strongly upon which differential cross section data is considered. Finally, the energy range covered by the *g11a* dataset will allow for characterization of the reaction in a $\sqrt{s}$ region which is dominated by non-resonant processes, yet not far-removed from the resonance region. Our results in the range 2.6 GeV$\leq \sqrt{s} <$2.84 GeV will certainly shed new light on theoretical treatments of non-resonant production.

1.6 Previous Partial Wave Analyses

Because polarization measurements for the $\gamma p \to K^+\Lambda$ reaction are so readily available, various partial wave analyses of this channel have been performed. Before we discuss the N^* resonance results of these analyses, however, it is important to discuss the non-resonant terms used in various models. Unlike other reactions, such as $\gamma p \to p\omega$, there is no clear choice of t- and u-channel (non-resonant) processes for strangeness production. Furthermore, coupling constants associated with many of the vertices of possible non-resonant diagrams (*e.g.* the $K^+p\Lambda$ coupling) have not been directly observed, adding more uncertainty to models. In the absence of a clear non-resonant picture, two major model types have been developed.

The isobar models, most notably of Thom [24] and Mart and Bennhold [25, 26], characterize the non-resonant contributions to $K^+\Lambda$ photoproduction via effective Lagrangian Feynman diagrams describing t- and u-channel exchanges. Mechanisms typically considered are shown in Figure 1.8. The diagrams included in analyses are varied. Most isobar analyses contain at least the diagrams called the *Born terms*: the s-channel proton exchange, t-channel K^+ exchange, and u-channel Λ exchange. In any analysis, however, even these most basic diagrams are given free coupling constant and form-factor parameters, as these values are not experimentally measured. Inclusion of further

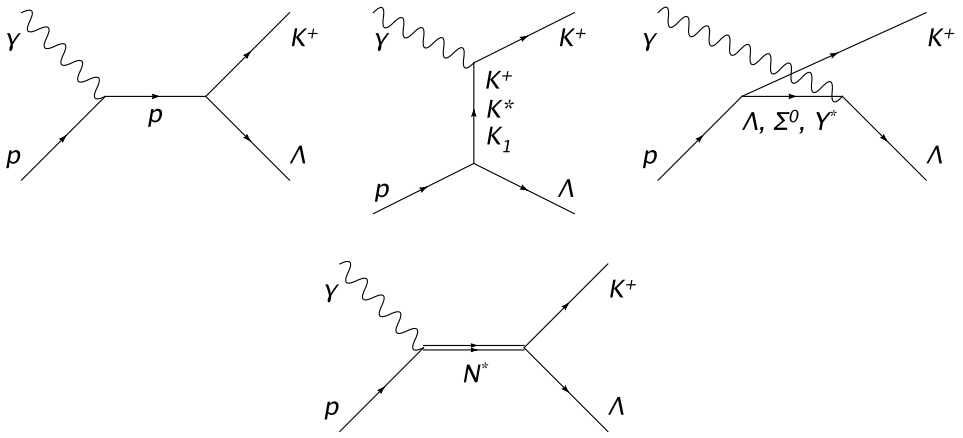

Figure 1.8: Shown above are the Feynman diagrams typical of isobar models (for example [24] or [25]). The top row shows (from left to right) the non-resonant s-, t-, and u-channel diagrams. The diagram at bottom shows s-channel production through an excited nucleon state.

diagrams, such as the u-channel excited hyperon exchanges ($\Lambda(1405)$ and $\Sigma(1385)$) of [27] has also shown interesting results.

A second method, investigated principally by the group at Ghent [28] and Guidal, Laget, and Vanderhaeghen [29], has been to model the t-channel exchange of strange mesons with Regge propagators rather than Feynman propagators. The Regge propagator is an elegant technique which describes the exchange of an entire family of particles characterized by the same quantum numbers but different spins (J). In this method, exchanges of high-J mesons likely to occur at high center-of-mass energies are considered. As such, Regge model builders have found it necessary to use high-energy data ($E_\gamma \approx 16$ GeV [30]) as constraints. We note that prior to this analysis, all world data for $K^+\Lambda$ photoproduction in the resonance region has been at $\sqrt{s} \leq 2.53$ GeV. At these energies there is no way of safely separating resonant and non-resonant production mechanisms. Thus, previous partial wave analyses have fit all processes simultaneously and found varying results for non-resonant production based on the resonant structures included [28].

We now present the results of several recent partial wave analyses of the $\gamma p \to K^+\Lambda$ reaction. The analysis of Mart and Bennhold [25] applied the tree-level isobar model to SAPHIR differential cross section data and found contributions of the $S_{11}(1650)$, $P_{11}(1710)$, and $P_{13}(1720)$ states as well as evidence for the existence of a "missing" D_{13} state at 1894 MeV. This analysis has been developed into the Kaon-MAID code, available at [31]. It was then shown in both [32] and [33] that features in the SAPHIR data at $\sqrt{s} \approx$1.9 GeV could be described by tuning non-resonant models and the need for a missing state was ambiguous. Further analysis of this data showed that a missing state in this energy range could help to explain the data, but its quantum numbers were not constrained by the data. An analysis [34] of early SAPHIR and CLAS data as well as πN scattering data found contributions $S_{11}(1650)$, $P_{13}(1720)$, and $P_{13}(1895)$ states. From these varied results, it is apparent that these early data were not enough to provide conclusive results.

There have also been analyses since the publication of the 2004 CLAS recoil polarization and later CLAS differential cross section measurements. The 2006 analysis from the Ghent group [28] analyzed forward-angle data in a Regge-plus-resonance approach and found evidence for the $S_{11}(1650)$, $P_{11}(1710)$, and $P_{13}(1720)$ states near threshold and P_{13} and P_{11} states at 1.9 GeV. In a dynamical coupled-channel analysis with the $\gamma p \to p\eta$, Juliá-Díaz *et al.* [35] found the need for an S_{11} state at $\sqrt{s} \approx 1.9$ GeV. Most recently, a coupled channel analysis by Sarantsev, *et al.* [36] showed evidence of the coupling of the $S_{11}(1535)$, $S_{11}(1650)$, and $P_{13}(1720)$ to $K^+\Lambda$ at threshold. Evidence for newly

observed $P_{11}(1840)$ and $D_{13}(2170)$ states was found.

The lack of consistency in partial wave analysis results is not due to a lack of effort. These analyses represent great ingenuity and dedication to the field. We remind the reader that five N^* states have been observed to couple to this channel near threshold [5]. Performing a partial-wave analysis in such a region where many partial waves may contribute is extremely difficult and requires data of high precision. As a more accurate picture of non-resonant production mechanisms is assembled and more polarization measurements performed, results should converge. We are fortunate that an easily analyzable channel such as $K^+\Lambda$ seems to provide so much resonant contribution.

1.7 Summary

The self-analyzing nature of the $\Lambda \to p\pi^-$ decay and the relatively simple spin structure of the $\gamma p \to K^+\Lambda$ reaction make it an excellent candidate for searches for excited nucleon intermediate states. As a clearer picture of the full excited nucleon spectrum is formed, the accuracy of the Constituent Quark Model can be truly evaluated and the contribution of other degrees of freedom to QCD can be assessed. Experiments performed in the last fifteen years have added a great deal of data to our knowledge of this reaction, but inconclusive and inconsistent partial wave analysis results suggest that more precise measurements are needed. In Chapter 6, we present our high-precision measurement of the $\gamma p \to K^+\Lambda$ differential cross section and recoil polarization. In Chapter 8, we use these measurements in a mass-independent partial wave analysis in search of N^* states.

Chapter 2

Thomas Jefferson National Accelerator Facility and the CLAS Detector

This analysis focuses on the *g11a* dataset collected in Experimental Hall B of the Thomas Jefferson National Accelerator Facility (TJNAF, JLab) in Newport News, Virginia. Though this analysis investigates the $\gamma p \to K^+\Lambda$ reaction, it should be noted that the *g11a* dataset was initially intended for another purpose. The data were collected in the Summer of 2004 as a part of the E04021 experiment (*Spectroscopy of Excited Baryons with CLAS: Search for Ground and First Excited States*), a high-statistics search for the Θ^+ pentaquark [37]. The run employed a loose trigger which allowed acquisition of final states that were not candidates for Θ^+ production. At the time of its collection, *g11a* was the world's largest dataset for many photoproduction reactions in the non-pQCD energy regime.

The *g11a* run conditions called for a tagged photon beam incident on a liquid Hydrogen target. The CEBAF Large Acceptance Spectrometer (CLAS) Detector was used to observe multi-particle final states with roughly 60% coverage of the full 4π solid angle. All of the *g11a* runs included in this analysis were produced with bremsstrahlung from a 4.023 GeV electron beam incident on a gold foil. The CLAS tagger hodoscope allowed measurement of photons with energies between 20% and 95% of the beam energy, producing data with center-of-mass energies between 1.55 GeV and 2.84 GeV. In its entirety, *g11a* is comprised of ≈20 billion triggers stored as 21 TB of raw data.

This chapter provides detail of the experimental setup including CEBAF, the Hall B tagger, the CLAS detector, and triggering.

2.1 Continuous Electron Beam Accelerator Facility (CEBAF)

The Continuous Electron Beam Accelerator Facility (CEBAF) at Jefferson laboratory is a 6.023 GeV end-point energy electron accelerator designed to deliver electron beam to each of JLab's three experimental halls. An aerial view of JLab is displayed in Figure 2.1. CEBAF is set apart from previous electromagnetic probes (SLAC, DESY, etc.) in its use of superconducting radio-frequency (RF) cavities for electron acceleration. The superconducting nature of the cavities provides two benefits to the overall acceleration: (1) the accelerator is more efficient as no energy is lost by electrons in the cavities, and (2) the non-resistive transmission of electrons through the cavities does not raise the cavities' temperature. The second of these features allows CEBAF to attain a 100% duty factor, as no down-time needs to be devoted to cooling the conducting elements of the

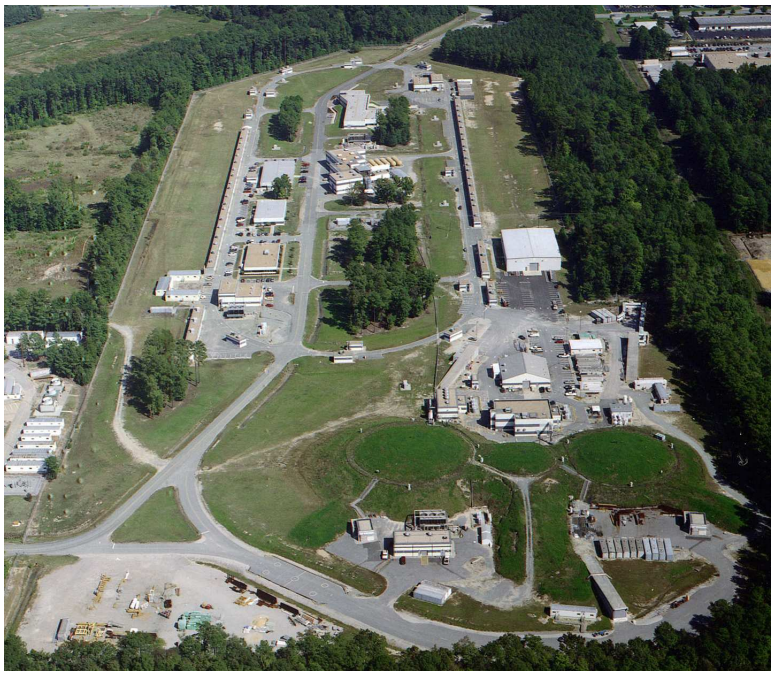

Figure 2.1: An aerial view of CEBAF. The accelerator ring lies underneath the "racetrack"-shaped figure in the top half of the picture. The experimental halls are underneath the three grassy knolls at the bottom of the picture. The CLAS detector is housed in Hall B, the middle hall. Image source: [38].

accelerator. This continuous delivery of electrons to the experimental halls allows for high data rates even at low beam currents, conditions ideal for coincidence experiments.

The injector is the source of CEBAF's electron beam. Free electrons are produced by three lasers (one for each experimental hall), independently pulsed at 499 MHz, incident on a GaAs photocathode. Use of three separate lasers allows for independent tuning of beam characteristics (current, polarization) for each experimental hall. The three lasers are pulsed 120° out of phase, giving the accelerator an overall frequency of 1497 MHz, with each experimental hall receiving electron bunches at 2 ns intervals. The electron bunches are then accelerated to 45 MeV via 2 1/4 RF cavities [39]. To insure that the three interleaved beams will be independently accessible, the electron bunches are cleanly separated using an optical chopper before being injected into the main accelerator.

CEBAF's main physics machine is a 7/8-mile recirculating "racetrack"-shaped accelerator ring. The accelerator's power lies in the 168 superconducting RF cavities in each of two parallel Linear Accelerators (LINACs). Recirculation is facilitated by bending magnets in the curved portions of the tracks (see Figure 2.2); electrons may pass through the pair of LINACs up to five times before being diverted to one of the experimental halls. A pass through each of the LINACs adds 600 MeV to the beam energy; the maximum energy attainable by the full five passes through the loop is 6 GeV. The 168 RF cavities in each of the LINACs are grouped into 20 cryomodules, which cool the cavities by immersion in liquid helium to a temperature of 2 K. At this temperature, the cavities are well within the superconducting regime of niobium [41] and thus transmit electrons non-resistively. A photograph of a typical superconducting RF cavity is provided in Figure 2.3. The accelerating gradient is produced by generating 1497 MHz standing RF waves in the cavities. The phase of

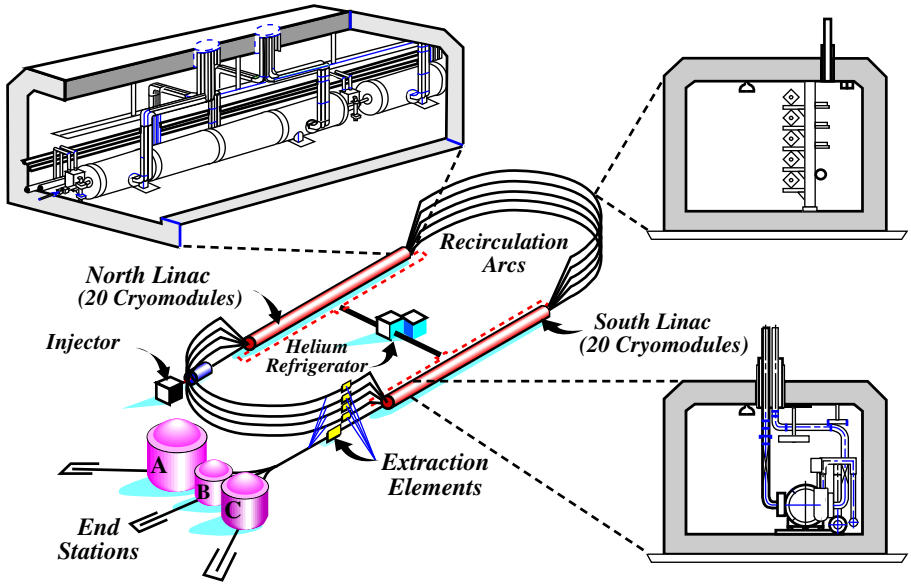

Figure 2.2: A schematic diagram of the Continuous Electron Beam Accelerator Facility. Shown in red are the LINACs composed of 168 (each) superconducting RF cavities grouped into 20 cryomodules. At top right is an exploded view of the recirculation arcs showing the five separate magnet assemblies for up to five beam passes. Experimental halls are shown at lower left. Image source: [40].

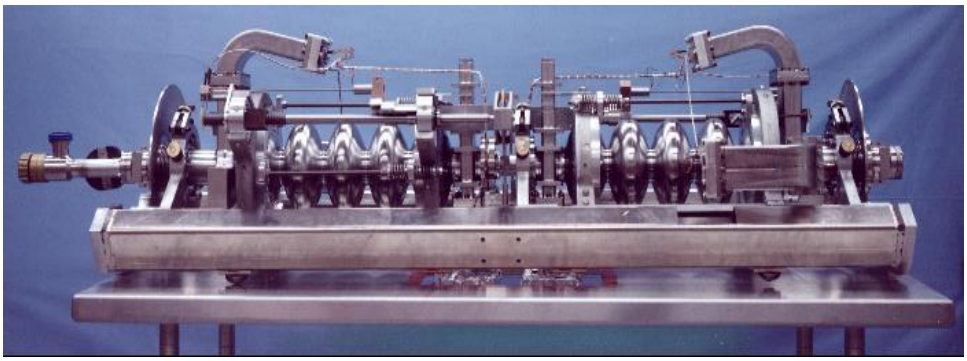

Figure 2.3: A picture of a superconducting RF cavity. Shown above is a pair of superconducting niobium RF cavities. The cavities are the innermost component characterized by the elliptical bulges perpendicular to the beam line. Image source: [38].

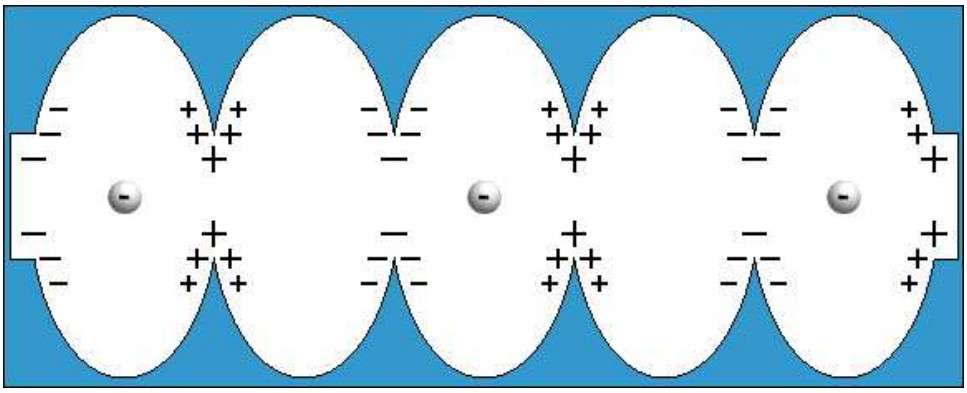

Figure 2.4: A schematic diagram of the superconducting RF cavity. Accelerating fields are established by charge accumulated on the inner tangs of the RF cavity (shown in diagram). These excess charges are the result of standing RF waves in the cavity. The phase of the waves follows the position of the electron bunch in the cavity, ensuring a positive force on the electrons at all times. Image source: [38].

the waves are matched to the electron bunches, creating a positive electric force on the electron bunches at all times (see Figure 2.4) [39]. Each RF cavity is independently instrumented to grant the accelerator a high degree of tunability.

Once a beam bucket has passed through the accelerator ring the desired number of times, it can be separated from the other two beams and sent to one of three experimental halls. At the end of the south LINAC (see Figure 2.2), the three beams are fanned out according to their energy before being sent to the accelerator ring's bending magnets. RF separator cavities make use of the 120° to divert specific electron bunches to a desired hall [39]. This feature allows Jefferson Laboratory to perform experiments requiring different beam energies and currents simultaneously. Though CEBAF is capable of delivering maximum energy (6 GeV) beam to Halls A, B, and C simultaneously, it cannot provide two halls with a single lower energy.

2.2 The Hall B Photon Tagger

For photoproduction experiments, the CEBAF electron beam is converted into bremsstrahlung photons via a gold foil radiator. The high atomic number and density of gold make it an excellent catalyst for the $e_{beam} + \mathrm{Au} \rightarrow e'_{beam} + \mathrm{Au}' + \gamma_{bremsstrahlung}$ reaction. Because the bremsstrahlung photons produced are not mono-energetic, Hall B is equipped with a powerful photon tagger that uses a large magnetic spectrometer to measure the energy of recoiling beam electrons. The energy of the bremsstrahlung photon is then calculated from energy conservation. A schematic diagram of the Hall B photon tagging system is given in Figure 2.5.

2.2.1 Radiator

Several different radiator foils are available for conversion of electron beam into bremsstrahlung photons in Hall B. For the *g11a* data-taking runs, the thickest of these was used, a gold foil with a thickness of 10^{-4} radiation lengths ($646 \mu g/cm^2$). A thinner foil (10^{-5} radiation lengths) was used for "normalization runs" which are not included in this analysis.

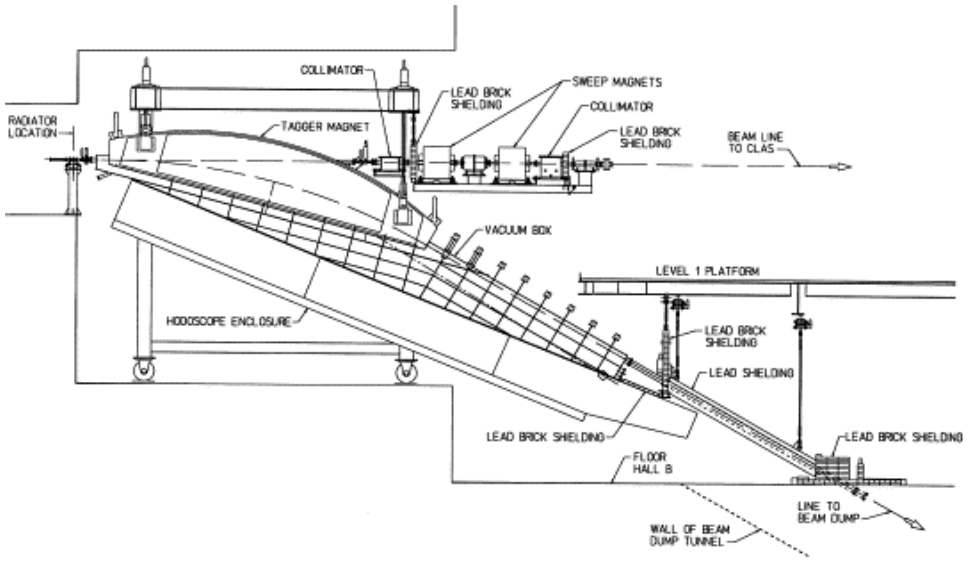

Figure 2.5: A schematic diagram of the Hall B photon tagging system. The Hall B photon tagger allows indirect measurement of photon energy. The energy of a recoil beam electron is measured by the tagger spectrometer (tagger magnet and hodoscope). The energy of the associated bremsstrahlung photon is then ascertained from energy conservation. The bremsstrahlung beam is then collimated and passed to the CLAS detector. Image source: [42].

2.2.2 Magnetic Spectrometer

The Hall B photon tagging system is a magnetic spectrometer designed to measure the energy of the recoiling electrons directly after interaction in the radiator. The photon tagger uses a 1.75T maximum field, normal-conducting dipole magnet to bend both recoiling and non-interacting electrons out of the beamline. Those electrons which did not interact with the radiator (and thus have an energy equal to the beam energy) are bent out of the beam line and discarded in the beam dump. Recoiling electrons (those that *did* interact with the radiator) are bent into the two hodoscope planes below the tagger magnet. Though the tagger magnet was designed to provide a resolution of $2 \times 10^{-4} \times E_{beam}$, the ultimate resolution of the tagger spectrometer is limited to $10^{-3} \times E_{beam}$ by the hodoscope resolution. The tagger's magnetic field is engineered to redirect recoil electrons with energies between 20% and 95% of the beam energy into the hodoscope.

The tagger hodoscope is comprised of two planes of scintillator detectors, each with a different purpose. The top plane consists of 384 thin scintillator paddles which determine the momentum of the recoiling electron (this plane is referred to as the *E-plane*). These E-plane scintillators are 20 cm long, 4 mm thick, range in width from 8 cm to 16 cm. The thinness of the scintillators makes energy lost by electrons as they pass through the material small. To give the effect of further segmentation and thus better resolution, the scintillators are arranged in an overlapping formation. The scintillator overlap increases the effective number of E-counters to 767 for an energy resolution of $\approx 10^{-3} \times E_{beam}$. The lower scintillator plane determines precise timing information of the recoiling electrons (hence called the *T-plane*). The T-plane lies 20 cm below the E-plane and is made up of 61 scintillators (*T-counters*). The T-counters are 2 cm thick which results in a timing resolution of 110 ps. All scintillators in both the T and E-planes are arranged so that electron trajectories are normal to their surfaces. A detailed schematic of the tagger magnet and hodoscope is given in Figure 2.6.

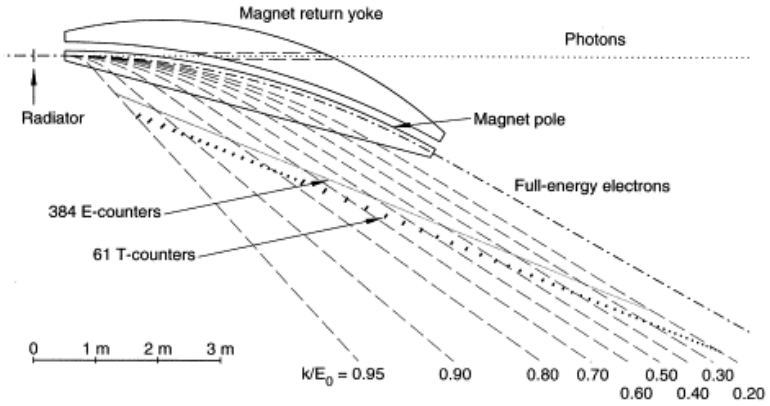

Figure 2.6: A schematic diagram of the Hall B tagger magnet and hodoscope. Dashed lines show the trajectories of recoil electrons associated with photons of given energies (E_0 is the beam energy). The photon tagger detects recoil electrons with energies between $0.2 \times E_0$ and $0.95 \times E_0$. E-counters cannot be seen individually because of their fine segmentation. Image source: [42].

2.2.3 Tagger Readout and Logic

E-counter scintillators are each instrumented with with a single photomultiplier tube (PMT), the signals of which are passed to a discriminator. T-counter scintillators are instrumented with a PMT at each end feeding a constant fraction discriminator (CFD). T-counter signals that pass the CFD are sent to a Master Or (MOR) and a time-to-digital converter (TDC) array. The TDCs allow access to precise timing information for each T-plane hit as well as the total number of hits recorded in the tagger. The total number of recoil electron hits in the tagger allows calculation of energy-dependent photon flux. The timing information of individual electrons is used to associate events recorded by the detector with individual photons during offline analysis. The T-counter MOR is used to set the *g11a* event trigger which then sends a stop signal to the E-counter TDC array. E-counter readout associated with this trigger is then written to the data stream along with T-counter readout that set the trigger. A schematic of the Hall B tagger logic is provided in Figure 2.7.

Before reaching the CLAS detector, the produced photon beam passes through three collimators. Any charged particles created by interaction of the photon beam and collimators are removed from the beamline by two sweep magnets placed between the collimators. A more detailed exposition of the Hall B Photon Tagger can be found in [42].

2.3 The CLAS Detector

The main physics detector in Experimental Hall B is the CEBAF Large Acceptance Spectrometer (CLAS) Detector. CLAS is comprosed of several detector subsystems, not all of which are useful for every experiment. The *g11a* run period used the start counter, drift chambers, time-of-flight scintillators, and toroidal magnet, as well as a *g11a*-specific physics target. These detector components that were used for the *g11a* production run will be described in greater detail below. A photograph and schematic drawing of the CLAS detector are given in Figures 2.8 and 2.9.

It is worth mentioning that CLAS has two other detector subsystems that are used primarily for electroproduction experiments. CLAS has a gas Čerenkov detector that is composed of 216 optical modules. In electroproduction experiments, the gas Čerenkov detector is used to distinguish recoil electron tracks from π tracks produced in the target [43]. CLAS is also equipped with forward electromagnetic lead-scintillator calorimeters (EC) that are used primarily for electroproduction

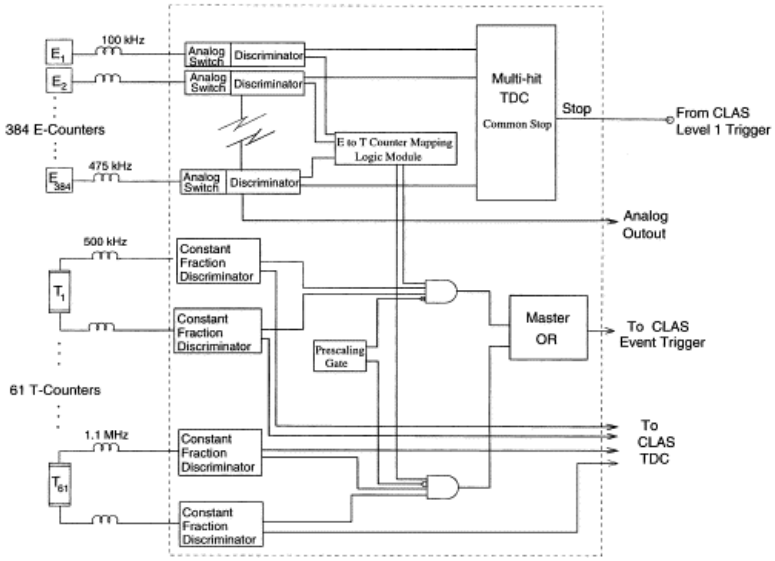

Figure 2.7: A schematic diagram of the Tagger instrumentation logic. Individual T- and E-counters are shown on the left-side of the diagram. T-counter hits are used to set the event trigger. The CLAS Level 1 trigger then provides a common stop to the E-counter TDC array. Image source: [42].

experiments. The EC serves several purposes including functioning as the main electron trigger for electroproduction experiments and detecting neutrals (γ, n). More information about these detector subsystems can be found in [43] and [44].

2.3.1 The *g11a* Cryotarget

CLAS's versatility as a detector has allowed the use of several target geometries and materials during production runs. The cryotarget cell used for the *g11a* run period was a cylindrical Kapton chamber 40 cm in length with a 2 cm radius [45]. The target material used was liquid H_2. A schematic of the *g11a* cryotarget is provided in Figure 2.10. Measurements of the target's temperature and pressure were taken approximately once per hour. Calculations of target density for each run have been made by M. Williams. The target density averaged over runs has been calculated to be $0.07177 g/cm^3$ with relative run-by-run fluctuations of about 0.1% [4].

2.3.2 Start Counter

The triggering scheme of the *g11a* run period benefited from the installation of a new start counter detector. The start counter is a PMT-instrumented scintillator detector that surrounds the CLAS cryotarget (see Figure 2.11). The start counter is divided into six sectors (matching CLAS), each of which is constructed of four independently-instrumented scintillator strips. Timing resolution of the start counter is ≈400 ps. Raw timing information from the start counter was not used for this analysis; however, start counter contributions to the trigger efficiencies played a large role in the analysis of the $\gamma p \to K^+\Lambda$ reaction in *g11a* (see §7.3.3). More information on the CLAS start counter can be found in [46].

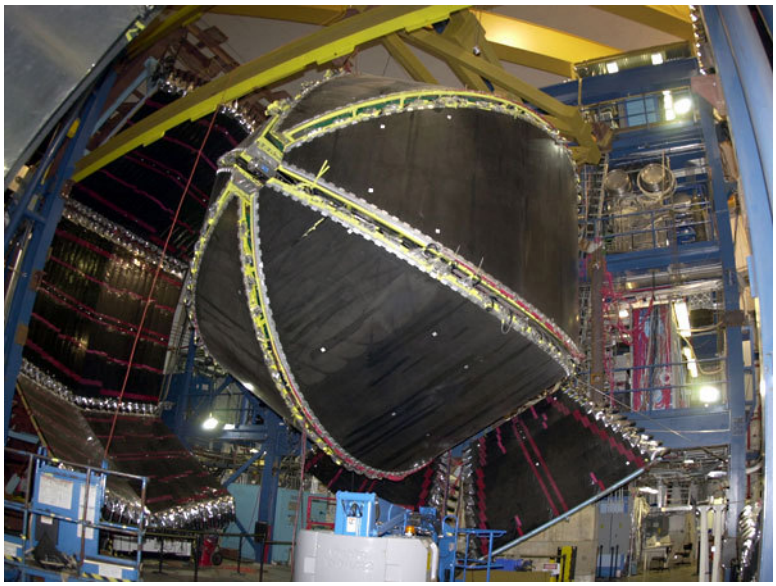

Figure 2.8: A photograph of the CLAS detector. This picture of CLAS is taken from the downstream direction. The six sections visible are the region-3 drift chambers. TOF scintillators are pulled away from the drift chambers and can be seen at left. Image source: [38].

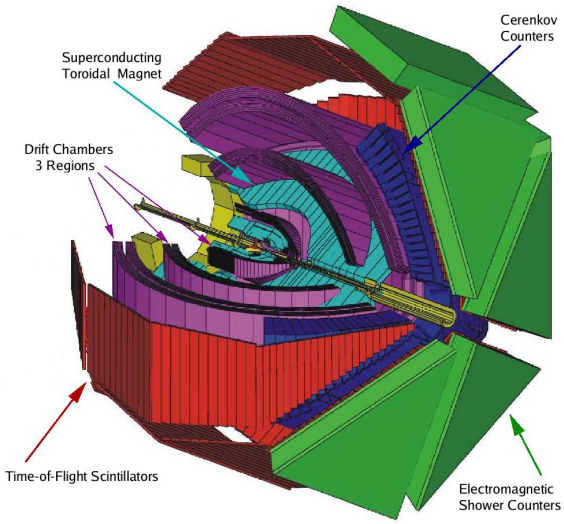

Figure 2.9: A schematic diagram of the CLAS detector. Detector subsystems are color-coded as follows: drift chambers shown in violet, toroidal magnet in light blue, TOF scintillators in red, Čerenkov detectors in dark blue, electromagnetic calorimeters in green. Image source: [38].

Figure 2.10: A schematic diagram of the *g11a* Cryotarget. The cryotarget cell used for the *g11a* run period was designed by Steve Christo. It was 40 cm long, 4 cm in diameter and filled with liquid H_2. Image source: [45].

2.3.3 Superconducting Toroidal Magnet

As a magnetic spectrometer, CLAS's analysis power lies in its magnetic field. CLAS's magnet is a superconducting toroidal magnet composed of six kidney-shaped coils connected in series, designed and tested by Oxford Instruments, Ltd. in Witney, UK. The toroidal magnet is capable of generating a maximum field strength of 3.5 T at an operating current of 3861 A. The six-fold cylindrical symmetry of CLAS is matched by the magnet geometry; the six torus coils are arranged at 60° intervals about the beamline. The magnet coils are located between the Region-1 and Region-3 drift chambers, restricting the bulk of the magnetic field to the volume encompassed by the tracking detectors. The torus coils are cooled to a temperature of 4.4K using liquid He supplied by CEBAF's central cryogenic facility. A photograph of the CLAS superconducting toroidal magnet is given in Figure 2.12.

For the *g11a* run period, the torus was run in *normal mode* at a current of 1920 A. This configuration created a maximum field of ≈1.8 T in a clockwise direction about the beamline when viewed from upstream. Thus, positively-charged tracks were bent away from the beamline, negative tracks towards the beamline. Operating at half of the maximum field strength, though a compromise in overall momentum resolution, allowed a greater acceptance for negatively-charged particles. More information regarding design and testing of the CLAS superconducting toroidal magnet can be found in [47].

2.3.4 Drift Chambers

CLAS is equipped with three drift chamber detector systems that detect charged tracks as they propagate through the detector. The drift chambers are divided into three regions (see Figure 2.13). Region 1 lies between the physics target/start counter and the innermost part of the toroidal magnet coils. The Region 2 drift chambers occupy the region of CLAS with the strongest magnetic field. The Region 3 drift chambers are the outermost tracking chambers, located outside of the magnet coils. The magnetic field strength is minimal in Regions 1 and 3.

Each region of the CLAS drift chambers is divided into six sectors, each of which subtends 60° of the plane perpendicular to the beamline. Each sector of each drift chamber is composed of two

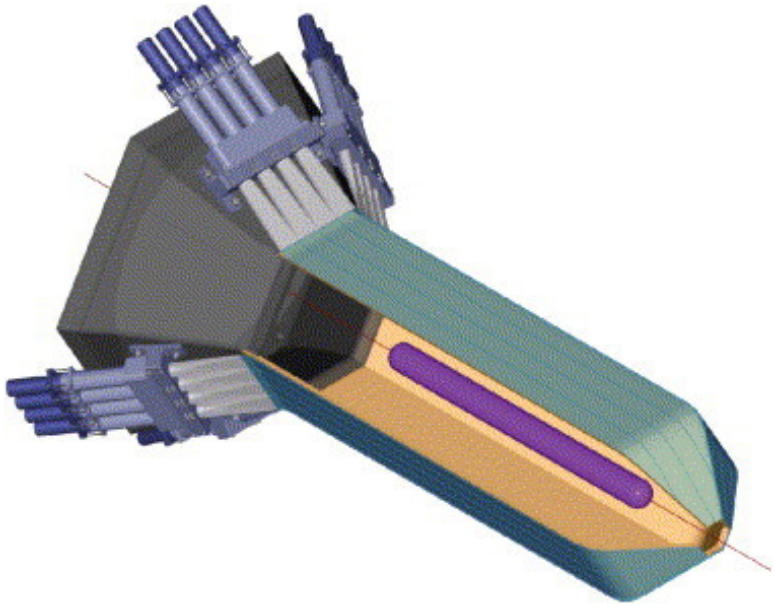

Figure 2.11: A schematic diagram of the CLAS Start Counter. The start counter used for the *g11a* run period is a six-sector scintillator detector. Each sector is composed of four independently-instrumented scintillator strips. Image source: [46].

superlayers. The superlayers house an array of drift cells defined by six 140 μm gold-plated Al field wires in a normal-hexagonal configuration around a 20 μm gold-plated tungsten sense wire. The drift cells are arranged such that adjacent cells share two field wires. The radius of drift cells ranged from 15-17 mm in Region 1 to 26-29 mm in Region 2 to 40-45 mm in Region 3. In each sector, one superlayer had wires oriented in the plane perpendicular to the beam line. The wires in the other superlayer were oriented at a 6° angle out of this plane to improve resolution in the ϕ-direction. The drift chambers were filled with a gas mixture of 90% Ar and 10% CO_2. During operation, field wires were kept at a negative high voltage, creating a potential difference between them and the sense wires. Electrons freed by charged tracks ionizing the gas mixture were then collected by the positively charged sense wires. Signals from the sense wires were processed by preamplifiers and amplifier discriminator boards before being recorded by TDCs. A more detailed exposition of the CLAS drift chamber system design, fabrication, and testing can be found in [48], [49], [50], and [51].

2.3.5 Time-Of-Flight Detectors

The final CLAS subsystem that is essential to this analysis is the Time-Of-Flight (TOF) scintillator shell. The TOF shell subsystem provides precise timing information for charged tracks as they exit CLAS. The TOF shell is a six-fold-segmented array of scintillator bars that are located about 4 m from the CLAS target and oriented perpendicular to the beamline. Each sector of the TOF shell is made up of 57 individual scintillator bars fabricated from Bicron BC-408 material. As the majority of tracks travel trough the forward region of CLAS (at an angle less than 45° from the beamline), scintillator bars in this region are narrower (15 cm). At less forward angles (greater than 45° from the beamline), TOF scintillators are wider (22 cm) (see Figure 2.14). The lengths of TOF scintillators varied from 32 to 445 cm, as dictated by the shape of the sectors. All scintillator bars in the TOF shell are 5.08 cm thick, a dimension that provides measurable signal for minimum-ionizing tracks.

Figure 2.12: Photograph of the CLAS Superconducting Toroidal Magnet. Image source: [47].

The TOF scintillators are each instrumented with two PMTs, one coupled to each end of the bar via a short Lucite light-guide. The eighteen least forward scintillator bars are coupled in nearest neighbor pairs, reducing them to nine effective scintillators. The timing resolution of the scintillators is between 80 and 160 ps. This wide range in timing resolution is due to the wide range in scintillator lengths.

Because of its excellent timing resolution and acceptance of charged tracks, the TOF shell was an important part of the *g11a* trigger. The TOF shell was also designed with the goal of aiding π/K separation for track momenta up to 2.0 GeV/c; thus, we relied heavily on the TOF detector for particle identification in this analysis. Further details concerning the design, construction, and testing of the TOF detector subsystem can be found in [52].

2.4 Beamline Devices

Physics experiments in Hall B benefit from several instruments used for beamline diagnostic studies. For *g11a*, instruments for measuring beam position and profile were located upstream from the CLAS detector. Beam positioning information was gathered by RF-cavity beam-position monitors (BPMs) located 36.0 and 24.6 m from the physics target [53]. Beam profile and current were measured with harp scanners, tungsten and iron wires that were pulled through the electron beam in the two directions perpendicular to the beamline. Electrons scattered by the harp wires were detected by PMT arrays located upstream from CLAS. Harp scanners were located at 36.7, 22.1, and 15.5 meters upstream from the CLAS target.

Instruments for measuring photon flux were located downstream from the CLAS detector. The total absorption shower counter (TASC) was a lead-glass scintillator array, assumed to have a 100% photon detection efficiency. The TASC could not be used with the higher-current *g11a* runs, and thus was only used for several lower-current "normalization" runs. Though not used during production runs, the TASC was a vital piece of hardware because it was used to calculate the *tagging ratio* of the tagger t-counters (the fraction of hits in the tagger t-counters that corresponded to photons that actually made it to the target). Another piece of diagnostic hardware, the pair spectrometer (PS), measured the rate of production of e^+e^- by an aluminum converter placed in the beamline. The PS was used during production runs, but was calibrated against the TASC during normalization runs. The pair counter (PC) utilized a four-scintillator array to detect e^+e^- pairs created by a thin

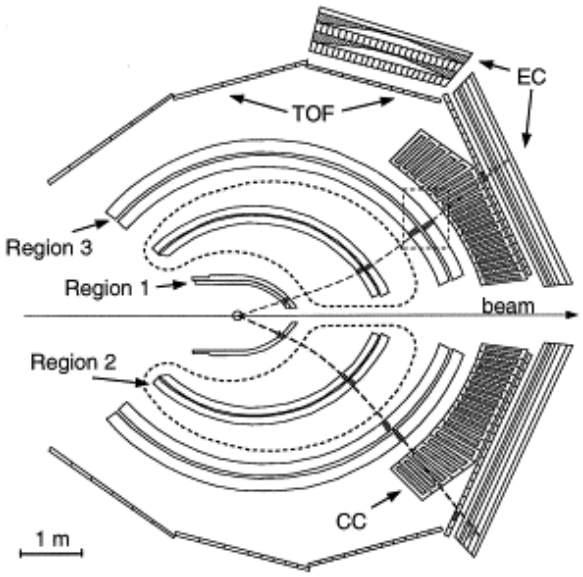

Figure 2.13: Diagram of the CLAS Detector Subsystems (cutaway). This image shows the locations of several detector subsystems inside of CLAS. Toroidal magnet coils are represented by the kidney-shaped dashed lines. The three different drift chamber regions are labeled. Shown are two positively-charged tracks being bent by the magnetic field in the volume between Regions 1 and 3. Image source: [48].

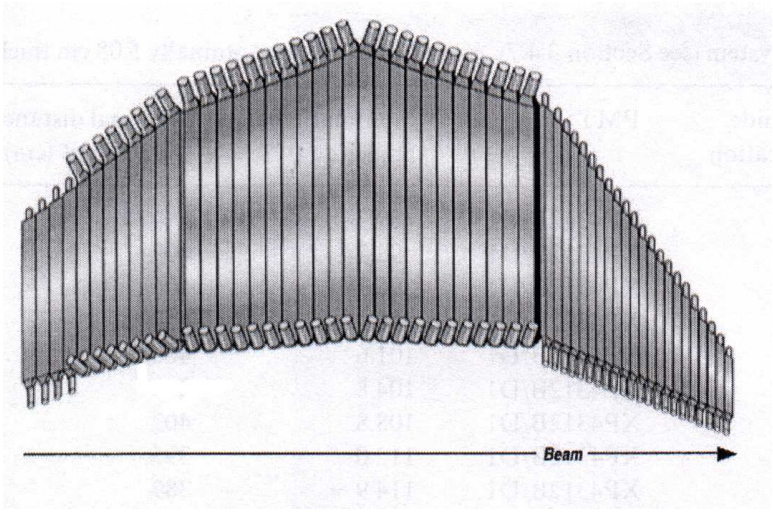

Figure 2.14: Diagram of the CLAS time-of-flight scintillators. Shown is one sector (one sixth of CLAS) of the TOF scintillator shell. Scintillator bars are instrumented with PMTs are each end. Image source: [52].

aluminum foil in the beamline. The PC was used to monitor photon beam profile downstream of the CLAS detector.

2.5 *g11a* Triggering and Data Acquisition

The *g11a* data run was designed with a somewhat specific purpose: to investigate the existence of a pentaquark state. To reduce the number of background events in the dataset, *g11a* used a more restrictive trigger than other CLAS production runs. For a given event to be recorded, it had to set both the tagger Master OR (MOR) and the CLAS Level 1 trigger within a coincidence window of 15 ns. To reduce the number of recorded events with center of mass energies below that of the theorized pentaquark, only the 40 tagger T-counters corresponding to the highest energy photons ($E_\gamma > 1.56$ GeV) were included in the MOR. Events created by lower-energy photons were recorded when a higher-energy photon was present in the same timing window. For an event to set the CLAS Level 1 trigger, coincidence between the start counter and TOF paddles had to be observed in two separate sectors. The window for TOF and start counter coincidence was set to 150 ns [4]. This constriant requires an event to have at least two charged tracks in order to be recorded. Once an event passed the *g11a* trigger, the data acquisition system (DAQ) collected from all detector subsystems information that was necessary for calibration and analysis.

2.6 Summary

Though not it's main purpose, the *g11a* dataset collected by the CLAS Detector in Hall B at Jefferson Laboratory is well-suited to study of hadron photoproduction in the non-perturbative QCD energy regime. Our analysis of $K^+\Lambda$ photoproduction in *g11a* benefits greatly from the tagged photon beam created by CEBAF and the energy resolution of the Hall B photon tagger. In this chapter, we have described the construction and motivation of the CLAS detector. In the next several chapters, we present detailed descriptions of our extraction of the $\gamma p \to K^+\Lambda$ signal in *g11a* (Chapter 3) and our functional understanding of the CLAS detector (Chapters 4 and 7).

Chapter 3

Data Reduction and Event Selection

The *g11a* dataset was collected by the CLAS Collaboration during the period of May 17 to July 29, 2004. *g11a* is comprised of roughly 20 billion triggers, represented as 21 TB of raw detector output data. Before physics analysis can be done, the dataset must be *cooked*; the raw signals must be interpreted as information regarding the track components and kinematics of each event. It is during the cooking process that detector components are checked for functionality and calibrated. *g11a* was cooked by Maurizio Ungaro at INFN [55]. At the time of this analysis, *g11a* was the world's largest photoproduction dataset in the medium-energy regime.

Because the Λ is neutral and unstable ($c\tau = 7.89$ cm), we gain access to it via its predominant charged decay mode, $\Lambda \rightarrow p\pi^-$. Unfortunately, the cross section for the $\gamma p \rightarrow K^+\Lambda$ reaction is small in comparison to more common reactions. Thus, the vast majority of the *g11a* dataset is composed of events that are extraneous to our analysis. In order to separate $\gamma p \rightarrow K^+\Lambda$ *signal* events from these irrelevant *background*, we began by examining a $++-$ charged track skim of the *g11a* dataset for $K^+\Lambda$ signal in the $K^+p\pi^-$ final state. We then examined a large portion (28%) of the full two-track dataset by investigating the $K^+p(pi^-)$ final state. This chapter outlines the procedures by which we have extracted $K^+\Lambda$ events from *g11a* as well as all cuts and corrections that were made to the data for both the two-track and three-track data sets.

3.1 Excluded Runs

The *g11a* dataset was collected in shorter intervals, called *runs*, each containing roughly 10 million triggers. This subdivision allowed the study of time-dependent detector and data acquisition problems to be addressed on a run-by-run basis. "*g11a*" refers to 386 individual CLAS runs between 43490 to 44133. Runs between 43490 and 44107 were collected with a 4.019 GeV electron beam, whereas runs between 44108 and 44133 were collected with a 5.021 GeV beam. Though it is possible to amalgamate the two beam energies into one analysis, we omit the higher-energy dataset from this analysis to avoid any systematic differences. Further, runs between 42490 and 43525 were part of the *g11a commissioning* period. These runs were taken in order to facilitate testing and set-up of CLAS and are not considered "production" runs. We omit these runs as well.

There are several other runs which were later found to be unreliable and are thus excluded from our analysis. While *g11a* was being recorded, a logbook was kept of all shift workers' observations. The CLAS *g11a* logbook entries for runs 43981-43982 show that there were problems with the drift chambers during these runs. Similarly, logbook entries for runs 43989-43991 show problems with the DAQ system. In order to study the *g11a* trigger, several runs were taken with different triggering

Excluded Run	Description
43490-43525	commissioning runs
44108-44133	5.021 beam energy
43675-43676, 43777-43778, 44013	alternate trigger
43989, 43990-43991, 44000-44002, 44007-44008, 44010-44012	TOF problem in sector 2
43586-43589, 43590-43596	TOF problem in sector 3
43588, 43757	abnormal $K^+\Lambda$ yield

Table 3.1: Table of *g11a* runs excluded from this analysis

schemes: 43675-6, 43777-8, 44013. Several runs showed systematic problems with the DC power supply to the TOF counters in sector 2 (runs 43989, 43990-1, 44000-2, 44007-8, 44010-2) and sector 3 (runs 43586-9, 43590-6). Lastly, runs 43588 and 43757 exhibited abnormal flux-normalized $K^+\Lambda$ yields (see §4.6) and are omitted from this analysis. All of the runs listed above are excluded from our analysis. A summary of these is provided in Table 3.1. The fraction of 4.019 GeV beam-energy triggers excluded by omitting these files is roughly 6%.

For the $K^+p\pi^-$ final state ("three-track") analysis, all *g11a* runs not mentioned as excluded were used. For the $K^+p(\pi^-)$ ("two-track") analysis, however, we used only runs in the range 43600-43906, roughly 28% of the full dataset. Because the amount of recorded $K^+\Lambda$ events in the two-track topology is larger than that of the three-track topology by a factor of the π^- acceptance ($\approx 20\%$), only a fraction of the two-track dataset is needed to provide comparable results.

3.2 Kinematic Fitting

Our analysis, as well as tagger and momentum corrections employed in our analysis, makes heavy use of kinematic fitting [56]. This section give a brief sketch of the purpose and utility of the kinematic fitter.

Kinematic fitting is a means of improving the precision of measured quantities by imposing constraints. When the CLAS detector records an event, the precision of the measured quantities is dictated by uncertainties inherent to the detector (tracking resolution). For a measured quantity, we say that:

$$\eta = y + \epsilon, \tag{3.1}$$

where y is the *actual* value that would have been measured by CLAS in the absence of measurement error ϵ, and η is the measurement result. For a given event, however, we may impose constrains (*i.e.* conservation of energy and momentum) based on a physics hypothesis which can be used to refine the measurements on an event-by-event basis and to obtain estimators for y (called $\hat{y}$).

The kinematic fitter developed at Carnegie Mellon uses the method of Lagrange multipliers to perform a least squares fit of a hypothesis, dictated by physics constraints, to the measured quantities. The process of kinematic fitting begins with the selection of a hypothesis for an event. As an example, assume that CLAS measures a n-track final state (t_1,t_2, ...t_n) and associates the event with a given photon, γ_0. A hypothesis that we wish to fit to the event is then represented by a physical reaction in which physical conservation laws are implicit. This hypothesis can have the same number of final-state particles (*i.e.* $\gamma p \to XYZ$) or it can assume that CLAS was unable to reconstruct one of the tracks (*i.e.* $\gamma p \to XYZ(W)$). In the former, the fit has four constraints:

conservation of energy and conservation of three-momentum. In the latter case, the fit is less-constrained; the momentum of the missed particle is unknown. The fit then uses the constraint equations to make estimations of the of the *actual* quantities.

In order to use the kinematic fit to select events, we need to determine a "goodness of fit" given a physics hypothesis. This goodness of fit comes naturally in the case of least squares fitting, as the minimization quantity follows a χ^2-distribution with $(q-d)$ degrees of freedom where q is the number of constraints and d is the number of unknown parameters [57]. We assign a *confidence level* (CL) to a fit and event as

$$CL = \int_{\chi^2}^{\infty} f(z;n)\,dz. \tag{3.2}$$

where z represents a fit quantity and $f(z;n)$ is the χ^2 probability density function with n degrees of freedom. The confidence level represents the probability that a second event chosen from a statistical distribution will yield a χ^2 greater than that obtained from the fit [58]. Confidence levels from events that satisfy the fit hypothesis will populate the range $(0,1]$ evenly. Events that are not properly described by the fit hypothesis will have very small confidence levels. Thus, to select events of a particular reaction from a dataset, we may kinematically fit each event using the reaction as our physics hypothesis and cut events which give a small confidence level (*e.g.* $CL < 10\%$). Because the CL distribution for signal events is flat, we will be cutting a small, well-understood percentage (10%) of signal. Our means of checking that the kinematic fit is working properly is to examine the *pulls* for each measured quantity, a measure of the difference between the measured quantity and the *actual* quantity relative to their errors. The pull z for a measurement y, estimation η, and errors $\sigma(y)$ and $\sigma(\eta)$ is written as

$$z = \frac{\eta - y}{\sqrt{\sigma^2(y) - \sigma^2(\eta)}}. \tag{3.3}$$

Pull distributions should be Gaussian distributions centered at 0 with unit mean.

A great deal of effort has been invested in building and testing the kinematic fitter for *g11a*, mostly in the area of calculating an empirical parametrization of the *g11a* covariance matrix. The result, as is demonstrated in the following sections, is an extremely efficient tool for both detector and data analysis.

3.3 Corrections to Measured Momenta

The CLAS detector's precision and powerful analysis tools such as the kinematic fit allow us to use CLAS data to examine systematic effects due to detector subsystems. The high statistics of the *g11a* dataset has allowed the CLAS collaboration to calculate empirical corrections for these systematics. Described in this section are the *eloss* package used to correct reconstructed tracks' momenta according to their energy losses in the detector and the tagger and momentum corrections derived by the PWA group at CMU. We have applied these three corrections to events in our analysis and found greater precision in reconstructed momenta.

3.3.1 Energy-Loss Corrections

The first tracking component of CLAS that a particle created in the target encounters is the Region 1 drift chamber, roughly 0.75 m from the event vertex. Thus, before the track's momentum and energy can be measured by CLAS, it may pass through material in which it loses energy, namely the target, target cell, beam pipe, start counter, and volume between start counter and inner drift chambers. To accurately analyze physics at or near the event vertex, the measured momenta were corrected according to track particle type and material through which it passed. For CLAS analyses, these corrections are handled by the *eloss* package, written by Eugene Pasyuk at ASU [59].

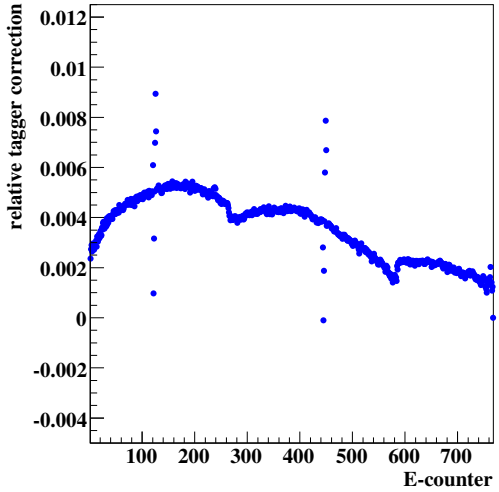

Figure 3.1: Shown above are the relative tagger corrections for each tagger E-counter for the *g11a* dataset as calculated in [4]. Sagging of the focal plane between its four support yokes can be seen in the structure of the corrections. The twelve points that do not follow the trend of the corrections are the result of mis-cabling of the E-counters during data taking. Image source [4].

In previous CLAS $\gamma p \to K^+\Lambda$ analyses, energy-loss corrections were applied to all particles assuming that their associated tracks began at the *event* origin. Due to the macroscopic path length of the Λ ($c\tau = 7.89$ cm), this correction is not correctly applied to the p and π^- tracks. In the three-track analysis where both the p and π^- momenta are observed, we are able to ensure a more accurate energy-loss correction. We first recalculated the event vertex using the K^+ momentum and idealized beam momentum. We then recalculated the Λ decay vertex using the p and π^- momenta. All vertex calculations were performed using *MVRT*, a vertexing package written by J. McNabb [12]. Finally, we applied energy-loss corrections these more accurately defined tracks.

3.3.2 Tagger Corrections

Physical distortions of the Hall B photon tagger's focal plane give rise to inaccuracies in its detection of recoil electrons and thus photon energy. This effect has been examined via a kinematic fit to the inclusive $\gamma p \to p\pi^+\pi^-$ channel in both the *g1c* [60] and *g11a* datasets [4]. Tagger corrections were calculated by comparing the *measured* photon energy to the energy constrained by the kinematic fit. A systematic correction was found for each tagger E-counter (see Figure 3.1). These results have been interpreted as due to sagging of the focal plane between its four support yokes [61]. This sag displaces the narrow E-counters from their ideal locations, causing them to detect electrons with slightly different energies.

We have applied the derived *g11a* tagger corrections to each event in this analysis according its associated tagger E-counter.

3.3.3 Momentum Corrections

The CLAS detector's momentum reconstruction power lies in its toroidal magnetic field and tracking chambers. Discrepancies exist between the magnetic field at the time of data taking and CLAS's "ideal" magnetic field map. Similarly, the spatial configuration of the drift chambers differs slightly

from the "ideal" configuration due to misalignment and wire sag. These discrepancies give rise to inaccuracies in the reconstructed momenta.

Momentum corrections for the *g11a* run period have been derived using the $\gamma p \to p\pi^+\pi^-$ channel [62]. Tagger and energy-loss corrections were applied to each $p\pi^+\pi^-$ event in which all final state tracks were reconstructed by CLAS. Three separate kinematic fits were then performed, each treating one of the detected final-state particles as "missing": $\gamma p \to p\pi^+(\pi^-)$, $\gamma p \to p(\pi^+)\pi^-$, and $\gamma p \to (p)\pi^+\pi^-$ hypotheses. Measured momenta for the "missing" particles were then compared to the missing momenta from the kinematic fits. Corrections were calculated for each CLAS sector and particle charge. Each sector was divided into twelve 5° bins in the azimuthal angle ϕ. Each ϕ bin was then divided into fifteen polar angle (θ) bins: nine 5° bins in the range $5^\circ \leq \theta < 50^\circ$, four 10° bins in $50^\circ \leq \theta < 90^\circ$, and two 25° bins in $90^\circ \leq \theta < 140^\circ$. Corrections to the magnitude of momentum for each track charge were calculated in each of the angular bins, and were typically found to be less than 10 MeV/c.

For our analysis, we applied momentum corrections to all final-state particles according to their charge and trajectory.

3.3.4 Effects of Corrections

We investigate the effects of the *g11a* energy and momentum corrections on the $\gamma p \to K^+\Lambda$ channel by plotting both the missing mass off the K^+ and $p\pi^-$ invariant mass before and after the corrections (see Fig 3.2). Events that are considered in this comparison are those that pass a kinematic fit to a $\gamma p \to K^+p\pi^-$ hypothesis with a confidence level of 1% or greater. Note that these quantities are both a measure of the Λ mass, which the PDG reports to be 1.115687 GeV/c^2. The effect on the $p\pi^-$ invariant mass distribution is minimal. The distribution's mean is shifted from 1.11497 GeV/c^2 to 1.11616 GeV/c^2, a difference of 0.0042% from the actual Λ mass. The width of the distribution is reduced from 1.771 MeV/c^2 to 1.622 MeV/c^2, an improvement of 8%. The missing mass off the K^+ distribution, however is rectified dramatically by the corrections. The measured missing mass distribution is non-Gaussian in shape, and cannot be fit reliably to a Gaussian and polynomial background. After corrections are applied, the distribution assumes a much more Gaussian shape with a mean of 1.11639 GeV/c^2 and width of 7.7449 MeV/c^2.

3.4 Event Filter: Kinematic Fits of $\gamma p \to K^+p\pi^-$ and $\gamma p \to K^+p(\pi^-)$

To facilitate easier data analysis, we wished to reduce the entire *g11a* dataset to a dataset containing only events that were likely to come from the $\gamma p \to K^+\Lambda$ reaction. This reduction was done primarily by the kinematic fitter. We begin with a discusstion of our fit to the three-track final state topology and follow with that of the two-track topology.

3.4.1 $\gamma p \to K^+p\pi^-$

For the $K^+p\pi^-$ topology, we began by applying to the data two very loose missing mass cuts:

(1) require total missing mass to be between -300 MeV/c^2 and 300 MeV/c^2

(2) require missing mass off K^+ to be less than 1.4 GeV/c^2.

These cuts greatly reduce the number of ineligible backgound events that we kinematically fit. We applied momentum and energy-loss corrections to the remaining candidate events. We then performed a $4C$ kinematic fit of the events to a $\gamma p \to K^+p\pi^-$ physics hypothesis. We used the results of this fit to cut out any events yielding a confidence level less than 1%.

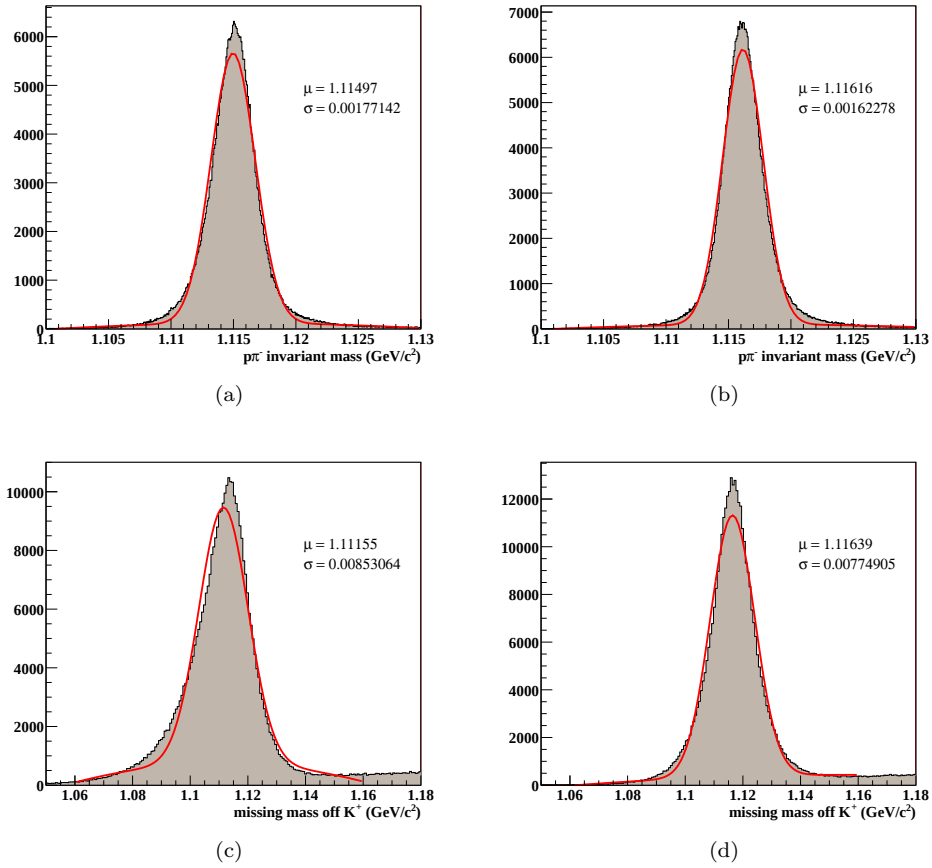

Figure 3.2: Plots showing the effects of energy-loss and momentum corrections on missing mass off K^+ and invariant mass of $p\pi^-$ system. Histograms (a) and (b) show the $p\pi^-$ invariant mass before and after energy and momentum corrections. Mean (μ) and variance (σ) of the distributions are from fits (shown in red) to Gaussian and 2^{nd}-order polynomial background. The difference is minimal due to the small break-up momentum of the Λ. Histograms (c) and (d) show the missing mass off K^+ before and after corrections. Fitting of the distributions is performed as in (a) and (b). Here, the effect of the corrections is noticeable. The fit demonstrates how the non-Gaussian shape of the distribution is tamed by the corrections.

Results of the kinematic fit are shown in figure 3.3. We see that the confidence level distribution for signal events is reasonably flat. This is a good indicator that the kinematic fit is working properly for this channel. Also shown is the effect of the confidence level cut on the missing mass off K^+ distribution. The 1% confidence level cut is extremely effective in its removal of background.

Were the kinematic fit perfect, the amount of signal lost to the 1% confidence level cut would be 1%, as described in §3.2. However, signal events which the e-loss and momentum corrections were not able to rectify are likely to have lower confidence levels because conservation of energy and momentum would have been harder for the kinematic fit to enforce. One possible source for such events are so called "hard scatters," or tracks that interact with the nuclei of detector material rather than electrons. Tracks that experience hard scatters before they are tracked by CLAS may exhibit large inaccuracies in their recorded momenta. Hard scatters affect a very small fraction of the data. A larger contributor to signal loss is non-Gaussian errors attributed to energy loss of tracks in material. The function describing the energy loss spectrum acutally takes the form of a skewed Landau distribution [5]. As the kinematic fitter assumes that this distribution is Gaussian, confidence levels are slightly inaccurate for these events. Fortunately we are able to simulate these effects and ensure that the same percentage of signal is lost in both data and Monte Carlo.

Using the 1% cut on confidence levels from a kinematic fit to $\gamma p \to K^+ p\pi^-$, we produced an analysis skim of the *g11a* dataset which includes some 1.8 M events. We then binned this dataset into 121 10 MeV-wide $\sqrt{s}$ bins in the range 1.630 GeV $\leq \sqrt{s} <$ 2.840 GeV. By fitting a Gaussian and linear background to the missing mass off K^+ distribution in each bin, we see that the background that passes the skim is less than 2% in most bins (see Figure 3.4). We then fit the total missing mass off K^+ distribution with double Gaussian and quadratic background functions to find a total of $\approx 1.563 \times 10^6$ $K^+\Lambda$ events in the skimmed dataset.

3.4.2 $\gamma p \to K^+ p(\pi^-)$

To skim possible $\gamma p \to K^+\Lambda$ events from the two-track dataset, we began by making two very loose missing mass cuts:

(1) require total missing mass to be within 300 MeV/c^2 of $m_{\pi^-} = 139.57018$ MeV/c^2

(2) require missing mass off K^+ to be less than 1.4 GeV/c^2.

Though missing the π^- increases statistics, it is also implies a less-restrictive $1C$ kinematic fit to $\gamma p \to K^+ p(\pi^-)$. Because of this, we applied a more stringent 5% confidence level cut. A plot showing the missing mass off K^+ distribution for all events in our skim of the *g11a* two-track topology is given in Figure 3.5. Notice that unlike the three-track topology, the background is significant in comparison to the signal.

Again we binned the data into 10-MeV-wide $\sqrt{s}$ bins, but this time over the larger energy range 1.62 GeV $\leq \sqrt{s} <$ 2.84 GeV. We then applied momentum corrections and tagger corrections were applied as described for the $K^+ p\pi^-$ topology. However, because the π^- track is not observed for the two-track analysis, we could not locate the Λ decay vertex using *MVRT*. Thus, energy-loss corrections were applied to all particles assuming track origins at the event vertex.

As with the $K^+ p\pi^-$ topology, we lose a percentage of the signal events to the confidence level cut. This percentage is greater than the ideal 5% because of hard scatters, as these effects cannot be accounted for by the confidence level calculation. We show in §4.2 that this effect is properly handled by our detector simulation, causing an equal fraction of Monte Carlo events to be removed by the confidence level cut.

By fitting the missing mass off K^+ distribution with double Gaussian and quadratic background functions, we find that the skim contains approximately 2.909^6 events.

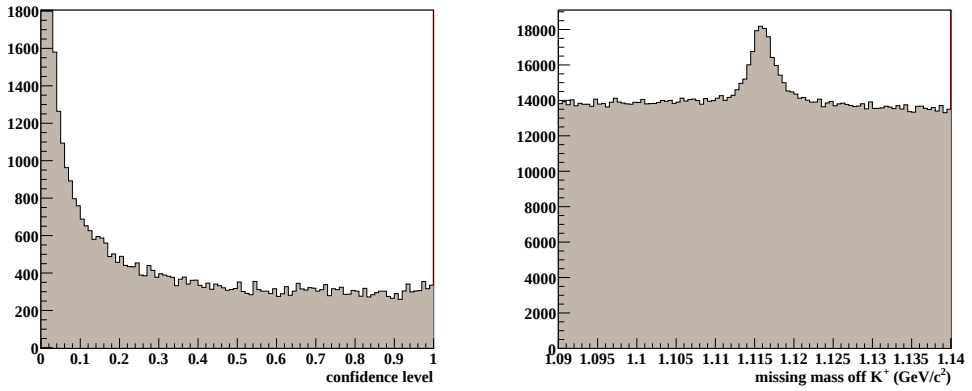

(a) (b)

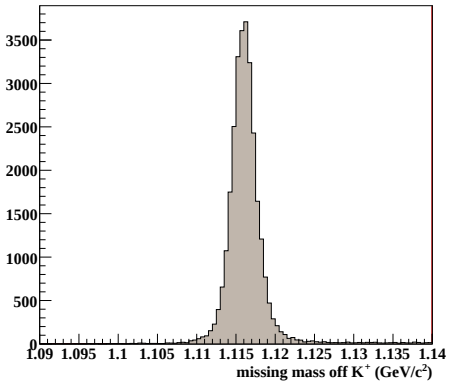

(c)

Figure 3.3: The above plots show the results of a kinematic fit to $\gamma p \rightarrow K^+ p \pi^-$ for events in run 43815. Plot (a) shows the confidence levels from all events. The confidence level is fairly flat above 0.4. Plot (b) show the missing mass off K^+ for all events in the run. There is a large amount of background, however, the Λ peak can be seen. Plot (c) shows the missing mass off K^+ distribution for events passing the 1% confidence level cut. The effect of the cut is dramatic.

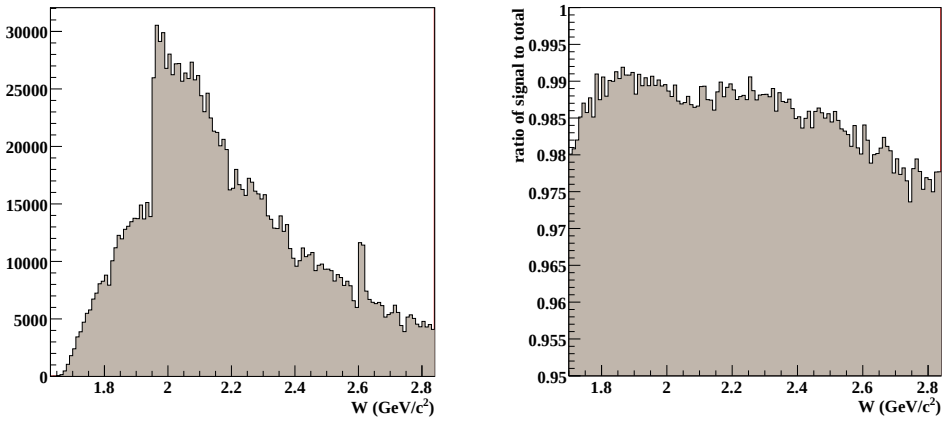

(a) (b)

Figure 3.4: Plots above show (a) yields and (b) ratio of signal to total yield from the three-track skim of $\gamma p \to K^+ p \pi^-$ from *g11a*. Signal was calculated by fitting missing mass off K^+ distribution in each 10 MeV-wide $\sqrt{s}$ bin to a Gaussian and linear background. Signal and background functions were then integrated over the range $\mu \pm 3\sigma$, where μ and σ are the mean and width from the fit in each bin. The skim is remarkably clean, with signal making up $\approx 98\%$ of the yield in each bin. Ratios are not shown for bins with $\sqrt{s} < 1.7$ GeV because low statistic limited reliable fits.

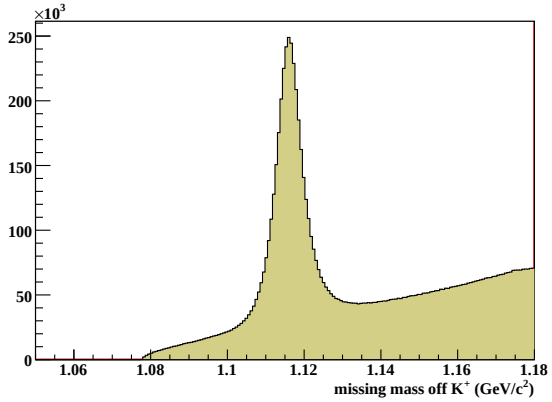

Figure 3.5: Shown above is the missing mass off K^+ distribution for all events in the $K^+ p$ skim of *g11a*. The less restrictive $1C$ kinematic fit allows more background to pass the skim than did the $4C$ fit on the $K^+ p \pi^-$ topology.

3.5 Particle Identification: Calculated Mass Cuts

We show in the previous section that the kinematic fit and confidence level cut is remarkably effiecient at separating background from the $\gamma p \to K^+\Lambda$ signal. We are able to further separate signal and background by considering timing information from the CLAS detector. Our analysis benefits from the fact that the $K^+\Lambda \to K^+p\pi^-$ system is the lowest-energy strange final state produced in CLAS. Most of the background events that we wish to subtract are events without associated strangeness (typically mis-identified $\pi^+p\pi^-$ final states). By using timing information, we are able to further separate protons and π^+s from K^+s, and remove events that do not include K^+s. It is in this sense that we refer to these cuts as *particle identification*.

For purposes of particle identification, the most instructive visualization of events in our skim is the *calculated mass plane*. Using tracking and timing information from CLAS, we are able to calculate a mass for each charged track observed in CLAS. By using the event vertex time (extrapolated from tagger T-counter information) and TOF counters, we are able to calculate the time taken by the particle to travel from its origin to the edge of CLAS, t. From drift chamber tracking information we calculate the path length of the track, d. We then construct the track's velocity β as

$$\beta = \frac{1}{c} d/t. \tag{3.4}$$

We then use the track's deflection as it traveled through CLAS's toroidal magnetic field to calculate the momentum of the track, $|\vec{p}|$. We can then use these measured quantities to calculate the mass of the particle, m_c, via the standard equation for the relativistic momentum of the particle

$$|\vec{p}| = \gamma m_c \beta c = \frac{1}{\sqrt{1-\beta^2}} m_c \beta c \tag{3.5}$$

which we can rewrite as

$$m_c = \sqrt{\frac{\vec{p}^2(1-\beta^2)}{\beta^2 c^2}}. \tag{3.6}$$

Because of the nature of the background in our channel, we wish to determine whether hypothesized K^+ tracks are actually K^+'s or mis-identified protons or π^+'s. We view each event by filling a two-dimensional histogram with the calculated masses (m_p, m_K)of the hypothesized proton and K^+ tracks for each event. The calculated mass plane for all events in our three-track skim of *g11a* is shown in figure 3.6. By looking at this projection of the data, we are able to see sources of background quite easily. There are four separated regions of the calculated mass plane:

(i) $m_p > 0.8$ GeV/c^2:
This region is populated predominantly by signal events. There is a very slight $p\pi^+\pi^-$ background that cannot be separated from signal in the calculated mass plane, but is mostly separated in the missing mass off K^+ distribution.

(ii) 0.4 GeV/$c^2 < m_p \leq 0.8$ GeV/$c^2 \cap m_K > 0.8$ GeV/c^2:
This region represents a small number of events that passed through the confidence level cut with positive tracks reversed (*i.e.* p mis-identified as K^+ and K^+ mis-identified as p) due to kinematic ambiguities. Such ambiguities occur infrequently and typically in higher-$\sqrt{s}$ bins. These events are also included in region (i) with tracks identified correctly and are cut from our analysis.

(iii) $m_p \leq 0.4$ GeV/$c^2 \cap m_K > 0.8$ GeV/c^2:
This region is populated by events for which the K^+ track is a mis-identified proton and the proton track is a mis-identified π^+. This region is strictly background, and its events are cut from the analysis.

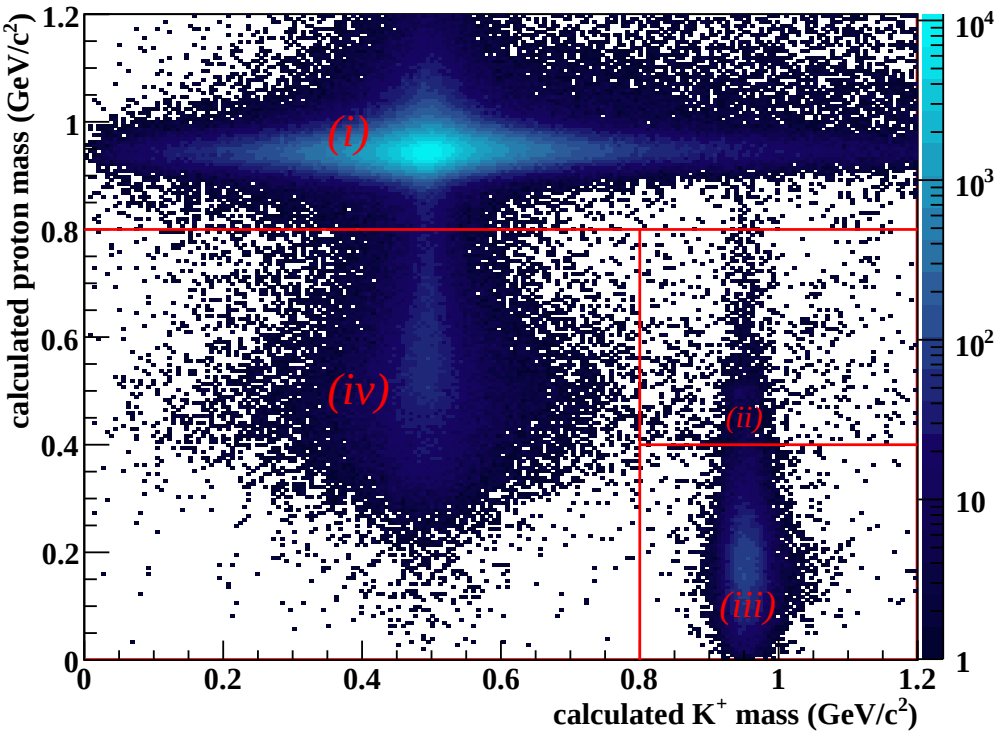

Figure 3.6: This plot shows the calculated mass for proton tracks versus the calculated mass for K^+ tracks for events in our $K^+p\pi^-$ skim of *g11a*. The plane is broken into four regions described in the text.

(iv) $m_p \leq 0.8$ GeV/$c^2 \cap m_K < 0.8$ GeV/c^2:
This region seems to be populated with events in which the K^+ track is correct, but the proton track is a mis-identified K^+. This would be a much more exotic final state, indicating at least one more missing particle with charge -1 and strangeness $+2$. It is highly unlikely that such events would make it through the kinematic fit with a confidence level greater than 1%. Upon further investigation, we have found that the events in this region are actually $\gamma p \to K^+\Lambda$ signal events with incorrect proton timing information. The majority of events in this region have the proton and π^- from Λ decay being detected by the same TOF counter in the same sector (see Fig 3.7). (This is more likely than in other channels due to the small break-up momentum of the Λ.) TOF counters in CLAS are instrumented with single-hit readout electronics, and thus are only able to record *one* time-of-flight for both particles. The time-of-flight of the first particle to hit the counter (typically the faster-moving π^-) is then assigned to both particles. This forces the calculated mass of the proton closer to that of the K^+. It should be noted that the missing mass off K^+ is unaffected for these events. As long as we are careful to make no other timing cuts, events in this region can be kept in our analysis.

The result of our particle identification studies is a cut removing regions (ii) and (iii) of the calculated mass plane. Events in the region $m_p \geq 0.8$ GeV/$c^2 \cup m_K < 0.8$ GeV/c^2 are kept. The effects of this particle identification cut are shown in Figure 3.8. Roughly 1.47 million events are left after the particle identification cut.

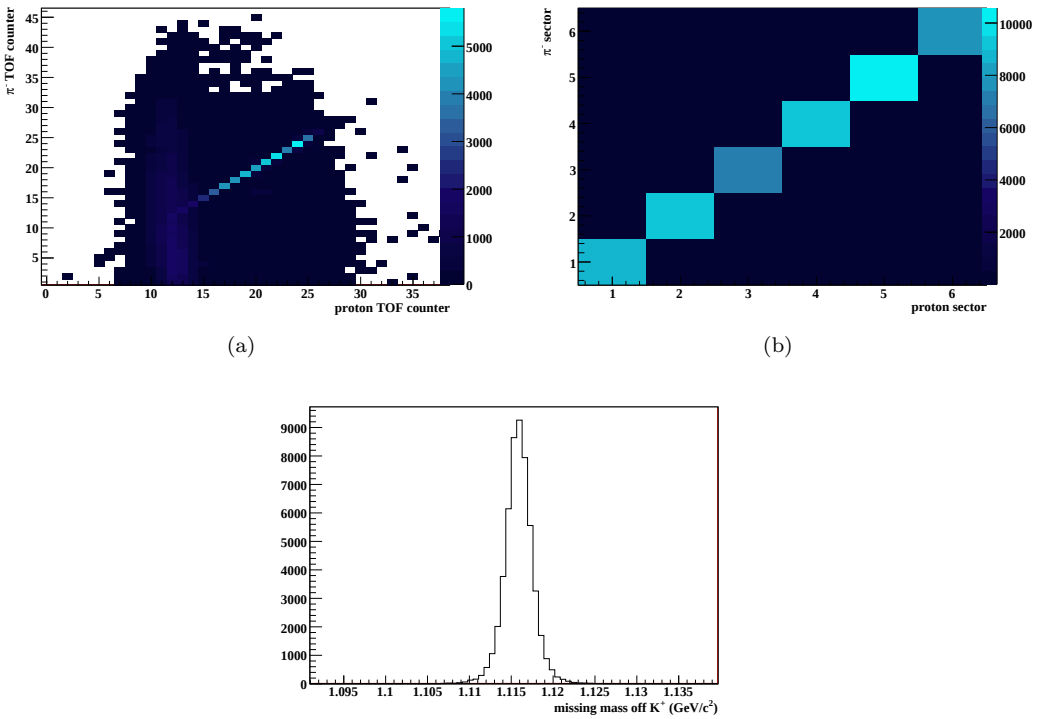

Figure 3.7: The plots above show (a) π^- TOF counter v. proton TOF counter, (b) π^- sector v. proton sector, and (c) the missing mass off K^+ distribution for events in region (iv) of the calculated mass plane (see Fig 3.6). The skewed proton calculated mass in this region is due to the proton and π^- hitting the same TOF paddle.

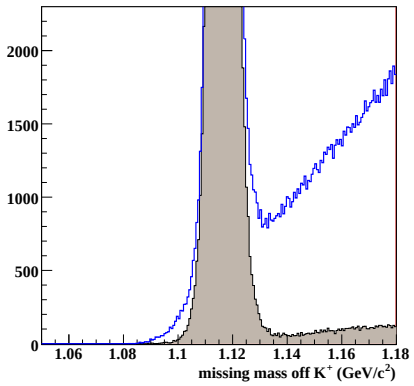

Figure 3.8: Figure (a) above shows the effect of the calculated mass particle identification cut on the missing mass off K^+ distribution from the three-track analysis. Missing mass off K^+ for all events is shown in blue. The distribution after the PID cut is shaded.

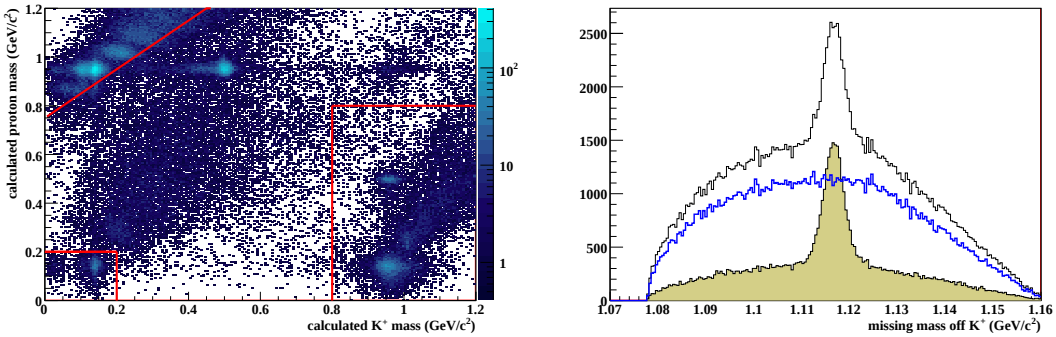

(a) (b)

Figure 3.9: Figure (a) shows the calculated mass plane for events in the *g11a* two-track topology with $\sqrt{s} < 1.660$ GeV. Cuts are defined in the text and displayed on the plot in red. Figure (b) shows the effect of these cuts on the missing mass off K^+ distribution. The unshaded histogram is filled with all events in the skim (with $\sqrt{s} < 1.660$ GeV). The blue histogram shows events removed by PID cuts and the shaded histogram shows events that pass the cuts.

For the two-track final state, we employ the calculated mass cuts as well. The two-track calculated mass plane diplays all of the same features described above. The less restrictive $1C$ kinematic fit allows some $\pi^+\pi^+$ background to pass the 5% confidence level cut (events for which the proton and K^+ are mis-identified π^+s). In order to remove this background, we make an extra cut requiring either the proton or K^+ mass to be greater than 0.200 GeV/c^2.

Upon further study, we found background level for in the two-track study for center-of-mass energies below 1.66 GeV to be excessive. Plots of the calculated mass plane and missing mass off K^+ distribution for these events is shown in Figure 3.9. We see from the calculated mass plane that a significant amount of this background is caused by $p\pi^+$ events for which the π^+ is mis-identified as a K^+. We cut these events by making a further calculated mass cut defined by the function

$$m_p < m_{K^+} + 0.75, \tag{3.7}$$

where m_t is the calculated mass of particle type t. As Figure 3.9 shows, this cut is very effective. Note that the histogram showing events cut by the particle identification shows no signal peak.

3.5.1 Signal Loss

Signal loss to the particle identification cuts described above is minimal. Figure 3.10 shows the missing mass off K^+ distribution for events removed by our calculated mass cuts in both the two- and three- track analyses. For the three-track analysis, we estimate the $K^+\Lambda$ content of the distribution by fitting to a double gaussian signal and linear background function. We find that the signal peak in the removed events distribution contains approximately 1770 events, 0.11% of the total $K^+\Lambda$ signal.

The amount of backgroung present in the two track analysis prevents us from simply using a signal peak to estimate the percentage of events lost to PID cuts. Thus, we employ the method of Feldman and Cousins [63] to estimate an upper bound on this loss. We begin by filling a histogram with all events from runs 43840 which pass the 5% confidence level cut. To estimate the total signal and background, we fit this distribution with a double Gaussian signal and quadratic background functions. We focus on the the range 1.111 GeV/$c^2 \leq m <$ 1.121 GeV/c^2, where m is the missing mass off K^+, and integrate the fit functions to find approximately 22888.49 signal and 4430.03

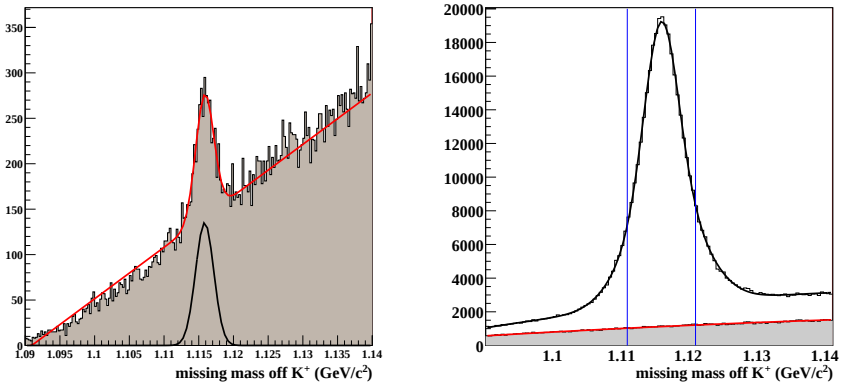

(a) (b)

Figure 3.10: Plot (a) shows the missing mass off K^+ distribution for events removed by PID cuts in the three-track analysis. The signal peak is apparent and an estimate is made by fitting with a Gaussian and linear functions. Plot (b) shows the distribution for all events in runs 43810-43819 (unshaded histogram) and a fit to a double Gaussian and quadratic background in black. The shaded histogram shows the missing mass off K^+ for events removed by the PID cuts. No signal peak is apparent. Shown in red is a fit of a quadratic function. The blue lines indicate the range considered for the application the Feldman-Cousins method (see text).

background events in this range. When we investigate the distribution for events removed by the PID cuts, we find that a total of 2187 events are present in the range considered. To obtain an estimate of the number of backgound events in this range, we fit the distribution with a quadratic function and obtain an estimate of 2176.17 events. The Feldman-Cousins method provides us with an upper-limit of 104.83 signal events at a 95% confidence level, roughly 0.45% of the total signal in this range.

3.6 Detector Performance Cuts

In order to accurately calculate a rate for any reaction in CLAS, we need to calculate a detector acceptance. For this analysis, we calculate a channel-specific acceptance using GSIM, a GEANT-based simulation of the CLAS detector. The accuracy of this simulation has been tested in great detail [64, 62]. For most regions of the detector and phase space, the simulation is very accurate; however, there are regions of the detector for which simulations are not reliable. We must cut from our analysis data and Monte Carlo events in these regions. We refer to such cuts as *detector performance cuts*. This section describes the cuts motivated by this analysis. We also list several cuts that are specific to this analysis, motivation for which can be found in Chapter 7.

3.6.1 Problematic TOF Paddles

By examining occupancies per TOF counter in both data and Monte Carlo, we were able to identify individual paddles for which the GSIM simulation was inaccurate. Data and Monte Carlo events for which any of the final state particles were detected by one of these problematic paddles were cut from the analysis. A list of the problematic TOF paddles in each sector is given in Table 3.2. Note that paddle 23 is removed in all sectors. Due to the 23^{rd} paddle's location on the boundary between

Sector	Removed Paddles
1	18,23,26,27,33
2	23
3	11,23
4	23,26
5	20,23
6	23,25,30,34

Table 3.2: The table above gives problematic TOF paddles which are removed from this analysis.

the first and second sections of the TOF wall, there is logical overlap between it and paddle 24. For tracks which hit both paddles 23 and 24, tracking is inconsistent and cannot be modeled properly by GSIM.

3.6.2 Minimum Proton Momentum Cut

Because they are much more susceptible to interactions with detector material, low-momentum protons are difficult to model accurately. Energy-loss corrections are difficult to apply to such tracks, and acceptance and track reconstruction are also affected. By selecting $\gamma p \to p\pi^+\pi^-$ events from the *g11a* dataset and Monte Carlo, one is able to empirically study the acceptance of proton tracks in all areas of the detector and for all proton momenta [62]. Events in which a π^+ and π^- were both detected were kinematically fit to the $\gamma p \to \pi^+\pi^-(p)$ hypothesis. The kinematic fit gives a refined value for the missing momentum. Based on whether the "missing" proton was actually detected by CLAS, an acceptance was assigned to the track based on the magnitude and production angle of the proton.

It is found found that for protons with magnitude of momentum less than 375 MeV/c, Monte Carlo acceptance did not match that of the data. Thus, we remove protons with $|\vec{p}| < 375$ MeV/c from our analysis in both data and Monte Carlo.

3.6.3 Fiducial Volume Cuts

The studies mentioned above also found physical regions of the detector which are not modeled properly by GSIM. The most prevalent of these are regions near the toroidal magnet coils. The magnetic field near the coils varies quite rapidly. Our map of the field is not accurate enough in these regions to account for this, and thus simulation is inaccurate here. Shown in Figure 3.11 are the effects of cuts removing particle tracks that are too close to the coils to model. We also place a cut on track polar angle in the forward direction at $\cos\theta = 0.985$ and sector-dependent polar angle cuts in the backwards direction.

3.6.4 Problematic Drift Chamber in Sector 5

In studying differences between cross sections from individual sectors in CLAS, we have isolated a discrepancy at a constant angle between sector 5 and the other sectors. Details of this study are given in §7.4 of this document. The discrepancy shows no momentum-dependence, so the tracking error must occur before the tracks are bent by the magnetic field. Because this discrepancy is dependent only upon production angle of the K^+ in the lab frame, we assume it to be the result of problems with the Region 1 drift chamber in this sector. We thus remove all tracks with lab production angle $\theta \in (0.45, 0.55)$ from both data and Monte Carlo in sector 5.

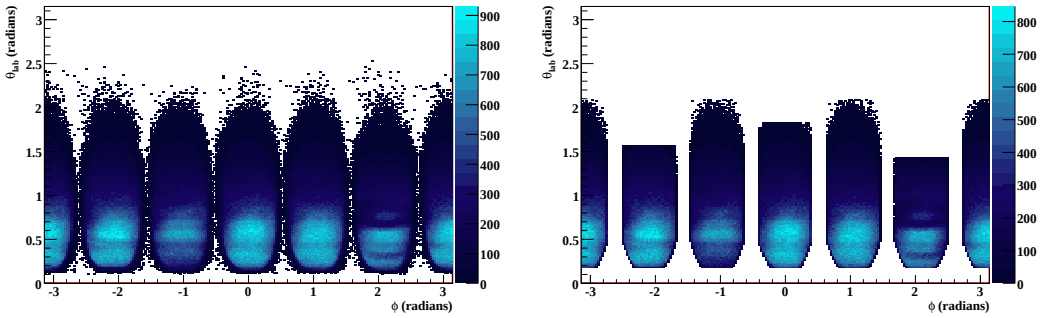

(a) (b)

Figure 3.11: Figure (a) above shows θ_{lab} v. ϕ for all tracks in our skim of *g11a*. Figure (b) shows the same distribution with fiducial cuts applied.

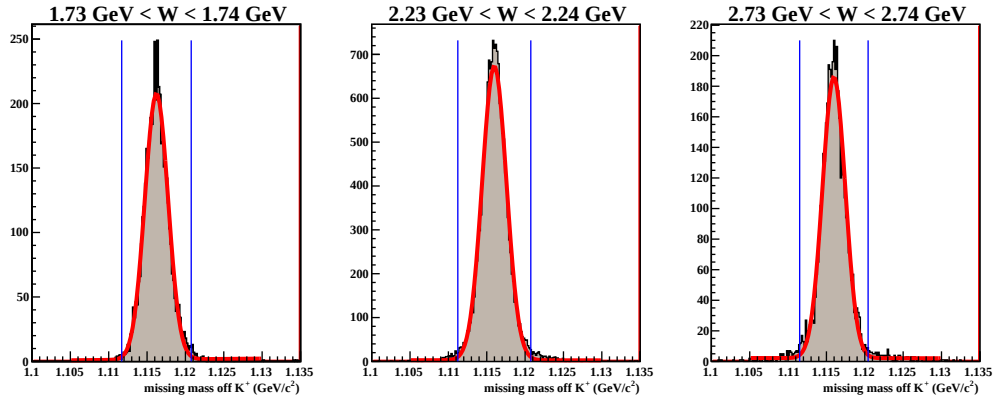

Figure 3.12: Shown above are missing mass of K^+ distributions after all cuts have been applied in several $\sqrt{s}$ bins. Fits to a Gaussian and linear background (shown in red) yield a mean and width for each distribution. The $\pm 2.5\sigma$ cut boundaries are shown in blue.

3.7 Missing Mass off K^+ Cuts: $K^+p\pi^-$ Topology

At this stage, any appreciable amount of background has been removed from the three-track dataset. Missing mass off K^+ distributions in several $\sqrt{s}$ bins are shown in Figure 3.12. As a final cut on this distribution, we fit Gaussian plus linear background to the missing mass peak in each $\sqrt{s}$ bin. According to the results of these fits, we keep all events that fall within 2.5σ of μ, where μ is the mean of the Gaussian for each bin.

3.8 Background Subtraction: $K^+p(\pi^-)$ Topology

For the two-track topology, we are able to further separate backgournd from signal. A powerful background subtraction method has been developed by the PWA group at CMU [66]. To use this method, we defined a metric based on three kinematic observables: cosine of the production angle of the K^+ in the CM frame ($\cos\theta^{K^+}_{CM}$), cosine of the proton angle in the Λ-helicity frame ($\cos\theta^{p}_{\Lambda HF}$),

and the azimuthal angle of the proton in the Λ-helicity frame ($\phi^p_{\Lambda HF}$), with ranges 2, 2, and 2π, respectively. This metric defines the "distance" between event i and event j to be

$$d^2_{ij} = \sum_{k=1}^{3} \left(\frac{\xi^i_k - \xi^j_k}{r_k} \right)^2 \tag{3.8}$$

where the ξ_k are the three kinematic observables for each event and r_k is the range for the k^{th} observable. For each event i in a W bin, we then used this distance function to find the 100 "closest" events. We then performed an un-binned maximum-likelihood fit of a Gaussian signal plus linear background function of the missing mass off of the K^+ to these 101 events.

The results of this fit are signal and background functions that are functions of the missing mass off K^+. We then evaluate the signal and background functions at m_i, the missing mass off K^+ value for event i, obtaining the values $s_i(m_i)$ and $b_i(m_i)$, respectively. We then assign to event i a Q-factor calculated as

$$Q_i = \frac{s_i}{s_i + b_i}. \tag{3.9}$$

As such, Q_i represents the probability that event i is a $K^+\Lambda$ event. Similarly, $(1 - Q_i)$ is the probability that i is a background event. By filling histograms with events weighted by their Q factor, we see the signal distribution as determined by the subtraction method. Figure 3.13 shows that this background subtraction method works very well.

3.9 Final Data Yields

We conclude this chapter by providing the total data yields as a functtion of center-of-mass energy after all cuts have been applied. A plot of this distribution for each analysis is shown in Figure 3.14. For the three-track dataset, we simply count the number of events in each $\sqrt{s}$ bin and find that the total number of events after cuts is 646612, approximately 41.3% of the number present in the skimmed dataset. For the two-track analysis, we need to consider our background subtraction method in counting our signal events. Thus, we sum the Q-factors of all events to find that about 1.657×10^6 events remain after all cuts, about 57.0% of the total present in the skim.

3.10 Summary

To investigate the $\gamma p \to K^+\Lambda$ reaction, we have exploited the $\Lambda \to p\pi^-$ decay mode and studied both $K^+p\pi^-$ and $K^+p(\pi^-)$ final state topologies in the *g11a* dataset. We have developed a series of particle identification cuts to select signal events from background. We have applied pre-existing detector performance cuts as well as several cuts motivated by our analysis to ensure that the data events we use in our analysis are able to be simulated in a consistent manner. For both topologies, signal losses due to our analysis cuts are minimal. For the three-track topology, background levels are negligible. For the two-track topology, we effectively separate signal and background by using an event-based background subtraction method.

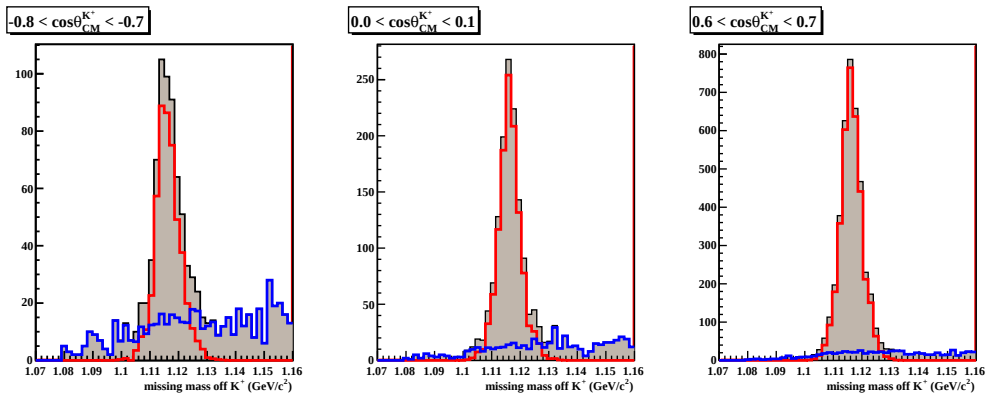

(a)

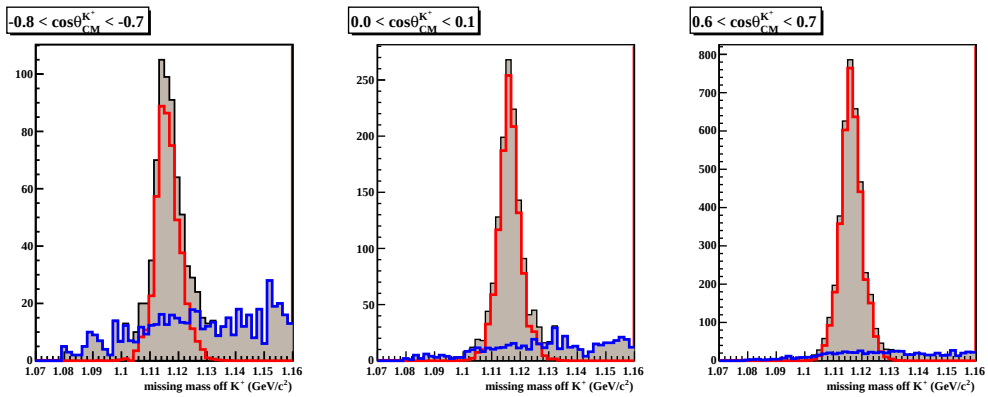

(b)

Figure 3.13: Shown above are the effects of the background subtraction method in three $\cos\theta^{K^+}_{CM}$ bins in (a) $\sqrt{s} = 2.005$ GeV and (b) $\sqrt{s} = 2.605$ GeV bins for the *g11a* pK^+ topology. The full missing mass off K^+ distributions are shown as shaded histograms. Signal is shown in red and background is shown in blue.

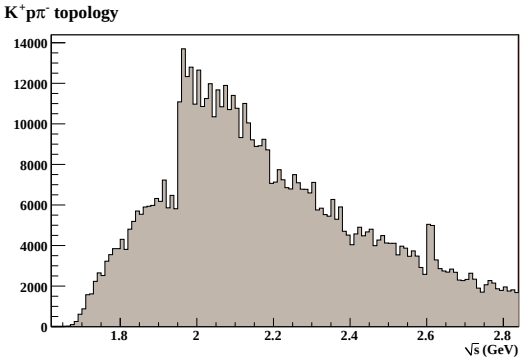

(a)

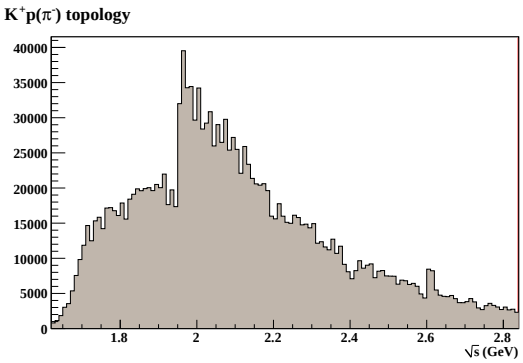

(b)

Figure 3.14: Shown are the final data yields after all cuts are applied for (a) the three-track and (b) two-track analyses.

Chapter 4

Acceptance Calculation and Normalization

In the previous chapter, we described the method by which we extracted $\gamma p \to K^+\Lambda$ yields from the *g11a* dataset. In order to parlay these data yields into a more meaningful quantity, the *differential cross section*, we need two more pieces of information: photon flux for the run period and detector acceptance. Calculating the photon flux allows us to measure the rate at which $K^+\Lambda$ is photoproduced. Detector acceptance refers to our understanding of the CLAS detector as a device with inherent inefficiencies. Knowing the probability that CLAS will reconstruct a track of a given particle type and kinematics allows us to remove detector- and analysis- based inefficiencies from this rate calculation. If done properly, acceptance and flux correction of the *g11a* yields will produce a differential cross section measurement that is independent of experimental method, a measurement of the true physical quantity. This chapter outlines the methods that we used to calculate and test acceptance for the CLAS detector, as well as work that went into calculation of photon flux for the *g11a* run period.

4.1 Detector Simulation

4.1.1 GSIM

We began our detector acceptance calculation by generating 300 million $\gamma p \to K^+\Lambda$ events. We refer to these events as the "raw" Monte Carlo (MC) events. Due to our acceptance calculation method (see §6.1), it was unnecessary to include a physics model of the production mechanism. Thus, the kinematic distribution of the raw $K^+\Lambda$ final state represents a pseudo-random sampling of the reaction's phase space (obeying only energy and momentum conservation).

To simulate the effects of the detector on these raw events, we employ a GEANT-based simulation of the CLAS detector called GSIM. GSIM is the standard simulation package for any of the CLAS Collaboration's analyses, and is programmed with information specific to each run. GSIM's main task is to simulate detector signals for each subsystem of CLAS based on the kinematics for each particle with which we supply it. To do so, GSIM takes as input the initial particle types, momenta, and positions for each raw MC event. GSIM uses spatial information regarding the CLAS detector materials and toroidal magnetic field to "swim" particles through the detector. GSIM also handles the decays of all unstable particles (both K^+ and Λ in our analysis). For each detector package that a given track passes through, GSIM generates a simulated signal. More details on GSIM can be found in [67]. Values of parameters used in the GSIM `ffread` card are provided in Table 4.1(a).

(a)

Parameter	Value
AUTO	1
KINE	1
MAGTYPE	2
MAGSCALE	0.4974 0.0
FIELD	2
GEOM	ALL
NOSEC	OTHE
TARGET	g11a
TGPOS	0.0 0.0 0.0
STZOFF	-10.00
STTYPE	1
RUNG	43852 1
BEAM	4.023

(b)

Flag	Value
R	43852
Y	
P	0x1f
f	1.0
a	1.0
b	1.0
c	1.0

Table 4.1: Values used for (a) GSIM `ffread` card and (b) GPP.

4.1.2 GPP and Momentum Smearing

The detector signals simulated by GSIM have been found to exhibit resolution better than that of the actual CLAS detector. To ensure that our Monte Carlo is as similar to the data as possible, we smear the timing signals by randomly displacing them from GSIM output values according to well-understood functions. We use another standard CLAS software package, GPP, to smear timing signals according to the specific detector subsystems which generated them. GPP smears signals from scintillator detector components according to that component's dimensions; a longer scintillator requires a wider, more diffuse smearing function. GPP allows the user to control the severity of the smearing. We have set the smearing level for scintillator timing signals to be 1.0. The flags and parameter values used in running GPP are provided in Table **??**(b).

In order to affect MC momentum resolution, GPP is also able to smear timing signals from CLAS drift chambers. It has been determined that the GPP drift chamber smearing produces too high a momentum resolution [4]. To study this effect, the kinematic fitter was used to fit $\gamma p \to p\pi^+\pi^-$ Monte Carlo events with tracking times smeared by GPP to a $\gamma p \to p\pi^+\pi^-$ hypothesis. Because the covariance matrix for the kinematic fitter was tuned on this channel, the confidence level distribution for a fit to data events is flat. The confidence level distribution for the kinematic fit to Monte Carlo events, however, exhibited a positive slope, indicating that the momentum resolution generated by GPP is higher than that of the data.

To smear tracking in the Monte Carlo effectively, we apply a momentum smearing algorithm. The CLAS tracking angles are smeared by randomly sampling from a Gaussian distribution. Distributions for each parameter are centered at the values of the tracking angle reported by GSIM and have width $1.85\sigma_{track}$, where σ_t is the resolution determined by tracking software. Smearing of the magnitudes of momenta is done in the same binning as was used for the *g11a* momentum corrections, and exhibited an average smearing of ≈ 2 MeV/c. In the $\gamma p \to p\pi^+\pi^-$ study, this smearing algorithm forced the confidence level distribution to be flat in all kinematic regions. The plot of confidence level for $\gamma p \to K^+ p\pi-$ and $\gamma p \to K^+ p(\pi^-)$ Monte Carlo events show that it is also effective for our analysis (see Figure 4.1).

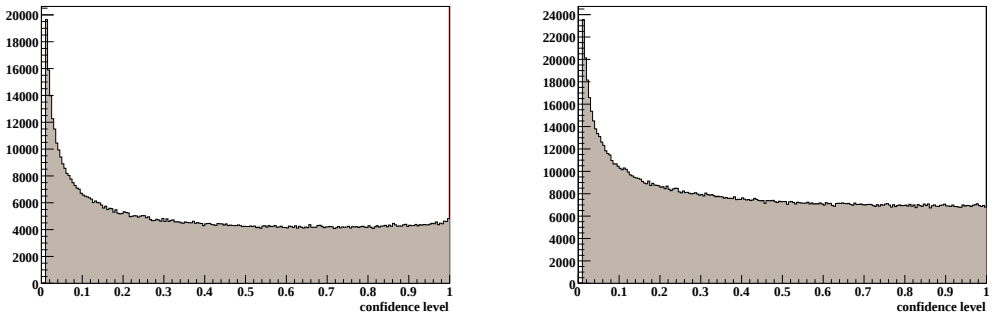

Figure 4.1: Shown above are confidence level distributions from a kinematic fit of $\gamma p \to K^+ p\pi^-$ Monte Carlo events to the (a) $\gamma p \to K^+ p\pi^-$ and (b) $\gamma p \to K^+ p(\pi^-)$ hypotheses. Resolution for these events is the product of GPP smearing of timing signals and the empirical smearing algorithm for tracking signals.

4.1.3 Trigger Simulation

GSIM accounts for whether individual detector components were able to reconstruct a given track in a Monte Carlo event. To accurately match the MC to the data, however, we must also take into account the efficiency of the *g11a* hardware trigger. We have discussed the *g11a* triggering scheme in greater detail in §2.5 and it should be noted that inefficiencies discussed in this section pertain to the CLAS Level 1 trigger. We identify two types of inefficiency in the *g11a* trigger: detector inefficiencies and logical inefficiencies.

Detector inefficiencies have been studied in great detail [62]. The kinematic fitter and confidence level cuts were used to identify $\gamma p \to p\pi^+\pi^-$ events in which all three final-state tracks were reconstructed. Only events for which the three final-state particles were reconstructed in different sectors were considered. The trigger word written into the data stream at the time the event was recorded indicated which sectors observed a coincidence between start counter and TOF wall, thus setting the Level 1 trigger. In each of these events, at least two sectors had to have set the trigger (otherwise, the event would not have been recorded). For each event, two tracks which set the trigger were identified. An efficiency map was then created for the third particle based on whether the trigger bit for that particle's sector was set. Maps were generated as a function of ϕ and TOF paddle in each sector for each particle type (proton, π^+, π^-).

An example of the trigger maps is given in Figure 4.2. One can notice structure in these maps which points to inefficiencies in detector subsystems. Paddle 33 shows no occupancy for either the proton or π^-, indicating that it is non-functioning. Paddle 18 displays a low efficiency for the proton and a ϕ-dependent efficiency for the π^-, indicating incorrect tuning of its input to the trigger (most likely, a high discriminator threshold). Other TOF paddles exhibit similar behavior. (Note that several of these paddles have been cut from analysis, as described in §3.6.1). Because we can identify these inefficiencies with specific elements or regions of the detector, we refer to them as detector inefficiencies.

We implement these efficiency maps in a statistical manner. For each track in a Monte Carlo event, we throw a random number $n \in [0, 1]$. If n is less than the efficiency given by the map for the particle type in the track's detector region, we count that track as having set the Level 1 trigger in its sector. If a Monte Carlo event does not have at least two tracks which set the trigger in this manner, the event is discarded. For the $K^+\Lambda$ channel, we apply the π^+ map to K^+ tracks based on the particles' similar ionization properties. We could not generate an efficiency map for the K^+ because no suitable channel – other than $K^+\Lambda$ – exists for analysis.

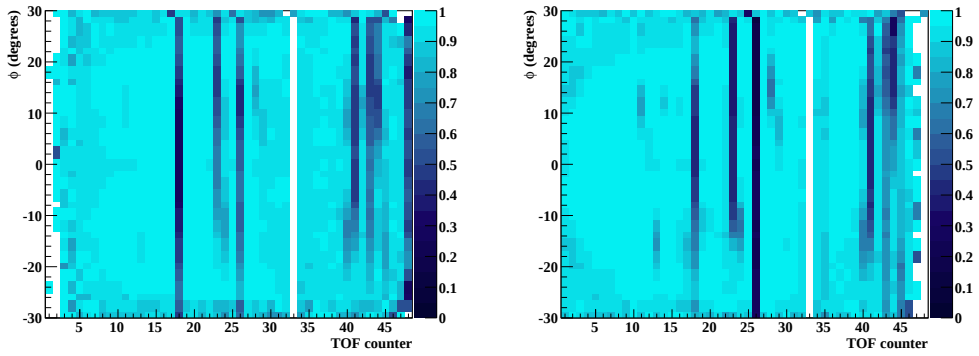

(a) (b)

Figure 4.2: The figure above shows a sample trigger efficiency maps from the study of *g11a* [62]. The two-dimensional histogram represents the probability that (a) a proton or (b) $\pi-$ in the indicated ϕ and TOF paddle will set the trigger in sector 1.

We have also tested the trigger efficiency maps to determine whether adding momentum dependence to the the map calculation provides a more accurate description of the trigger efficiency (see §7.3.2). In principal, the map should display some momentum dependence due to the lower interaction probability of higher-momentum particles. We have found no major momentum-dependence to the trigger efficiency and thus deem the above treatment to be adequate.

4.1.4 Start Counter

We have discussed the *g11a* start counter in §2.3.2. Motivated by differences between our preliminary differential cross sections and those of Robert Bradford, we have identified the start counter as the source of a subtle, but important difference between data and Monte Carlo. The Λ is relatively long-lived in comparison to other baryons produced in CLAS. Because of the similarity of the Λ's mean path length ($c\tau_\Lambda = 7.89$ cm) and the distance from the target to the start counter (≈ 10 cm), there is a non-negligible probability that a Λ produced in the target will decay outside of the start counter. For such an event, the neutral Λ would not create a hit in the start counter; thus, coincidence between the start counter and TOF wall would not be registered in its sector. Even if the K^+ set the trigger in its sector, the Level 1 trigger would not be set. Thus, events for which the Λ decays outside of the start counter are not recorded by in the data stream.

In order to reproduce this effect in the Monte Carlo, we tested two methods. First, we reconstructed the Λ decay vertex using MVRT and the proton and π^- momenta. We then cut any events (from both data and Monte Carlo) for which the Λ decay vertex was outside of the physical volume of the start counter. After testing this method, we abandoned it due to resolution issues caused by the small opening angle of the proton and π^-. A more detailed exposition of this cut and its shortcomings can be found in §7.3.3.

Our final approach was to make a statistical cut on the Monte Carlo events. For a given MC event, we used the event vertex (calculated using MVRT on the K^+ momentum and idealized beam location) and the Λ momentum, $\vec{p}_\Lambda$ (reconstructed from proton and π^- momenta) to calculate the intersection of the Λ trajectory with the start counter. We refer to the distance between the vertex and this intersection point along $\vec{p}_\Lambda$ as d. We then calculated the Λ lifetime t in the lab frame as

$$t(\beta) = \gamma\tau = \tau/\sqrt{1-\beta^2}, \tag{4.1}$$

where $\tau = 2.632 \times 10^{-10}$ s is the lifetime of a Λ at rest, and β is the velocity of the Λ calculated from its momentum. We then calculated the mean distance δ that the Λ would have traveled prior to decaying as

$$\delta(\beta) = \beta c t. \tag{4.2}$$

We then constructed a probability $P(\beta)$ that the Λ would have decayed *after* it traveled a distance d (*i.e.* outside of the start counter) as

$$P(\beta) = e^{-d/\delta(\beta)} = e^{-d/(\beta c t)}. \tag{4.3}$$

Finally, we throw a random number $n \in [0, 1]$; if n is less than $P(\beta)$, we discard the event. Note that, unlike the cut on secondary vertex position described above, this cut is *only* applied to the Monte Carlo events. More information on the construction and validity of this cut can be found in [68].

4.2 Effects of Analysis Cuts on Monte Carlo

As a final check of the similarity between data and Monte Carlo, we investigate the signal lost due to analysis cuts (confidence level, and particle identification). In order to extract an accurate differential cross section, we must be sure that the analysis cuts affect data and MC in the same way. If the covariance matrix that was tuned for the data were inaccurate for the MC, or if the MC were simply not treating the $\gamma p \to K^+\Lambda$ channel properly, then applying a confidence level cut to data and MC would not be consistent. Because we have seen (Figure 4.1) that the confidence level distribution from the kinematic fit to the MC is flat, we are encouraged to think that GSIM and the kinematic fitter are working properly. To support this, we fill missing mass off K^+ histograms for data and accepted Monte Carlo events from the three-track analysis before and after a 1% confidence level cut and detector performance cuts are applied. Figure 4.3 shows the effects of the skim and detector performance cuts on data events from runs 43810-43819 and accepted Monte Carlo. To extract the number of data signal events, we fit the data histograms to a Gaussian and fourth-order polynomial background. We then integrate the Gaussian signal functions over the range $(\mu_d - 2.5\sigma_d, \mu_d + 2.5\sigma_d)$, where μ and σ are the mean and width returned by the fit. This method shows that $\approx 89.44\%$ of the $K^+\Lambda$ signal events pass the cut. For the accepted Monte Carlo, no fitting is necessary for signal extraction; all events in the distribution are $K^+\Lambda$ events. However, we do fit the histograms to obtain mean and width (μ_{MC} and σ_{MC}). Fit to a Gaussian yields $\mu_{MC} = 1.1158$ GeV/c^2 and $\sigma_{MC} = 1.293$ MeV/c^2. We then integrate the Monte Carlo histograms over the interval $(\mu_{MC} - \sigma_{MC}, \mu_{MC} + \sigma_{MC})$ and find that $\approx 88.95\%$ of the Monte Carlo events pass the confidence level cut, an impact consistent with that of the data.

In §3.2, we discussed possible short-comings of the kinematic fitter. The most prominent of these is most likely its inability to handle the non-Gaussian errors due to energy loss of tracks in dense detector regions. Due to the similarity of the effects of the confidence level cut on data and Monte Carlo, we infer that such energy losses are correctly modeled by the detector simulator, GSIM.

We have shown in §3.5.1 that the number of $K^+\Lambda$ data events lost to our particle identification cuts is about 0.11% for the three-track analysis and no greater than 0.43% for the two-track analysis. To make sure that the particle identification cuts have the same effect on Monte Carlo events, we need only plot the calculated mass distribution for the Monte Carlo events. This plot is provided for the three-track final state in Figure 4.4. We see that region (*iii*), the region corresponding to $p\pi^+\pi^-$ background, is essentially empty. Region (*ii*) shows a small number of $K^+p\pi^-$ events which passed the 1% confidence level cut in the incorrect positive track permutation (*i.e.* proton identified as K^+ and K^+ identified as proton). By cutting events in regions (*ii*) and (*iii*), we omit less than 0.7% of the Monte Carlo events, on par with the effect of our particle identification on the data. We include this loss of signal as a systematic uncertainty.

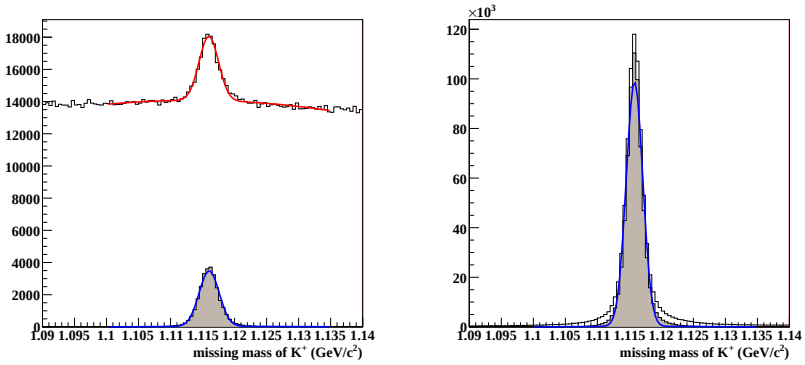

(a) (b)

Figure 4.3: The histograms in (a) show the missing mass off K^+ distribution for all events in runs 4381-43819 of *g11a* before (unshaded) and after (shaded) a 1% confidence level cut is applied. Fits to a gaussian and fourth-order background are shown in blue and red. The histograms in (b) show Monte Carlo events before and after the confidence level cut. A fit to a Gaussian is displayed in blue.

Also worth noting is the existence of Monte Carlo events in region (iv) of the calculated mass plane. This region is populated by events for which the proton timing is incorrect, forcing the calculated proton mass to be near that of a K^+. This effect is also present in the data and is described in greater detail in 3.5.

Particle identification cuts for the two-track analysis are the same for $\sqrt{s} > 1.66$ GeV. For $sqrts < 1.66$ GeV, however, our additional cut that requires $m_p < m_{K^+} + 0.75$ GeV must be tested on the Monte Carlo. Figure 4.5 shows the effects of the particle identification cuts on the missing mass off K^+ distributions of Monte Carlo events with $\sqrt{s} < 1.66$ GeV. By fitting Gaussian signal and quadratic background functions to the distributions, we find that only 3.4% of the Monte Carlo events in this energy range are lost to the PID cuts. We have shown in Figure 3.9 that no appreciable amout of data signal is removed by this cut. Thus, we include this 3.4% loss of Monte Carlo as a systematic uncertainty for $\sqrt{s} < 1.66$ GeV.

4.3 Systematic Study of Acceptance Uncertainty

In order to study the accuracy of our acceptance calculation, we are able to exploit the CLAS detector's design and produce acceptance-corrected yields from each of the six sectors independently. By comparing these independent acceptance corrected yields to the mean yield for the entire detector, we may estimate the acceptance uncertainty's contribution to the uncertainty of our final results.

To begin this study, we identify events with individual sectors based on the location of K^+ tracks (*i.e.* an event with K^+ track in sector 2 is assigned to sector 2) in each of thirteen 10-MeV-wide $\sqrt{s}$ bins. Because we are ultimately interested in the effects of the uncertainty on our differential cross section and polarization measurements, we fill histograms in $\cos\theta^{K^+}_{CM}$ for each of the independent sectors. The data yields from each sector in the $\sqrt{s} = 2.005$ GeV bin are shown in Figure 4.6(a). Note that the uncorrected data yields are very different between the sectors due to sector-dependent detector inefficiencies (TOF paddles, drift chamber wires). We then acceptance correct these data yields using our calculated acceptance in each sector. Figure 4.6(b) shows the acceptance-corrected yields for each sector plotted with the mean acceptance corrected yield. It is encouraging to see that even though the data yields from independent sectors were quite different,

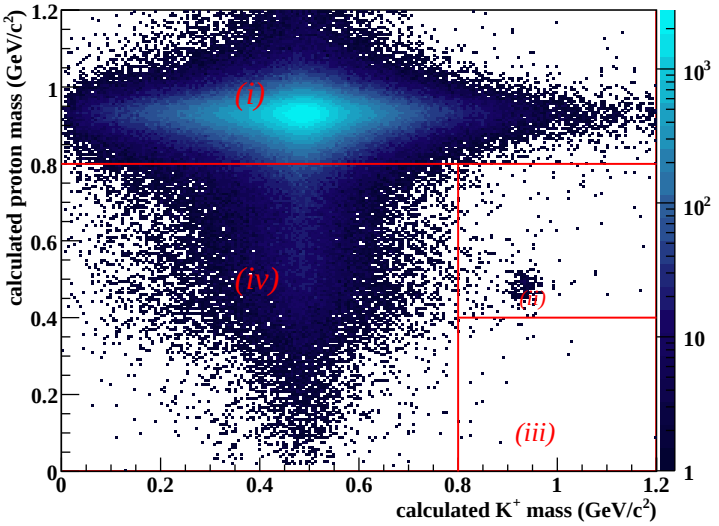

Figure 4.4: Shown above is the calculated proton mass versus calculated K^+ mass distribution for all Monte Carlo events. The number of events in regions (ii) and (iii), those cut by our particle identification cuts, is very small.

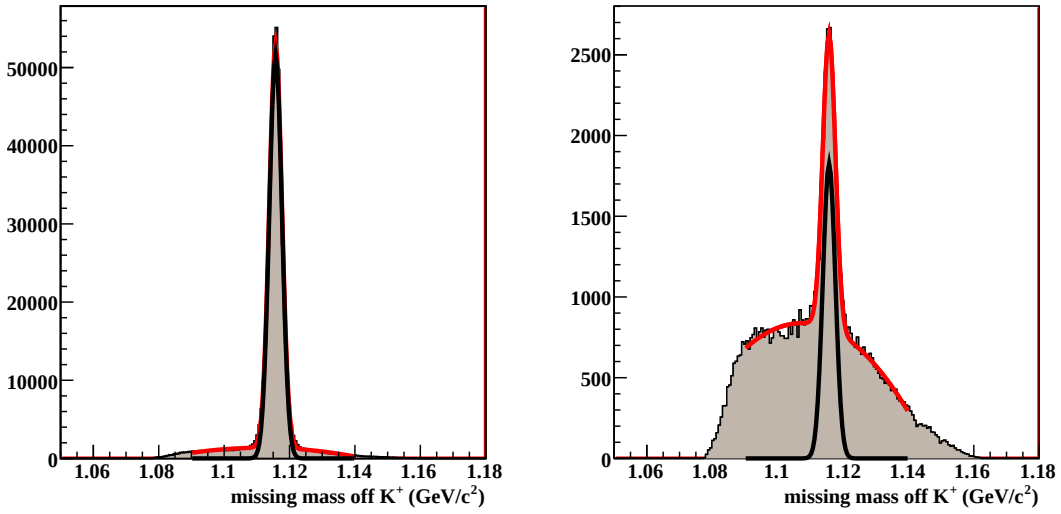

Figure 4.5: Figure (a) above shows the missing mass off K^+ distribution of all Monte Carlo events with $\sqrt{s} < 1.66$ GeV. Fit to a Gaussian and quadratic background show that there are roughly 3.87×10^5 events in the signal peak. Figure (b) shows the distribution of events cut by particle identification. Fitting reveals 13400 events in this peak, only 3.4% of the total.

$\sqrt{s}$ bins used	Average $\sqrt{s}$	$\overline{\sigma_\eta}$
1.805, 1.905	1.855	0.0314
2.005, 2.105	2.055	0.0486
2.205, 2.305	2.255	0.0486
2.455, 2.555	2.505	0.0430
2.605, 2.655	2.630	0.0680
2.705, 2.755, 2.805	2.755	0.0521

Table 4.2: The table above lists bins and results from our study of acceptance uncertainty.

acceptance corrections have made all of the sectors roughly equal. Figure 4.6(c) displays the ratios of each sector's acceptance-corrected yield. There is no apparent $\cos\theta_{CM}$ dependence in these ratios.

Some discrepancies still exist between the independent sectors and the mean. We wish to determine whether these discrepancies can be accounted for by statistical fluctuations or whether we need to assign a supplemental uncertainty due to our acceptance calculation. Here, we closely follow the work in [4]. At this point, errors on the acceptance corrected yields are purely statistical (due to data and Monte Carlo occupancies). For data obeying a normal distribution, we expect that

$$\sum_{c,s} \Theta(\sigma_{c,s}^2 - (y_{c,s} - \overline{y_c})^2) \approx 0.68N, \tag{4.4}$$

where s and c denote sector and $\cos\theta_{CM}$ bin, $\sigma_{c,s}$ is the (statistical) error associated with acceptance corrected yield $y_{c,s}$, $\overline{y_c}$ is the mean acceptance corrected yield, Θ is the Heaviside step function, and N is the total number of points considered. Eq. 4.4 represents the ideal situation where 68% percent (one standard deviation) of the $y_{c,s}$ fall within statistical error of the mean value μ_c. When we test this ideal hypothesis on the acceptance corrected yields in the $\sqrt{s} = 2.005$ GeV bin, we find that only 59.3% of the points satisfy this criterion. Thus, we can assign a supplemental error, σ_η, which we attribute to inaccuracy of our acceptance calculation:

$$\sum_{c,s} \Theta(\sigma_{c,s}^2 + (\sigma_\eta y_{c,s})^2 - (y_{c,s} - \overline{y_c})^2) = 0.68N. \tag{4.5}$$

The discrete nature of the sum in equation 4.5 makes an explicit calculation of σ_η difficult. In order to determine σ_η, we calculate the percent of points that satisfy the Heaviside function in eq. 4.5 for increasing values of σ_η. A plot of these values for the $\sqrt{s} = 2.005$ GeV bin is shown in Figure 4.7(a). We then perform a linear fit to these values to obtain, $\overline{\sigma_\eta}$, the error which satisfies eq. 4.5. In this bin, we find $\overline{\sigma_\eta} = 4.86\%$.

We then perform this same study considering the other twelve $\sqrt{s}$ bins. In order to bolster statistics, we add the acceptance corrected yields from adjacent $\sqrt{s}$ bins. The bins considered, combination method, and $\overline{\sigma_\eta}$ values are given in Table 4.2. We provide a plot of the extracted acceptance error versus center-of-mass energy in Figure 4.7(b). A fit of these points to a linear function shows that the error is characterized by

$$\sigma_\eta(\sqrt{s}) = 0.0243\sqrt{s} - 0.00890. \tag{4.6}$$

For the energy range of our analysis, this characterization dictates errors between $\sigma_\eta(1.635GeV) = 3.08\%$ and $\sigma_\eta(2.835GeV) = 6.00\%$. Though this uncertainty has been calculated using the three-track analysis only, we show in §6.2.2 that this acceptance uncertainty accounts for differences between results of the two analyses.

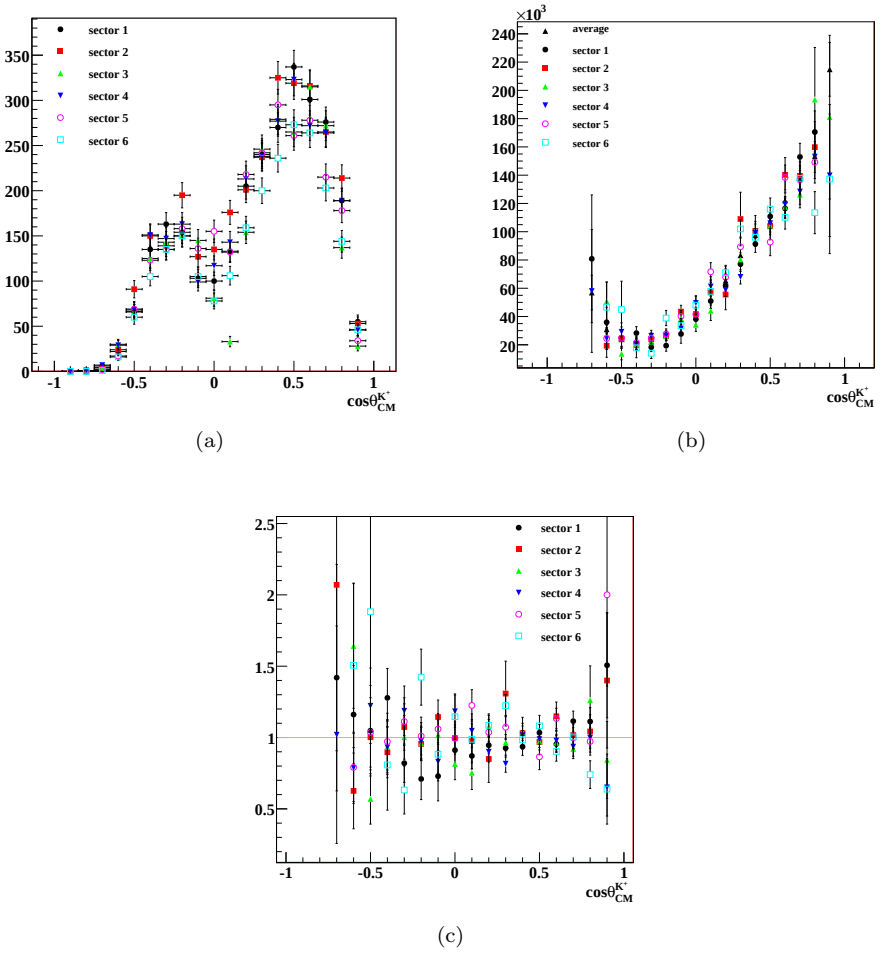

(a) (b)

(c)

Figure 4.6: The plots above show steps in the acceptance uncertainty calculation for the $\sqrt{s} = 2.005$ GeV bin. Plot (a) shows the sector-dependent data yields, whereas plot (b) shows theses yields after acceptance correction along with the mean acceptance-corrected yield. Plot (c) shows the ratios of each sector's acceptance corrected yield to the mean.

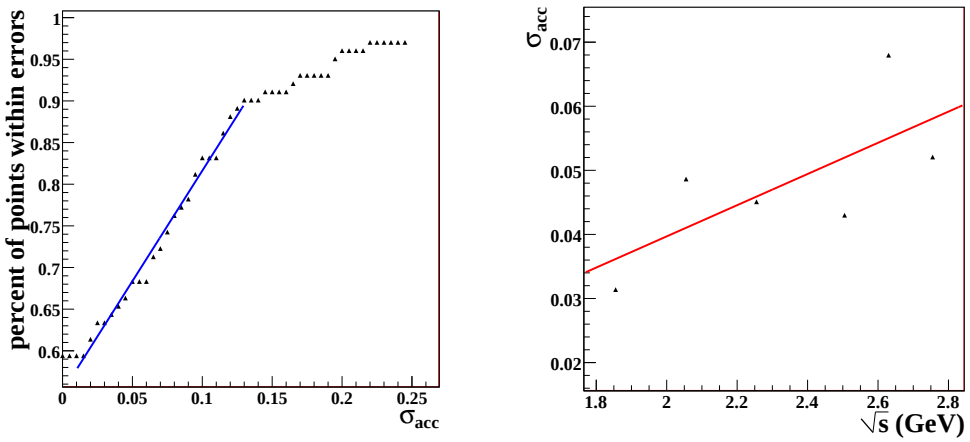

(a) (b)

Figure 4.7: Plot (a) shows the percentage of acceptance corrected yield points that satisfy the Heaviside function in eq. 4.5 versus σ_η. A fit of the points to a straight line is shown in red and is used to determine the value of σ_η which satisfies eq. 4.5. Values of $\overline{\sigma_\eta}$ versus center-of-mass energy are shown in (b).

4.4 Target Characteristics

In order to calculate a production probability from our data, we need to have an idea of how many target protons were available to the photon beam. Such information is characterized by the target length, atomic properties, and density. The target dimensions and substance (liquid H_2) are discussed in §2.3.1. The density of the target, however, is not a static quantity. Density is related to the target temperature and pressure, which is measured for each CLAS run. From these measurements, the density has been calculated on a run-by-run basis [4]. It is found that the average *g11a* target density, $\overline{\rho}$, for the *g11a* run period is

$$\overline{\rho} = 0.07177 \frac{g}{cm^3} \tag{4.7}$$

with a variance of

$$\sigma_{\overline{\rho}} = 6.776 \times 10^{-9} \frac{g}{cm^3}, \tag{4.8}$$

or roughly 0.1%.

4.5 Photon Normalization

The final ingredient that we need to calculate a production cross section is the number of photons incident on the target during our experiment, the so-called *photon flux*. To calculate the flux, we make use of the *gflux*, a standard CLAS analysis package [69]. Typically, photon fluxes are observed at low current by comparing hits in the photon tagger and the resulting hits in an instrument such as the CLAS total absorption counter (TAC) located in front of the target. Because *g11a* was collected with a much higher current (≈60 nA) than the TAC could handle, the $gflux$ method was devised. *gflux* uses a clever method of determining the rate of electron hits in the tagger T-counters which are not associated with a production trigger in CLAS. The rate for each T-counter

in each run is determined by sampling T-counter hits during a fraction of the run. This rate is then used to calculate the total number of electrons that hit each T-counter. *gflux* then corrects for the detector *live time*, the fraction of the run for which the detector was "ready" to record data. (CLAS experiences *dead time* when its data acquisition system is busy writing events.) Finally, *gflux* corrects each total T-counter flux for the fraction of photons which do not pass through the volume of the target, a roughly 10% T-counter-dependent correction.

During preliminary analysis of the *g11a* dataset, inconsistencies in current dependence of flux-normalized data yields were found. This effect has been studied and corrected [4]. Flux-normalized $p\omega$ yields were calculated from four separate *g11a* runs: 43532, 43582, 44106, and 43626. The four runs used were chosen for their differing beam currents (between 30 and 70 nA). CLAS live times were then calculated using two methods: by considering the DAQ scaler clocks (the same method used by *gflux*) and by considering noise measured by the Faraday cup. In order to make the two live times roughly agree, the scaler clock live time had to be applied twice (*i.e.* correcting by the square of the live time correction). After applying this correction, iw was found that the current dependence of the normalized yield was removed. We apply this correction to photon fluxes for all runs used in this analysis.

For the purposes of this analysis, it is useful to obtain the flux in each of our 10-MeV-wide $\sqrt{s}$ bins. To do so, we calculate the flux per T-counter for each run using $gflux$ applying the *g11a* live time correction. We then rebin the flux according to each T-counter's associated E-counters and divide these fluxes among the appropriate $\sqrt{s}$ bins. We then sum the flux over all runs used in our analysis to get the total flux per $\sqrt{s}$ bin.

Finally, we need to account for the effects of the *g11a* trigger. Recall that the tagger Master-Or (MOR) only collected signals from the first 40 tagger T-counters (discussed in §2.5). Events generated by photons which would send the recoil electron into T-counters between 41 and 61 would not be recorded unless a second recoil electron happened to hit one of the first 40 T-counters in the same tagger window. Poisson statistics were used to correct for these untriggered T-counters [4]. It was found that the cut-off between triggered and untriggered tagger energies was at $E_\gamma \approx 1.57$ GeV, or $\sqrt{s} \approx 1.955$. The probability that an event with $\sqrt{s} \leq 1.955$ was recorded due to a separate electron setting the MOR in another T-counter was calculated to be $P_{trig} = 0.46669$. This probability was then used to effectively scale-down the flux in all bins with $\sqrt{s} \leq 1.955$ GeV. Plots of flux-normalized yields v. W show that this correction restores continuity to our normalized yields (Figure 4.8). Note that we cannot correct the bin centered at 1.955 GeV in a consistent manner due to the energy cut-off of the trigger. In addition, we note that the flux-normalized yields in the $\sqrt{s} = 2.735$ GeV and $\sqrt{s} = 2.745$ GeV bins do not follow the general trend of the surrounding bins. These faulty $\sqrt{s}$ bins are attributed to an improperly-functioning T-counter (T9).

4.6 Flux-normalized Yields

As a final check of our photon flux calculation, we examined the flux-normalized yields for each run. We can calculate $\mathcal{N}_r$, the flux-normalized $K^+\Lambda$ yield from run r as

$$\mathcal{N}_r = \frac{Y_r}{\mathcal{F}_r}, \tag{4.9}$$

where Y_r and $\mathcal{F}_r$ are the data yield and total (corrected) photon flux from run r, respectively. σ_r, the error in $\mathcal{N}_r$ for run r reflects statistical errors for the data yield and photon flux for that run. Figure 4.9 shows the flux-normalized yields per run for runs used in this analysis. We note that several runs exhibit $\mathcal{N}$'s that are far from the average value. A plot of the extracted data yields shows that for several of these runs (43900,44036,44101,44102), an inaccurate $\mathcal{N}$ is due perhaps to low statistics (these are short runs). Runs 43588 and 43757 exhibit abnormal $\mathcal{N}$'s, but are sufficiently populated. We cut these runs from further analysis.

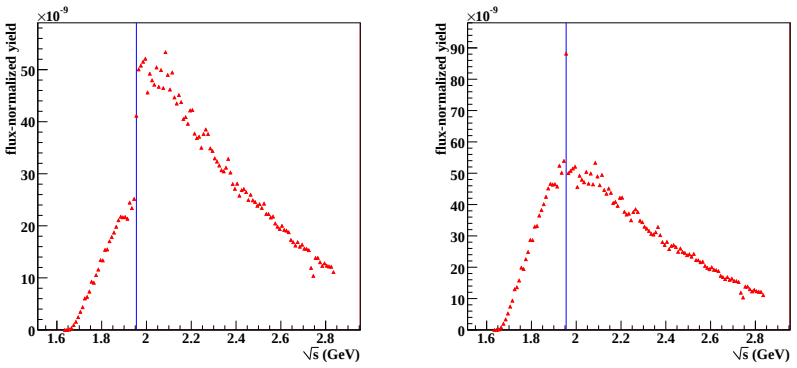

(a) (b)

Figure 4.8: Shown above are the flux-normalized yields v. $\sqrt{s}$ before (a) and after (b) the untriggered T-counter correction. The correction restores rough continuity to the trend of the yields versus $\sqrt{s}$. The blue line in each plot marks the energy of the trigger cut-off, $\sqrt{s} \approx 1.955$ GeV.

For the remaining runs, we calculate the weighted mean flux-normalized yield to be

$$\overline{\mathcal{N}} = \frac{\sum_r \mathcal{N}_r/\sigma_r^2}{\sum_r 1/\sigma_r^2} = 2.617 \times 10^{-9}. \tag{4.10}$$

Using this $\overline{\mathcal{N}}$, we may then calculate the mean variance in $\mathcal{N}$, $\overline{\sigma^2}$, weighted by the σ_r as

$$\overline{\sigma^2} = \frac{\sum_r (\mathcal{N}_r - \overline{\mathcal{N}})^2/\sigma_r^2}{\sum_r 1/\sigma_r^2} = 8.691 \times 10^{-21}, \tag{4.11}$$

making $\sqrt{\overline{\sigma^2}}/\overline{\mathcal{N}} \approx 3.5\%$. As the photon flux is an important part of the differential cross section extraction, we quote the this variance as a systematic uncertainty in our calculations in Chapter 6.

4.7 Summary

To calculate acceptance for the $\gamma p \to K^+ p \pi^-$ reaction, we have processed 300 million raw Monte Carlo events using GSIM, a GEANT-based simulation of the CLAS detector. We then processed the resulting accepted Monte Carlo using the same analysis software as was used for data events. Trigger effects not included in GSIM were accounted for by a trigger efficiency cut and Λ decay/start counter simulation.

Uncertainties as pertain to differential cross section and recoil polarization calculations have been investigated. We assign a 3.4% systematic uncertainty to bins with $\sqrt{s} < 1.66$ GeV due to MC signal lost to particle identification cuts. In all other $\sqrt{s}$ bins, we assign a 0.7% uncertainty due to signal loss to PID cuts. A 0.1% systematic uncertainty is attributed to fluctuations in target density. We have estimated the uncertainty in our acceptance calculation to be $\sqrt{s}$-dependent and on the order of 5%. Photon flux has been calculated using $gflux$, and we have calculated the variance in our flux-normalized $K^+\Lambda$ yields to be roughly 3.5%.

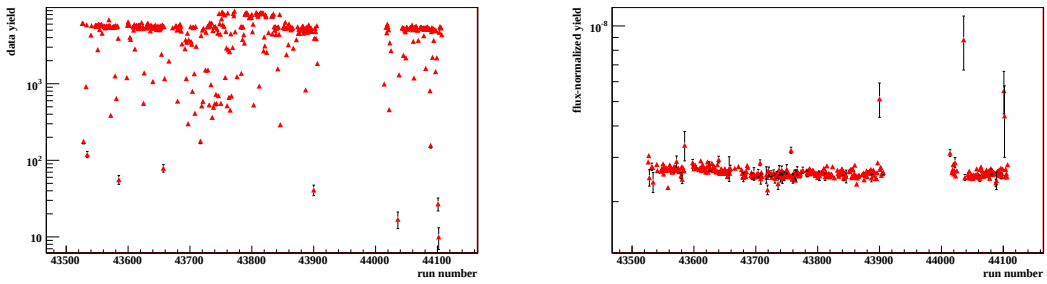

(a) (b)

Figure 4.9: Shown above are $K^+\Lambda$ data yields (a) and flux-normalized yields (b) per run from the *g11a* three-track analysis. Several runs show abnormal flux-normalized yields. Runs 43900, 44036, 44101, and 44102 are due to low statistics.

Chapter 5

Partial Wave Analysis Techniques and Amplitude Formulæ

At the heart of our analysis is the powerful partial wave analysis software suite developed by the PWA Group at Carnegie Mellon [74, 4]. The methods contained therein are essential to our search for excited nucleon intermediate states in the $\gamma p \to K^+\Lambda$ reaction; however, we also make use of them in our extraction of differential cross section and polarization results. To this end, we have exploited both unbinned maximum likelihood and binned χ^2 fitting techniques. In this chapter, we outline the basis and some of the formulæ involved in our fitting procedures. We conclude the chapter by providing an introduction to the amplitudes we have used to characterize the $\gamma p \to K^+\Lambda$ reaction.

5.1 Notation

In what follows, we adopt the notation set forth in [4]. We denote the photon, target proton, K^+, and Λ four-momenta by k, p_i, q, and p_Λ, respectively. In the center-of-mass frame, we align the z-axis with the direction of the photon momentum, $\hat{k}$, and use this as the axis of angular momentum quantization. For a given particle x, we denote the mass and spin projection of x by w_x and m_x, respectively. The Mandelstam variables are defined in the typical manner for two-to-two scattering [70]:

$$s = (p_i + k)^2 = (q + p_\Lambda)^2 \tag{5.1a}$$
$$t = (k - q)^2 = (p_i - p_\Lambda)^2 \tag{5.1b}$$
$$u = (k - p_\Lambda)^2 = (p_i - q)^2. \tag{5.1c}$$

We represent the Lorentz-invariant phase space element as $d\Phi(X) = \phi(X)dX$, where X is the set of all independent kinematic variables describing the $\gamma p \to K^+\Lambda \to K^+p\pi^-$ reaction. We assume the detector acceptance to be dependent upon kinematics and denote it by $\eta(X)$. For amplitude formulæ, we denote the Dirac γ matrices (in the Dirac basis) as

$$\gamma^0 = \begin{pmatrix} \mathbf{1} & 0 \\ 0 & -\mathbf{1} \end{pmatrix}, \gamma^i = \begin{pmatrix} 0 & \sigma_i \\ -\sigma_i & 0 \end{pmatrix}, \gamma^5 = \begin{pmatrix} 0 & \mathbf{1} \\ \mathbf{1} & 0 \end{pmatrix}, \tag{5.2}$$

where $\mathbf{1}$ is the 2×2 identity matrix and σ_i are the Pauli spin matrices

$$\sigma_1 = \begin{pmatrix} 0 & 1 \\ 1 & 0 \end{pmatrix}, \sigma_2 = \begin{pmatrix} 0 & -i \\ i & 0 \end{pmatrix}, \sigma_3 = \begin{pmatrix} 1 & 0 \\ 0 & -1 \end{pmatrix}. \tag{5.3}$$

In fitting formulæ, we denote the set of fit parameters as $\vec{x}$. We may then write the Lorentz-invariant transition amplitude $\mathcal{M}$ as

$$|\mathcal{M}(\vec{x},X)|^2 = \sum_{m_i,m_\gamma,m_f} |\sum_a \alpha_a(\vec{x},X)\mathcal{A}^a_{m_i,m_\gamma,m_f}(X)|^2, \tag{5.4}$$

where α_a are complex functions dependent upon fit parameters and kinematics, and $\mathcal{A}^a_{m_i,m_\gamma,m_f}(X)$ are the known parts of the partial wave amplitudes based on kinematics and spin projections of the target, photon, and final state baryon (m_i, m_γ, and m_f, respectively). Here, the sum over a denotes the sum over different amplitudes that contribute to the process. The transition matrix element expressed above represents the full reaction, $\gamma p \to K^+ p\pi^-$, *i.e.* including the $\Lambda \to p\pi^-$ amplitude.

Once we have extracted the differential cross section and recoil polarization observables from our analysis, we perform binned least-squares fits to these results. We thus define the reduced transition matrix amplitude $\mathcal{M}_r$, which describes only the $\gamma p \to K^+\Lambda$ portion of the reaction, as

$$|\mathcal{M}_r(\vec{x},X)|^2 = \sum_{m_i,m_\gamma,m_\Lambda} |\sum_a \alpha_a(\vec{x},X)\mathcal{A}^a_{m_i,m_\gamma,m_\Lambda}(X)|^2, \tag{5.5}$$

where m_Λ represents the hyperon spin projection. While the binned χ^2 fit lacks the stability of the event-based fit, it allows us to include results from other analyses in our fits. These observables are unmeasurable in *g11a*, namely the double polarization observables C_x and C_z which have been measured in CLAS [13].

5.2 Extended Maximum Likelihood Fitting

In order to extract differential cross sections and polarization results, we rely on an event-based fit. The event-based fit differs from the more common χ^2 fit in that it requires no angular binning of the data. Whereas a χ^2 fit will base the minimization of a fit function on its estimation of a few points, the event-based fit treats each event individually, and thus has many more degrees of freedom. For this reason, the event-based fit is generally more stable. We have divided our dataset into 10-Mev-wide $\sqrt{s}$ bins to facilitate interpretation of our PWA results. In each of these $\sqrt{s}$ bins, we perform a maximum likelihood fit to relevant partial wave amplitudes. The work in this section follows that of Chung [71] and Williams [4].

5.2.1 The Extended Likelihood Function

In any fitting procedure, we wish to find estimators, $\hat{x}$, for the fit parameters $\vec{x}$. In a maximum likelihood fit, the fit function that grants us access to these parameters is the extended maximum likelihood function defined by

$$\mathcal{L} = \left(\frac{\overline{n}^n}{n!}e^{-\overline{n}}\right)\prod_i^n \mathcal{P}(\vec{x},X_i) \tag{5.6}$$

in a given $\sqrt{s}$ bin with n data events. Here $\mathcal{P}(\vec{x},X_i)$ is the probability density function (discussed below) and the term in brackets is the Poisson probability of observing n events given an expected number $\overline{n}$. For an event i, the probability density function is represented by

$$\mathcal{P}(\vec{x},X_i) = \frac{|\mathcal{M}(\vec{x},X_i)|^2\eta(X_i)\phi(X_i)}{\mathcal{N}(\vec{x})} \tag{5.7}$$

where $\phi(X_i)$ is the phase space element and $\eta(X_i)$ is the detector acceptance for event i. $\mathcal{N}$ is a normalization factor chosen such that the integral of $\mathcal{P}(\vec{x},X_i)$ over all possible event kinematics is unity. Maximizing (5.6) by varying the fit parameters, $\vec{x}$, yields the estimators, $\hat{x}$, which best

describe the data. Recall that the transition probability $\mathcal{M}(\vec{x}, X_i)$ for event i contains the partial wave amplitudes weighted by the $\vec{x}$-dependent α's. Thus, by maximizing $\mathcal{L}$ we are able to determine the strengths and phases of each partial wave.

A vital part of the likelihood method is the calculation of $\overline{n}$, the expected number of events in each $\sqrt{s}$ bin. In order to calculate $\overline{n}$, we begin with the empirical definition of σ, the total cross section for the $\gamma p \to K^+\Lambda$ reaction

$$\sigma = \frac{N}{\mathcal{F}\rho_t \ell_t N_A / A_t}. \tag{5.8}$$

Here, N is the number of $\gamma p \to K^+\Lambda$ scattering events, $\mathcal{F}$ is the number of incident photons, N_A is Avogadro's number, and ρ_t, ℓ_t, and A_t are the density, length, and atomic weight of the target. We may also write the cross section in term of the transition probability for the scattering event as

$$\sigma = \frac{1}{4}\frac{(2\pi)^4}{2(s-w_p^2)} \int |\mathcal{M}(\vec{x}, X)|^2 d\Phi(X), \tag{5.9}$$

where the factor of if $1/4$ comes from averaging over the spins of the initial state γ and proton. By equating (5.8) and (5.9), we obtain the following expression for the expected number of scattering events:

$$N = \frac{\mathcal{F}\rho_t \ell_t N_A}{A_t}\frac{(2\pi)^4}{8(s-w_p^2)} \int |\mathcal{M}(\vec{x}, X)|^2 d\Phi(X). \tag{5.10}$$

It is important to keep in mind that N is the expected number of scattering events, not necessarily the number that we would have observed due to imperfect detector acceptance. In order to account for our detector's imperfect acceptance, we simply fold the kinematically-dependent acceptance into the integral in (5.10). Thus, we calculate the number of scattering events which we would have observed to be

$$\overline{n} = \frac{1}{4}\frac{\mathcal{F}\rho_t \ell_t N_A}{A_t}\frac{(2\pi)^4}{8(s-w_p^2)} \int |\mathcal{M}(\vec{x}, X)|^2 \eta(X) d\Phi(X). \tag{5.11}$$

As presented in Chapter 4, the acceptance of the CLAS detector is very complicated; we have no way of characterizing it analytically as a function of kinematic variables. Thus, in order to perform the integral in (5.11), we rely on GSIM, a GEANT-based Monte Carlo simulation. We generate N_{raw} $\gamma p \to K^+\Lambda$ events according to phase-space kinematics. We can then substitute the integral (5.11) with a sum over the raw Monte Carlo events

$$\int |\mathcal{M}(\vec{x}, X)|^2 \eta(X) d\Phi(X) \approx \frac{\int d\Phi(X)}{N_{raw}} \sum_j^{N_{raw}} \eta(X_j) |\mathcal{M}(\vec{x}, X_j)|^2. \tag{5.12}$$

Each raw event, j, is then processed with GSIM and all analysis cuts resulting in an acceptance $\eta(X_j) = 0, 1$ for that event. Because we treat each raw event individually, $\eta(X_j)$ takes the values 0 or 1 for each j. We can then simplify (5.12) as

$$\int |\mathcal{M}(\vec{x}, X)|^2 \eta(X) d\Phi(X) \approx \frac{\int d\Phi(X)}{N_{raw}} \sum_j^{N_{acc}} |\mathcal{M}(\vec{x}, X_j)|^2, \tag{5.13}$$

where the sum is now over only the N_{acc} events which passed our detector acceptance simulation and analysis cuts (*accepted* events).

All that remains to in our calculation of $\overline{n}$ is to perform the integral over phase space, $\int d\Phi(X)$. Calculating the integral for two-to-two scattering is rather straight-forward and can be found in many texts (see [70]):

$$\int d\Phi(X) \quad = \quad \int \delta^4(p_i + k - p_\Lambda - q) \frac{d^3\vec{p}_\Lambda}{(2\pi)^3 2E_\Lambda} \frac{d^3\vec{q}}{(2\pi)^3 2E_{K^+}}$$

$$
\begin{aligned}
&= \frac{1}{4(2\pi)^6}\int \delta(\sqrt{s}-E_\Lambda-E_{K^+})\frac{|\vec{p}_\Lambda|^2 d\Omega}{E_\Lambda E_{K^+}} \\
&= \frac{1}{4(2\pi)^6}\int \frac{|\vec{p}_\Lambda|^2 d\Omega}{\sqrt{s}} \\
&= \frac{[(s-(w_\Lambda+w_{K^+})^2)(s-(w_\Lambda-w_{K^+})^2)]^{1/2}}{8(2\pi)^5 s}. \qquad (5.14)
\end{aligned}
$$

We can now combine (5.11), (5.13), and (5.14) to write an expression for the expected number of observed data events as

$$\overline{n} = \frac{\mathcal{S}(s)}{N_{raw}}\sum_j^{N_{acc}} |\mathcal{M}(\vec{x}, X_j)|^2. \qquad (5.15)$$

where

$$\mathcal{S}(s) = \frac{\mathcal{F}\rho_t \ell_t N_A}{A_t}\frac{[(s-(w_\Lambda+w_{K^+})^2)(s-(w_\Lambda-w_{K^+})^2)]^{1/2}}{64\pi s(s-w_p^2)} \qquad (5.16)$$

has no dependence upon fit parameters or kinematics other than s.

We can also use this Monte Carlo method to impose the normalization of the probability density function $\mathcal{P}(\vec{x}, X)$. Enforcing unit normalization of $\mathcal{P}(\vec{x}, X)$,

$$\int \mathcal{P}(\vec{x}, X) = \frac{1}{\mathcal{N}(\vec{x})}\int |\mathcal{M}(\vec{x}, X)|^2 \eta(X)\phi(X) dX = 1, \qquad (5.17)$$

implies that

$$\mathcal{N}(\vec{x}) = \int |\mathcal{M}(\vec{x}, X)|^2 \eta(X) d\Phi(X). \qquad (5.18)$$

Once again, we can perform the integral over kinematic variables using the Monte Carlo method:

$$\mathcal{N}(\vec{x}) \approx \frac{\int d\Phi X}{N_{raw}}\sum_j^{N_{acc}} |\mathcal{M}(\vec{x}, X_j)|^2 = \mathcal{C}(s)\overline{n}, \qquad (5.19)$$

where

$$\mathcal{C}(s) = \frac{8(s-w_p^2)}{(2\pi)^4}\frac{A_t}{\mathcal{F}\rho_t\ell_t N_A}. \qquad (5.20)$$

5.2.2 Log Likelihood

As n becomes large, the product over all data events in (5.6) becomes more complicated. As the minimization algorithm that we employ uses the partial derivatives of $\mathcal{L}$ with respect to individual fit parameters, this large product can become computationally intensive. To ease calculation and optimization of the likelihood, we take the negative natural logarithm of $\mathcal{L}$ to be left with

$$
\begin{aligned}
-\ln(\mathcal{L}) &= -\sum_i^n \mathcal{P}(\vec{x}, X_i) - n\ln\overline{n} + \ln n! + \overline{n} \\
&= -\sum_i^n \ln\left(|\mathcal{M}(\vec{x}, X_i)|^2 \eta(X_i)\phi(X_i)\right) + \overline{n} + \ln n! + n\ln\mathcal{C}(s) \\
&= -\sum_i^n \ln\left(|\mathcal{M}(\vec{x}, X_i)|^2\right) - \sum_i^n \ln\left(\eta(X_i)\phi(X_i)\right) + \overline{n} + \ln n! + n\ln\mathcal{C}(s). \qquad (5.21)
\end{aligned}
$$

Because the $-\ln(\mathcal{L})$ is a monotonically decreasing function of $\mathcal{L}$, minimization of $-\ln(\mathcal{L})$ implies maximization of $\mathcal{L}$. Note that only two of the terms in (5.21) are dependent upon the fit parameters;

in order to minimize $-\ln(\mathcal{L})$ we need only consider these terms. Thus, we can reduce (5.21) to only terms that interest us for fitting:

$$\begin{aligned} -\ln(\mathcal{L}) &= -\sum_{i}^{n} \ln|\mathcal{M}(\vec{x}, X_i)|^2 + \overline{n} + const \\ &= -\sum_{i}^{n} \ln|\mathcal{M}(\vec{x}, X_i)|^2 + \frac{\mathcal{S}(s)}{N_{raw}} \sum_{j}^{N_{acc}} \ln|\mathcal{M}(\vec{x}, X_j)|^2 + const. \end{aligned} \tag{5.22}$$

A more detailed treatment of likelihood fitting can be found in [4].

5.2.3 Background Weighting

For our two-track final-state topologies (both *g11a* and *g1c*), we use the PWA Group's background subtraction method to assign a Q_i value to each event (see §3.8 or [66]). This Q_i is the probability that event i is a signal event. We have seen that the majority of background events for the $\gamma p \to K^+ p\pi^-$ channel are events with a $\pi^+ p\pi^-$ for which the π^+ is mis-identified as a K^+. Because $K^+\Lambda$ is the only state with associated strangeness possible in this energy regime (dictated by missing mass off $K^+ < 1.14$), we know that any non-signal events in our data sample are non-strange background events. Because of this, we are able to treat the amplitudes for signal and background events as non-interfering. Thus, we can include the Q_i factor for each event in the likelihood function as [4]

$$-\ln(\mathcal{L}) = -\sum_{i}^{n} Q_i \ln|\mathcal{M}(\vec{x}, X_i)|^2 + \frac{\mathcal{S}(s)}{N_{raw}} \sum_{j}^{N_{acc}} \ln|\mathcal{M}(\vec{x}, X_j)|^2 + const. \tag{5.23}$$

5.3 Least-Squares Fitting

In addition to the log-likelihood fitting, our analysis also makes extensive use of the more common least-squares fitting method. Once we have extracted differential cross section and recoil polarization results using the likelihood method, we are able to perform least-squares fits to these data. For this analysis, the benefit of the least-squares fit is that it allows us to also fit to results of other analyses which *g11a* cannot measure. In the case of $K^+\Lambda$ photoproduction, these supplementary results are the double-polarization observables, C_x and C_z, that were measured by CLAS in 2004 [13].

The fundamental difference between the least-squares fit and the likelihood method described in the previous section is the binning of the data. While the likelihood method treats each event in a $\sqrt{s}$ bin independently (each event is then a degree of freedom for the fit), the least-squares method considers only the results derived from these events. We say that the least-squares fit is a "binned" fit because each point to which we fit (*i.e.* $d\sigma/dt$ point at a value of $\cos\theta_{CM}$ in a specific $\sqrt{s}$ bin) represents all of the events that fall within the range of that point. Due to the greatly reduced number of degrees of freedom, the least-squares fit is generally much less computationally intensive. In a typical $\sqrt{s}$ bin for our analysis, event-based and least-squares fits to the same set of partial waves may have $\approx 20,000$ and ≈ 35 degrees of freedom, respectively. The vastly decreased number of degrees of freedom does lead to a loss in stability of fit results which can be mitigated by performing multiple fit iterations.

As in the likelihood fit, we seek to determine the estimators, $\hat{x}$, for the set of fit parameters $\vec{x}$ for n data points. Here the n data points are the measured observables $\mathcal{O}_i(X_i)$ associated with the kinematic values X_i. These measurements may be either $d\sigma/dt$, recoil polarization, or double-polarization observables, but for now, we consider only one type. The fit function in a least-squares fit is the χ^2 defined as

$$\chi^2 = \sum_{i}^{n} \frac{(\mathcal{O}_i(X_i) - \hat{\mathcal{O}}(\vec{x}, X_i))^2}{\sigma_i^2}, \tag{5.24}$$

where σ_i is the error associated with $\mathcal{O}_i(X_i)$ and $\hat{\mathcal{O}}(\vec{x}, X_i)$ is the hypothetical value of observable $\mathcal{O}$ built from fit parameters and the kinematic variables of point i. For measurements pertaining to this analysis, the $\hat{\mathcal{O}}(\vec{x}, X_i)$ are functions of $\alpha_a(\vec{x}, X_i)\mathcal{A}^a_{m_i,m_\gamma,m_\Lambda}(X_i)$ for the α_a and $\mathcal{A}$ given in (5.5).

5.3.1 Calculation of $d\sigma/dt$

In the case where $\mathcal{O}_i(X_i) = \frac{d\sigma}{dt}(X_i)$, we are able to calculate the differential cross section by considering (5.9). We rewrite the expression for the total cross section in differential form:

$$d\sigma(\vec{x}, X) = \frac{1}{4}\frac{(2\pi)^4}{2(s-w_p^2)}|\mathcal{M}(\vec{x}, X)|^2 d\Phi(X). \tag{5.25}$$

We then exploit the expression for the phase space element $d\Phi(X)$ in (5.14), allowing us to write (5.25) as

$$d\sigma(\vec{x}, X) = \frac{1}{4}\frac{(2\pi)^4}{2(s-w_p^2)}|\mathcal{M}(\vec{x}, X)|^2 \frac{1}{4(2\pi)^6}\frac{|\vec{p}_\Lambda| d\Omega}{\sqrt{s}}. \tag{5.26}$$

Using the expression for t given in (5.1), we can write t explicitly as

$$\begin{aligned} t &= w_p^2 + w_\Lambda^2 + 2E_i E_\Lambda + 2|\vec{p}_i||\vec{p}_\Lambda|\cos\theta_{CM} \\ &= w_p^2 + w_\Lambda^2 + 2E_i E_\Lambda + \frac{s-w_p^2}{\sqrt{s}}|\vec{p}_\Lambda|\cos\theta_{CM}, \end{aligned} \tag{5.27}$$

where $\cos\theta_{CM}$ is the center-of-mass production angle of the K^+. Taking the differential and rearranging leaves

$$d\cos\theta_{CM} = \frac{\sqrt{s}}{s-w_p^2}\frac{dt}{|\vec{p}_\Lambda|}. \tag{5.28}$$

Substituting this into the solid angle element in (5.26) gives

$$\begin{aligned} d\sigma(\vec{x}, X) &= \frac{1}{4}\frac{(2\pi)^4}{2(s-w_p^2)}|\mathcal{M}(\vec{x}, X)|^2 \frac{1}{4(2\pi)^6}\frac{|\vec{p}_\Lambda|}{\sqrt{s}}\frac{\sqrt{s}}{s-w_p^2}\frac{dt d\phi}{|\vec{p}_\Lambda|} \\ &= \frac{1}{32(2\pi)^2(s-w_p^2)^2}|\mathcal{M}(\vec{x}, X)|^2 dt d\phi. \end{aligned} \tag{5.29}$$

Integrating over ϕ yields

$$\frac{d\sigma}{dt}(\vec{x}, X) = \frac{1}{64\pi(s-w_p^2)^2}|\mathcal{M}(\vec{x}, X)|^2. \tag{5.30}$$

Calculations of the other observable quantities (P_Λ, C_x, C_z) are left to Chapter 7.

5.4 Fitting Multiple Datasets

We often find it advantageous to include information from multiple $\sqrt{s}$ bins into a single fit. In such situations, we must construct a fit function (χ^2 or $\mathcal{L}$) which accounts for all datasets equally. We construct this total fit function, ψ, by simply summing the fit functions from all datasets:

$$\psi = \sum_d^{N_d} \psi_d, \tag{5.31}$$

where ψ_d is the fit function from dataset d, and N_d is the total number of datasets being fit. We should note that for (5.31) to be consistent, the ψ_d must all be either χ^2 *or* $-\ln(\mathcal{L})$ functions.

5.5 MINUIT

In order to perform fits with many degrees of freedom, significant computing power is needed. Fortunately, the software which we use to handle the minimization of fit functions and calculation of fit parameter errors, MINUIT, is an efficient, well-vetted standard in the experimental physics community [72].

We specifically employ a MINUIT minimization algorithm called MIGRAD, which is based upon the Davidon-Fletcher-Powell (DFP) variable metric method. The DFP is an iterative process which assumes that the gradient $\vec{g}(\vec{x}) = \vec{\nabla} F(\vec{x})$ of the minimization function $F(\vec{x})$ with respect to the fit parameters $\vec{x}$ can be calculated explicitly. In the majority of our fits, we supply MIGRAD with randomized initial values, $\vec{x}_0$, of the fit parameters. MIGRAD then uses the gradient of $\vec{g}(\vec{x})$ to find another value of the fit parameters, $\vec{x}_1$, for which $F(\vec{x}_1) < F(\vec{x}_0)$. The $\vec{x}_0$ are then replaced by the $\vec{x}_1$, and a new set of fit parameters, $\vec{x}_2$ is found in the same manner. MIGRAD repeats this process until the difference in the minimization function between consecutive iterations, $\delta F \equiv F(\vec{x}_n) - F(\vec{x}_{n-1})$, is less than some user-defined tolerance.

In order to speed the calculations, we supply MIGRAD with partial derivatives of the fit functions with respect to the fit parameters. In the case of the log-likelihood fit,

$$\frac{\partial(-\ln \mathcal{L})}{\partial x_j} = -\sum_i^n Q_i \left(\frac{1}{|\mathcal{M}(\vec{x}, X_i)|^2} \frac{\partial |\mathcal{M}(\vec{x}, X_i)|^2}{\partial x_j} \right) + \frac{\mathcal{S}(s)}{N_{raw}} \sum_i^{N_{acc}} \frac{\partial |\mathcal{M}(\vec{x}, X_i)|^2}{\partial x_j}. \tag{5.32}$$

For the least-squares fit to differential cross section measurements, the gradients can be computed as

$$\frac{\partial \chi^2}{\partial x_j} = \left(\frac{1}{64\pi(s - w_p^2)^2} \frac{\partial |\mathcal{M}(\vec{x}, X_i)|^2}{\partial x_j} \right) \sum_i^n \frac{2}{\sigma_i^2} \left(\frac{d\sigma}{dt}(\vec{x}, X_i) - \frac{d\sigma}{dt} \right). \tag{5.33}$$

For both cases, we compute the partial derivatives of the $|\mathcal{M}(\vec{x}, X)|^2$ as

$$\frac{\partial |\mathcal{M}(\vec{x}, X_i)|^2}{\partial x_j} = \sum_{m_i, m_\gamma, m_f} 2\Re \left(\sum_a \frac{\partial \alpha_a(\vec{x}, X_i)}{\partial x_j} \mathcal{A}_a \sum_{a'} \alpha_{a'}(\vec{x}, X_i) \mathcal{A}^*_{a'}(X_i) \right). \tag{5.34}$$

5.6 Partial Wave Amplitudes

The theoretical basis for our partial wave analysis has been developed by M. Williams and C. Meyer of the CMU PWA Group. The group's method uses a covariant framework to construct fully Lorentz-invariant amplitudes, removing any frame-dependence to calculations. The foundation of this technique is the eponymous Rarita-Schwinger presented in [73]. In this framework, we use the Dirac spinors and polarization and angular momentum tensors familiar to quantum field theory calculations to describe initial and final states in our analysis. We combine integer-spin polarization tensors and Dirac spinors to create polarization tensors for the N^* states.

The complexity of the resulting amplitudes and the overwhelming number of events we consider in an event-based fit requires powerful and efficient computational methods. (Recall that likelihood fitting requires us to compute the complex value of each amplitude for each data, accepted and raw Monte Carlo event.) The `qft++` package developed by M. Williams is a `C++` computation package that allow us access to the machinery of covariant field theory calculations via an elegant interface [74]. For event-based fits, we use `qft++` to calculate these amplitudes explicitly based on the 4-vectors associated with individual particles in each event. For binned fits, we generate 4-vectors corresponding to the kinematics represented by fit points. We then calculate amplitudes based on these kinematics and calculate observables from these amplitudes.

In this chapter, we provide formulæ for the amplitudes used in this analysis. Amplitudes describing resonant processes (excited nucleon intermediate states) are not specific to this analysis, and a more detailed treatment can be found in [4].

5.6.1 Fundamentals

Here we present the basic building blocks of the covariant tensor formalism. The construction of these objects can be found in [75] and [4]. The Dirac spinors u representing a spin-$\frac{1}{2}$ particle with momentum p, energy E, mass w, and spin polarization $m = \pm\frac{1}{2}$ are denoted by

$$u(p,m) = \sqrt{E+w}\begin{pmatrix} \chi \\ \frac{\vec{\sigma}\cdot\vec{p}}{E+w}\chi \end{pmatrix} \tag{5.35}$$

where χ is the two-component spinor of the particle. In order to preserve Lorentz invariance, we have

$$\overline{u} = u^\dagger\gamma_0. \tag{5.36}$$

We can write the polarization vector $\epsilon^\mu(p,m)$ for a spin-1 particle with momentum p and spin polarization m as

$$\epsilon^\mu(p,m) = \Lambda^\mu_\nu(p)\epsilon^\nu(0,m), \tag{5.37}$$

where $\epsilon^\nu(0,m)$ are the rest-frame polarization vectors constructed to be the eigenvectors of the S^2 and S_z angular momentum operators:

$$\epsilon^\nu(0,\pm1) = \mp\frac{1}{\sqrt{2}}(0,1,\pm i,0), \quad \epsilon^\nu(0,0) = (0,0,0,1). \tag{5.38}$$

We can use the spin-1 polarization vector to construct the rank-2 polarization tensor, $\epsilon_{\mu\nu}(p,m)$, which describes a spin-2 particle:

$$\epsilon_{\mu\nu}(p,m) = \sum_{m_1,m_2}(1m_1\ 1m_2|2m)\epsilon_\mu(p,m_1)\epsilon_\nu(p,m_2), \tag{5.39}$$

where $(1m_1\ 1m_2|2m)$ is the Clebsch-Gordon coefficient which couples spin $(1m_1)$ and $(1m_2)$ states to a spin $(2m)$ state. For integer $J \geq 2$, this process is generalized to build the rank-J polarization tensor which describes a spin-J particle:

$$\epsilon^J_{\mu_1\mu_2\ldots\mu_J}(p,m) = \sum_{m_{J-1},m_1}((J-1)m_{J-1}\ 1\ m_1|Jm)\epsilon_{\mu_1\mu_2\ldots\mu_{J-1}}(p,m_{J-1})\epsilon_{\mu_J}(p,m_1). \tag{5.40}$$

We can now combine (5.40) and (5.35) to construct the polarization tensor for a half-integer-spin particle with $J = n + \frac{1}{2} \geq \frac{3}{2}$. This rank-$n$ tensor is built from the spin-n polarization tensor and the spin-$\frac{1}{2}$ Dirac spinor as

$$u_{\mu_1\mu_2\ldots\mu_n}(p,m) = \sum_{m_n,m_{\frac{1}{2}}}(nm_n\ \frac{1}{2}m_{\frac{1}{2}}|Jm)\epsilon_{\mu_1\mu_2\ldots\mu_n}(p,m_n)u(p,m_{\frac{1}{2}}). \tag{5.41}$$

We construct integer-spin projection operators as

$$\mathcal{P}^J_{\mu_1\mu_2\ldots\mu_J\nu_1\nu_2\ldots\nu_J}(p) = \sum_m \epsilon_{\mu_1\mu_2\ldots\mu_J}(p,m)\epsilon^*_{\nu_1\nu_2\ldots\nu_J}(p,m) \tag{5.42}$$

and half-integer-spin projection operators as

$$\mathcal{P}^J_{\mu_1\mu_2\ldots\mu_J\nu_1\nu_2\ldots\nu_J}(p) = \frac{1}{2w}\sum_m u_{\mu_1\mu_2\ldots\mu_J}(p,m)\overline{u}_{\nu_1\nu_2\ldots\nu_J}(p,m). \tag{5.43}$$

Finally, for two particles a and b with momenta p_a and p_b, we construct the spin-ℓ orbital angular momentum tensor $L^{(\ell)}_{\mu_1\mu_2\ldots\mu_\ell}$ as

$$L^{(\ell)}_{\mu_1\mu_2\ldots\mu_\ell}(p_{ab}) = (-)^\ell\mathcal{P}^{(\ell)}_{\mu_1\mu_2\ldots\mu_\ell\nu_1\nu_2\ldots\nu_\ell}(P)p^{\nu_1}_{ab}p^{\nu_2}_{ab}\ldots p^{\nu_\ell}_{ab}, \tag{5.44}$$

where $P = (p_a + p_b)$ and $p_{ab} = \frac{1}{2}(p_a - p_b)$ are the total and relative momenta of the ab system.

5.6.2 The $\Lambda \to p\pi^-$ Decay Amplitude

Because we concern ourselves with extraction of the Λ recoil polarization, it is necessary to include the amplitude for the $\Lambda \to p\pi^-$ decay explicitly in our amplitudes. We follow the treatment of [76], which writes the transition amplitude as

$$\begin{aligned} \mathcal{A}_{\Lambda\to p\pi^-} &= \overline{u}_p(A - B\gamma_5)u_\Lambda \\ &= \left(\frac{E_p + w_p}{2w_p}\right)^{1/2} \chi_p^\dagger \left(A + B\frac{\vec{\sigma}\cdot\vec{p}_f}{E_p + w_p}\right)\chi_\Lambda \end{aligned} \tag{5.45}$$

where

$$\overline{u}_p = \left(\frac{E_p + w_p}{2w_p}\right)^{1/2} \left(\chi_p^\dagger, \frac{\vec{\sigma}\cdot\vec{p}_f}{E_p + w_p}\chi_p^\dagger\right) \tag{5.46}$$

$$u_\Lambda = \begin{pmatrix} \chi_\Lambda \\ 0 \end{pmatrix}, \tag{5.47}$$

are the 4-component Dirac spinors in the Λ rest frame and A and B are constants. In order to calculate the values of A and B from measured quantities, we follow [76] and rewrite (5.45) as

$$\mathcal{A}_{\Lambda\to p\pi^-} = \left(\frac{E_p + w_p}{2w_p}\right)^{1/2} \chi_p^\dagger(x + y\vec{\sigma}\cdot\hat{n})\chi_\Lambda, \tag{5.48}$$

with $x = A$, $y = |\vec{p}_f|B/(E_f + w_p)$, and $\hat{n} = \vec{p}_f/|\vec{p}_f|$ denoting the unit vector along the direction of the proton momentum. These parameters can be related to the quantities which characterize the Λ decay, α_- and Δ, defined as

$$\alpha_- = 2\Re\frac{xy^*}{|x|^2 + |y|^2} = \frac{2|x||y|cos(\Delta)}{|x|^2 + |y|^2}. \tag{5.49}$$

Here, Δ is the relative phase between the two terms in the decay amplitude. The values of α_- and Δ have been empirically determined as $\alpha_- = 0.642 \pm 0.013$ [5] and $\Delta = 7.7^\circ \pm 4.0^\circ$ [76]. Using these values, we set $|x| = A = 1$ and calculate $B/A = 6.88e^{i\Delta}$, absorbing the Λ decay normalization into an overall scale factor for each full production amplitude. Thus, we write the final decay amplitude as

$$\mathcal{A}_{\Lambda\to p\pi^-} = \overline{u}_p(1 - 6.88e^{i\Delta}\gamma_5)u_\Lambda \tag{5.50}$$

For least-squares fits to $K^+\Lambda$ production results, we do not include the $\Lambda \to p\pi^-$ amplitude in the full amplitudes. In order to compare fit results from these fits and event-based fits in which the full Λ decay is used, we have calculated the average magnitude of the decay amplitude to be

$$\langle|\mathcal{A}_{\Lambda\to p\pi^-}|\rangle = \left(\langle|\mathcal{A}_{\Lambda\to p\pi^-}|^2\rangle\right)^{1/2} = 2.184 \tag{5.51}$$

by averaging over raw Monte Carlo events.

5.6.3 Non-resonant Processes

We consider several non-resonant production mechanisms: t-channel K^+, $K^*(892)$, and $K_1(1270)$ exchanges and u-channel Λ exchange. These choices are motivated by the work of Adelseck and Saghai [79]. Diagrams characterizing these amplitudes are given in Figure 5.1. The amplitude for each of these processes is then dressed with a monopole form factor for each of the two vertices to model physical particle sizes.

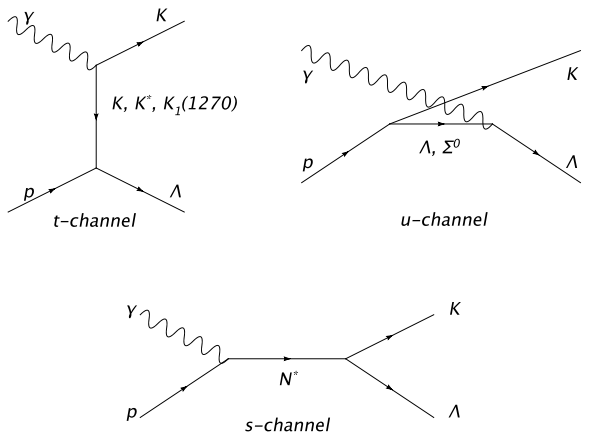

Figure 5.1: Shown above are diagrams characterizing the $\gamma p \to K^+\Lambda$ production mechanisms considered in this analysis. (Image produced by [77].)

t-channel K^+ Exchange

The most basic possible t-channel process is exchange of a virtual pseudoscalar particle with strangeness $+1$ (*i.e.* the K^+ meson). The amplitude for this process is written quite simply as

$$\mathcal{A}^{K(bare)}_{\gamma p\to K^+\Lambda} = i(g_{K^+})\overline{u}(p_\Lambda, m_\Lambda)\gamma^5 u(p_i, m_i)\frac{1}{t - w^2_{K^+}}q_\mu\epsilon^\mu, \tag{5.52}$$

where g_{K^+} is an overall scale factor for the K^+ exchange process, q is the 4-momentum of the external K^+, and ϵ is the photon polarization vector. We then add a monopole form factor for each vertex to get

$$\mathcal{A}^{K}_{\gamma p\to K^+\Lambda} = F_m(t, w_K, \Lambda_{\gamma KK})F_m(t, w_K, \Lambda_{Kp\Lambda})\mathcal{A}^{K(bare)}_{\gamma p\to K^+\Lambda}, \tag{5.53}$$

where the F take the form

$$F_m(t, w, \Lambda) = \frac{\Lambda^2 - w^2}{\Lambda^2 - t}, \tag{5.54}$$

and the Λs are the cut-off mass for the interaction. Thus, the t-channel 0^- exchange amplitude has three fit parameters (g_{K^+}, $\Lambda_{\gamma KK}$, and $\Lambda_{Kp\Lambda}$).

t-channel K^* Exchange

There are two distinct Lorentz-invariant amplitudes that we can construct for the t-channel vector meson (K^*) exchange. In what follows, we represent the momentum and spin of the exchange particle as $x = k - q$ and m_x, and the K^* mass is denoted by $w_{K^*} = 891.66$ MeV/c^2. The first, which we refer to as the K^*_E (electric coupling) amplitude, can be written as

$$\mathcal{A}^{K^*_E(bare)}_{\gamma p\to K^+\Lambda} = (g_{K^*_E})\overline{u}(p_\Lambda, m_\Lambda)\gamma^\mu u(p_i, m_i)\epsilon_\mu(x, m_x)\frac{1}{t - w^2_{K^*}}\epsilon^{\nu\alpha\beta\lambda}\epsilon^*_\nu(x, m_x)q_\alpha k_\beta\epsilon_\lambda(k, m_\gamma), \tag{5.55}$$

where $g_{K^*_E}$ is an overall scale factor for the process, $\epsilon_\mu(x, m_x)$ and $\epsilon_\mu(k, m_\gamma)$ are the polarization vectors of the exchange particle and the incoming photon and $\epsilon^{\mu\nu\alpha\beta}$ is the Levi-Civita tensor. Because the K^* is an intermediate particle, and is not directly observed, we must sum over its

possible spins states m_x. Thus, we use the projection operator $\mathcal{P}^{(1)}_{\mu\nu}(p)$ for a spin-1 particle with momentum p, written as [70]

$$\mathcal{P}^{(1)}_{\mu\nu}(p) = \sum_m \epsilon_\mu(p,m)\epsilon^*_\nu(p,m) = -g_{\mu\nu} + \frac{p_\mu p_\nu}{p^2}. \tag{5.56}$$

Adding the sum to the amplitude leaves us with

$$\begin{aligned}
\mathcal{A}^{K^*_E(bare)}_{\gamma p\to K^+\Lambda} &= \sum_{m_x}(g_{K^*_E})\overline{u}(p_\Lambda,m_\Lambda)\gamma^\mu u(p_i,m_i)\epsilon_\mu(x,m_x)\frac{1}{t-w^2_{K^*}}\epsilon^{\nu\alpha\beta\lambda}\epsilon^*_\nu(x,m_x)q_\alpha k_\beta\epsilon_\lambda(k,m_\gamma)\\
&= (g_{K^*_E})\overline{u}(p_\Lambda,m_\Lambda)\gamma^\mu u(p_i,m_i)\frac{1}{t-w^2_{K^*}}\epsilon^{\nu\alpha\beta\lambda}q_\alpha k_\beta\epsilon_\lambda(k,m_\gamma)\left(-g_{\mu\nu}+\frac{x_\mu x_\nu}{w^2_{K^*}}\right)\\
&= (g_{K^*_E})\overline{u}(p_\Lambda,m_\Lambda)\gamma_\nu u(p_i,m_i)\frac{1}{t-w^2_{K^*}}\epsilon^{\nu\alpha\beta\lambda}q_\alpha k_\beta\epsilon_\lambda(k,m_\gamma),
\end{aligned} \tag{5.57}$$

where the last step follows from $\epsilon^{\mu\nu\alpha\beta}p_\mu p_\nu q_\alpha k_\beta = 0$ for the totally antisymmetric tensor $\epsilon^{\mu\nu\alpha\beta}$.

The other possible amplitude, the magnetic coupling, can be written as

$$\begin{aligned}
\mathcal{A}^{K^*_M(bare)}_{\gamma p\to K^+\Lambda} &= i\sum_{m_x}(g_{K^*_E})\overline{u}(p_\Lambda,m_\Lambda)x^\mu\sigma_\mu{}^\nu u(p_i,m_i)\epsilon_\nu(x,m_x)\frac{M}{t-w^2_{K^*}}\epsilon^{\alpha\beta\lambda\delta}\epsilon^*_\alpha(x,m_x)q_\beta k_\lambda\epsilon_\delta(k,m_\gamma)\\
&= i(g_{K^*_E})\overline{u}(p_\Lambda,m_\Lambda)x^\mu\sigma_\mu{}^\alpha u(p_i,m_i)\frac{M}{t-w^2_{K^*}}\epsilon^{\alpha\beta\lambda\delta}q_\beta k_\lambda\epsilon_\delta(k,m_\gamma),
\end{aligned} \tag{5.58}$$

where $\sigma_\mu{}^\nu \equiv \frac{i}{2}[\gamma_\mu,\gamma^\nu]$ is the Dirac σ matrix and $g_{K^*_M}$ is the amplitude scale factor. As in the 0^- exchange, we apply monopole form factors at each vertex:

$$\mathcal{A}^{K^*_E}_{\gamma p\to K^+\Lambda} = F_m(t,w_{K^*},\Lambda^E_{\gamma KK^*})F_m(t,w_{K^*},\Lambda^E_{K^*p\Lambda})\mathcal{A}^{K^*_E(bare)}_{\gamma p\to K^+\Lambda} \tag{5.59}$$

$$\mathcal{A}^{K^*_M}_{\gamma p\to K^+\Lambda} = F_m(t,w_{K^*},\Lambda^M_{\gamma KK^*})F_m(t,w_{K^*},\Lambda^M_{K^*p\Lambda})\mathcal{A}^{K^*_M(bare)}_{\gamma p\to K^+\Lambda}. \tag{5.60}$$

Note that amplitudes given in (5.60) and (5.60) each contain three fit parameters.

t-channel $K_1(1270)$ Exchange

Finally, we consider exchange of the pseudovector (1^+) $K_1(1270)$. This amplitude can be written as

$$\begin{aligned}
\mathcal{A}^{K_1(bare)}_{\gamma p\to K^+\Lambda} &= \sum_{m_x}(g_{K_1})\overline{u}(p_\Lambda,m_\Lambda)\gamma^\mu\gamma^5 u(p_i,m_i)\epsilon_\mu(x,m_x)\frac{1}{t-w^2_{K_1}}\epsilon^{*\nu}(x,m_x)\epsilon_\nu(k,m_\gamma)\\
&= (g_{K_1})\overline{u}(p_\Lambda,m_\Lambda)\gamma^\mu\gamma^5 u(p_i,m_i)\mathcal{P}^{(1)\,\nu}_\mu(x,m_x)\frac{1}{t-w^2_{K_1}}\epsilon_\nu(k,m_\gamma),
\end{aligned} \tag{5.61}$$

where g_{K_1} is the amplitude scale factor and $w_{K_1} = 1.272$ GeV/c^2. We apply monopole form factors to get

$$\mathcal{A}^{K_1}_{\gamma p\to K^+\Lambda} = F_m(t,w_{K_1},\Lambda_{\gamma KK_1})F_m(t,w_{K_1},\Lambda_{K_1p\Lambda})\mathcal{A}^{K_1(bare)}_{\gamma p\to K^+\Lambda}. \tag{5.62}$$

Thus, $\mathcal{A}^{K_1}_{\gamma p\to K^+\Lambda}$ also contains three fit parameters.

u-channel $\frac{1}{2}^+$ Exchange

For $\gamma p\to K^+\Lambda$, u-channel processes can proceed through the exchange of a $J^P = \frac{1}{2}^+$ particle. In this analysis, we consider exchanges of both the ground-state Λ and the excited hyperon $\Lambda(1800)$. For the u-channel processes, the exchange momentum is given by $x = p_i - q$, and m_x is used to

denote the spin of the exchanged baryon. The amplitudes for these processes differ only in the mass dependence of the propagator, so we may write the amplitude for the u-channel process as

$$\begin{aligned}\mathcal{A}^{u(bare)}_{\gamma p\to K^+\Lambda} &= \sum_{m_x}(g_u)\overline{u}(p_\Lambda,m_\Lambda)\gamma^5 u(x,m_x)\frac{1}{u-w_x^2}\overline{u}(x,m_x)k^\mu\sigma_{\mu\nu}\epsilon^\nu(k,m_\gamma)u(p_i,m_i)\\ &= (g_u)\overline{u}(p_\Lambda,m_\Lambda)\gamma^5\mathcal{P}(x)\frac{1}{u-w_x^2}k^\mu\sigma_{\mu\nu}\epsilon^\nu(k,m_\gamma)u(p_i,m_i)\end{aligned} \tag{5.63}$$

where g_u is a scale factor, w_x is the mass of the exchange particle, and $\mathcal{P}^{\frac{1}{2}}(x)$ is the projection operator for a spin-$\frac{1}{2}$ particle with momentum x. We then apply a dipole form-factor to the amplitude to get

$$\mathcal{A}^{u}_{\gamma p\to K^+\Lambda} = F_d(u,w_x,\Lambda_x)\mathcal{A}^{u(bare)}_{\gamma p\to K^+\Lambda}, \tag{5.64}$$

where

$$F_d(u,w,\Lambda) = \frac{\Lambda^4}{\Lambda^4+(u-w^2)^2}, \tag{5.65}$$

and Λ is the mass cut-off for the form factor.

s-channel Proton Exchange

We also consider the s-channel exchange of the (off-shell) proton. Following the work of [24], we construct the amplitude for this diagram as

$$\begin{aligned}\mathcal{A}^{s_p}_{\gamma p\to K^+\Lambda} &= \sum_{m_x} i(g_{K\Lambda N})\overline{u}(p_\Lambda,m_\Lambda)\gamma^5 u(x,m_x)\frac{1}{s-w_p^2}\\ &\quad\times\overline{u}(x,m_x)(e\gamma^\alpha\epsilon_\alpha(k,m_\gamma)+\mu_p\gamma^\beta k_\beta\gamma^\rho\epsilon_\rho(k,m_\gamma)u(p_i,m_i) \qquad (5.66)\\ &= \sum_{m_x} i(g_{K\Lambda N})\overline{u}(p_\Lambda,m_\Lambda)\gamma^5\frac{1}{s-w_p^2}\\ &\quad\times\mathcal{P}(x)(e\gamma^\alpha\epsilon_\alpha(k,m_\gamma)+\mu_p\gamma^\beta k_\beta\gamma^\rho\epsilon_\rho(k,m_\gamma)u(p_i,m_i), \qquad (5.67)\end{aligned}$$

where $x = k+p_i$ is the exchanged momentum, and e and μ_p are the electric coupling factor and proton magnetic moment. Note that this amplitude differs from that of s-channel resonant processes in that its propagator is evaluated at the proton mass ($w_p = 938.272$ MeV). Here, $g_{K\Lambda N}$ is the coupling factor associated with the final state vertex. The value of this factr has bee estimated, but these estimates are typically the results of large-scale fits or *ad hoc* SU(3) relations to the πNN coupling. These values range between 3.6 [24] and 11.5 [78]. We discuss this diagram and its effect on our analysis further in §8.2.

5.6.4 Resonant Processes

The most important amplitudes for our analysis are the s-channel amplitudes which describe $K^+\Lambda$ photoproduction through an excited nucleon (N^*) intermediate state characterized by spin and parity J^P. We use these amplitudes for our "Mother Fit" as well as for resonance searches in our partial wave analysis. One of the interesting features of the $\gamma p \to K^+\Lambda$ reaction is its iso-spin filtering; the Δ resonances ($I_\Delta = \frac{3}{2}$) do not couple to the $K^+\Lambda$ ($I_\Lambda = \frac{1}{2}$, $I_K = 0$) final state. The full $\gamma p \to N^* \to K^+\Lambda$ can be treated in two halves: the production amplitude $\gamma p \to N^*$ ("$\frac{1}{2}^+1^- \to J^P$"), and the decay amplitude $N^* \to K^+\Lambda$ ("$J^P \to 0^-\frac{1}{2}^+$"). In what follows, we refer to the momentum and spin of the intermediate N^* as P_N and M_N, respectively. Here, we follow the work of [4].

The $J^P \to K^+\Lambda$ Amplitude

We first consider the $J^P \to K^+\Lambda$ amplitudes for which $P = (-)^{J+\frac{1}{2}}$. Below, we denote the Dirac spinors of the Λ and J^P states as $\overline{u}(p_\Lambda)$ and $u(P_N, M_N)$, respectively. Beginning with the $J^P = \frac{1}{2}^-$ state, we have

$$\mathcal{A}_{\frac{1}{2}^- \to K^+\Lambda} \sim \overline{u}(p_\Lambda, m_\Lambda) u(P_N, M_N), \tag{5.68}$$

as the decay can only proceed through an S-wave. For the $J^P_{N^*} = \frac{3}{2}^+$, we must couple the initial and final states by adding a unit of orbital angular momentum (P-wave). This amplitude is constructed by adding the $L = 1$ orbital angular momentum tensor, $L^{(1)}_\mu(p_{K\Lambda})$ to get:

$$\mathcal{A}_{\frac{3}{2}^+ \to K^+\Lambda} \sim \overline{u}(p_\Lambda, m_\Lambda) L^{(1)}_\mu(p_{K\Lambda}) u^\mu(P_N, M_N), \tag{5.69}$$

where $p_{K\Lambda} = \frac{1}{2}(p_K - p_\Lambda)$ is the relative momentum used to define $L^{(1)}$. This can be generalized to give the decay amplitude

$$\mathcal{A}_{J^P \to K^+\Lambda} \sim \overline{u}(p_\Lambda, m_\Lambda) L^{(\ell)}_{\mu_1\mu_2\ldots\mu_\ell}(p_{K\Lambda}) u^{\mu_1\mu_2\ldots\mu_\ell}(P_N, M_N), \quad \ell = 1, 2, 3, \ldots \tag{5.70}$$

Next, we consider J^P states with $P = (-)^{J-\frac{1}{2}}$. The $\frac{1}{2}^+ \to K^+\Lambda$ decay can proceed only through P-wave, with an amplitude written as

$$\mathcal{A}_{\frac{1}{2}^+ \to K^+\Lambda} \sim \overline{u}(p_\Lambda, m_\Lambda) L^1_\mu(p_{K\Lambda}) \gamma^\mu\gamma^5 u(P_N, M_N), \tag{5.71}$$

where the γ^5 is included for parity conservation. This form is easily generalized to higher J:

$$\mathcal{A}_{J^P \to K^+\Lambda} \sim \overline{u}(p_\Lambda, m_\Lambda) L^\ell_{\mu_1\mu_2\ldots\mu_\ell}(p_{K\Lambda}) \gamma^{\mu_1}\gamma^5 u^{\mu_2\ldots\mu_\ell}(P_N, M_N), \quad \ell = 1, 2, 3, \ldots \tag{5.72}$$

The $\gamma p \to J^P$ Amplitude

In our above treatment of decay amplitudes, we constructed amplitudes in definite states of $L - S$. If we use the $L - S$ basis for the production amplitudes, the amplitudes for different couplings to a given J^P differ only by a factor of the center-of-mass energy [4]. Because we group events according to center-of-mass energy, the amplitudes for these couplings for any event would differ only by a constant, rendering our fit insensitive to the differences in the amplitudes.

To avoid this problem, we write production amplitudes characterizing the $\gamma p \to J^P$ reaction in the multipole basis. In this basis, we think of the photon spin as coupling to the orbital angular momentum of the γp system to produce a state of pure spin and parity denoted by j^p. This j^p is then coupled to the proton spin to produce the J^P value of the N^*. Because both the photon and proton have their momenta aligned with $\hat{z}$, we can conclude that $\ell_z = 0$. Thus, $m_\gamma = \pm 1$ and $m_\ell = 0$ combine to give $m_j = \pm 1$ and j cannot be 0. We divide the amplitudes into two types: *electric* coupling with $p = (-)^j$ and *magnetic* couplings with $p = (-)^{j+1}$. We denote the states with $j^p = 1^-, 2^+, \ldots$ by $E1, E2, \ldots$ and those with $j^p = 1^+, 2^-, \ldots$ by $M1, M2, \ldots$

A table summarizing the quantum numbers of the different multipole states is provided in 5.1.

Couplings to J^P States with $P = (-)^{J+\frac{1}{2}} = \{\frac{1}{2}^-, \frac{3}{2}^+, \frac{5}{2}^-, \ldots\}$

We first consider the $J^P = \frac{1}{2}^-$ amplitude. In order that we conserve angular momentum and parity, the photon and proton must be in an $\ell = 0$ or $\ell = 2$ state. Coupling the photon to the $\ell = 0$ state gives $j^p = 1^-$, whereas the $\ell = 2$ state can give $j^p = 1^-, 2^-, 3^-$. As described above, we must then couple the j^p states to the proton spin to get J^P. Only the $j^p = 1^-$ states can couple to the proton

J^P	Mulitpoles	$s_{p\gamma}$	$\ell_{p\gamma}$	$s_{p\gamma}$	$\ell_{p\gamma}$	$s_{p\gamma}$	$\ell_{p\gamma}$
$(\frac{1}{2})^-$	E1	$\frac{1}{2}$	0	$\frac{3}{2}$	2		
$(\frac{3}{2})^-$	E1,M2	$\frac{1}{2}$	2	$\frac{3}{2}$	0	$\frac{3}{2}$	2
$(\frac{5}{2})^-$	M2,E3	$\frac{1}{2}$	2	$\frac{3}{2}$	2	$\frac{3}{2}$	4
$(\frac{7}{2})^-$	E3,M4	$\frac{1}{2}$	4	$\frac{3}{2}$	2	$\frac{3}{2}$	4
$(\frac{9}{2})^-$	M4,E5	$\frac{1}{2}$	4	$\frac{3}{2}$	4	$\frac{3}{2}$	6
$(\frac{1}{2})^+$	M1	$\frac{1}{2}$	1	$\frac{3}{2}$	1		
$(\frac{3}{2})^+$	M1,E2	$\frac{1}{2}$	1	$\frac{3}{2}$	1	$\frac{3}{2}$	3
$(\frac{5}{2})^+$	E2,M3	$\frac{1}{2}$	3	$\frac{3}{2}$	1	$\frac{3}{2}$	3
$(\frac{7}{2})^+$	M3,E4	$\frac{1}{2}$	3	$\frac{3}{2}$	3	$\frac{3}{2}$	5
$(\frac{9}{2})^+$	E4,M5	$\frac{1}{2}$	5	$\frac{3}{2}$	3	$\frac{3}{2}$	5

Table 5.1: Quantum numbers describing multipole couplings for $\gamma p \to J^P$. In the left column, J^P gives the total spin and parity of the system (and thus of N^*). In the right three columns, the $\ell_{p\gamma}$'s give the orbital angular momenta between proton and γ. The $s_{p\gamma}$'s give the spin of the $p\gamma$ system in the LS basis, solely for comparison. These quantum numbers are then coupled via either the electric or magnetic multipoles to the J^P.

$(\frac{1}{2}^+)$ to yield $J^P = \frac{1}{2}^-$. Hence, we say that the $J^P = \frac{1}{2}^-$ state couples only to the $E1$ multipole and we write the amplitude for this process as

$$\begin{aligned} \mathcal{A}^{E1}_{\gamma p \to \frac{1}{2}^-} &\sim \overline{u}(P_N, M_N)\gamma^\mu\gamma^5 u(p_i, m_i)\left(\mathcal{P}^{(1)}_{\mu\nu}(P_N)\epsilon^\nu(k, m_\gamma)\right) \\ &\sim \overline{u}(P_N, M_N)\gamma^\mu\gamma^5 u(p_i, m_i)\epsilon_\mu(k, m_\gamma). \end{aligned} \tag{5.73}$$

Next, we consider the $J^P = \frac{3}{2}^+$ state. Allowed ℓ values of the γp system for this reaction are $\ell = 1$ and $\ell = 3$. The photon can couple to $\ell = 1$ to give $j^p = 1^+, 2^+$, and to $\ell = 3$ to give $j^p = 2^+, 3^+, 4^+$. Of these, only the $j^p = 1^+$ ($M1$ multipole) and $j^p = 2^+$ ($E2$ multipole) states can couple with the proton to give $J^P = \frac{3}{2}^+$. The discarded $E2$ amplitude from the $\ell = 3$ coupling has the same angular distribution as that of the $\ell = 1$ coupling. Because the $\ell = 1$ coupling represents both multipoles, we may discard the $\ell = 3$ coupling and write the amplitude compactly as

$$\mathcal{A}^{mp=j^+}_{\gamma p \to \frac{3}{2}^+} \sim \overline{u}^\mu(P_N, M_N)\gamma^\nu\gamma^5\mathcal{P}^{(j)}_{\mu\nu\alpha\beta}(P_N)L^{(1)\alpha}(p_{p\gamma})\epsilon^\beta(k, m_\gamma)u(p_i, m_i), \tag{5.74}$$

where $p_{p\gamma} = p_i - k$, and $mp = j^+$ characterizes the multipole ($j = 1$ for magnetic, $j = 2$ for electric). This amplitude can be generalized by extension of the projection operator and angular momentum tensor to yield amplitudes for higher J states:

$$\mathcal{A}^{mp=j^p}_{\gamma p \to J^P} \sim \overline{u}^{\mu_1\mu_2\ldots\mu_\ell}(P_N, M_N)\gamma^\nu\gamma^5\mathcal{P}^{(j)}_{\mu_1\mu_2\ldots\mu_\ell\nu\alpha_1\alpha_2\ldots\alpha_\ell\beta}(P_N)L^{(\ell)\alpha_1\alpha_2\ldots\alpha_\ell}(p_{p\gamma})\epsilon^\beta(k, m_\gamma)u(p_i, m_i), \tag{5.75}$$

where $\ell = J - \frac{1}{2}$, $j = J - \frac{1}{2}$ or $j = J + \frac{1}{2}$, and $p = (-)^{J+\frac{1}{2}}$. For each $J^P > \frac{1}{2}^-$, there are two possible multipole couplings, one electric and one magnetic.

Couplings to J^P States with $P = (-)^{J-\frac{1}{2}} = \{\frac{1}{2}^+, \frac{3}{2}^-, \frac{5}{2}^+, \ldots\}$

Finally, we consider amplitudes for couplings to J^P states with $P = (-)^{J-\frac{1}{2}}$. We begin with $J^P = \frac{1}{2}^+$. Here, $\ell = 1$ is the only possibility for the angular momentum of the γp system. ℓ can couple to the photon spin to give $j^p = 1^+$ or 2^+, however, only the 1^+ ($M1$ multipole) can couple with the proton to give total $J^P = \frac{1}{2}^+$. We can write the amplitude for this process as

$$\mathcal{A}^{M1}_{\gamma p \to \frac{1}{2}^+} \sim \overline{u}(P_N, M_N)\gamma^\alpha L^{(1)}_\alpha(p_{p\gamma})\gamma^\mu\epsilon_\mu(k, m_\gamma)u(p_i, m_i). \tag{5.76}$$

The $J^P = \frac{3}{2}^-$ state can be created with the γp system in either the $\ell = 0$ or $\ell = 2$ states. These couple to the photon to give $j^p = 1^-$ for $\ell = 0$ and $j^p = 1^-, 2^-, 3^-$ for $\ell = 2$. Of these, only the $j^p = 1^-$ and $j^p = 2^-$ states can contribute. We may write the amplitude for both of these processes as

$$\mathcal{A}^{mp=j^-}_{\gamma p \to \frac{3}{2}^-} \sim \overline{u}^{\mu}(P_N, M_N)\gamma^{\nu}\gamma^{\alpha}\mathcal{P}^{(j)}_{\mu\nu\alpha\mu'\nu'\alpha'}(P_N)L^{(2)\mu'\nu'}(p_{p\gamma})\epsilon^{\alpha'}(k, m_{\gamma})u(p_i, m_i), \tag{5.77}$$

where $j = 1, 2$.

This can be generalized to higher J states with $P = (-)^{J-\frac{1}{2}}$ as

$$\begin{aligned}\mathcal{A}^{mp=j^p}_{\gamma p \to J^P} \quad \sim \quad & \overline{u}^{\mu_1\mu_2\ldots\mu_{\ell-1}}(P_N, M_N)\gamma^{\mu_\ell}\gamma^{\mu_{\ell+1}}\mathcal{P}^{(j)}_{\mu_1\mu_2\ldots\mu_{\ell+1}\nu_1\nu_2\ldots\nu_{\ell+1}}(P_N) \times \\ & L^{(\ell)\nu_1\nu_2\ldots\nu_{\ell+1}}(p_{p\gamma})\epsilon^{\nu_{\ell+1}}(k, m_{\gamma})u(p_i, m_i),\end{aligned} \tag{5.78}$$

where $\ell = J + \frac{1}{2}$, $j = J - \frac{1}{2}$ or $j = J + \frac{1}{2}$, and $p = (-)^{J-\frac{1}{2}}$. Once again, each $J^P > \frac{1}{2}^+$ has one electric and one magnetic coupling to γp.

5.6.5 Constructing the $\gamma p \to J^P \to K^+\Lambda$ Amplitude

We can now combine amplitudes for $\gamma p \to J^P$ and $J^P \to K^+\Lambda$ to construct the amplitude for the the full $\gamma p \to J^P \to K^+\Lambda$ reaction. We define the quantities X_{PROD} and X_{DECAY} from (5.70), (5.72), (5.75), and (5.78) as

$$\mathcal{A}_{\gamma p \to J^P} \equiv \overline{u}_{\mu_1\mu_2\ldots\mu_{J-\frac{1}{2}}}(P_N, M_N)X^{\nu\mu_1\mu_2\ldots\mu_{J-\frac{1}{2}}}_{PROD}\epsilon_{\nu}(k, m_{\gamma})u(p_i, m_i) \tag{5.79}$$

$$\mathcal{A}_{J^P \to K^+\Lambda} \equiv \overline{u}(p_{\Lambda}, m_{\Lambda})X^{\mu_1\mu_2\ldots\mu_{J-\frac{1}{2}}}_{DECAY}u_{\mu_1\mu_2\ldots\mu_{J-\frac{1}{2}}}(P_N, M_N). \tag{5.80}$$

X_{PROD} and X_{DECAY} are thus the "meat" of the production and decay amplitudes. To create the full amplitude, we simply combine $\mathcal{A}_{\gamma p \to J^P}$ and $\mathcal{A}_{J^P \to K^+\Lambda}$ and sum over the possible spin states of the intermediate J^P state:

$$\begin{aligned}\mathcal{A}_{\gamma p \to J^P \to K^+\Lambda} &= \sum_{M_N} \overline{u}(p_{\Lambda}, m_{\Lambda})X^{\mu_1\mu_2\ldots\mu_{J-\frac{1}{2}}}_{DECAY}u_{\mu_1\mu_2\ldots\mu_{J-\frac{1}{2}}}(P_N, M_N)\overline{u}_{\nu_1\nu_2\ldots\nu_{J-\frac{1}{2}}}(P_N, M_N) \times \\ &\qquad X^{\nu\nu_1\nu_2\ldots\nu_{J-\frac{1}{2}}}_{PROD}\epsilon_{\nu}(k, m_{\gamma})u(p_i, m_i)\mathcal{R}(s) \\ \mathcal{A}_{\gamma p \to J^P \to K^+\Lambda} &= \overline{u}(p_{\Lambda}, m_{\Lambda})X^{\mu_1\mu_2\ldots\mu_{J-\frac{1}{2}}}_{DECAY}\mathcal{P}_{\mu_1\mu_2\ldots\mu_{J-\frac{1}{2}}\nu_1\nu_2\ldots\nu_{J-\frac{1}{2}}}(P_N) \times \\ &\qquad X^{\nu\nu_1\nu_2\ldots\nu_{J-\frac{1}{2}}}_{PROD}\epsilon_{\nu}(k, m_{\gamma})u(p_i, m_i)\mathcal{R}(s),\end{aligned} \tag{5.81}$$

where $\mathcal{R}(s)$ is included as the mass dependence of the J^P state. Because we bin finely in $\sqrt{s}$, we are able to treat $\mathcal{R}(s)$ as a bin-dependent (complex) constant and extract the s-dependence of the J^P state by performing independent fits in each bin.

5.7 Summary

In this chapter, we have developed the machinery of our fitting procedure. The methods and formulæ used for both likelihood and least-squared fits are described. We provide a brief synopsis of the covariant tensor formalism used for amplitude calculations. We motivate and construct the amplitudes used for resonant s-channel and non-resonant t- and u-channel photoproduction of the $K^+\Lambda$ system as well as the $\Lambda \to p\pi^-$ decay amplitude. These techniques are used both for extraction of results (Chapter 6) and our partial wave analysis (Chapter 8).

Chapter 6

Differential Cross Section and Recoil Polarization Measurements

.

In the previous chapters, we have described all of our methods for extracting $\gamma p \to K^+\Lambda$ yields from the *g11a* dataset. We have also outline our calculations of our detector acceptance and photon normalization. In this chapter, we combine these three elements to extract the measureable quantites characteristic of the reaction given an unpolarized beam and target: the differential cross section and Λ recoil polarization. Results are given from both the two- and three-track final state analyses. We note several features of the differential cross section and polarization results that are interesting in light of the search for excited nucleon states. We conclude by comparing these results to previous measurements.

Here, we remind the reader that we have fully developed two analyses of $K^+\Lambda$ production in the *g11a* dataset: the $K^+p\pi^-$ and $K^+p(\pi^-)$ topologies. In this chapter, we present measurements from these independent analyses. The level of agreement displayed by the results of the two analyses lends creedence to our treatment of CLAS acceptance, signal extraction, and systematics in the previous chapters.

6.1 The Mother of All Fits

In Chapter 4, we described our method of acceptance calculation using GSIM and phase-space $\gamma p \to K^+\Lambda \to K^+p\pi^-$ Monte Carlo events. As described, this method is incomplete because the phase-space distribution of Monte Carlo events does not necessarily match the data distribution created by more complicated production processes. Past analyses ([13]) have investigated the effect of a more "physical" Monte Carlo on acceptance calculations by producing Monte Carlo events according to a forward-peaked $\cos\theta_{CM}$ distribution (thus modeling t-channel production) [80].

We ensure the best possible match of our Monte Carlo and data by performing an "complete" expansion of the data in each $\sqrt{s}$ bin. For this fit, we use the maximum-likelihood method (see §5.2) to fit the set of s-channel $\gamma p \to J^P \to K^+\Lambda \to K^+p\pi^-$ amplitudes with $\frac{1}{2}^{\pm} \leq J^P \leq \frac{11}{2}^{\pm}$ to the data. Herein, we refer to this fit as the "Mother of All Fits." We do not interpret the results of the Mother Fit as physics results; rather we only exploit the fit as a nearly complete expansion of the data in a set of basis functions. For the level of complexity of the $K^+\Lambda$ channel, the amplitudes used in the Mother Fit constitute a basis complete enough to describe the data in all physical distributions and correlations.

6.1.1 Amplitude Parametrization

As described in §5.6.4, the s-channel amplitudes with $J^P = \frac{1}{2}^{\pm}$ have only a magnetic or electric multipole coupling and are each parametrized by two (real) fit parameters. For the purposes of our fit, these amplitudes can be written as

$$A_{\gamma p \to \frac{1}{2}^+ \to K^+\Lambda \to K^+ p\pi^-} = r_{\frac{1}{2}^+} e^{i\phi_{\frac{1}{2}^+}} \mathcal{A}^{\Lambda\to p\pi^-}_{m_\Lambda, m_f} \mathcal{A}_{E1, m_i, m_\gamma, m_\Lambda} \tag{6.1}$$

$$A_{\gamma p \to \frac{1}{2}^- \to K^+\Lambda \to K^+ p\pi^-} = r_{\frac{1}{2}^-} e^{i\phi_{\frac{1}{2}^-}} \mathcal{A}^{\Lambda\to p\pi^-}_{m_\Lambda, m_f} \mathcal{A}_{M1, m_i, m_\gamma, m_\Lambda}, \tag{6.2}$$

where $r_{\frac{1}{2}^\pm}$ and $\phi_{\frac{1}{2}^\pm}$ represent overall scale and phase parameters, respectively, and $\mathcal{A}^{\Lambda\to p\pi^-}_{m_\Lambda, m_f}$ and $\mathcal{A}_{MP, m_i, m_\gamma, m_\Lambda}$ are the amplitudes for Λ decay and production for the specified spin polarizations. As such, the $J^P = \frac{1}{2}^{\pm}$ amplitudes contribute a total of four parameters to the Mother Fit.

Amplitudes for $J \geq \frac{3}{2}$ are complicated by the fact that for each J^P, both electric and magnetic couplings contribute. We are able to remove the ambiguity in the production and decay couplings for a given J^P amplitude by writing the full amplitude as

$$A_{\gamma p \to J^P \to K^+\Lambda \to K^+ p\pi^-} = f_{MP}(\theta_{J^P}) r_{J^P} e^{i\phi_{J^P}} \mathcal{A}^{\Lambda\to p\pi^-}_{m_\Lambda, m_f} \mathcal{A}_{MP, m_i, m_\gamma, m_\Lambda}, \tag{6.3}$$

where MP denotes the specific multipole coupling. θ_{J^P} is a fit parameter included to allow the fit to manipulate the ratio of the two multipoles through the function f defined as

$$f_{MP}(\theta_{J^P}) = \left\{ \begin{array}{ll} \cos\theta_{J^P} & \text{for electric multipoles} \\ \sin\theta_{J^P} & \text{for magnetic multipoles} \end{array} \right\}. \tag{6.4}$$

This parametrization requires the $J^P \to K^+\Lambda$ decay coupling for a given J^P be the same for both multipole productions while providing freedom in the relative strengths of the multipoles. Through the use of these trigonometric functions, we ensure that $\sum_{MP} f^2_{MP} = 1$. Thus, from each J^P partial wave with $J \geq \frac{3}{2}$, we have three fit parameters. Taking into account all of the partial waves used, we see that our Mother Fit contains a total of thirty-four independent fit parameters.

6.1.2 Fit Accuracy

The outcome of the Mother Fit is a weight for each accepted and raw Monte Carlo event given by the final fit parameters and amplitudes. We are able to check how well the fit matches the accepted Monte Carlo to the data by comparing data and weighted accepted Monte Carlo distributions in each $\sqrt{s}$ bin. For our reaction, for a fixed center-of-mass energy there are three physical parameters which characterize the reaction: the production angle ($\cos\theta_{CM}$) defined by the K^+ trajectory and the z-axis (photon momentum direction) and the proton polar and azimuthal angles in the Λ-helicity-frame ($\theta^p_{\Lambda HF}$ and $\varphi^p_{\Lambda HF}$).

Figure 6.1 shows the effect of the fit weighting on the production angle distributions for two $\sqrt{s}$ bins for both the two- and three-track topologies. Shown are the $\cos\theta^K_{CM}$ distributions of the data and accepted Monte Carlo before and after weighting by fit results. We see that the agreement in this distribution between the weighted accepted Monte Carlo and the data is excellent, a good preliminary indicator that our Mother Fit is working. It is also interesting to note that in the lower center-of-mass energy bins, the effects of the the fit weighting are less drastic; the difference between the phase-space Monte Carlo and the data is slight. However, for higher energy bins where the $K^+\Lambda$ production is dominated by t-channel exchange, the fit weighting is dramatic.

We must also ensure that correlations between the characteristic kinematic variables are properly matched. Figure 6.2 shows the effects of fit weighting on the $\varphi^p_{\Lambda HF}$ v. $\cos\theta^p_{\Lambda HF}$ distributions in bins of $\cos\theta^K_{CM}$ for both the two- and three-track topologies. Physics and detector acceptance combine to make the two-dimensional data distributions far from flat. We find that the weighted Monte Carlo distributions match those of the data in all kinematic correlations and deem the fits effective.

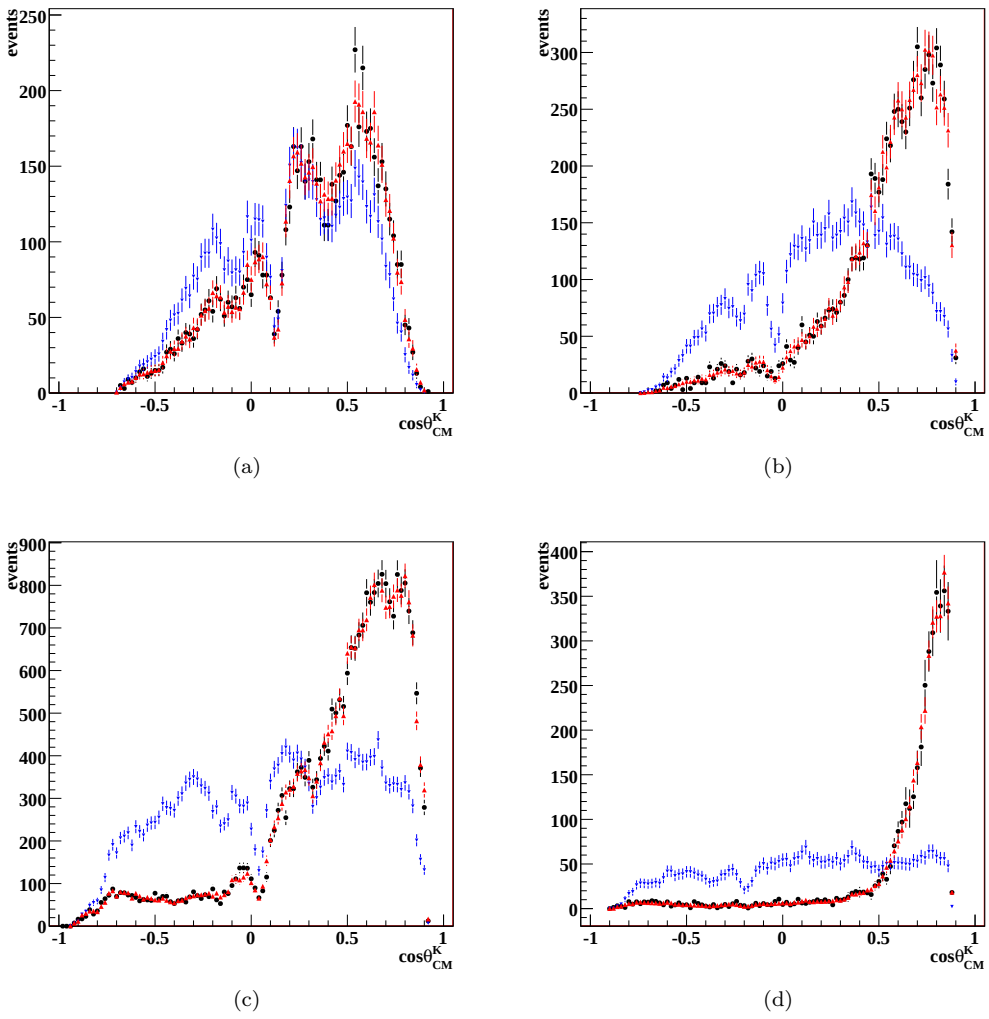

Figure 6.1: Shown above are $\cos\theta^K_{CM}$ yields for the data (black) and Monte Carlo before (blue) and after (red) fit weighting. The top plots show the distributions for the three-track topology in the (a) $\sqrt{s} = 1.905$ GeV and (b) $\sqrt{s} = 2.305$ GeV bins. The bottom plots represent the two-track topology distributions for the (c) $\sqrt{s} = 2.105$ GeV and (d) $\sqrt{s} = 2.705$ GeV bins. Overall agreement between data and weighted accepted MC is very good.

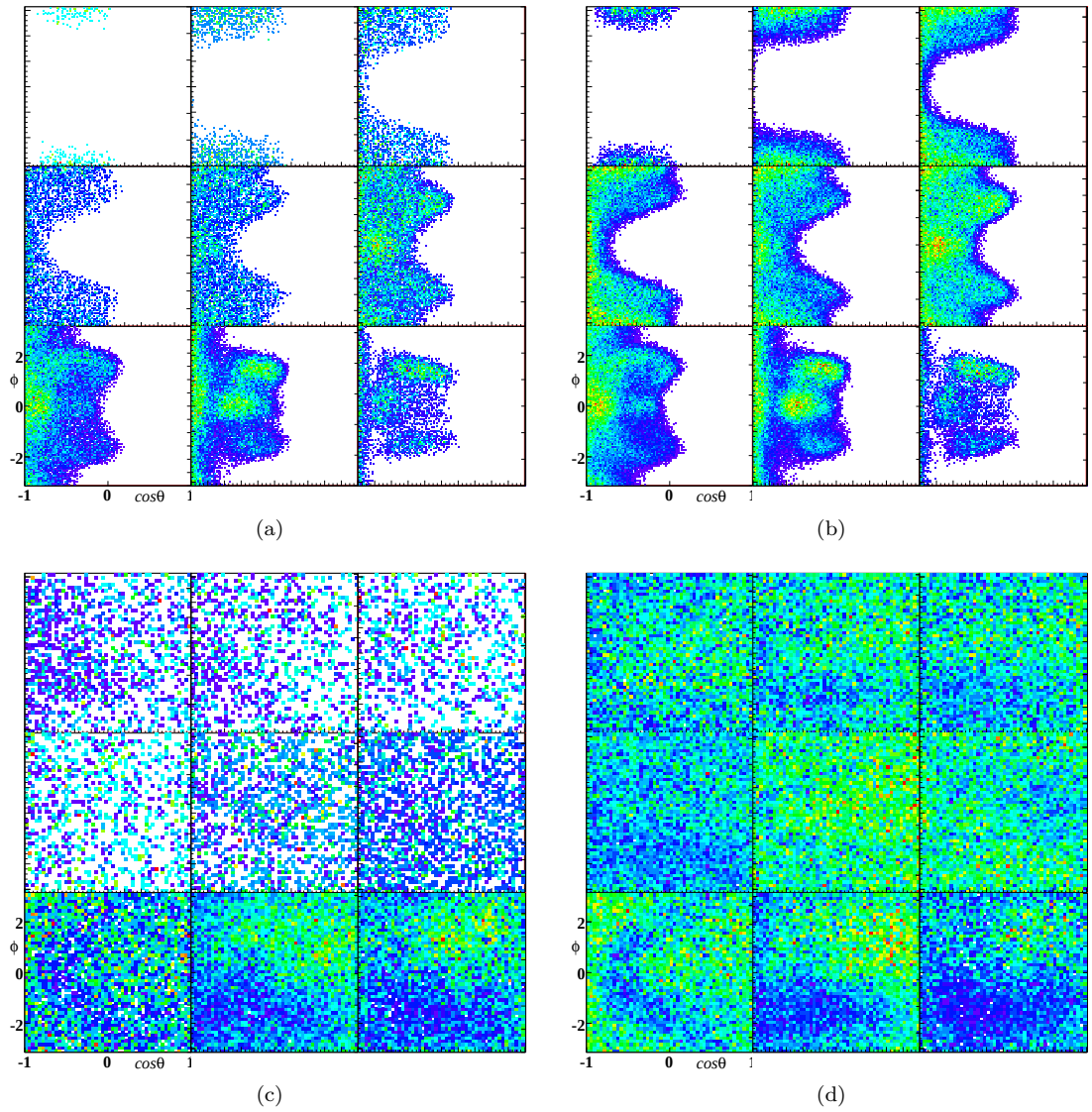

(a) (b)

(c) (d)

Figure 6.2: Shown above are plots of $\phi^p_{\Lambda HF}$ v. $\cos\theta^p_{\Lambda HF}$ for data and weighted accepted Monte Carlo in bins of $\cos\theta^K_{CM}$. Figures (a) and (b) show the data and Monte Carlo events (respectively) in the range 2.000 GeV $\leq \sqrt{s} <$ 2.050 GeV from the tree-track final state topology. Figures (c) and (d) show the data and Monte Carlo events in the range 2.500 GeV $\leq \sqrt{s} <$ 2.550 GeV from the two-track final state topology. In each figure, each of the nine plots represents a 0.2-unit-wide bin in $\cos\theta^K_{CM}$, from backward angles at top left to forward angle at bottom right. The axes in all plots show the same ranges ($-\pi \leq \phi \leq \pi$, $-1.0 \leq \cos\theta \leq 1.0$). All correlations present in the data are represented in the weighted Monte Carlo.

Factor	Value	Description	Source
A_t	1.00794 g/mol	target atomic weight	
ρ_t	0.7177±0.0008 g/cm^3	target density	[4]
ℓ_t	40±0.05 cm	target length	[45]
N_A	6.022141×10^{23} mol^{-1}	Avogadro's constant	[5]

Table 6.1: Table of *g11a* Target Factors

6.2 Differential Cross Sections

For scattering processes, the *differential cross section*, $d\sigma$ is a measurable quantity which describes the likelihood of an interaction for a given set kinematics. For a photoproduction experiment such as $K^+\Lambda$ production in *g11a*, $d\sigma$ is a measure of the probability per unit incident flux that the $K^+\Lambda$ final state will be produced per unit solid angle. The differential cross section is a quantity that is inherent to the initial state particles. For this analysis, a measurement of the $\gamma p \to K^+\Lambda$ differential cross section is of great interest, as discrepancies exist among world data for the reaction. In this section, we present differential cross section results from our analyses of both two- and three-track final state topologies.

6.2.1 Calculation

In what follows, we quote differential cross section measurements as a function of $\cos\theta^K_{CM}$. As such, we calculate $d\sigma/d\cos\theta^K_{CM}$ for a given kinematic range as

$$\frac{d\sigma}{d\cos\theta^K_{CM}} = \left(\frac{A_t}{\mathcal{F}(\sqrt{s})\rho_t\ell_t N_A}\right)\frac{\mathcal{Y}(\sqrt{s},\theta^K_{CM})}{(\Delta\cos\theta^K_{CM})\eta(\sqrt{s},\theta^K_{CM})}, \tag{6.5}$$

where A_t, ρ_t, and ℓ_t are the target atomic weight, density, and length (respectively), N_A is Avogadro's constant, $\mathcal{F}(\sqrt{s})$ is the corrected number of photons impingent on the target in each $\sqrt{s}$ bin, and $\Delta\cos\theta^K_{CM} = 0.10$ is the width of our binning in $\cos\theta^K_{CM}$ and is the same for all kinematic regions. A summary of the values of target factors used in this analysis are given in Table 6.1. For the three-track analysis, $\mathcal{Y}(\sqrt{s},\cos\theta^K_{CM})$ is the detected data yield in each $(\sqrt{s},\cos\theta^K_{CM})$. For the two-track analysis, we consider the weighting of each event from our background subtraction by calculating the data yield to be

$$\mathcal{Y}(\sqrt{s},\cos\theta^K_{CM}) = \sum_i^N Q_i, \tag{6.6}$$

where N is the number of data events in the $(\sqrt{s}, cos\theta^K_{CM})$ bin and Q_i is the signal probability of event i (see §3.8). We calculate the acceptance in a given bin as

$$\eta(\sqrt{s}, cos\theta^K_{CM}) = \frac{\sum_i^{N_{acc}} |\mathcal{M}_i|^2}{\sum_j^{N_{raw}} |\mathcal{M}_j|^2} \tag{6.7}$$

where N_{acc} and N_{raw} are the numbers of accepted and raw Monte Carlo events, and $|\mathcal{M}_i|^2$ is the event physics weights calculated with from the results of the Mother Fit.

Source	Value	Description
Particle Identification	0.11%	signal loss to PID, three-track analysis (§3.5.1)
	0.45%	signal loss to PID, two-track analysis (§3.5.1)
	3.4%	two-track MC for $\sqrt{s} < 1.66$ GeV (§4.2)
Confidence Level Cuts	3%	data/MC loss due to CL cut [81]
Acceptance	3-6%	Acceptance study (§4.3)
$\Lambda \to p\pi^-$ branching fraction	0.5%	exp. uncertainty in BF [5]
Target Density	0.11%	Std. dev. of target measurement per run [4]
Target Length	0.125%	target survey precision [45]
Photon Normalization	7.3%	based upon run-to-run normalized yields [81]
Photon Transmission Efficiency	0.5%	propagation of photons to target [81]
Live-time	3%	DAQ live time [4]

Table 6.2: Table of Systematic Errors

6.2.2 Errors

Statistical errors in each $(\sqrt{s}, \cos\theta^K_{CM})$ are given by

$$\sigma^2_{\mathcal{Y}} = \left\{ \begin{array}{ll} \mathcal{Y} & \text{for three-track analysis} \\ \mathcal{Y} + (\sum_i^N \sigma_{Q_i})^2 & \text{for two-track analysis} \end{array} \right\}. \tag{6.8a}$$

$$\sigma^2_{acc} = N_{acc} \tag{6.8b}$$

$$\sigma^2_{raw} = N_{raw}. \tag{6.8c}$$

Table 6.2 gives a summary of the values of systematic errors that apply to this analysis. The systematic uncertainty of our acceptance calculation has been discussed earlier in this text, as noted. Values for the normalization errors can be found in [81]. Exact numerical values for the overall systematic error for each $d\sigma$ point are given with the results in Appendix A. Overall normalization uncertainty combines photon normalization, photon transmission efficiency, and live-time uncertainties for a total of 7.9%. All of the uncertainties in the Table 6.2 combine for a total systematic uncertainty of $\approx 10.4\%$ (dependent upon analysis topology).

6.2.3 Results

We have calculated differential cross section measurements for the $\gamma p \to K^+\Lambda$ reaction from the two- and three-track analyses independently. Figures 6.3 through 6.9 show the final $d\sigma/d\cos\theta^K_{CM}$ results in each $\sqrt{s}$ bin (10 MeV wide). The numerical values of the results can be found in Appendix A. We present no differential cross section measurements for the $\sqrt{s} = 1.955$ GeV, 2.735 GeV, and 2.745 GeV bins for reasons discussed in §4.5. Error bars on the points in these figures represent statistical errors as described in eq (6.8a). In all, we present measurements at 2076 kinematic points.

Several features of the differential cross section are worth noting. At low $\sqrt{s}$ values ($\sqrt{s} < 1.89$ GeV), the cross section is relatively linear in $\cos\theta^K_{CM}$. Above $\sqrt{s} = 1.89$ GeV, a backwards peak is present in $d\sigma$, and by $\sqrt{s} \approx 2.39$, we observe the backward and forward peaks to be separated. At all energies above $\sqrt{s} \approx 1.94$ GeV, the forward peak in the differential cross section is recognizable. For energies above $\sqrt{s} \approx 2.4$ GeV, the forward peak dominates the differential cross section, suggesting the dominance of t-channel production mechanisms. In the energy range 2.0 GeV $\leq \sqrt{s} < 2.7$ GeV, we observe many interesting, localized features in the differential cross section, indicative of higher-J resonant production mechanisms.

These plots also illustrate how much larger the acceptance is for the two-track topology. Though the three-track analysis is perhaps simpler due to its very low background levels, the two-track analysis is essential for understanding $K^+\Lambda$ production near threshold and at backward angles.

Global differences between results from the different topologies are minimal. To illustrate this, we calculate the weighted difference between the two results in a given $(\sqrt{s}, \cos\theta^K_{CM})$ bin as

$$\Delta(\sqrt{s}, \cos\theta^K_{CM}) = \frac{x_2 - x_3}{\sqrt{\sigma_2^2 + \sigma_3^2 + (\overline{x}\sigma_\eta(\sqrt{s}))^2}}, \tag{6.9}$$

where x_i and σ_i are the $d\sigma$ result and its error in the given kinematic bin from the i-track analysis, $\overline{x}$ is the average of the two results from the given kinematic, and $\sigma_\eta(\sqrt{s})$ is the $\sqrt{s}$-dependent (relative) acceptance uncertainty calculated in §4.3. The Δ distribution for all results is given in Figure 6.11. Fitting a gaussian to the Δ distribution for all bins which have a result from both topologies shows it to be normally distributed with mean -0.212 and width of 0.982. The -0.212 offset mean indicates that the three-track results are larger than the two-track results, though by only 0.212 standard deviations. The roughly unit width shows that the statistical and acceptance errors account for the variation of the two results.

The consistency of the two results allows us to create an average measurement of the two weighted according to their statistical errors. For each $(\sqrt{s}, \cos\theta^K_{CM})$ bin in which both a two- and three-track measurement has been made, we calculate the weighted mean value of the cross section and error as

$$\overline{x}(\sqrt{s}, \cos\theta^K_{CM}) = \frac{\sum_i x_i/\sigma_i^2}{\sum_j 1/\sigma_j^2} \tag{6.10a}$$

$$\overline{\sigma}^2(\sqrt{s}, \cos\theta^K_{CM}) = \left(\sum_i 1/\sigma_i^2\right)^{-2} \left(\frac{1}{\sigma_2^2} + \frac{1}{\sigma_3^2} + \frac{2\rho}{\sigma_2\sigma_3}\right), \tag{6.10b}$$

where x_i $(i = 2, 3)$ is the result from the i-track analysis with statistical error σ_i. In the error calculation, ρ is the correlation factor of the two results. Because our two-track dataset represents ≈28% of the full *g11a* dataset, we assume that it contains 28% of the events in the three-track dataset and consequently set $\rho = 0.28$. Note that though 28% of the three-track events are also present in the two-track dataset, these events comprise only ≈ 16.8% of the two-track dataset. Thus, our estimate of $\rho = 0.28$ is a comfortable overestimate of the measurements' correlation. For $(\sqrt{s}, \cos\theta^K_{CM})$ bins in which only one measurement has been made, we simply use that result as the average value. We account for the offset in the two results (shown in Figure 6.11) by scaling errors for these points by 1.212. Figures 6.21-6.23 show the weighted average differential cross sections as a function of $\sqrt{s}$ in each of nineteen 0.10-unit-wide $\cos\theta^K_{CM}$ bins.

6.3 Λ Recoil Polarization

The weak $\Lambda \to p\pi^-$ decay is a well-understood phenomenon. Because of this, we are able to use the explicit form of the $\Lambda \to p\pi^-$ amplitude in our amplitude generation (see §5.6.2). Interference between the Λ s- and p-wave decay transitions causes an asymmetry in the proton momentum distribution in the Λ rest frame [82]. This asymmetry allows access to the spin polarization of the Λ via observation of the final state proton distribution. From the *g11a* dataset, we measure the quantity P_Λ, the polarization of the Λ in the direction normal to the production plane.

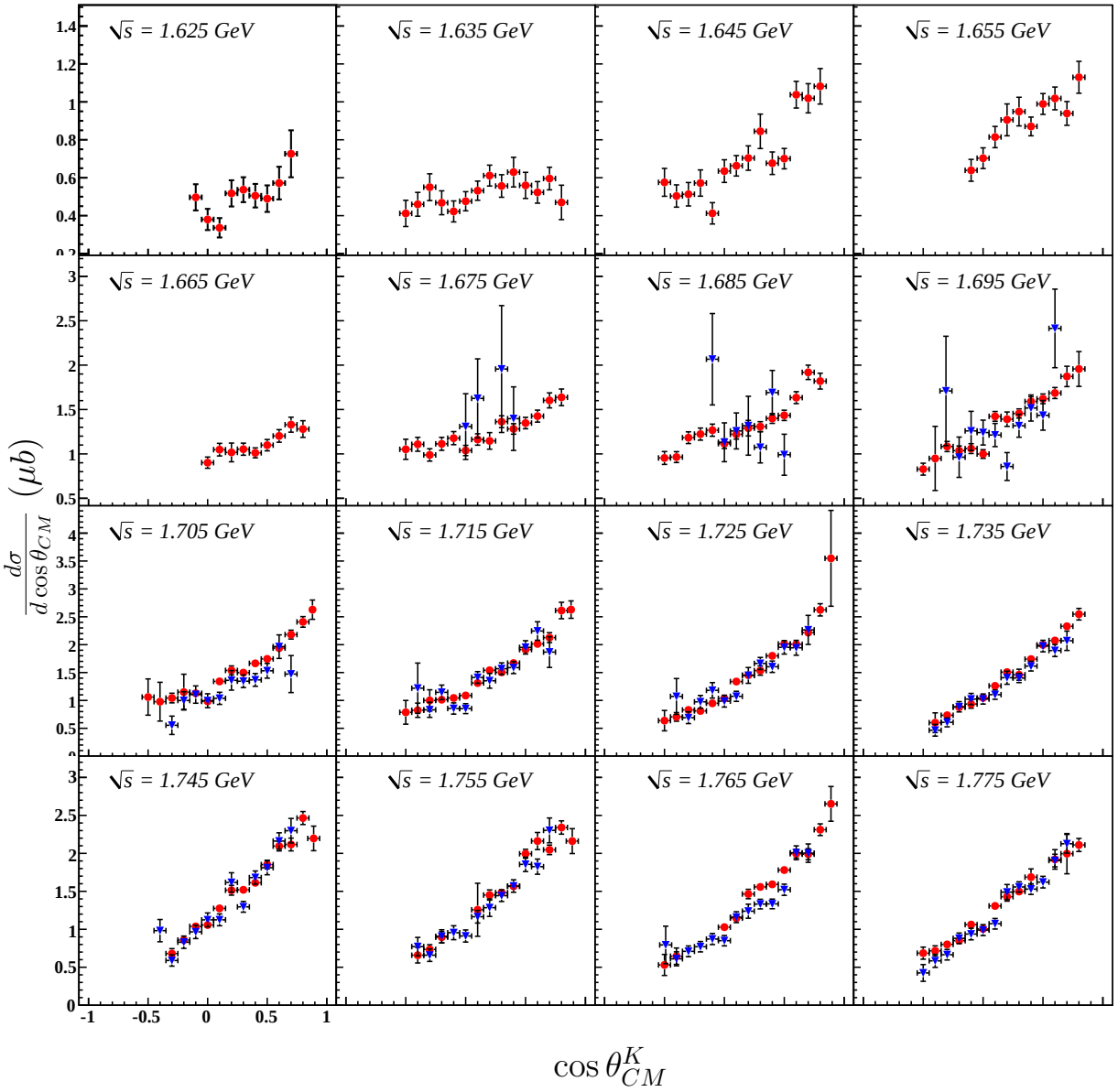

Figure 6.3: $d\sigma/d\cos\theta^K_{CM}$ (μb) v. $\cos\theta^K_{CM}$: Differential cross section results for the energy range 1.62 GeV $\leq \sqrt{s} <$ 1.78 GeV. Results from the three-track analysis are shown in blue (triangles), those of the two-track analysis in red (circles). All plots have the same $\cos\theta^K_{CM}$-axis range and vertical axis ranges are the same for the four plots in each row.

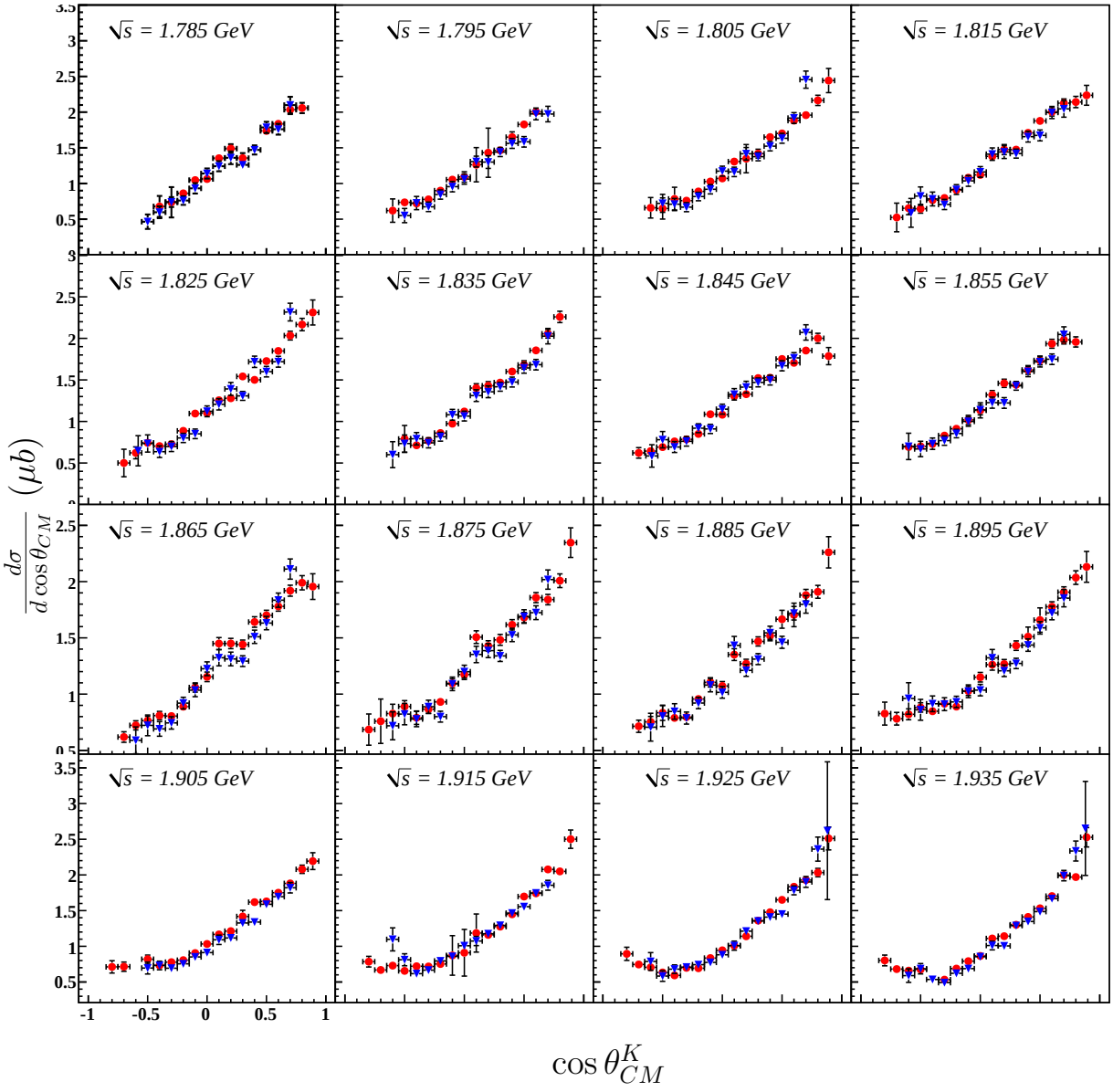

Figure 6.4: $d\sigma/d\cos\theta^K_{CM}$ (μb) v. $\cos\theta^K_{CM}$: Differential cross section results for the energy range 1.78 GeV $\leq \sqrt{s} <$ 1.94 GeV. Results from the three-track analysis are shown in blue (triangles), those of the two-track analysis in red (circles). All plots have the same $\cos\theta^K_{CM}$-axis range and vertical axis ranges are the same for the four plots in each row.

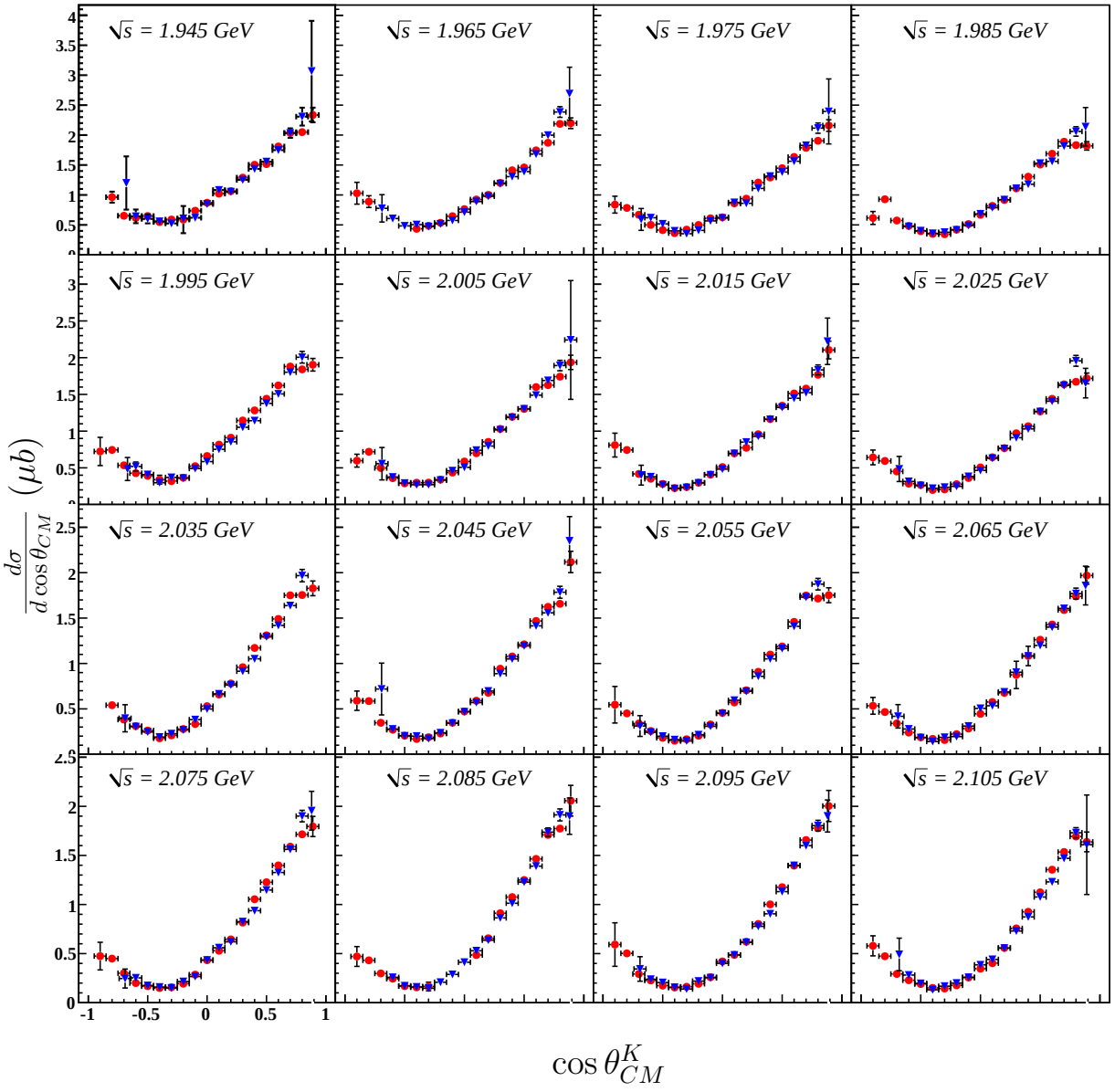

Figure 6.5: $d\sigma/d\cos\theta^K_{CM}$ (μb) v. $\cos\theta^K_{CM}$: Differential cross section results for the energy range 1.94 GeV $\leq \sqrt{s} <$ 2.11 GeV. Results from the three-track analysis are shown in blue (triangles), those of the two-track analysis in red (circles). All plots have the same $\cos\theta^K_{CM}$-axis range and vertical axis ranges are the same for the four plots in each row.

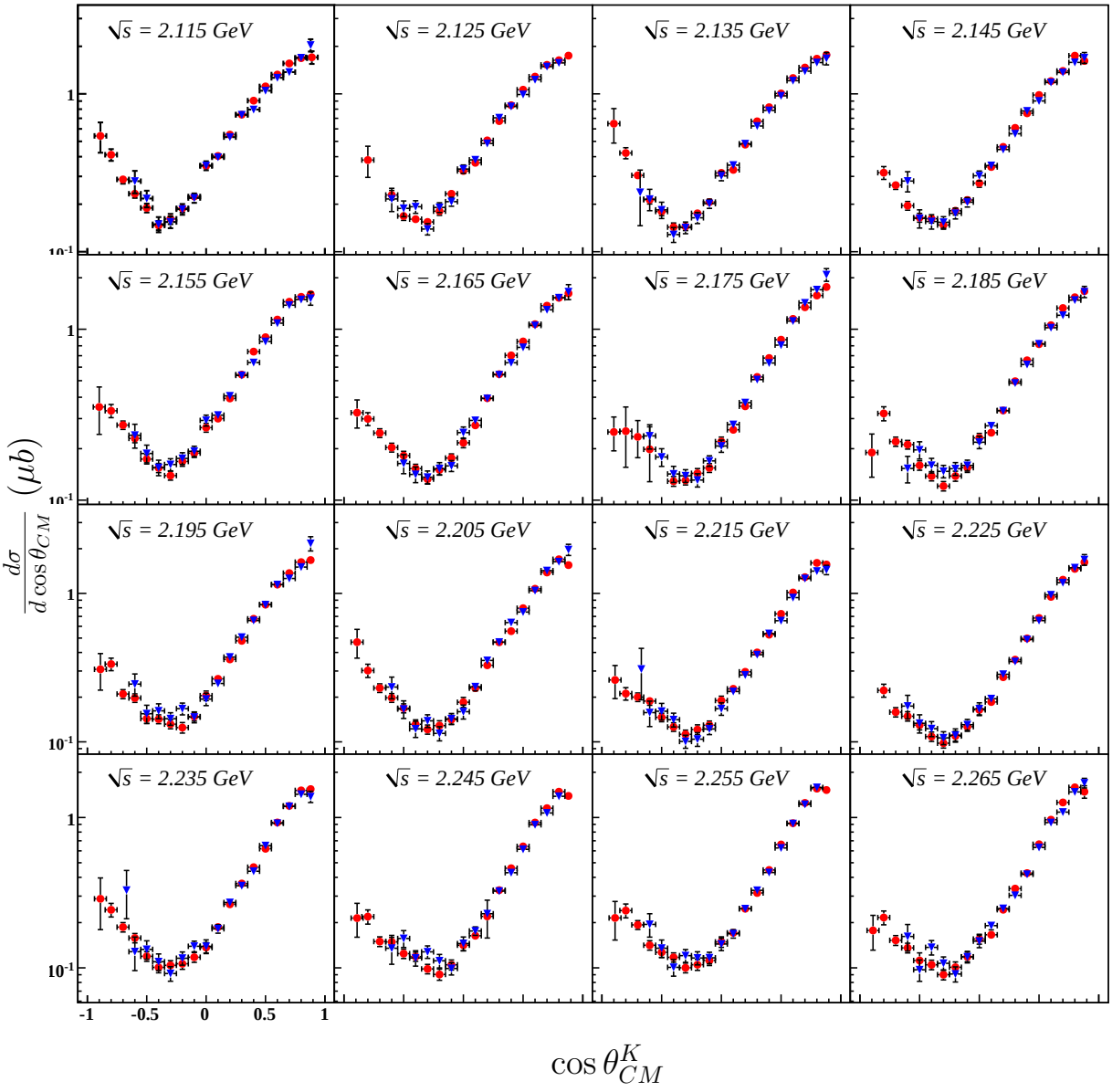

Figure 6.6: $d\sigma/d\cos\theta^K_{CM}$ (μb) v. $\cos\theta^K_{CM}$: Differential cross section results for the energy range 2.11 GeV $\leq \sqrt{s} <$ 2.27 GeV. Results from the three-track analysis are shown in blue (triangles), those of the two-track analysis in red (circles). All plots have the same $\cos\theta^K_{CM}$-axis range and vertical axis ranges are the same for the four plots in each row. Vertical axes are logarithmic scale.

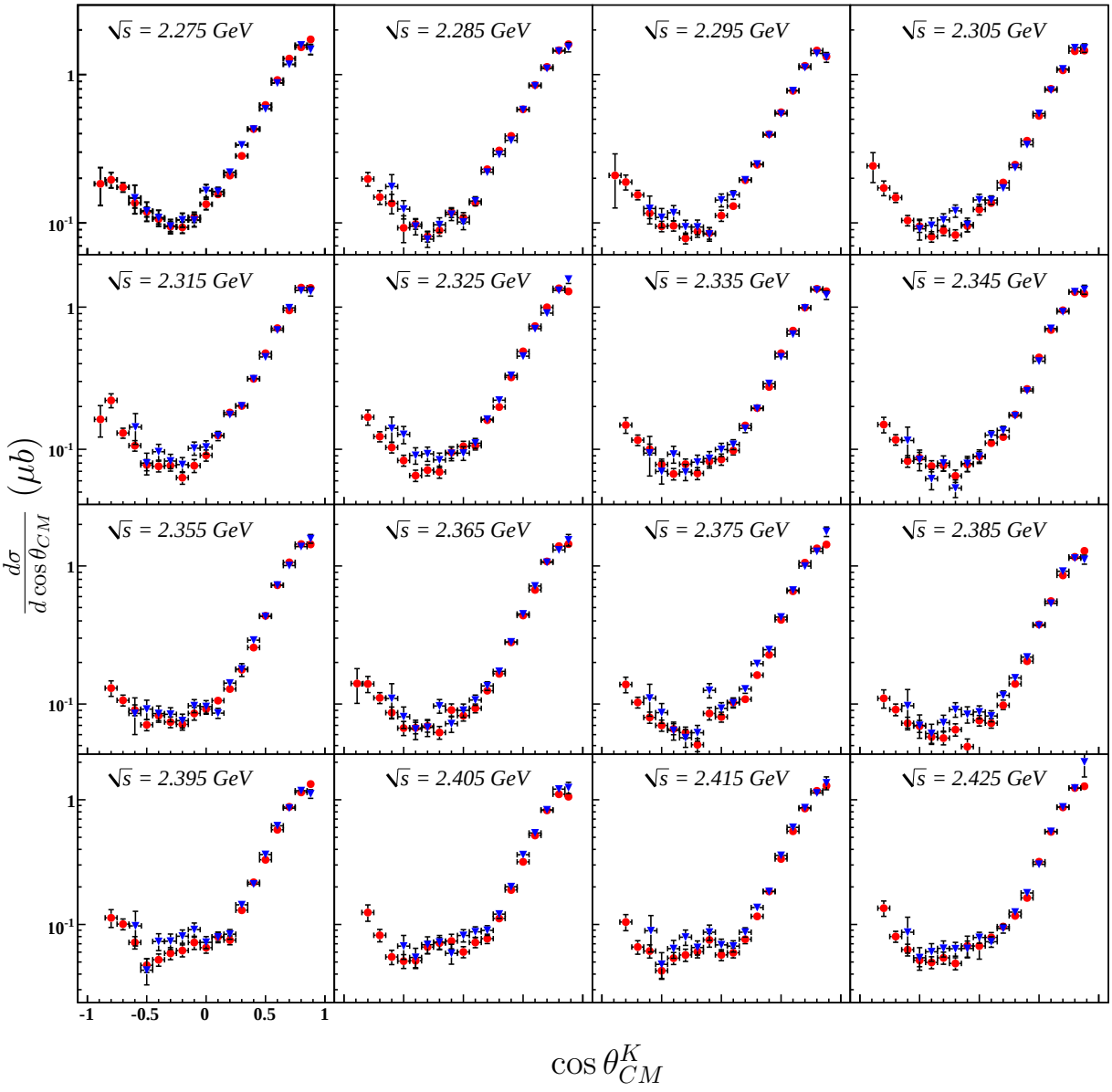

Figure 6.7: $d\sigma/d\cos\theta^K_{CM}$ (μb) v. $\cos\theta^K_{CM}$: Differential cross section results for the energy range 2.27 GeV $\leq \sqrt{s} <$ 2.43 GeV. Results from the three-track analysis are shown in blue (triangles), those of the two-track analysis in red (circles). All plots have the same $\cos\theta^K_{CM}$-axis range and vertical axis ranges are the same for the four plots in each row. Vertical axes are logarithmic scale.

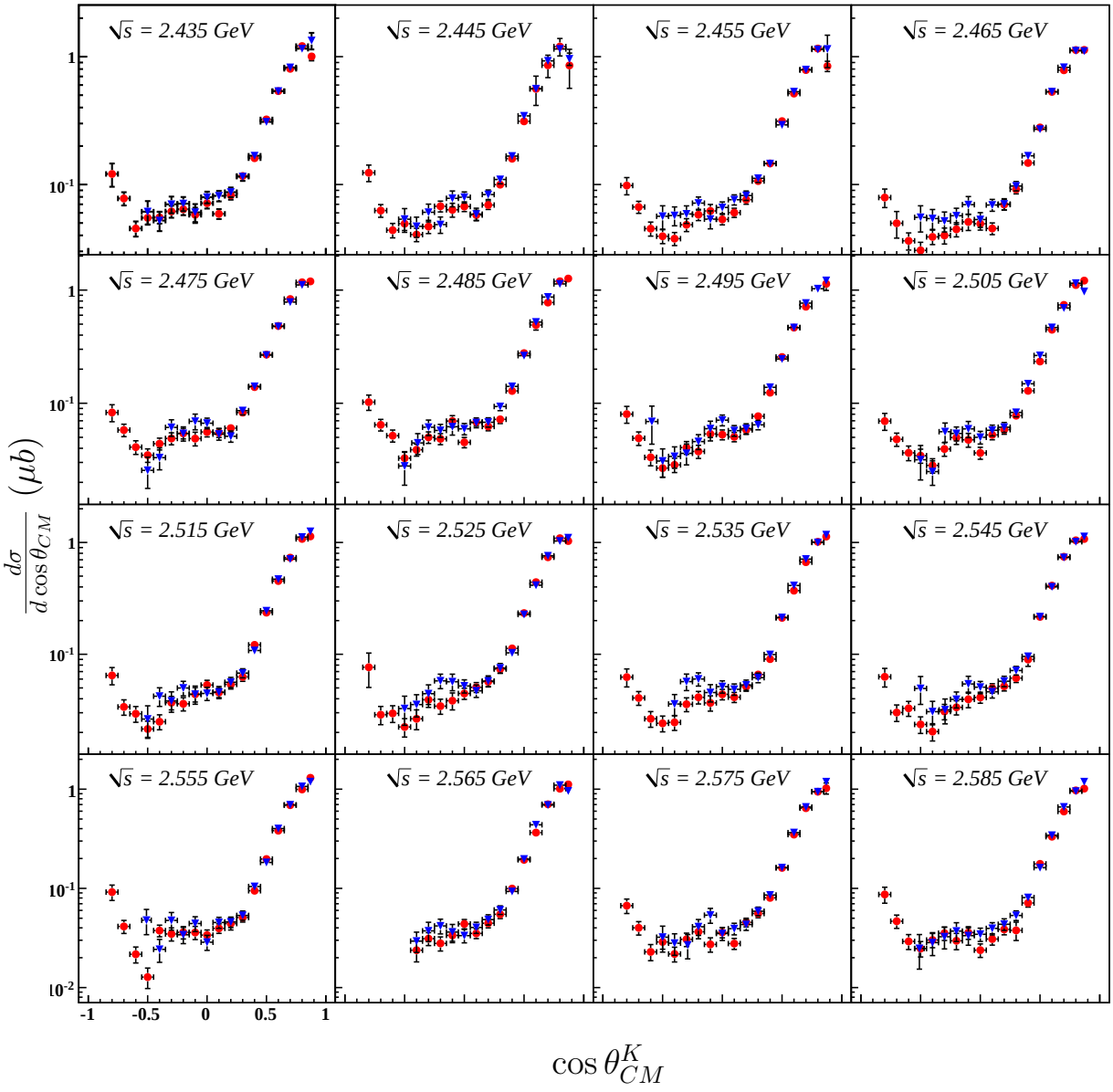

Figure 6.8: $d\sigma/d\cos\theta^K_{CM}$ (μb) v. $\cos\theta^K_{CM}$: Differential cross section results for the energy range 2.43 GeV $\leq \sqrt{s} <$ 2.59 GeV. Results from the three-track analysis are shown in blue (triangles), those of the two-track analysis in red (circles). All plots have the same $\cos\theta^K_{CM}$-axis range and vertical axis ranges are the same for the four plots in each row. Vertical axes are logarithmic scale.

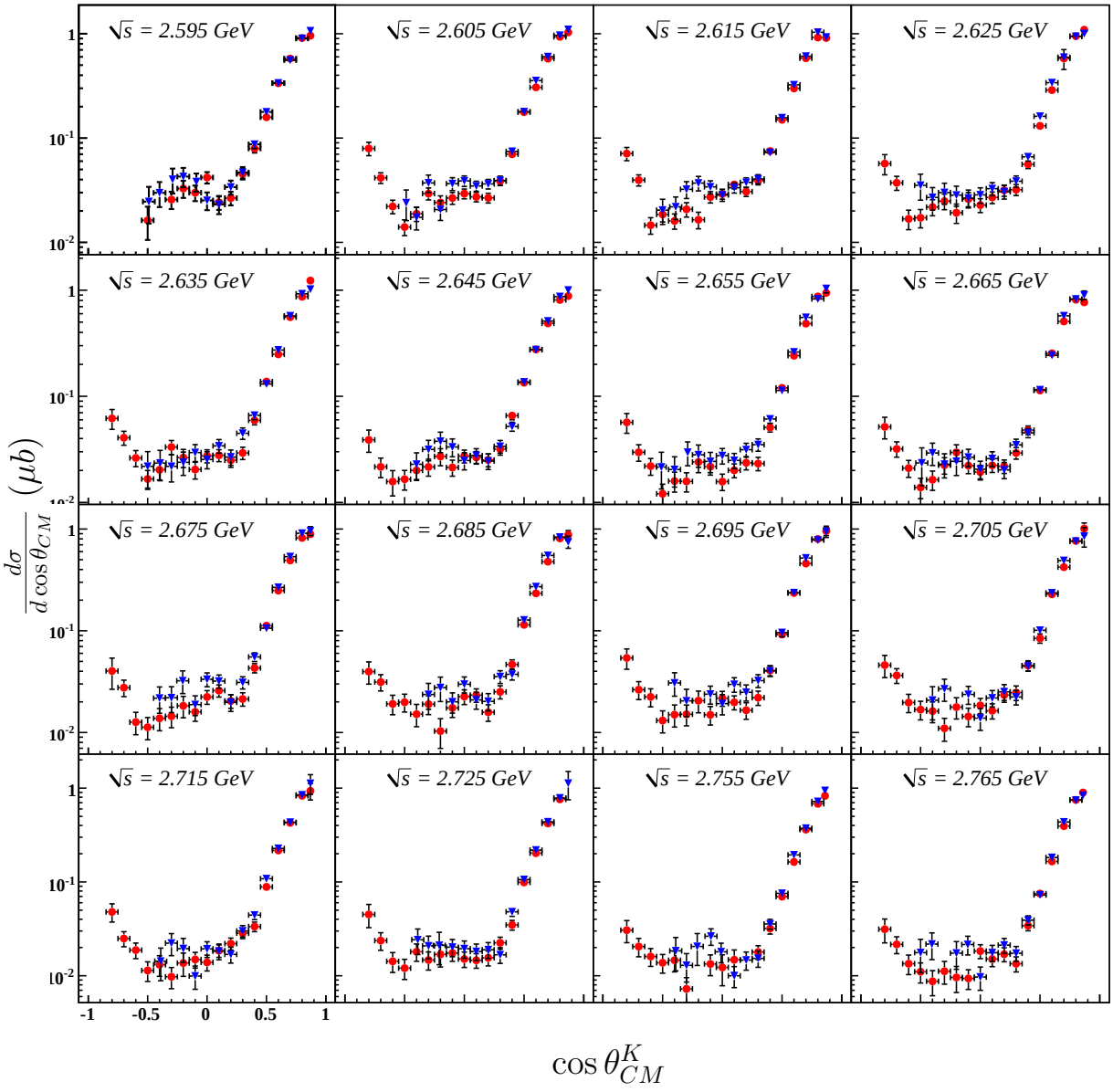

Figure 6.9: $d\sigma/d\cos\theta^K_{CM}$ (μb) v. $\cos\theta^K_{CM}$: Differential cross section results for the energy range 2.59 GeV $\leq \sqrt{s} <$ 2.77 GeV. Results from the three-track analysis are shown in blue (triangles), those of the two-track analysis in red (circles). All plots have the same $\cos\theta^K_{CM}$-axis range and vertical axis ranges are the same for the four plots in each row. Vertical axes are logarithmic scale.

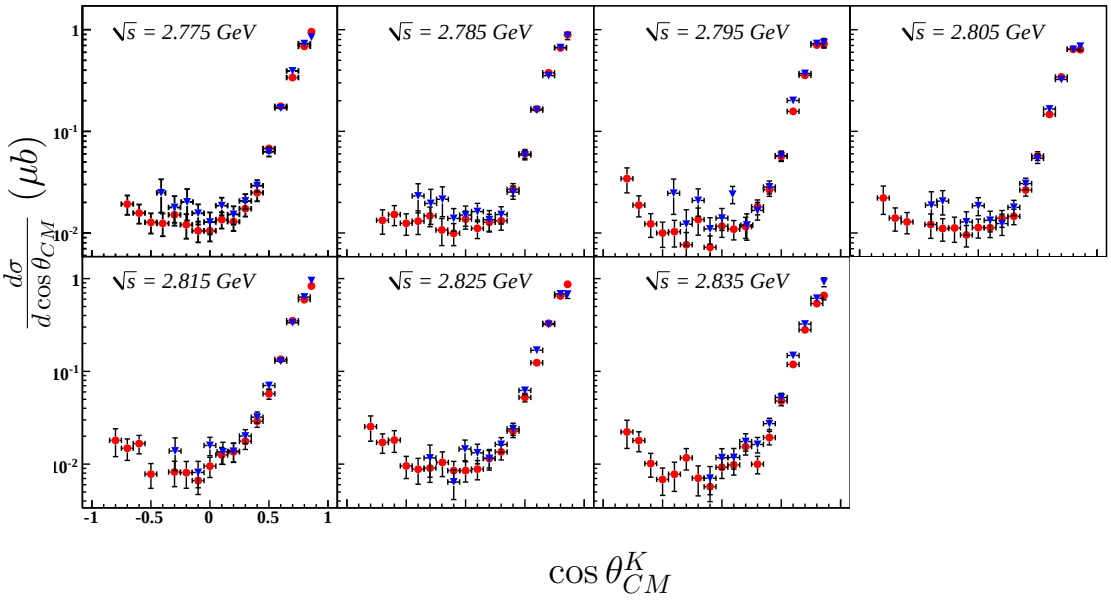

Figure 6.10: $d\sigma/d\cos\theta^K_{CM}$ (μb) v. $\cos\theta^K_{CM}$: Differential cross section results for the energy range 2.77 GeV $\leq \sqrt{s} <$ 2.84 GeV. Results from the three-track analysis are shown in blue (triangles), those of the two-track analysis in red (circles). All plots have the same $\cos\theta^K_{CM}$-axis range and vertical axis ranges are the same for the four plots in each row. Vertical axes are logarithmic scale.

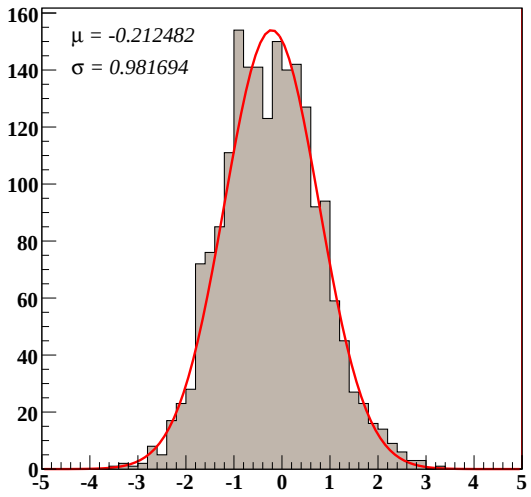

Figure 6.11: Histogram of the weighted difference between two- and three-track $d\sigma/d\cos\theta^K_{CM}$ results. This quantity is described in the text.

6.3.1 Calculation

Because we have chosen the z-axis as our direction of angular momentum quantization, we are able to easily calculate the recoil polarization, P_Λ generated by a given set of amplitudes and fit parameters. Recall that the mother fit provides an expansion of the data in all physically relevant distributions, including distributions of the final state proton. Each s-channel amplitude used in the Mother Fit produces a specific Λ polarization for a given kinematic region. Fitting with a complete basis of s-channel amplitudes which explicitly include the Λ decay gives access to the Λ polarization.

From the resulting Mother Fit parameters, we project the observed recoil polarization at all values of $(\sqrt{s}, \cos\theta^K_{CM})$ where we have made differential cross section measurements (*i.e.* kinematic regions where we have data). We generate s-channel $\gamma p \to K^+\Lambda$ amplitudes with $\frac{1}{2}^\pm \leq J^P \leq \frac{11}{2}^\pm$ for each of these kinematics, keeping the Λ-polarization dependence. We write the total amplitudes describing the process (including fit parameters from the Mother Fit) as $A^{m_\gamma, m_i, M}_{\gamma p \to K^+\Lambda}$, where M denotes the spin of the Λ along the z-axis. For calculation, we construct a two-component wave-function for the process as

$$\psi_M(\sqrt{s}, \cos\theta^K_{CM}) = \begin{pmatrix} A^{m_\gamma, m_i, M=+}(\sqrt{s}, \cos\theta^K_{CM}) \\ A^{m_\gamma, m_i, M=-}(\sqrt{s}, \cos\theta^K_{CM}) \end{pmatrix}, \tag{6.11}$$

where $M = \pm$ indicates Λ spin aligned or anti-aligned with $\hat{z}$. Because we have written our amplitudes in the S_z-basis, we can use the Pauli spin matrices to project out P_Λ which is the polarization along $\hat{y}$:

$$\begin{aligned} P_\Lambda &= \frac{1}{N} \sum_{m_\gamma, m_i} \psi^\dagger \sigma_y \psi \\ &= \frac{i}{N} \sum_{m_\gamma, m_i} \left(A^{m_\gamma, m_i, +} A^{* m_\gamma, m_i, -} - A^{m_\gamma, m_i, -} A^{* m_\gamma, m_i, +} \right), \end{aligned} \tag{6.12}$$

where

$$N = \sum_{m_\gamma, m_i} \sum_M |A^{m_\gamma, m_i, M}(\sqrt{s}, \cos\theta^K_{CM})|^2 \tag{6.13}$$

is a normalization factor.

6.3.2 Error Estimation

Though this extraction method is very powerful and quick in the presence of the Mother Fit, it lends no *a priori* method of assigning statistical errors to the P_Λ values. To estimate statistical errors, we consider the differences in P_Λ for adjacent $\sqrt{s}$ values and fixed $\cos\theta^K_{CM}$. We begin by assigning to each $P_\Lambda(\sqrt{s}, \cos\theta^K_{CM})$ point the "statistical" error [4]

$$\sigma_s^2(\sqrt{s}, \cos\theta^K_{CM}) = \frac{1}{2} \sum_{i=-1}^{1} \left(P_\Lambda(\sqrt{s} + i \cdot 10\text{MeV}, \cos\theta^K_{CM}) - \overline{P}_\Lambda(\sqrt{s}, \cos\theta^K_{CM}) \right)^2, \tag{6.14}$$

where $\overline{P}_\Lambda$ is the mean of the three points considered. To establish consistency between error bars in a given $\sqrt{s}$-bin, we then applied a smoothing procedure; we assign the statistical error for a given P_Λ point to be the average of the statistical errors of it and its neighboring points in $\cos\theta^K_{CM}$.

To estimate the systematic error on P_Λ measurements, we need to consider the effect of our measured acceptance uncertainty. We begin by considering a theoretical $\cos\theta^p_{\lambda HF}$ distribution shown in Figure 6.12(a) (note that the distribution is normalized). Recall that this distribution is related to P_Λ with form $1 + P_\Lambda \alpha_- \cos\theta^p_{\Lambda HF}$. Thus, P_Λ is extracted by fitting a linear function to this distribution. To investigate σ_η's effect on the extraction of this slope, we have used the toy model described below and several values of σ_η. Here, we provide as an example the case where $\sigma_\eta = 2.5\%$.

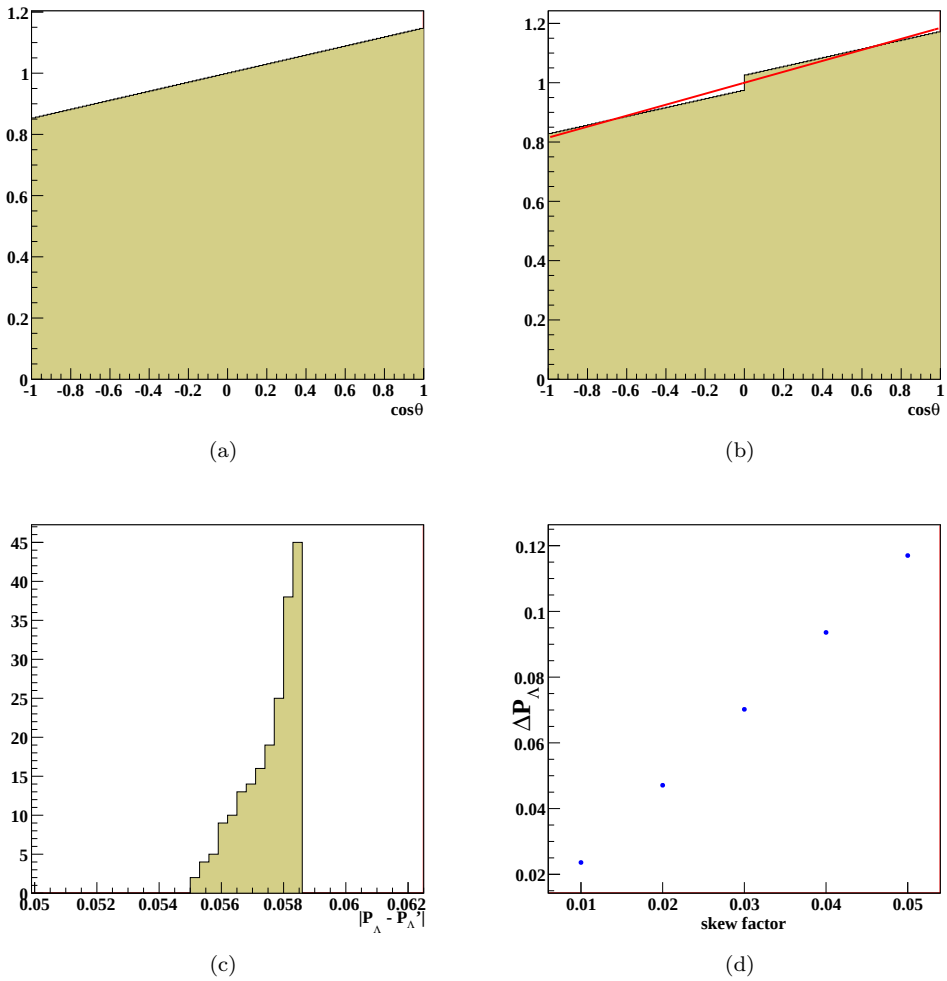

Figure 6.12: Plots showing steps in our estimation of acceptance uncertainty effect on P_Λ. Figure (a) shows an ideal $\cos\theta$ distribution with slope $P_\Lambda = 0.4$. Figure (b) shows the same distribution distorted by an uncertainty of 2.5%. Figure (c) shows the $|P_\Lambda - P'_\Lambda|$ distribution as described in the text. Figure (d) shows the maximum difference in recoil polarizations, ΔP_Λ, v. distribution skew factor (see text).

To simulate the effect of a 2.5% acceptance uncertainty, we skew the $\cos\theta^{p}_{\Lambda HF}$ distribution by a factor of 1.025 for values of $\cos\theta > 0.0$ and by 0.975 for $\cos\theta \leq 0.0$. We then fit this skewed histogram to obtain a new slope and recoil polarization, which we call P'_{Λ}. We repeat this process for all values of the initial slope between 0.0 and 1.0 at 0.01 intervals. Plotting the $|P_{\Lambda} - P'_{\Lambda}|$ distributions shows that for all values of P_{Λ}, our acceptance uncertainty causes a difference uncertainty less than 0.0585.

We repeat this process for the values of σ_{η} indicated in Figure 6.12(d). The manner in which we skew the $\cos\theta^{p}_{\Lambda HF}$ for a given σ_{η} represents a wort case scenario; the effect of our acceptance uncertainty is most likely much less drastic. As such, the effect $\Delta P_{\Lambda} \approx 11.7$ given by the 5% acceptance uncertainty is a gross over-estimate. We use as the systematic uncertainty associated with our P_{Λ} measurements half of this value, $\Delta P_{\Lambda} = 0.0585$.

6.3.3 Results

Figures 6.13-6.20 show the P_{Λ} results from our two- and three-track analyses of *g11a* in 10-MeV-wide $\sqrt{s}$ bins versus $\cos\theta^{K}_{CM}$. Note that though normalization issues prevented us from making a differential cross section measurement in the $\sqrt{s} = 1.955$ GeV, 2.735 GeV, and 2.745 GeV bins, we are able to measure P_{Λ} in these bins as the quantity is independent of normalization. Our extraction method permits us to project a recoil polarization measurement at every $(\sqrt{s}, \cos\theta^{K}_{CM})$ value for which we have a $d\sigma$ point. However, sparsely populated $(\sqrt{s}, \cos\theta^{K}_{CM})$ bins present inconsistent results as the Mother Fit does not have enough information. We present results at kinematics for which extraction yielded consistent results in comparison with neighboring bins. Only statistical errors are displayed on the points. In all, we present P_{Λ} measurements at 1708 kinematic points.

Interesting structures in P_{Λ} over the range 1.7 GeV $\leq \sqrt{s} \leq$ 2.6 GeV suggest the presence of interfering s-channel resonances. Further comment on these is left to our partial wave analysis (Chapter 8). Here, we only note that as the forward peak in the differential cross section becomes more dominant (with increasing $\sqrt{s}$, we see that the recoil polarization in the forward direction tends to -1, indicating a large amount of polarization out of the scattering plane.

As with the $d\sigma/d\cos\theta$ measurements, agreement between the two results is very good. We thus calculate an average value of the recoil polarization in the manner given by eq. (6.10). We display the averaged values of all of our measurements versus $\sqrt{s}$ in bins of $\cos\theta^{K}_{CM}$ in Figures 6.21-6.23.

6.4 Comparison to Previous Measurements

Though *g11a* represents the most precise dataset for study of the $\gamma p \to K^{+}\Lambda$ reaction to date, comparison to earlier results is a necessary step in the validation of our results. Several experiments have produced differential cross sections in the energy range 1.62 GeV $\leq \sqrt{s} <$ 2.5 GeV. At the time of this analysis, two of the more recent measurements, those of Glander (SAPHIR, 2004) and Bradford (CLAS, 2005) showed a large amount of discrepancy. In this section, we provide comparisons to both of these results and show that agreement with the previous CLAS result is very good. We also provide differential cross section comparisons to results at very backward and forward angles made by the LEPS Collaboration (Hicks, 2007 and Sumihama 2006, respectively). Recoil polarization measurements have also been made in the energy range 1.62 GeV $\leq \sqrt{s} <$ 2.35 GeV by the collaborations at CLAS, SAPHIR, and GRAAL. We demonstrate excellent agreement with these results while showing a great increase in range and precision.

6.4.1 Differential Cross Sections

CLAS 2005 and SAPHIR 2004

The CLAS Collaboration published differential cross sections for the $\gamma p \to K^{+}\Lambda$ reaction from analyses of the *g1c* dataset in April of 2004 (J. McNabb, *et al.* [22]) and March of 2006 (R. Bradford, *et al*

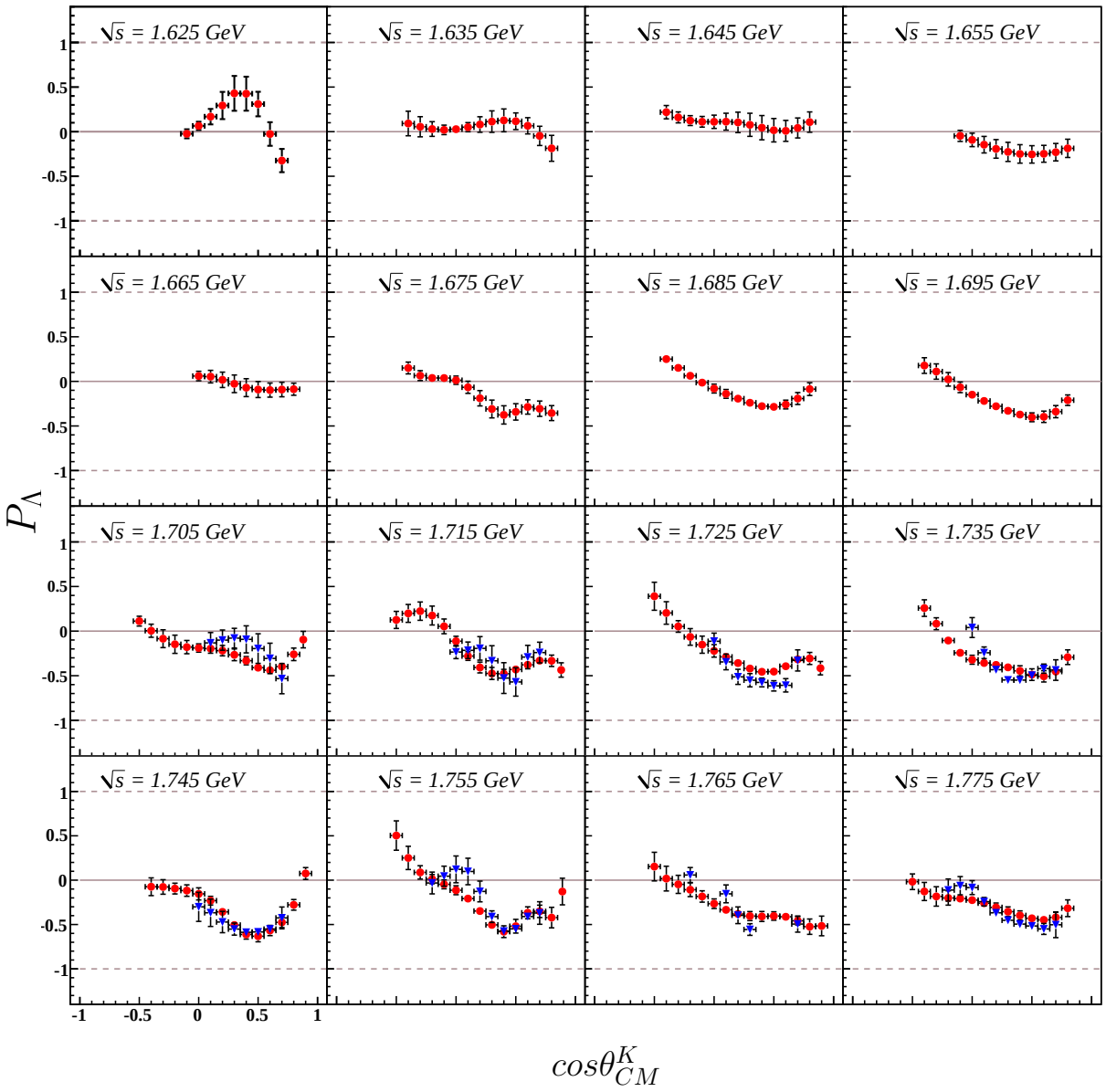

Figure 6.13: P_Λ v. $\cos\theta^K_{CM}$: Λ recoil polarization results v. $\cos\theta^{K^+}_{CM}$ for the energy range 1.62 GeV $\leq \sqrt{s} <$ 1.78 GeV. Results from the three-track analysis are shown in blue (triangles), those of the two-track analysis in red (circles).

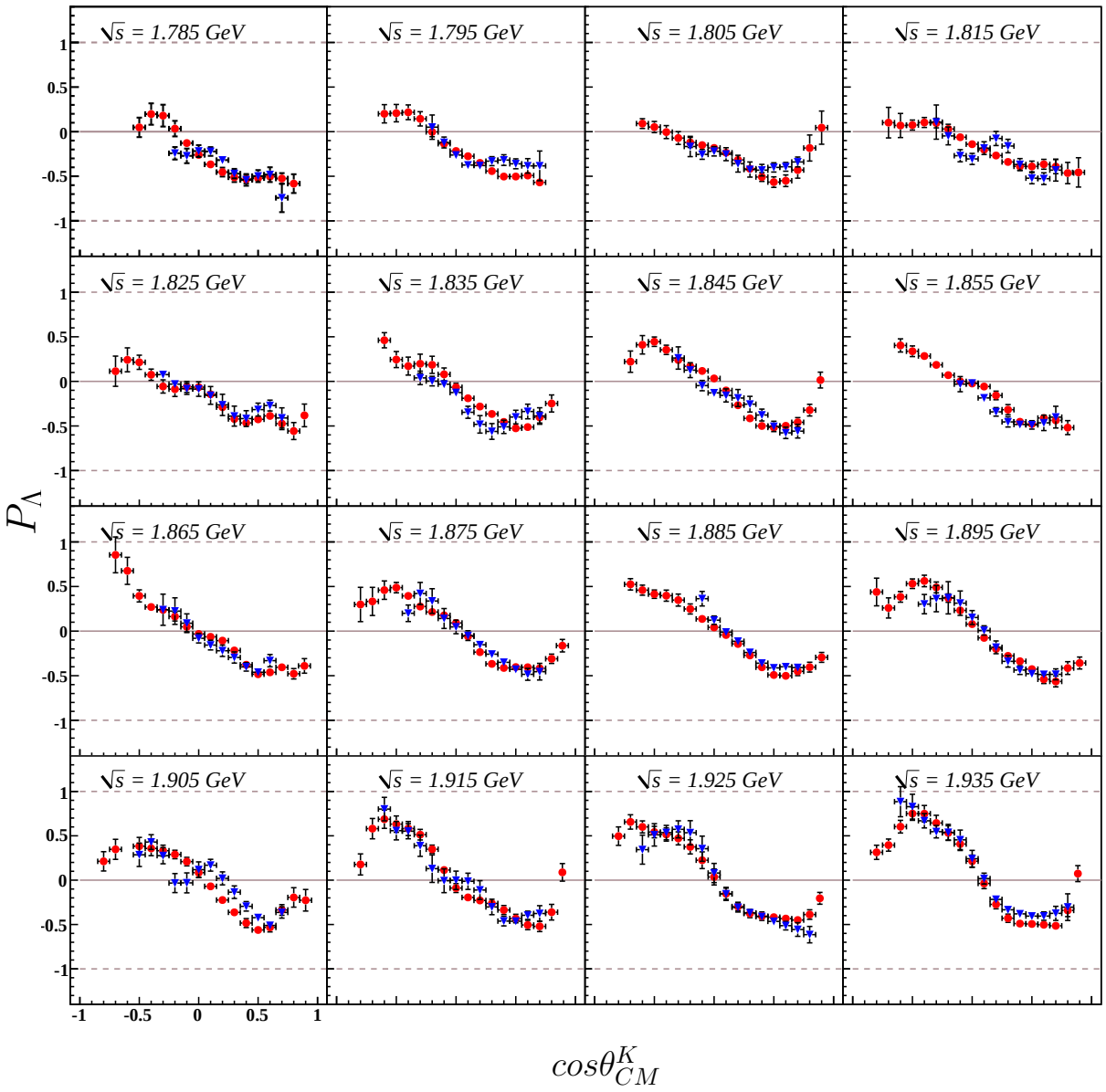

Figure 6.14: P_Λ v. $\cos\theta^K_{CM}$: Λ recoil polarization results v. $\cos\theta^{K^+}_{CM}$ for the energy range 1.78 GeV $\leq \sqrt{s} <$ 1.94 GeV. Results from the three-track analysis are shown in blue (triangles), those of the two-track analysis in red (circles). Errors displayed are statistical.

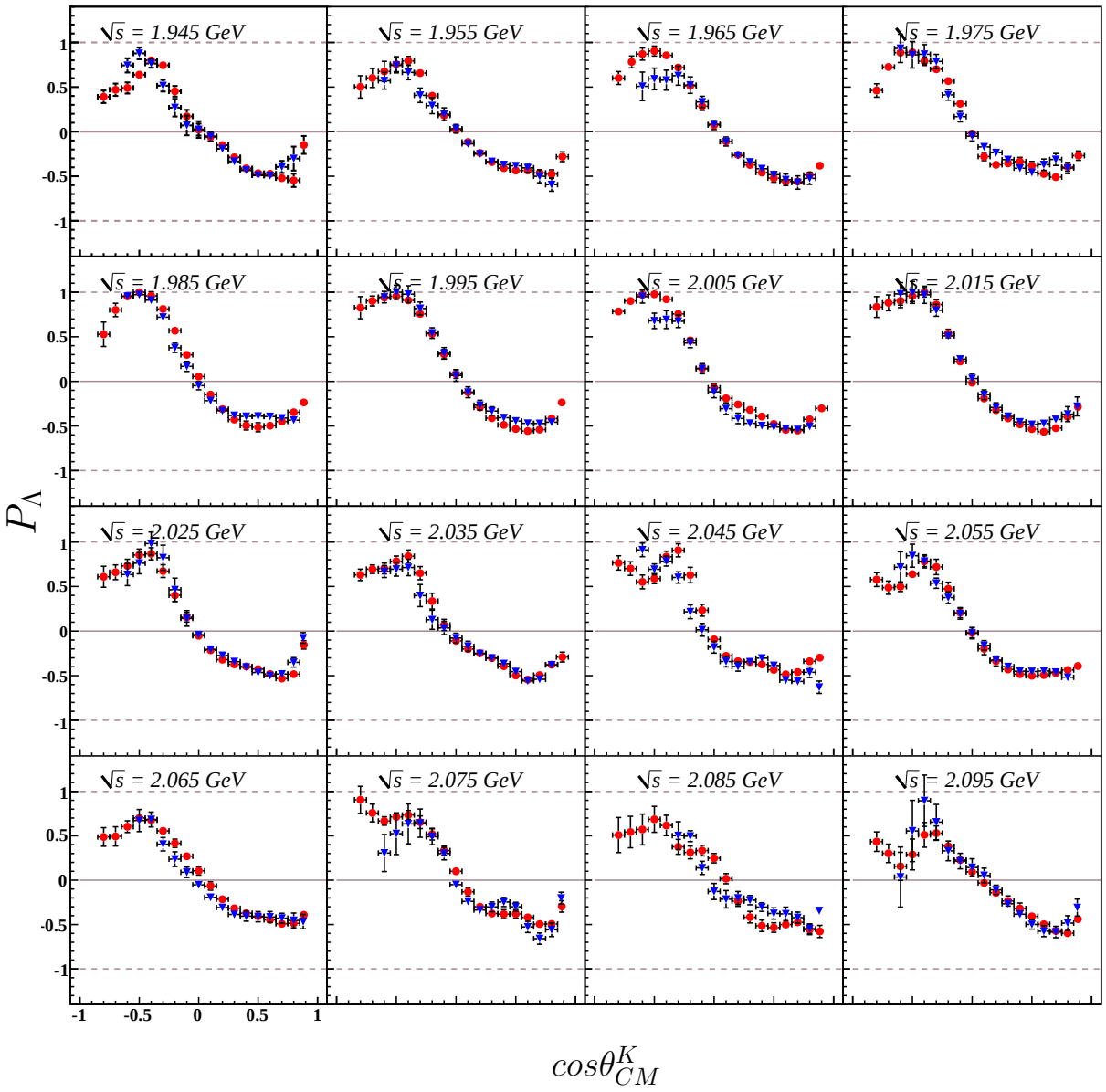

Figure 6.15: P_Λ v. $\cos\theta^K_{CM}$: Λ recoil polarization results v. $\cos\theta^{K^+}_{CM}$ for the energy range 1.94 GeV $\leq \sqrt{s} <$ 2.10 GeV. Results from the three-track analysis are shown in blue (triangles), those of the two-track analysis in red (circles). Errors displayed are statistical.

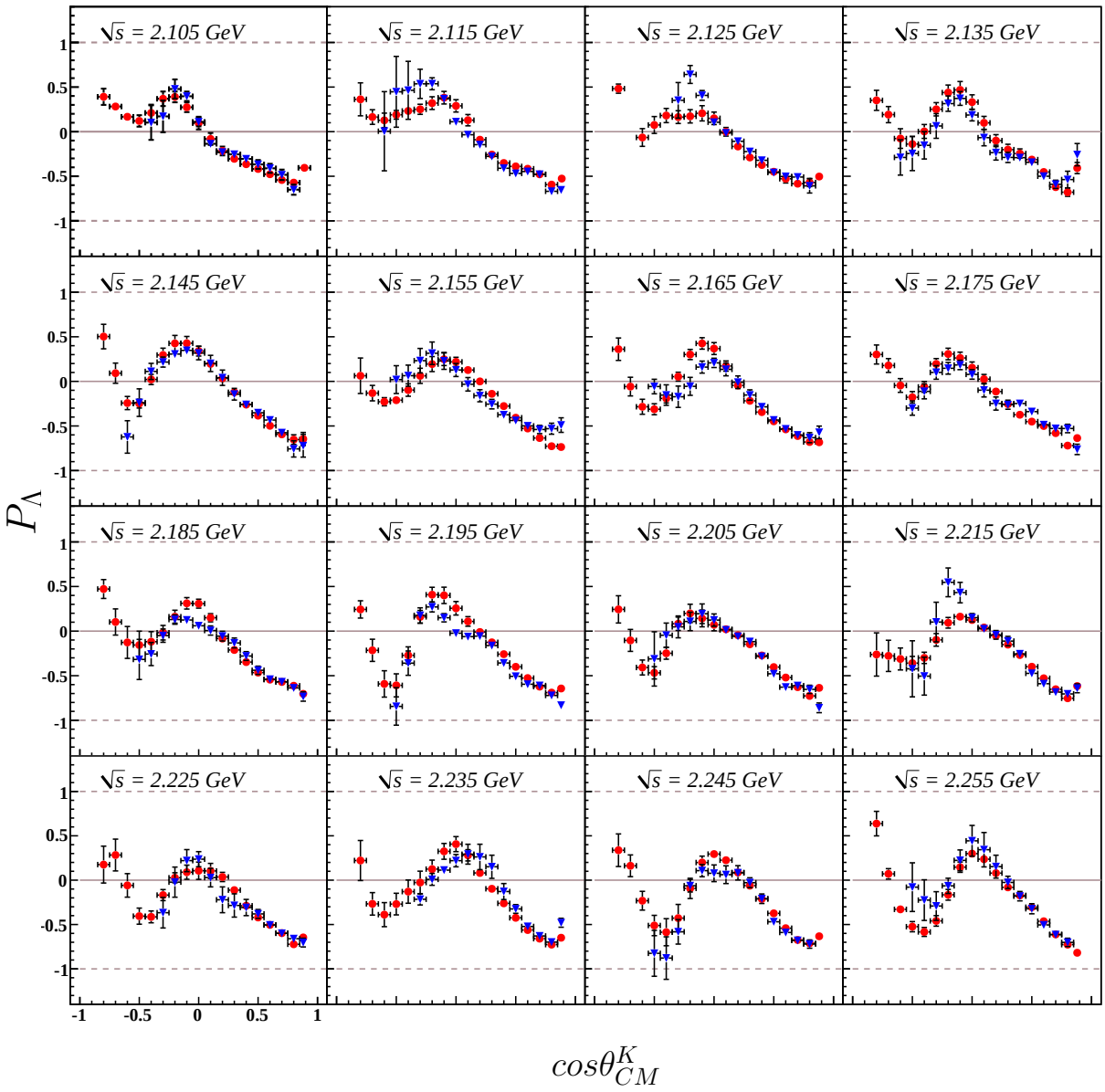

Figure 6.16: P_Λ v. $\cos\theta^K_{CM}$: Λ recoil polarization results v. $\cos\theta^{K^+}_{CM}$ for the energy range 2.10 GeV $\leq \sqrt{s} <$ 2.26 GeV. Results from the three-track analysis are shown in blue (triangles), those of the two-track analysis in red (circles). Errors displayed are statistical.

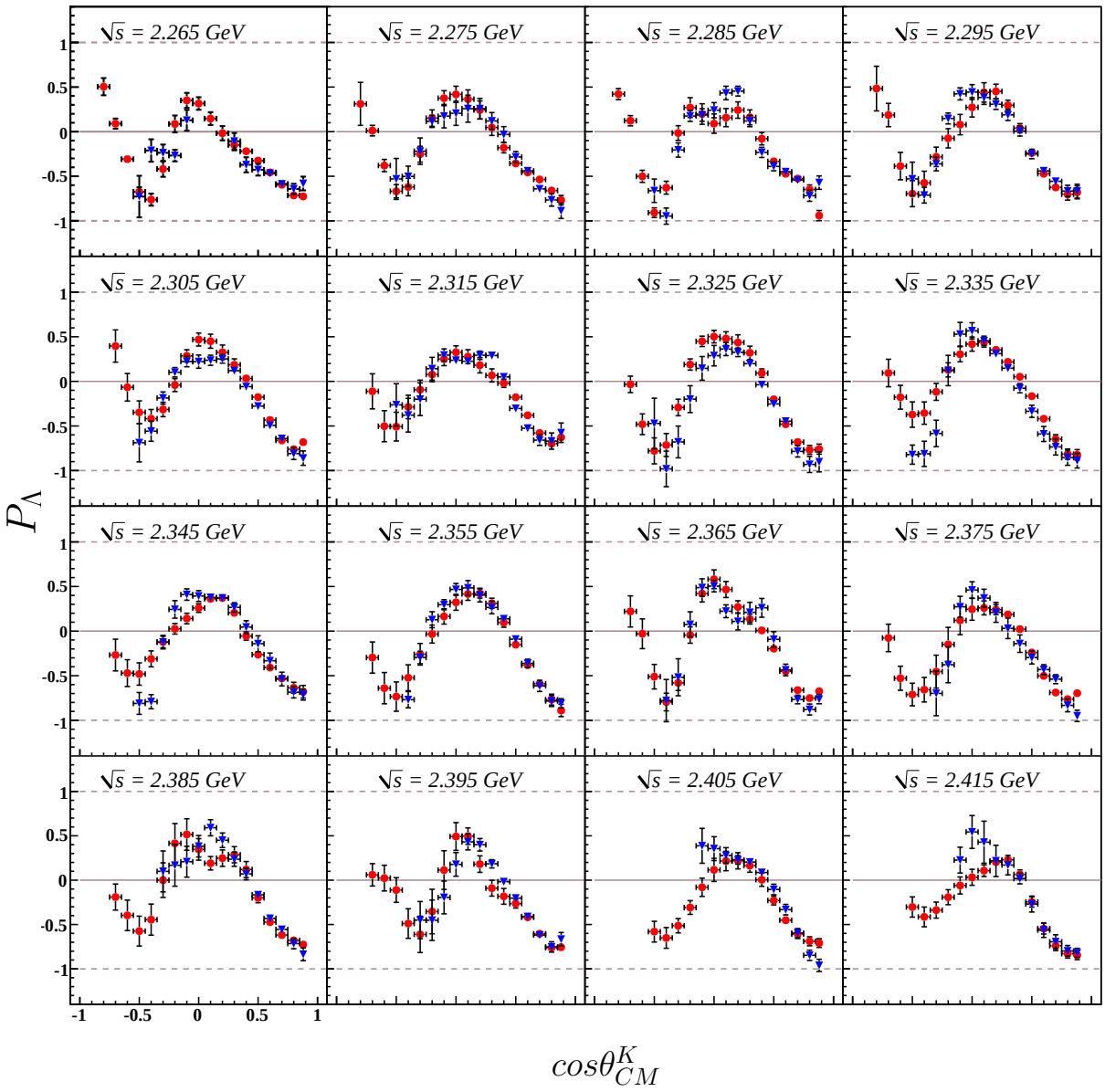

Figure 6.17: P_Λ v. $\cos\theta^K_{CM}$: Λ recoil polarization results v. $\cos\theta^{K^+}_{CM}$ for the energy range 2.26 GeV $\leq \sqrt{s} <$ 2.42 GeV. Results from the three-track analysis are shown in blue (triangles), those of the two-track analysis in red (circles). Errors displayed are statistical.

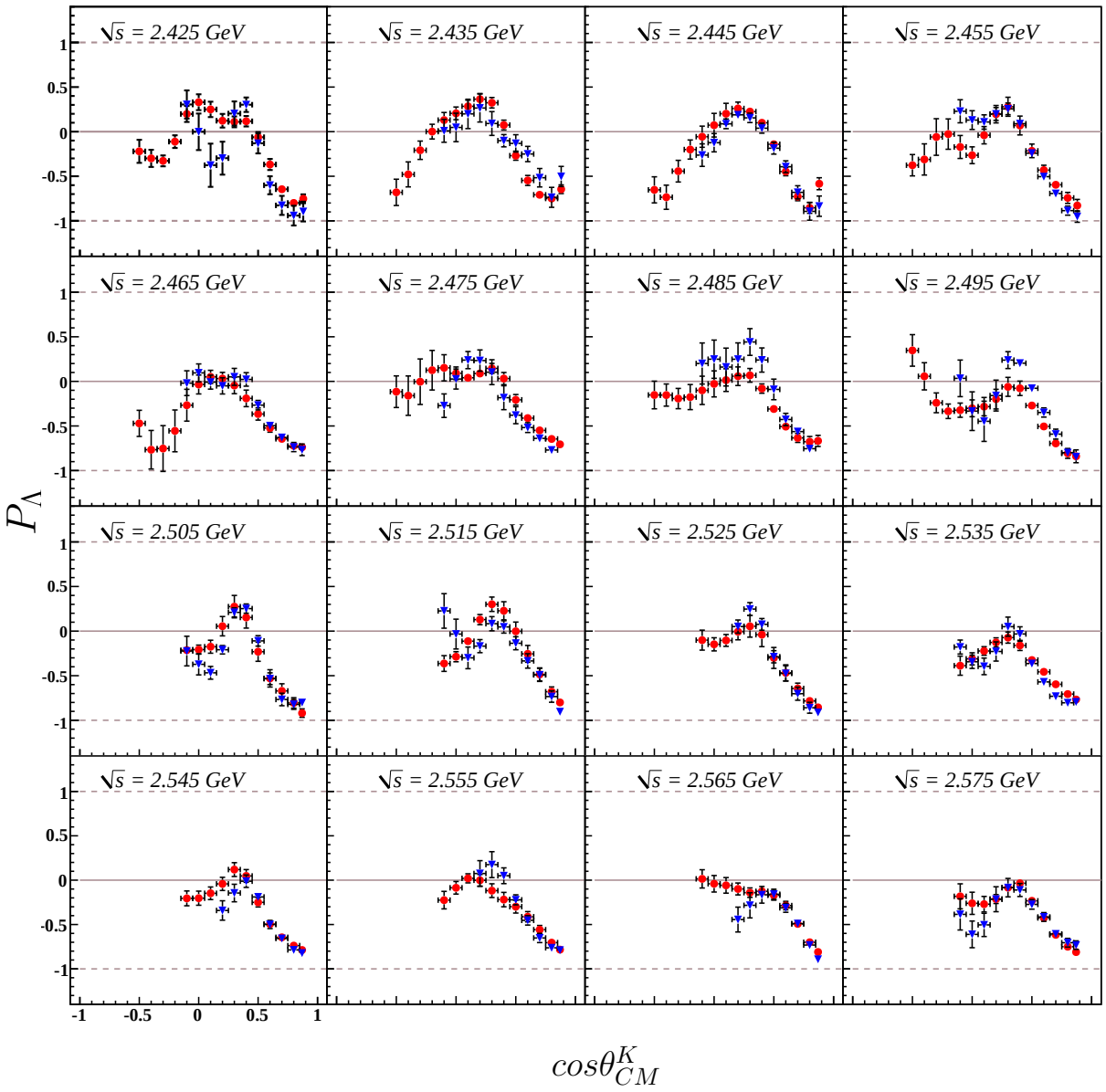

Figure 6.18: P_Λ v. $\cos\theta^K_{CM}$: Λ recoil polarization results v. $\cos\theta^{K^+}_{CM}$ for the energy range 2.42 GeV $\leq \sqrt{s} <$ 2.58 GeV. Results from the three-track analysis are shown in blue (triangles), those of the two-track analysis in red (circles). Errors displayed are statistical.

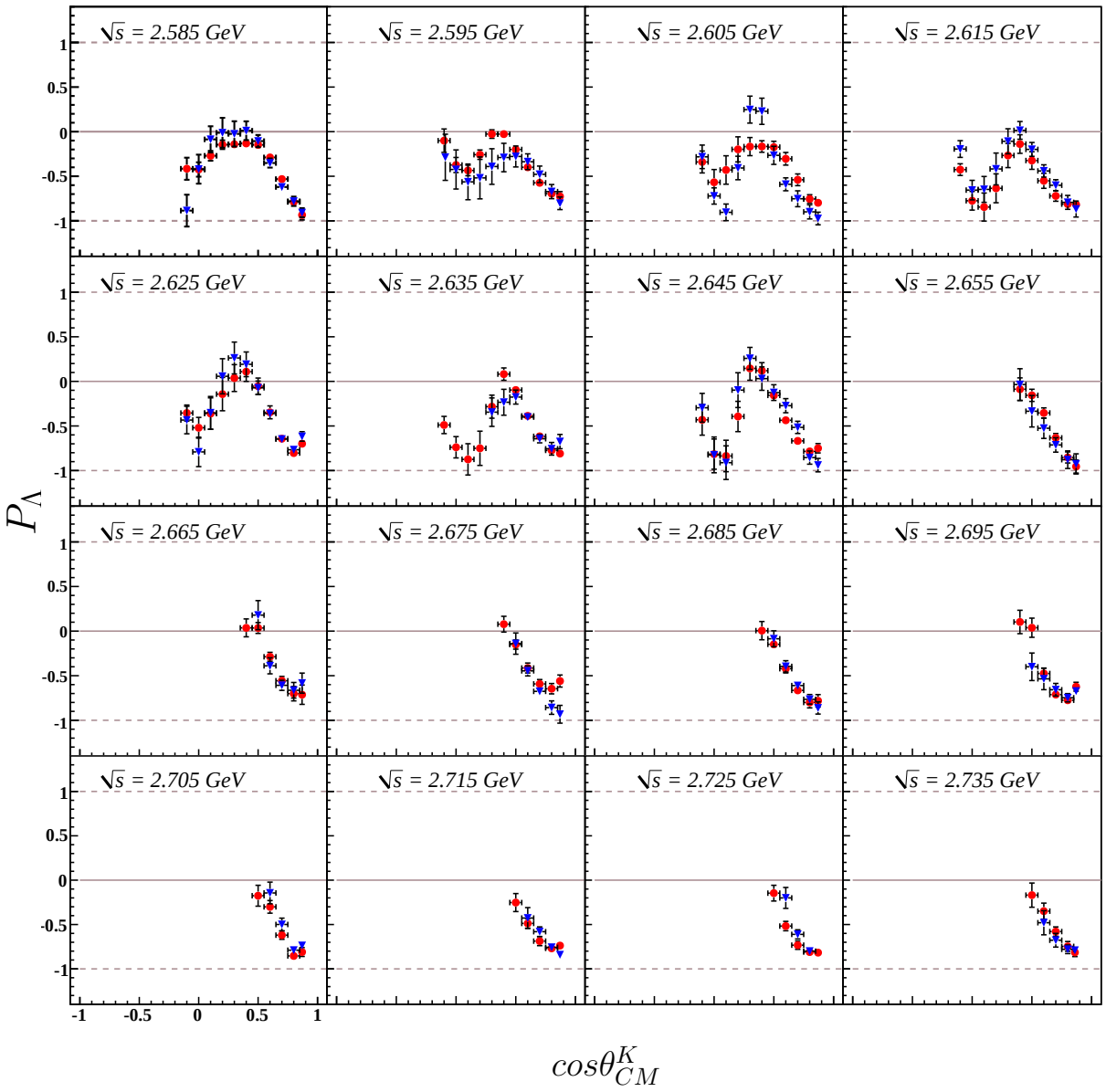

Figure 6.19: P_Λ v. $\cos\theta^K_{CM}$: Λ recoil polarization results v. $\cos\theta^{K^+}_{CM}$ for the energy range 2.58 GeV $\leq \sqrt{s} <$ 2.74 GeV. Results from the three-track analysis are shown in blue (triangles), those of the two-track analysis in red (circles). Errors displayed are statistical.

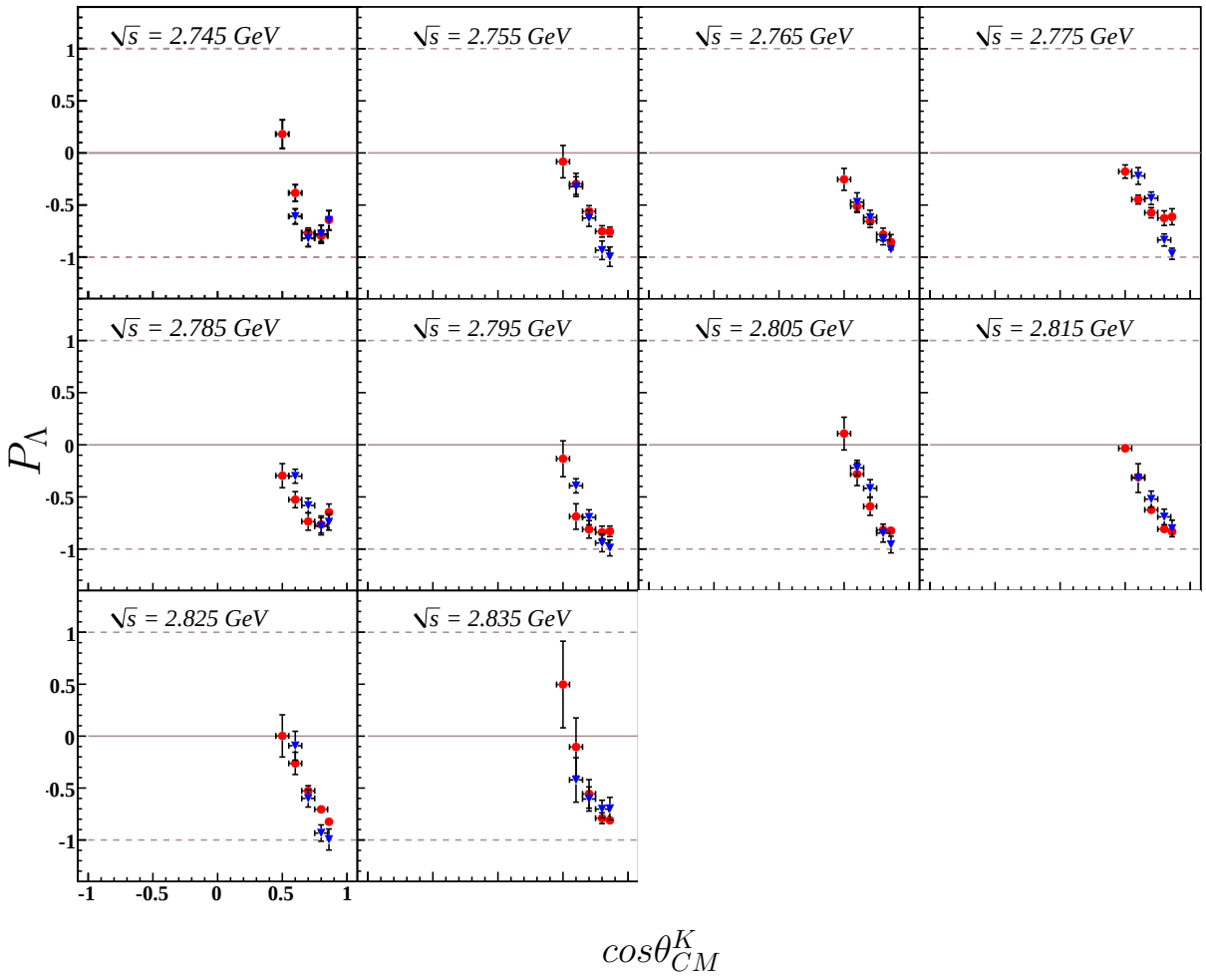

Figure 6.20: P_Λ v. $\cos\theta^K_{CM}$: Λ recoil polarization results v. $\cos\theta^{K^+}_{CM}$ for the energy range 2.74 GeV $\leq \sqrt{s} <$ 2.84 GeV. Results from the three-track analysis are shown in blue (triangles), those of the two-track analysis in red (circles). Errors displayed are statistical.

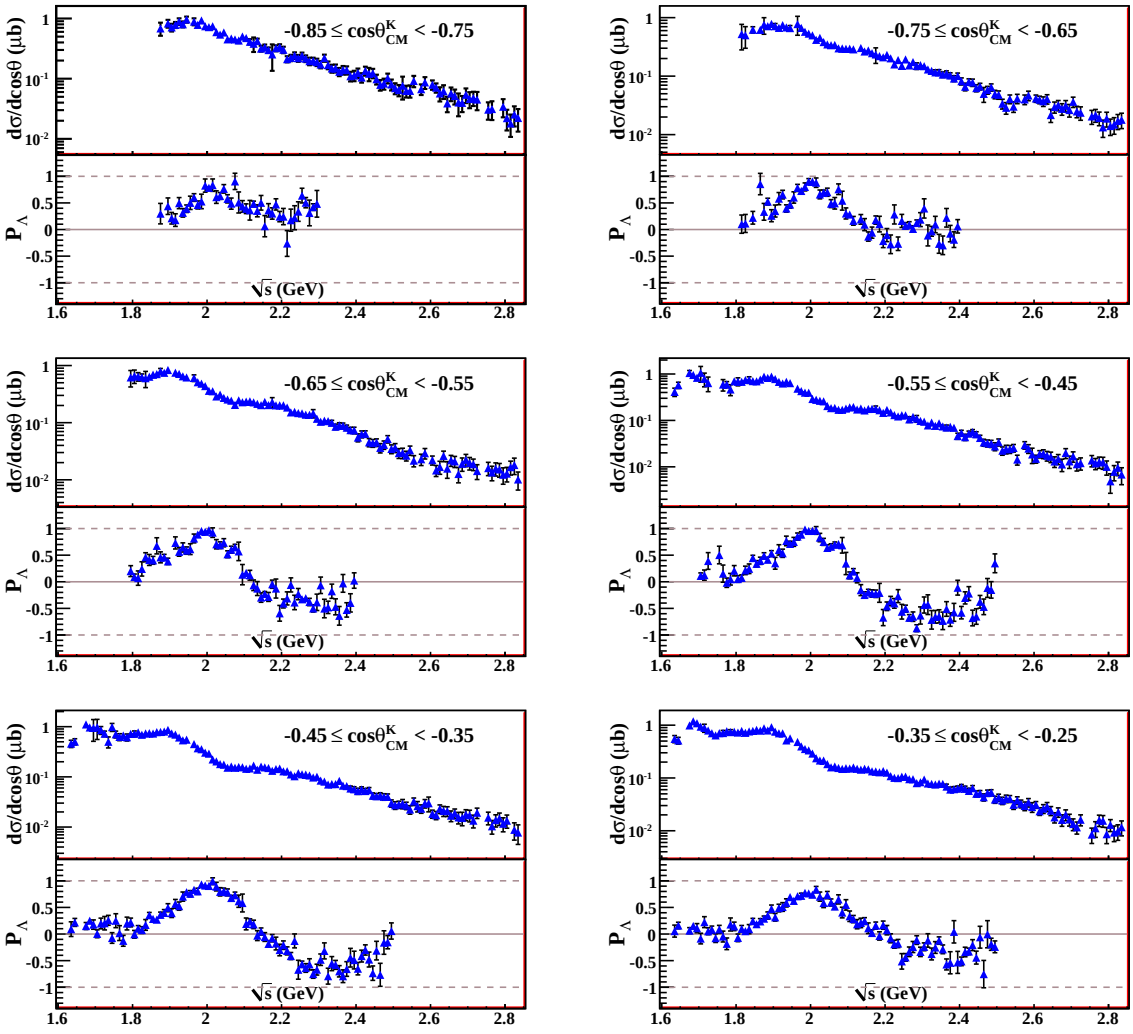

Figure 6.21: Weighted mean $d\sigma/d\cos\theta^K_{CM}$ and P_Λ results v. $\sqrt{s}$ for backward production angles. Differential cross sections are plotted above recoil polarizations from the indicated $\cos\theta^K_{CM}$ bin. Errors displayed are statistical.

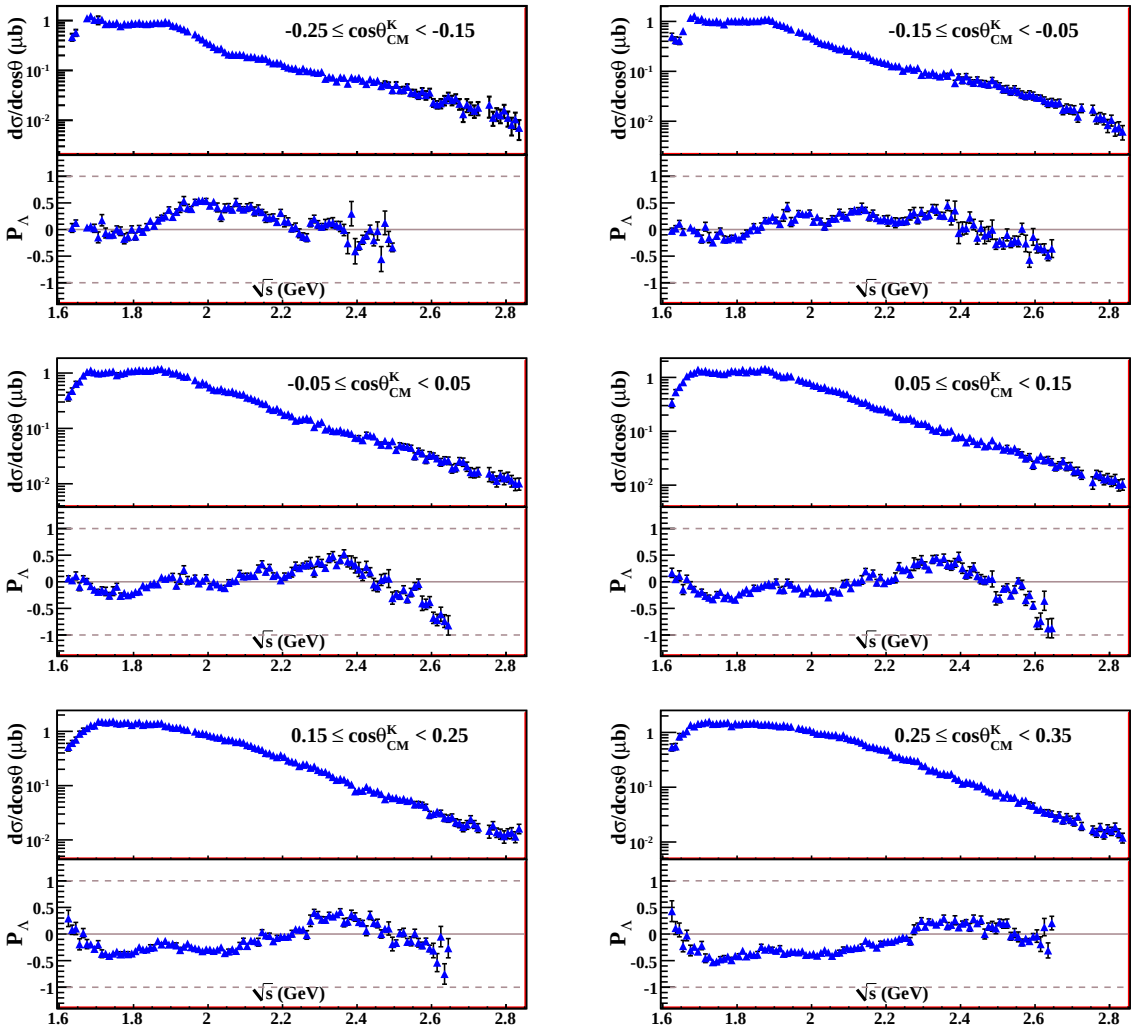

Figure 6.22: Weighted mean $d\sigma/d\cos\theta^K_{CM}$ and P_Λ results v. $\sqrt{s}$ for middle production angles. Differential cross sections are plotted above recoil polarizations from the indicated $\cos\theta^K_{CM}$ bin. Errors displayed are statistical.

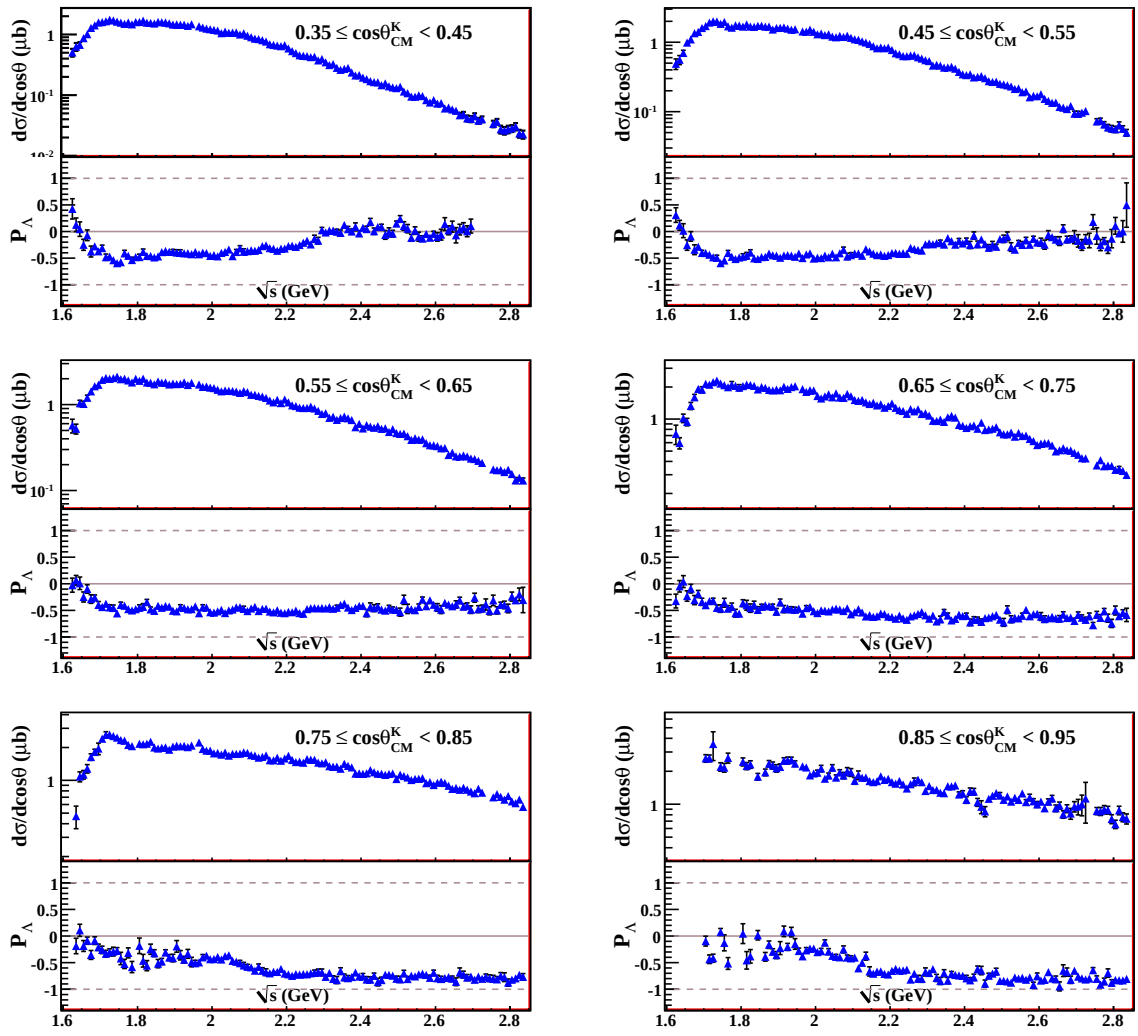

Figure 6.23: Weighted mean $d\sigma/d\cos\theta^K_{CM}$ and P_Λ results v. $\sqrt{s}$ for forward production angles. Differential cross sections are plotted above recoil polarizations from the indicated $\cos\theta^K_{CM}$ bin. Errors displayed are statistical.

[11]). Together, these results cover the energy range 1.62 GeV $\leq \sqrt{s} <$ 2.54 GeV. At the time of its publication, the CLAS *g1c* results reflected the world's largest, most precise $K^+\Lambda$ photoproduction dataset. However, differential cross sections published by the SAPHIR Collaboration in 2004 (Glander, *et al.* [10]) showed markedly different values for the $\gamma p \to K^+\Lambda$ cross sections; SAPHIR results are up to 50% lower in some kinematic regions. Though the CLAS *g1c* measurement represented a much larger dataset (roughly 6×10^5 $K^+\Lambda$ events vs. SAPHIR's 5.2×10^5), the discrepancy was troubling.

Figures 6.24 and 6.25 show comparisons of the CLAS *g1c* and SAPHIR results with our *g11a* differential cross sections versus $\sqrt{s}$ in bins of production angle. Note that energy binning for the earlier CLAS analysis is slightly wider than for our analysis; the *g1c* analyses used 25-MeV-wide bins in E_γ. We have, however, maintained the same $\cos\theta^K_{CM}$ binning as the *g1c* analyses. Binning for the SAPHIR analyses is much wider, reflecting the smaller statistics of the experiment. SAPHIR's production angle binning has the same width as ours, however bin edges are offset by 0.05. The reader will also note that these figures represent only the energy range where the earlier analyses produced results. Comparison of these three results is very encouraging. The CLAS *g11a* and *g1c* measurements show excellent agreement at almost all kinematics. The SAPHIR results agree with the CLAS results only at threshold and at backward angles.

Several features of the CLAS cross sections are worthy of note. The sizable hump in the differential cross section at backward angles and $\sqrt{s} \approx 1.9$ GeV is evident in both measurements. A second hump feature in the differential cross section is observable at backward angles (most clearly in $-0.25 \leq \cos\theta^K_{CM} < -0.15$) at $\sqrt{s} \approx 2.15$ GeV. Such features exist in the differential cross section at forward angles, however they are much less pronounced due to the more dominant t-channel production.

Localized discrepancies between the CLAS *g11a* and *g1c* results exist. For $\cos\theta^K_{CM}$, the *g11a* differential cross section results display a larger $\sqrt{s}$-dependence than the *g1c* results. In this region, the *g1c* results are relatively flat in $\sqrt{s}$. Our extremely clean $K^+\Lambda$ signal peak in this region combined with our powerful background subtraction method make it hard to believe that background events are contributing to the higher *g11a* $d\sigma$ at $\sqrt{s} < 2.0$ GeV. The flatness of the *g1c* differential cross section in this most forward bin for $\sqrt{s} > 2.3$ GeV is also suspicious when considering prominence of t-channel production in this region. A possible explanantion for this discrepancy is that in the previous CLAS analyses, Monte Carlo was not weighted to simulate the effects of physics. As we have shown in Figure 6.1, the difference between phase-space MC and our weighted MC is striking, especially at forward angles. Due to the efficiency of our skim and particle identification cuts and the agreement between the two- and three-track *g11a* analyses, we are confident in our results in this region.

Differences in the two CLAS measurements also exist for $\sqrt{s} < 1.85$ GeV at forward angles. The rise from threshold is much more dramatic in the *g11a* results than in those of *g1c*. The discrepancy could possibly be explained by the overwhelming background in this region. Because statistics in these kinematic bins are much lower relative to other regions, $d\sigma$ results are much more sensitive to background. Once again, we are confident of our kinematic fit and background subtraction method in these regions.

Finally, Figure 6.26 shows the integrated differential cross section from the CLAS *g11a* and *g1c* and SAPHIR Glander measurements in the range $-0.45 \leq \cos\theta_{CM} < 0.45$. Agreement between the two CLAS measurements is very good, while the SAPHIR data are roughly 20% lower.

LEPS 2006 and 2007

Differential cross section measurements of $\gamma p \to K^+\Lambda$ were published by the LEPS collaboration in 2006 (Sumihama, *et al.* [14]) and 2007 (Hicks, *et al.* [15]). Though these measurements occupy a much smaller region of the reaction's phase space, precision measurements at extreme forward and backward angles are useful in studying t- and u-channel production mechanisms.

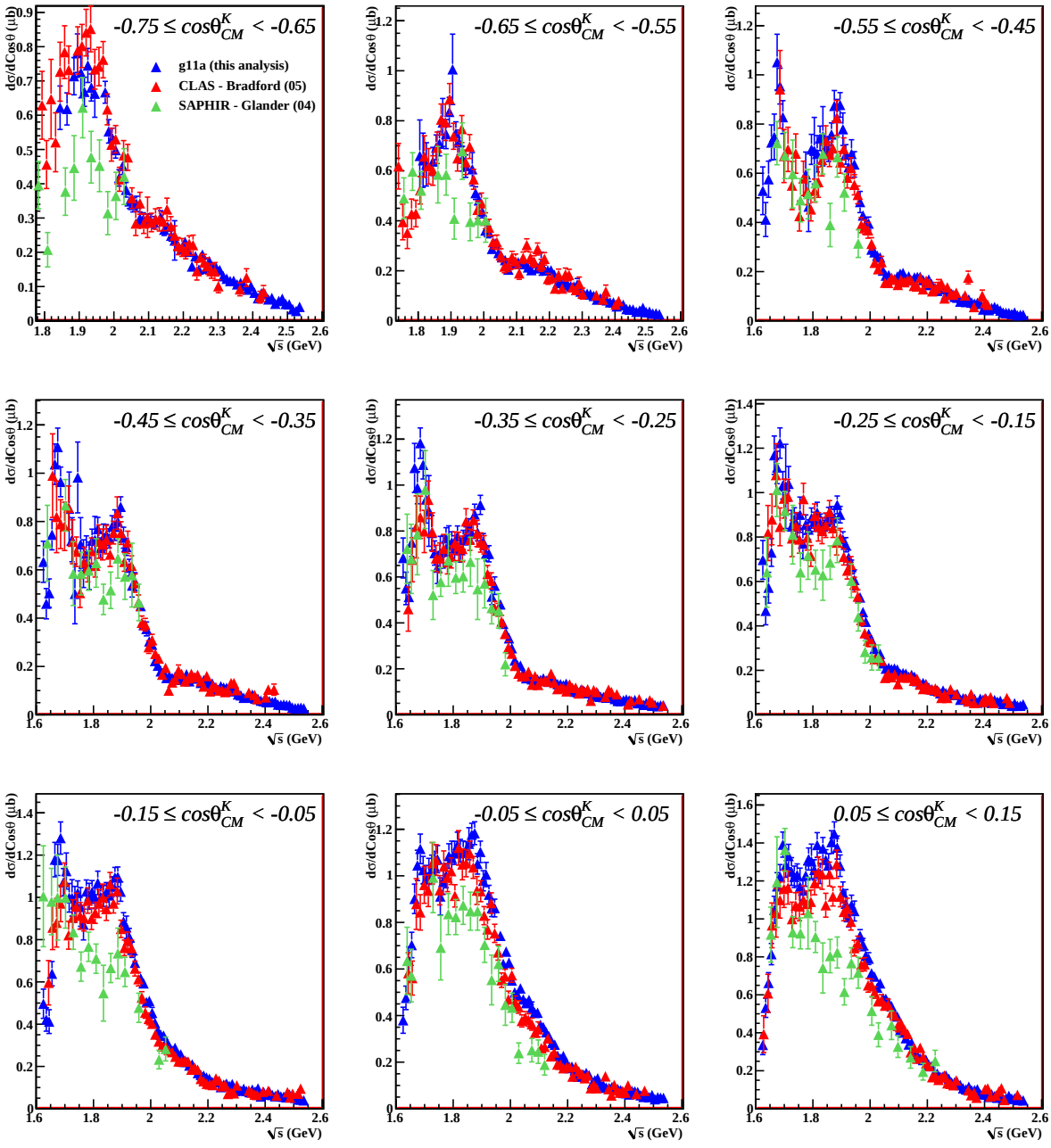

Figure 6.24: Comparison of $d\sigma/d\cos\theta^K_{CM}$ measurements: SAPHIR 2004, CLAS *g1c*, *g11a*. The plots above show differential cross section measurements from the CLAS *g1c* (red), SAPHIR 2004 (green), and this analysis (blue) versus center-of-mass energy in bins of production angle.

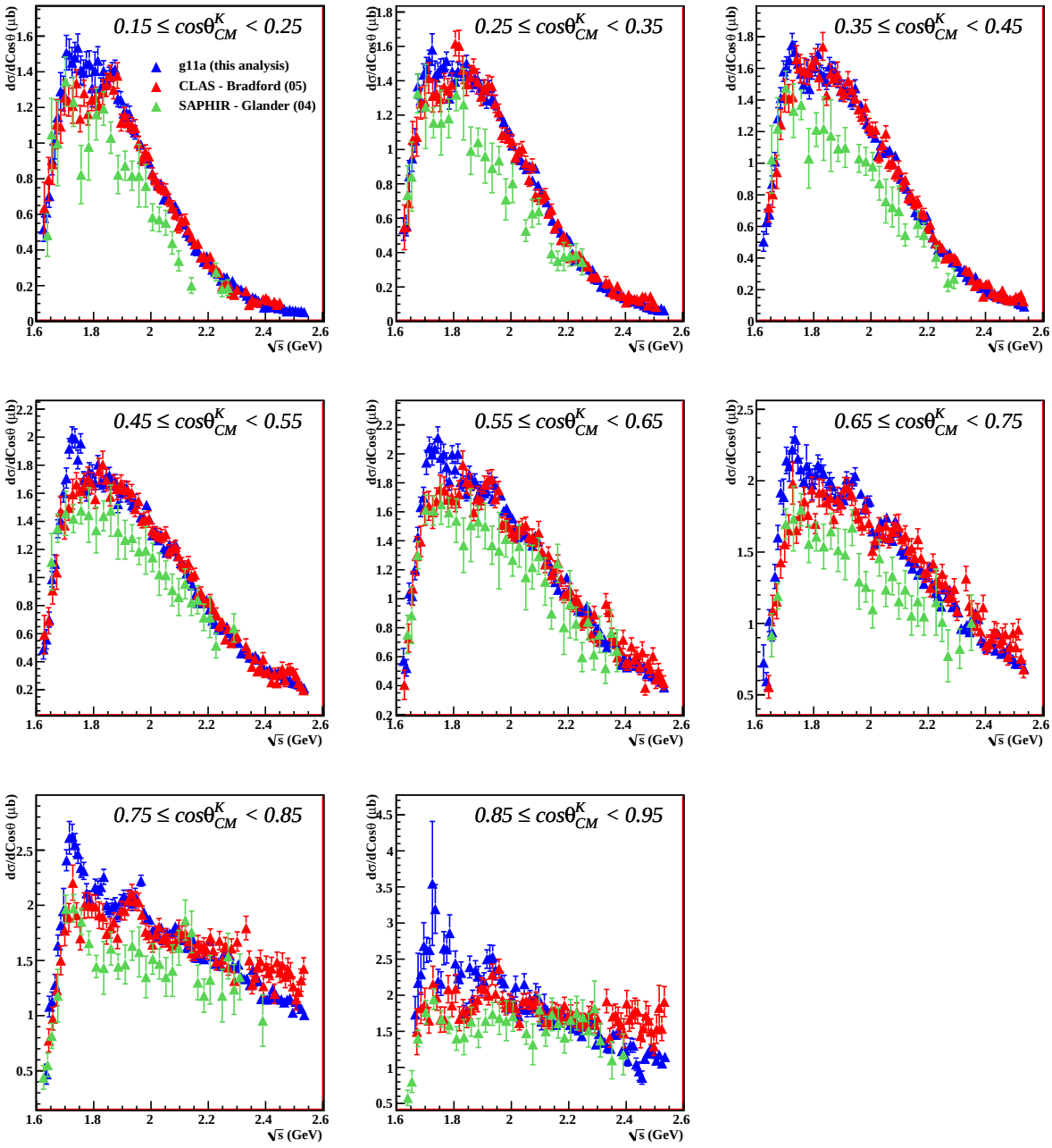

Figure 6.25: Comparison of $d\sigma/d\cos\theta^K_{CM}$ measurements: SAPHIR 2004, CLAS *g1c*, *g11a*. The plots above show differential cross section measurements from the CLAS *g1c* (red), SAPHIR 2004 (green), and this analysis (blue) versus center-of-mass energy in bins of production angle.

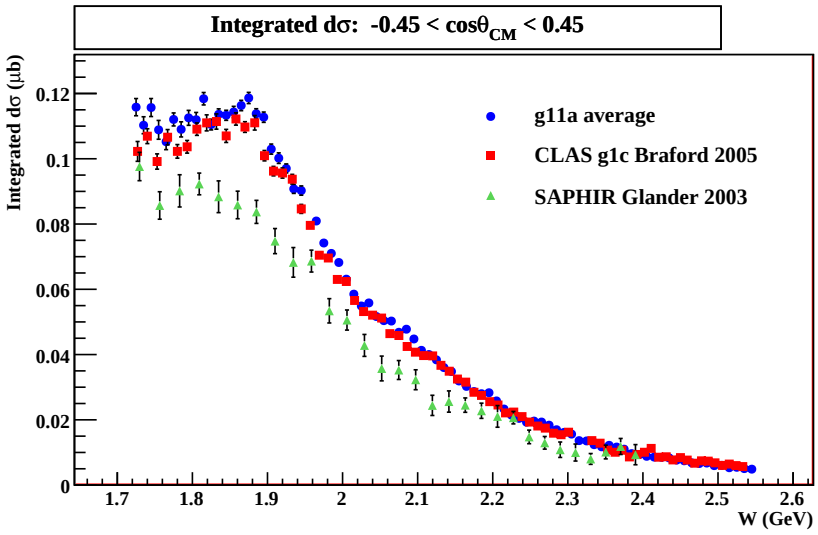

Figure 6.26: The plot above shows differential cross sections from the *g11a* (blue), CLAS *g1c* (red), and SAPHIR 2003 (green) measurements. Agreement between the CLAS results is excellent, whereas the SAPHIR results are ≈ 20% lower.

The LEPS results at forward angles occupy the energy range 1.934 GeV $\leq \sqrt{s} \leq$ 2.31 GeV and three 0.1-wide $\cos\theta^K_{CM}$ bins covering $0.70 \leq \cos\theta^K_{CM} < 1.0$. We present comparisons of these results to our *g11a* measurements in overlapping $\cos\theta^K_{CM}$ bins as indicated in Figure 6.27. From these figures, we see that the high-statistics of the *g11a* dataset (the LEPS results represent only 2.2×10^4 events) affords us a much finer binning in energy. Error bars for the most forward bin are of comparable size for the two experiments, though at less forward angles, *g11a* produces a much more precise measurement. We see that the LEPS results typically agree with the more forward of our two overlapping $\cos\theta^K_{CM}$ bins. The LEPS results confirm the downward trend in the *g11a* $d\sigma$ in the most forward bin except in the range 2.15 GeV $\leq \sqrt{s} \leq$ 2.25 GeV, where both results display a bump feature. Otherwise, overall agreement is good.

The LEPS 2007 backward angle measurements encompass the energy range 1.95 GeV $\leq \sqrt{s} \leq$ 2.29 GeV and are divided into two 0.1-wide bins in $-1.0 \leq \cos\theta^K_{CM} < 0.8$. A comparison of these measurements to our *g11a* measurements in overlapping bins are provided in Figure 6.27. Energy binning for these measurements is much wider than that of the forward angle measurement. The points from our *g11a* analysis are sparse in the most backward bin; however, the large error bars on both results suggest that they are consistent. Comparison to the more forward LEPS bin is obfuscated by the wide $\sqrt{s}$ binning. The LEPS point at $\sqrt{s} = 1.95$ GeV is generally lower than our points in that region, though it is a reasonable average of the shape of our cross section results. The LEPS point at $\sqrt{s} = 2.097$ GeV is definitely lower than our points in the region. The trends versus $\sqrt{s}$ of the two results match well with an decent overall agreement in scale.

6.4.2 Λ Recoil Polarization

We now present comparisons to several previous measurements of the Λ recoil polarization, P_Λ. In the same paper which presented the first CLAS measurements of the $\gamma p \rightarrow K^+\Lambda$ differential cross sections, J. McNabb *et al.* also published measurements of P_Λ from thier analysis of the *g1c* dataset [22]. McNabb used the traditional method of extracting P_Λ which involves fitting the proton momentum distribution in the Λ-helicity-frame, extracting the polarization from its slope.

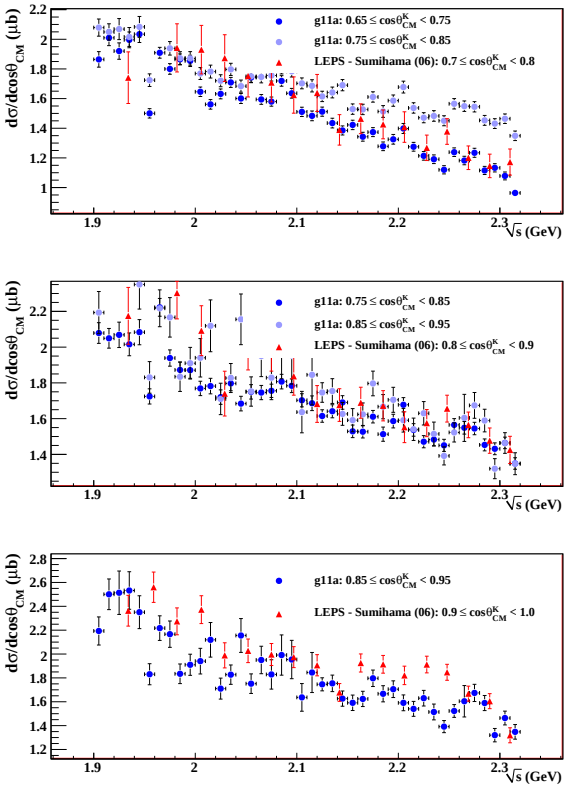

(a)

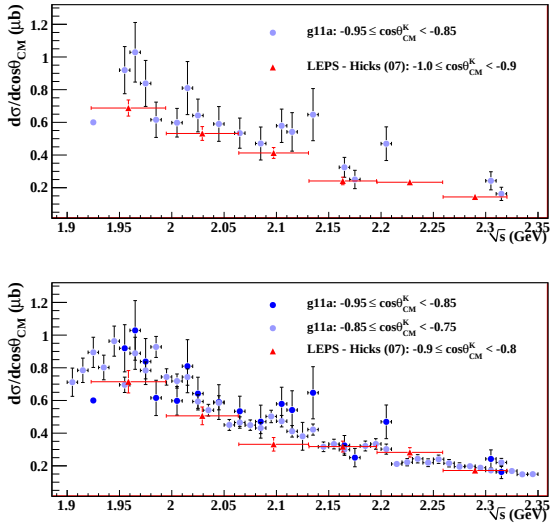

(b)

Figure 6.27: Comparison of $d\sigma/d\cos\theta^K_{CM}$ Measurements: LEPS and *g11a*. The plots above show differential cross section measurements from this analysis (blue tones) and the LEPS 2006 (a) and 2007 (b) measurements (red) versus center-of-mass energy in bins of production angle. All errors are statistical.

In order to bolster statistics for this method, McNabb consolidated bins from his differential cross section measurement. Most of his quoted P_Λ points represent 0.2-wide $\cos\theta^K_{CM}$ and 0.25-MeV-wide binning in E_γ. We present comparisons of our *g11a* results to the *g1c* results in Figures 6.28 and 6.29. Agreement between the two results is very good and displays the power and accuracy of our extraction of via the Mother Fit. Several features of the polarization that are hinted at by the *g1c* results are by our measurements.

We also present comparisons to P_Λ measurements published by the SAPHIR Collaboration with their 2004 differential cross section results [10]. Note that though there is a large discrepancy between differential cross section results from the SAPHIR and CLAS analyses, agreement in the recoil polarization, a normalization-independent quantity, is very good.

We conclude with a comparison of the most recent measurement of P_Λ, that published by the GRAAL Collaboration in 2007 (Lleres, *et al.* [23]). The GRAAL results cover the region 1.62 GeV $\leq \sqrt{s} \leq$ 1.92 GeV in six wide production angle bins ($\approx 20°$-wide bins). Figure 6.30 shows that the GRAAL measurements are in excellent agreement with those of *g11a*, and that they provide more backwards coverage at low $\sqrt{s}$ than *g11a* allows. Agreement is slightly better for our more forward production angle bins. This can be explained by the forward-peaked differential cross section in this energy range and GRAAL's very wide production angle binning and their reporting of bin ranges rather than bin centroids.

The overall agreement between our fit-extracted recoil polarization and the traditionally-extracted measurements of previous analyses is validation of our method. The accuracy of our Mother Fit combined with the enormous statistics of the dataset make the *g11a* results unmatched in precision and range. Our measurement of the recoil polarization at energies above $\sqrt{s} \approx 2.6$ GeV will allow us a more accurate understanding of non-resonant production mechanisms.

6.5 Summary

We have measured differential cross sections and recoil polarizations for the $\gamma p \to K^+\Lambda$ reaction in the range 1.620 GeV $\leq \sqrt{s} <$ 2.840 GeV. We have calculated these quantities using both the K^+p and $K^+p\pi^-$ final-state topologies and shown that the independent results are consistent. These results show many interesting features which we will scrutinize in the Chapter 8. The *g11a* measurements of the differential cross section show very good agreements with previous CLAS and LEPS results and sheds new light on discrepancies between SAPHIR and CLAS results. Our extraction of the Λ recoil polarization shows excellent agreement with the world's data. The *g11a* dataset has yielded the most sensitive measurements of $K^+\Lambda$ photoproduction to date and is justified by its access to energies above the resonance region ($\sqrt{s} >$ 2.6 GeV). In the following chapter, we exploit the precision of our measurement by performing a partial-wave analysis, searching for excited nucleon production.

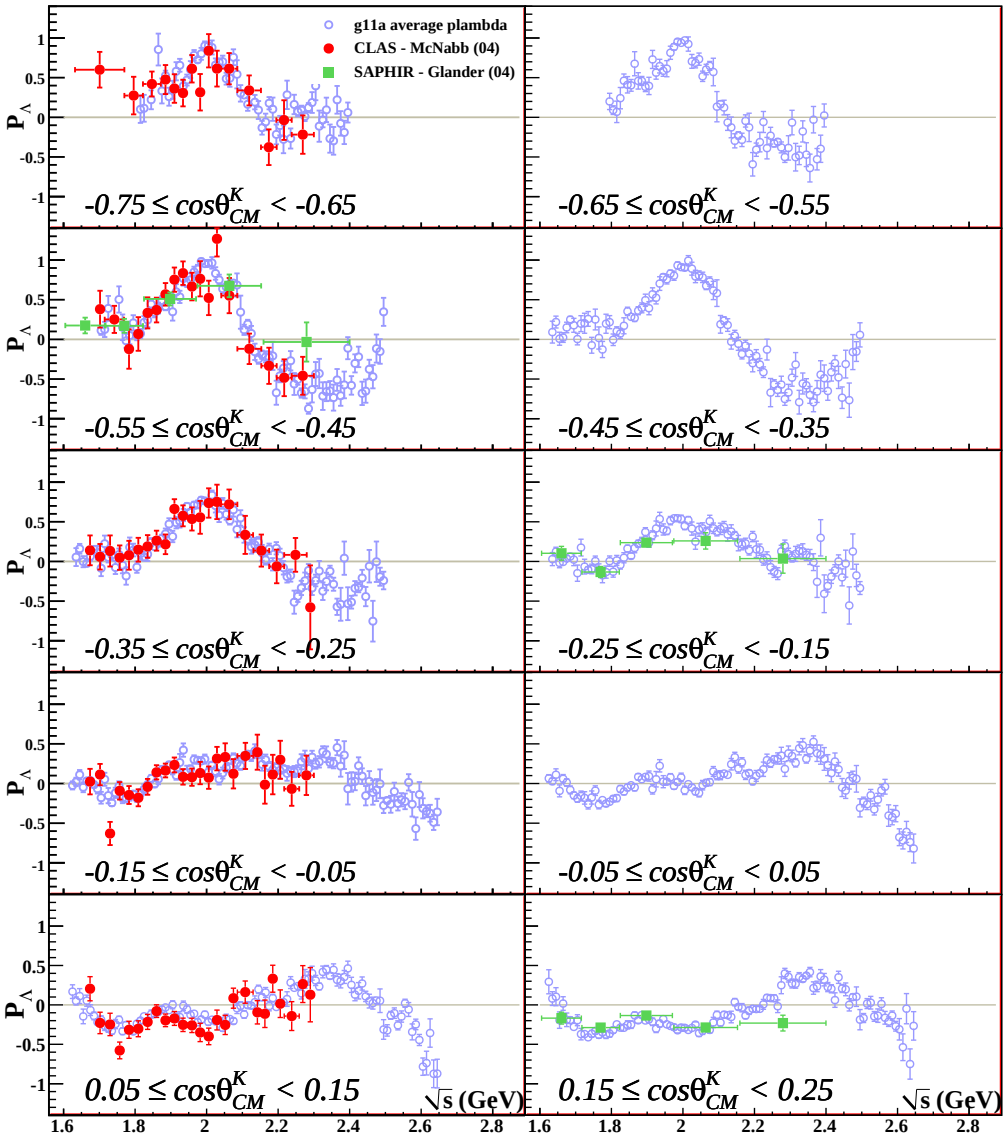

Figure 6.28: The plots above show Λ recoil polarization measurements from this analysis (blue), the previous CLAS (McNabb 2004) measurements (red), and the 2004 SAPHIR measurements versus center-of-mass energy in bins of production angle. $\cos\theta^K_{CM}$ ranges indicated on each plot indicate the *g11a* measurements plotted. Most of McNabb's measurements represent 0.2-wide $\cos\theta^K_{CM}$ bins. SAPHIR's measurements represent roughly 30°-wide angular bins. All error bars reflect statistical errors only.

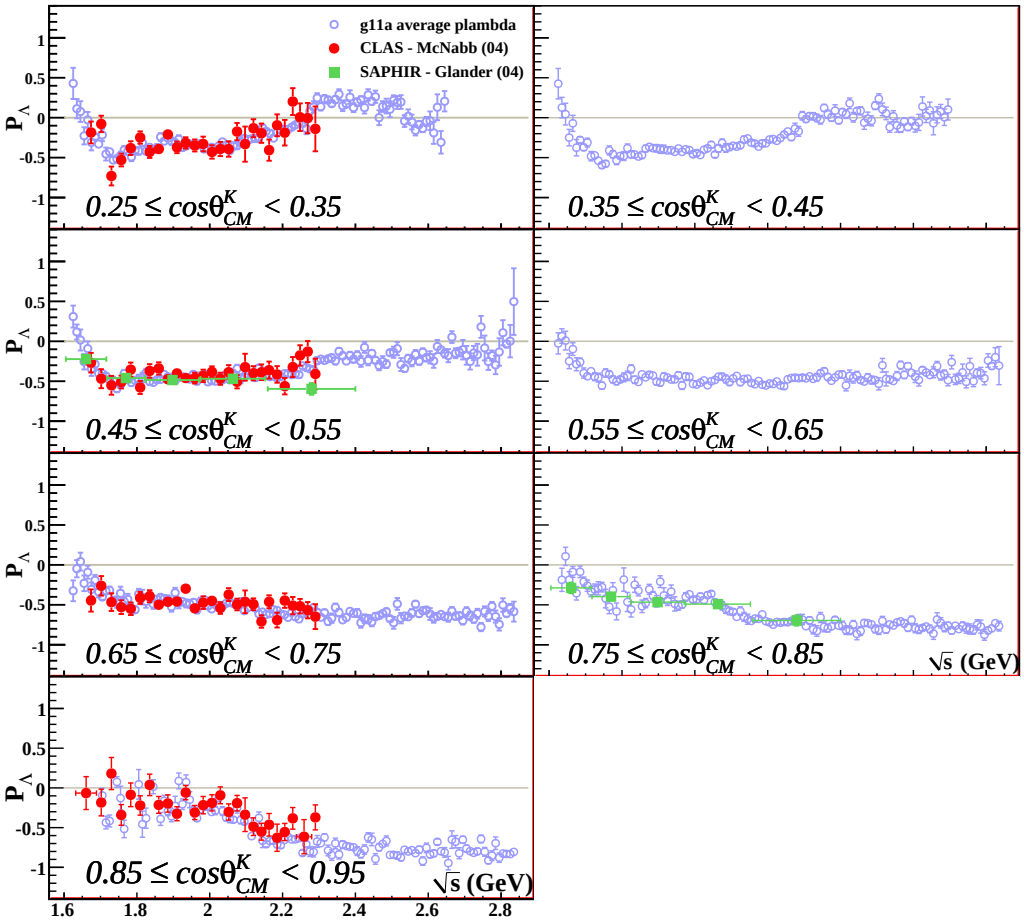

Figure 6.29: The plots above show Λ recoil polarization measurements from this analysis (blue), the previous CLAS (McNabb 2004) measurements (red), and the 2004 SAPHIR measurements versus center-of-mass energy in bins of production angle. $\cos\theta^K_{CM}$ ranges indicated on each plot indicate the *g11a* measurements plotted. Most of McNabb's measurements represent 0.2-wide $\cos\theta^K_{CM}$ bins. SAPHIR's measurements represent roughly 30°-wide angular bins. All error bars reflect statistical errors only.

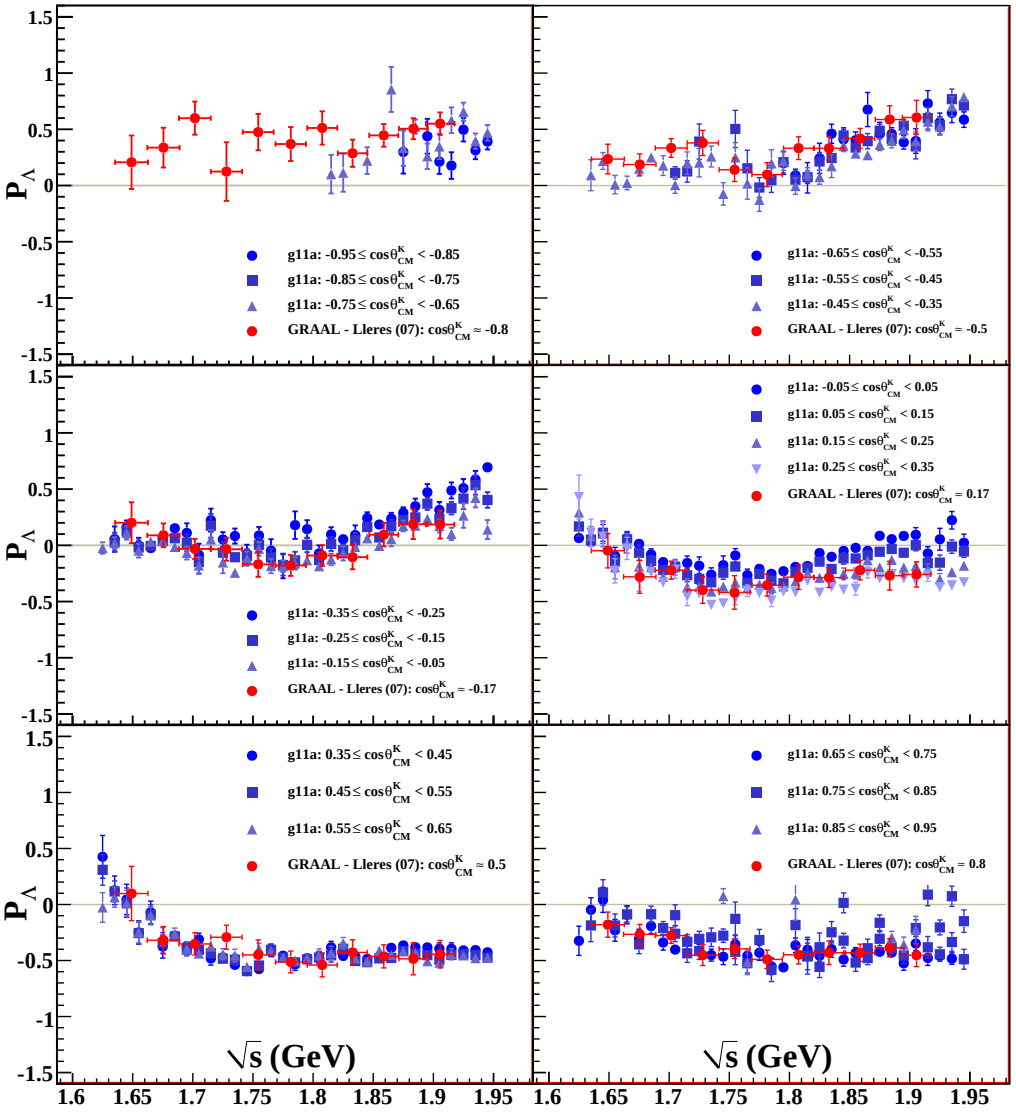

Figure 6.30: The plots above show Λ recoil polarization measurements from this analysis (blue shades) and the 2007 GRAAL measurements (red) versus center-of-mass energy in bins of production angle. $\cos\theta^K_{CM}$ ranges for each result are indicated on each plot. Binning in production angle for the GRAAL results is $\approx 20°$. All error bars reflect statistical errors only.

Chapter 7

Systematic Studies

In performing this analysis, we were fortunate that there were two existing high-precision measurements of $K^+\Lambda$ photoproduction using the CLAS detector, the 2002 analysis of J. McNabb [12] and the 2005 analysis of Robert Bradford [13]. Though both *g1c* and *g11a* were collected using the CLAS detector, significant differences exist between the two run periods. Our preliminary extraction of the differential cross section from the *g11a* dataset showed several systematic discrepancies when compared to the CLAS *g1c* results. In an effort to understand these discrepancies, we investigated possible causes and ultimately refined our *g11a* cross section. Our study of these sources of these differences occupied the five months from November 2007 to March 2008.

Our reanalysis of the *g1c* dataset described in this chapter produced the same results as the CLAS 2005 analysis. We then investigated several possible causes of systematic uncertainties in our analysis of *g11a* including data reduction efficiency, Monte Carlo simulation, and trigger efficiency. We have found that the main source of the discrepancy between the *g1c* and preliminary *g11a* measurements is a triggering inefficiency due to Λ decays outside of the start counter that is not simulated in the Monte Carlo. Once this inefficiency was discovered, we continued on to check *g11a*'s internal consistency by comaring sector-wise differential cross sections.

The reader should remember that the purpose of this chapter is to describe checks of the g11a dataset motivated by our preliminary results. (Our final measurements are presented in Chapter 6.) All of the cuts that resulted from the studies described in this chapter have been applied to the analyses described in Chapters 3 and 4; this chapter shows the necessity of these cuts.

7.1 Preliminary *g11a* $d\sigma$ and comparison to the CLAS *g1c* result

The *g1c* run is a photoproduction on liquid hydrogen dataset that was recorded by the CLAS Collaboration in the Fall of 1999. Though *g1c* and *g11a* were taken by the same detector, there are several key differences in the experimental set-up of the two experiments. The *g1c* run utilized a circularly polarized photon beam which enabled extraction of double-polarization observables, C_x and C_z. The dataset was collected using a single-charged-track trigger, whereas the *g11a* trigger required two charged tracks in the final state. The start counter used for *g1c* was a six coupled-paddle design as opposed to the highly-segmented *g11a* start counter. Finally, the *g1c* physics target was smaller than the *g11a* target (17.85 cm in length versus 40 cm, respectively) and was centered in the CLAS detector. The full *g1c* dataset is comprised of three separate datasets yielded by different accelerator beam energies: 2.4, 2.9, and 3.1 GeV. The 2.4 and 3.1 GeV datasets were used by McNabb and Bradford to extract differential cross sections in the range 1.631 GeV $\leq \sqrt{s} \leq$ 2.533 GeV.

John McNabb and Robert Bradford, then Carnegie Mellon University graduate students working with Professor Reinhard Schumacher, produced independent analyses of the $\gamma p \to K^+\Lambda$ in the *g1c* dataset. Both analyses relied on detection of the final-state p and K^+ and identification of Λ events via the $p(\gamma, K^+)\Lambda$ missing mass. Bradford's initial extraction of $d\sigma/d\cos\theta$ from the *g1c* dataset yielded results that were systematically 10% lower than McNabb's. Bradford then spent a year examining differences between the two analyses and found that the discrepancy was caused by problems with both McNabb's and Bradford's acceptance calculations. Bradford repeated both analyses and found $d\sigma/d\cos\theta$ measurements to be in excellent agreement [13]. Herein, we refer to Bradford and McNabb's combined efforts as the "*g1c*" results.

Our initial extraction of the $\gamma p \to K^+\Lambda$ differential cross section cross section also presented disagreement with the *g1c* result. We provide plots of the two measurements in Figure 7.1. Rather than a constant systematic discrepancy that would suggest a normalization error, the difference between our preliminary *g11a* result and the *g1c* result increases with $\sqrt{s}$. Disagreement exists at all $\cos\theta^K_{CM}$ values; however, the discrepancy is more drastic in the forward direction ($\cos\theta^K_{CM} \geq 0.0$). Integrating the differential cross section over a well-populated range in $\cos\theta^K_{CM}$ shows that the overall discrepancy increases with $\sqrt{s}$, as shown in Figure 7.2. Thus, the discrepancy could not be explained by an error in overall normalization.

7.2 Data reduction and topology differences

7.2.1 Application of Kinematic Fit to *g1c*

As stated in Chapter 3, our identification of $\gamma p \to K^+\Lambda$ events in the *g11a* dataset via the $K^+p\pi^-$ final state was extremely efficient. Our final working skim of the dataset was very clean, exhibiting $< 2\%$ background in most $\sqrt{s}$ bins. This cleanliness can be attributed to two specifics of the analysis: the requirement that all three final-state particles be detected, and the use of the Kinematic Fitter and confidence level-cuts to remove background. Neither of these methods were available to the *g1c* analysis; a three-track final state would have yielded significantly lower statistics and a kinematic fitter was not yet available at the time. Where we have used the kinematic fit to remove background from our dataset, the *g1c* analysis used several well-engineered timing and missing mass cuts. As such, we concerned ourselves with possible differences that could cause systematic differences between the two measurements.

To investigate the effects of kinematic fitting, we skimmed possible $K^+\Lambda$ events from the *g1c* 2.4 GeV beam energy dataset using a two-track final state (K^+p detected). We performed a 1-C kinematic fit of all events to a $\gamma p \to pK^+(\pi^-)$ hypothesis and kept events with a confidence level greater than 1%. We then applied a cut which kept all events with a missing mass off of the K^+ less than 1.2 GeV/c^2. Finally, we applied the same calculated mass cut described for our *g11a* three-track analysis in §3.5 ($m_{K^+} < 0.8$ GeV/c^2 OR $m_p > 0.8$ GeV/c^2). In order to separate background and signal events, we employed the background fitting method described in §3.8.

To calculate detector acceptance, we generated 5×10^6 phase-space Monte Carlo $\gamma p \to K^+\Lambda$ events. We then processed the raw Monte Carlo with the standard CLAS analysis software with all smearing parameters set as they were in the *g1c* analysis [13]. We calculated photon normalization using gflux (see §4.5).

We then performed an unbinned maximum likelihood fit ("Mother Fit") using s-channel amplitudes with $\frac{1}{2}^{\pm} \leq J^P \leq \frac{11}{2}^{\pm}$ in each of four $\sqrt{s}$ bins: $1.805GeV$, $2.005GeV$, $2.205GeV$, $2.255GeV$. From these fits, we then extracted differential cross sections for the *g1c* dataset following the same procedure discussed in §6.1. Comparisons of these results with previous *g1c* results in three $\sqrt{s}$ bins are shown in Fig. 7.3. Overall agreement is good, although our *g1c* results exhibit more statistical fluctuation due to the narrower $\sqrt{s}$ binning. Each of the four energy bins agreed with Bradford's result well. In none of these energy bins do we see discrepancies that would explain the $\approx 40\%$

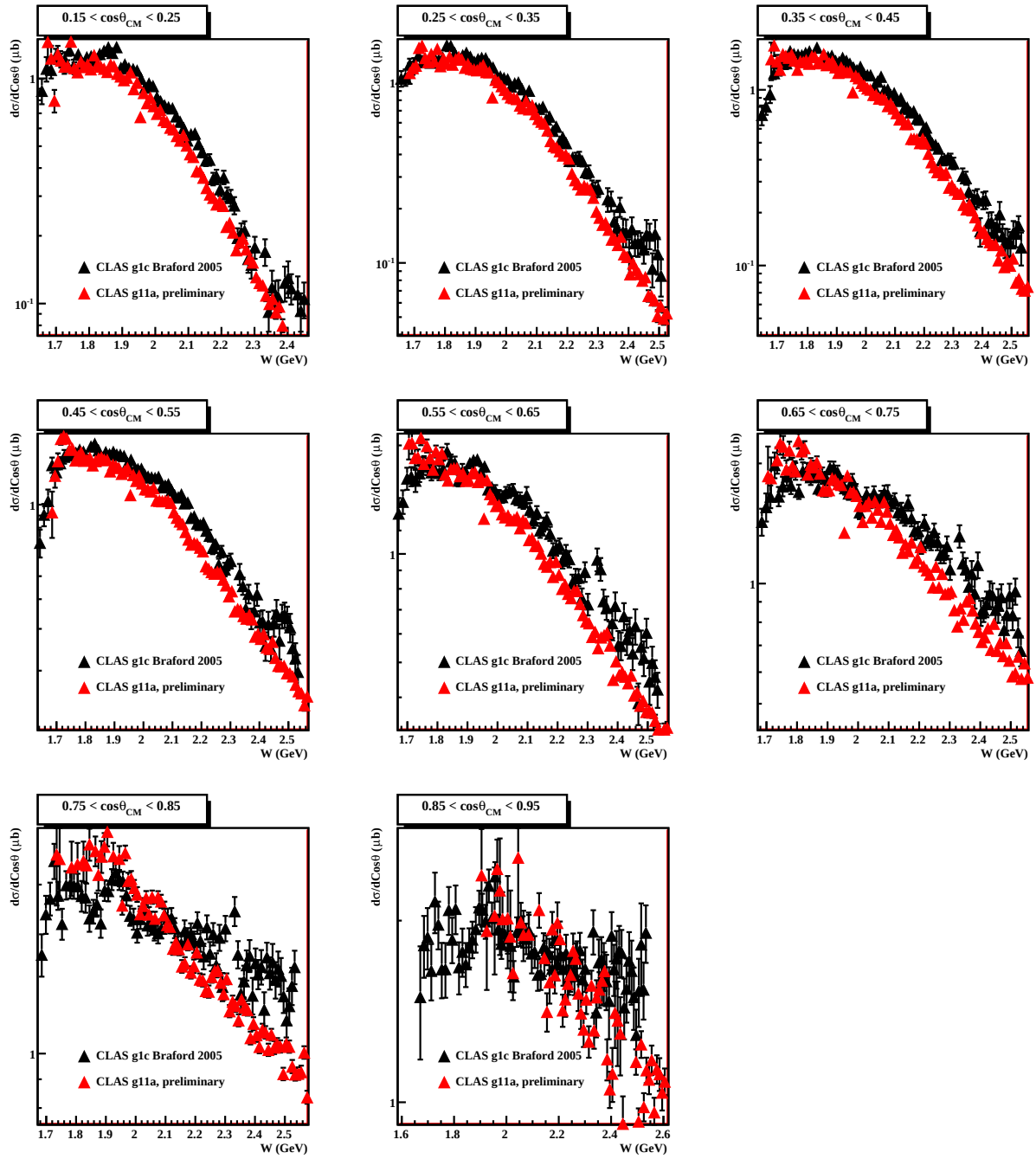

Figure 7.1: Comparison of *g1c* and preliminary *g11a* $\frac{d\sigma}{d\cos\theta}$ for forward K^+ angles. $\frac{d\sigma}{d\cos\theta}$ is shown above in bins of $\cos\theta^K_{CM}$ versus $\sqrt{s}$. The preliminary *g11a* result is systematically lower than the *g1c* result in most angles for most values of $\sqrt{s}$. In the very forward direction, the *g11a* $d\sigma$ decreases more strongly with $\sqrt{s}$ than the *g1c* result.

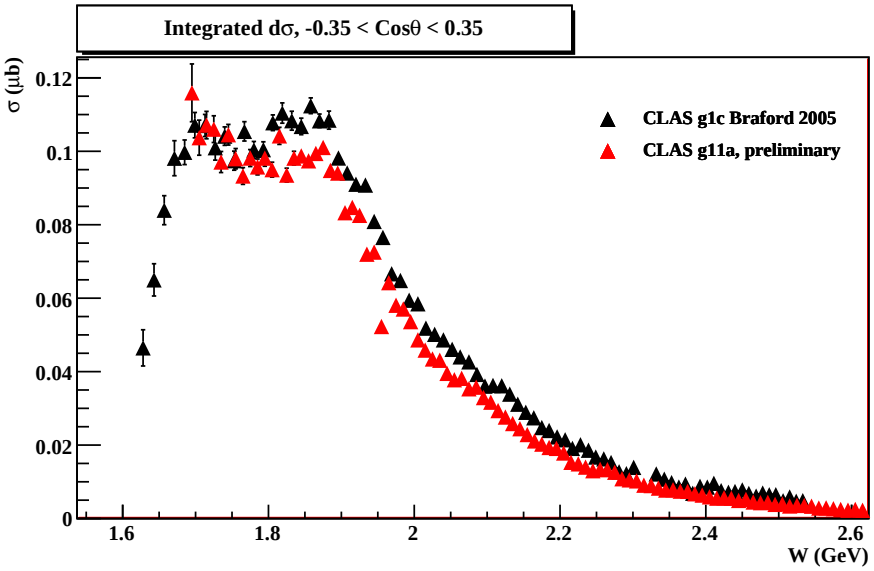

(a)

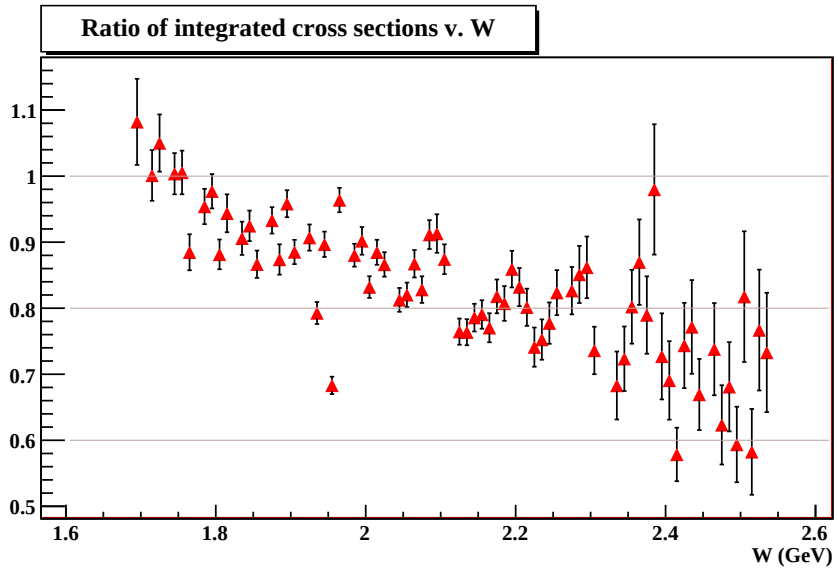

(b)

Figure 7.2: Comparison of $\frac{d\sigma}{d\cos\theta}$ from *g1c* and preliminary *g11a* for $\gamma p \rightarrow K^+\Lambda$, integrated over $-0.35 < \cos\theta^K_{CM} < 0.35$ (a) This plot shows both the *g1c* and preliminary *g11a* results integrated over the range $-0.35 < \cos\theta^K_{CM} < 0.35$. The disparity between the two measurements is apparent. Plot (b) shows the ratio of the *g11a* measurement to the *g1c* measurement. The discrepancy increases with increasing $\sqrt{s}$ to a maximum of $\frac{g11a}{g1c} \approx 0.6$.

difference between *g1c* and *g11a* shown in Fig. 7.2.

7.3 Detector and Simulation Issues

There exist several major differences in the experimental setup of the CLAS detector for the the *g1c* and *g11a* run periods. These include, but are not limited to, photon energy range, electron/photon beam polarization, target location, start counter hardware, and triggering scheme. These differences should all be taken into account by the CLAS Monte Carlo processing suite, GSIM. However, in light of the discrepancies between the *g1c* and preliminary *g11a* results, we have scrutinized all elements of our acceptance calculation. In this section, we outline our studies of TOF paddle efficiencies, trigger simulation, and examination of triggering for data and Monte Carlo.

7.3.1 TOF Paddle Survey

At the time that our analysis began, a detailed study of systematic errors in the *g11a* dataset had already been performed [62]. As a result of this study, detector components that were not functioning properly during the *g11a* run period and could not be accounted for in Monte Carlo simulations were identified. Cuts removing these detector components from our analysis were made manifest in the form of fiducial cuts and TOF paddle knockout cuts discussed in §3.6. The analysis that produced this study, however, used the much higher-statistics $\gamma p \to p\pi^+\pi^-$ channel for most of its systematic error analyses. The study makes no direct observation of CLAS's acceptance for K^+ tracks.

To investigate our ability to simulate the TOF counter's detection of K^+ mesons, we filled histograms of occupancy versus TOF counter in each sector for data and accepted Monte Carlo. These are shown in Figure 7.4. The differences between relative occupancies for data and Monte Carlo show paddles in CLAS that are not adequately modeled by GSIM. Most of these paddles are accounted for by the TOF knockout cuts prescribed by [62]. Unaccounted for, however, are the number 23 TOF counters in sectors 1, 2, 3, 4, and 6 (paddle 23 was previously cut in sector 5). We see that the data occupancies for the number 23 TOF counter are low in comparison to its nearest neighbors. The accepted Monte Carlo somewhat resembles this feature, however the level of accuracy in the simulation is questionable.

In each sector of CLAS, TOF counter 23 is located on the edge between the two most forward sections of the TOF wall. Paddles 23 and 24 overlap to a certain degree, making reconstruction of tracks passing through the two paddles difficult to trust. Such events which confuse the tracking software are assigned to TOF counter number 0 and are cut by this analysis. In light of these inconsistencies, we also cut track which were associated with paddle 23 from our analysis in all sectors. Exclusion of paddle 23 from our analysis produced localized increases in differential cross section on the order of 2-3%.

7.3.2 Test of a momentum-dependent trigger efficiency simulation

As previously mentioned, the PWA group at CMU made use of the $\gamma p \to p\pi^+\pi^-$ reaction to investigate systematic errors in the *g11a* dataset [62]. One of the most useful results of this analysis is the trigger efficiency map described in §4.1.3. Because the *g11a* trigger efficiency is not simulated by GSIM, scaling by the trigger efficiency for each type of particle is applied to the Monte Carlo.

Due to the channel used for their study, the CMU group did not glean any direct trigger efficiency information for K^+ tracks. The most accessible reaction for a similar analysis including kaons is the $\gamma p \to K^+\Lambda \to K^+p\pi^-$ channel. However, due to the small break-up energy of the $\Lambda \to p\pi^-$, the vast majority of $\gamma p \to K^+p\pi^-$ present a final state with the p and π^- detected in the same sector. Thus, the trigger would be set by at most two sectors. After careful study, we have determined that no suitable channel exists in *g11a* for study of the K^+ trigger efficiency.

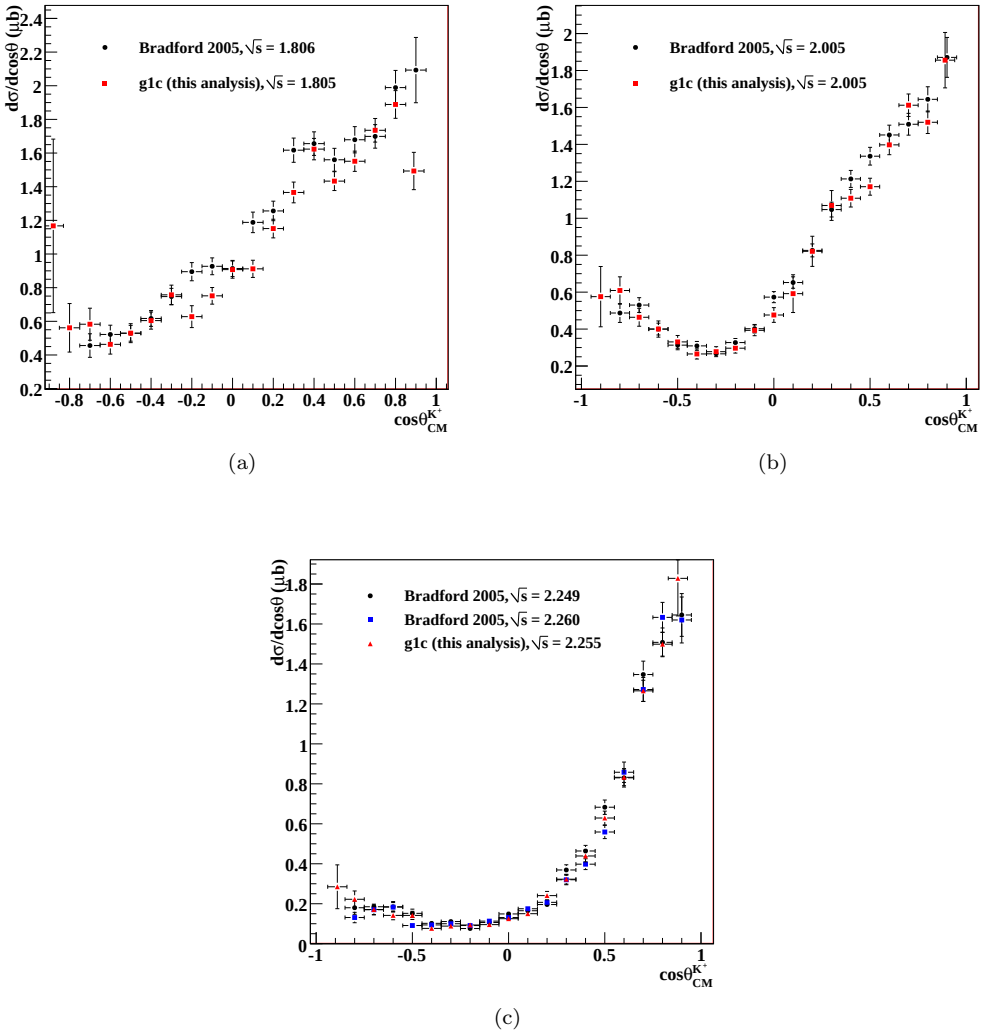

Figure 7.3: Comparisons of *g1c* differential cross sections: Bradford v. this analysis. (a) This plot shows $d\sigma/dcos\theta^{K^+}_{CM}$ results for $\sqrt{s} \approx 1.8$ GeV bin. Bradford's results are shown in black, the results of this analysis in red. Overall agreement is good. Disagreement at the extreme edges is due to low statistics. (b) This plot shows differential cross sections in the $\sqrt{s} \approx 2.005$ GeV bin. Overall agreement is again very good. (c) This plot shows our results in the $\sqrt{s} = 2.255$ GeV bin (red points) along with those of Bradford's $\sqrt{s} = 2.249$ GeV (black) and $\sqrt{s} = 2.260$ GeV (blue) bins. Once again, agreement is good. We observe no systematic difference in the two results that would suggest the trend shown in Fig. 7.2. From these, we conclude that analysis cuts are not the source of the discrepancy between *g11a* and *g1c* results.

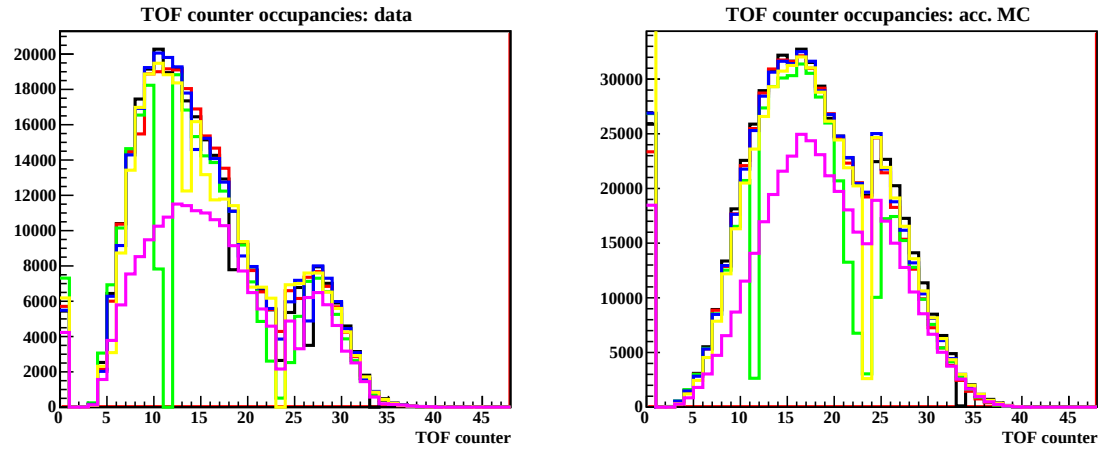

Figure 7.4: Occupancies per TOF counter per sector for data and accepted Monte Carlo. Differences in relative occupancies between data and accepted Monte Carlo per TOF counter hint at inconsistencies in the CLAS simulation software. Most poorly-simulated paddles were previously excluded from our analysis. Mismatch between occupancies for paddle 23 in all sectors motivate its removal from further analysis.

In light of this, we attempted to refine the existing *g11a* trigger efficiency map. Because the main components of the CLAS *g11a* trigger, the start counter and the TOF counters, are scintillator detectors, we expect its efficiency to be dependent upon the momentum of a given track. We have investigated this by repeating the study of the $\gamma p \to p\pi^+\pi^-$ channel in *g11a* with a further segmentation of the data. For each particle type, we calculate an efficiency map as a function of ϕ, TOF paddle, and track momentum ($|\vec{p}|$). We used a 500-MeV/c-wide binning in the range 0.0 GeV $< |\vec{p}| <$ 3.5 GeV for each particle type. We found no appreciable difference between the existing *g11a* trigger efficiency map and the maps generated for any of the momentum bins for either the p or π tracks. Thus, we use the existing efficiency map, applying the π^+ map K^+ tracks in our analysis.

7.3.3 Start Counter

As described in Chapter 2, the *g11a* trigger required a coincidence between the tagger Master OR, and the CLAS Level 1 trigger. Further, for the CLAS Level 1 trigger to be set, a coincidence was required between the start counter and TOF wall in two different sectors. The Λ is a relatively long-lived neutral particle, with $c\tau = 7.89$ cm, on the same length scale as the start counter radius ($\approx$ 10 cm). Thus, we expect that there is a subset of $K^+\Lambda$ events for which the Λ decays into its charged daughter particles outside of the start counter. As the start counter is a scintillator detector, such events (neglecting any incidental hits from other events or cosmic backgrounds) would not set the CLAS Level 1 trigger in the sector associated with the Λ. Such an effect is not compensated for in the Monte Carlo, as GSIM provided no trigger information from the start counter.

Secondary Vertex Cut

To investigate this, we plot the secondary vertex (Λ decay vertex) positions calculated using MVRT and the p and π^- momenta for both data and accepted Monte Carlo (see Figure 7.5). The data displays a significant drop in occupancy at the physical dimensions of the start counter; the Monte

Carlo does not. In order to make the Monte Carlo more accurately reflect the data, we cut all events for which the reconstructed secondary vertex is outside the physical dimensions of the start counter (shown in Figure 7.5).

We then repeated our Mother Fit procedure with this start counter cut applied to both data and Monte Carlo. The resulting differential cross sections are in better agreement with the *g1c* result and are described below. In order to test the robustness of this cut, we repeated the analysis with start counter cuts defined by different radial dimensions (distance from beamline to start counter) smaller than the actual start counter. All cuts produced differential cross sections in agreement with the cut defined by the actual start counter volume.

Though results from this "physical" secondary vertex cut were in much better agreement with the *g1c* results, systematic differences of up to 10% still existed in some energy ranges. These differences encouraged us to further investigate the efficiency of this cut. By scrutinizing the secondary vertex diagrams presented in Figure 7.5, it is easy to see that using MVRT to reconstruct the Λ decay vertex presents some resolution problems. In Figure 7.5(b), we see that there is some "bleed through" of the calculated secondary vertex outside of the physical volume of the start counter. More interesting to our analysis, however, are the ρ vs. z distributions shown in 7.5(a) and (c). While MVRT is efficient for many vertexing applications, it is understandable that it would have problems reconstructing the Λ decay vertex due to the small opening angle of the proton and π^-.

Λ Decay Simulation for Monte Carlo

In light of the inefficiencies of the "physical" start counter cut, we sought to create a "statistical" cut that would be applied only to the Monte Carlo. This cut is based upon determining the distance that a Λ would have needed to travel in order to have decayed outside of the start counter based on its primary (event) vertex position and momentum. For each Monte Carlo event, we begin by calculating the event vertex, $\vec{r}_0 = (x_0, y_0, z_0)$ by applying MVRT to the K^+ momentum and idealized beam position. We then reconstruct $\vec{p}_\Lambda = (p_\Lambda, \theta, \phi)$ as the sum of proton and π^- momenta. We may then calculate the point of intersection, $\vec{r}_{int} = (x_{int}, y_{int}, z_{int})$, between $\vec{p}_\Lambda$ and the start counter. If the point of intersection lies in the main body of the start counter ($z_{int} \leq 12$ cm), the path length, l between event vertex and the intersection is easy to calculate and is given by

$$l = \frac{(10cm)}{\sin\theta\cos\phi'}. \tag{7.1}$$

Here, 10 cm is the shortest distance from the beam line to the start counter and ϕ' is the azimuthal angle in each sector, $\phi' \in [-30°, 30°]$. If the point of intersection is in the nose of the start counter ($z_{int} > 12$ cm), geometry makes the calculation a bit more complicated, giving

$$l = \frac{12cm + 10cm - z_0}{\cos\theta + \sin\theta\cos\phi'}. \tag{7.2}$$

Using the Λ's characteristic lifetime, $\tau = 2.63 \times 10^{-10}$ s, we can then calculate the characteristic lifetime of the Λ as observed in the laboratory frame to be

$$t = \gamma\tau = \frac{\tau}{\sqrt{1-\beta^2}}, \tag{7.3}$$

where β is calculated from $\vec{p}_\Lambda$. We also calculate the distance d that the Λ would have traveled in time t to be

$$d = \beta ct. \tag{7.4}$$

Finally, we consider the exponential nature of the Λ decay and construct the probability $P(\beta)$ that the given Λ will intersect the start counter before it decays as

$$P(l, \beta) = exp\{-l/d\} = exp\{-l/(\beta ct)\} \tag{7.5}$$

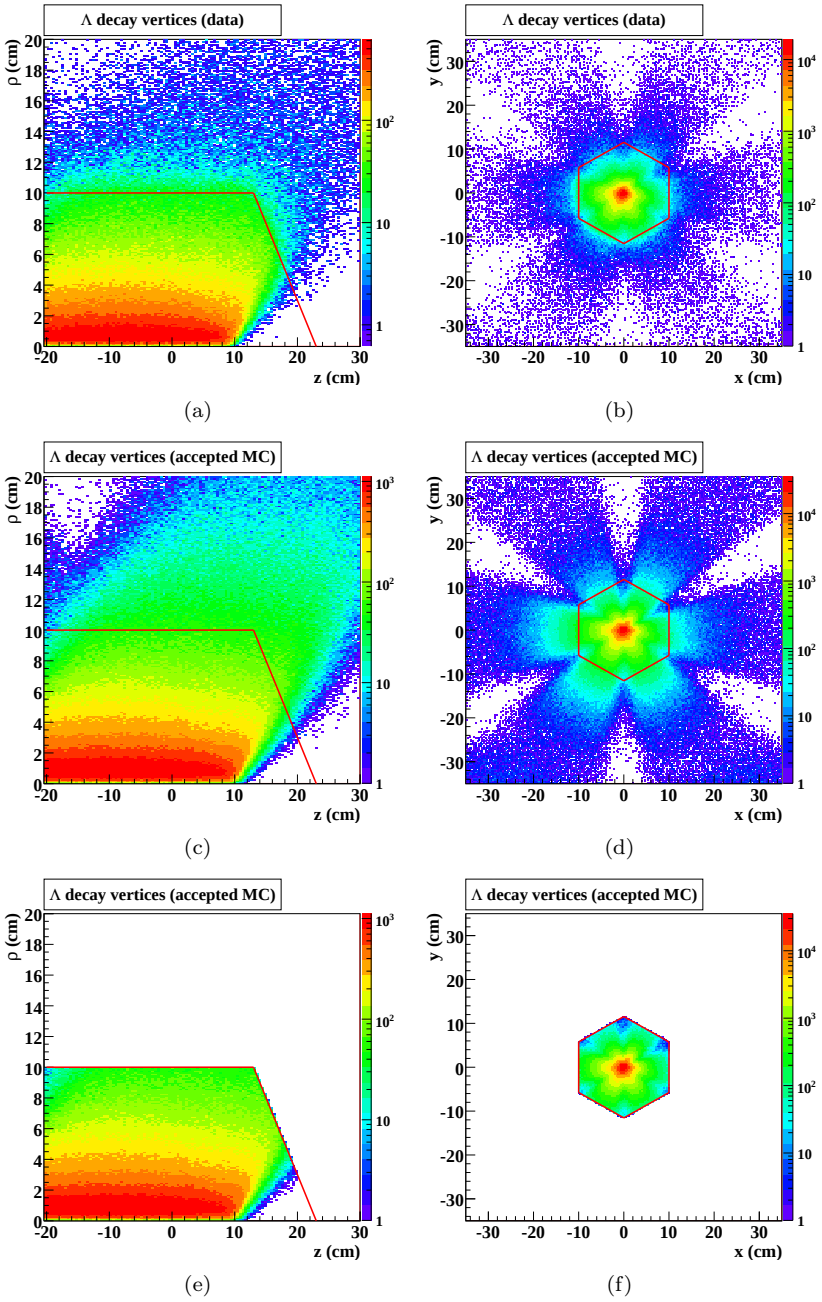

Figure 7.5: Λ decay vertices for *g11a* data and Monte Carlo. The plots above show Λ decay vertices for *g11a* data ((a) and (b)) and accepted Monte Carlo ((c) and (d)). Plots (a) and (c) show distance from beam-line (ρ) v. z. Plots (b) and (d) show distance from y v. x. In all plots, start counter dimensions are shown by thin red lines. The effect of the start counter in the data is striking. Events which for which the Λ decays outside of the start counter do not set the CLAS Level 1 trigger and are thus not recorded in the data. This effect is not reproduced in the Monte Carlo. (e) and (f) show the accepted Monte Carlo events kept by our cut on secondary vertex position (applied to MC and data).

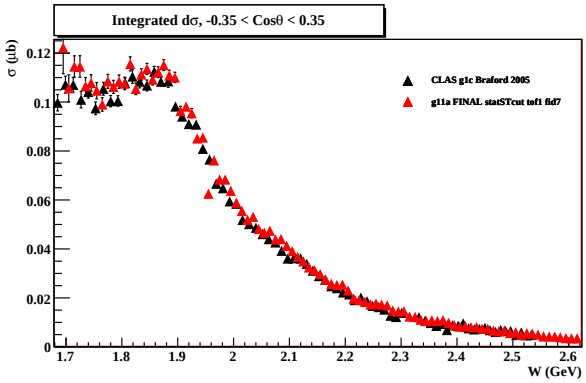

Figure 7.6: Shown above is a comparison of the differential cross section results from *g1c* (black) and this analysis (red) integrated over the range $[-0.35, 0.35]$. The *g11a* result includes the statistical start counter simulation as described in the text. Agreement between the two results is far better than that shown in Figure 7.2.

In order to treat this decay in a probabilistic manner, we generate a random number n in the interval $[0, 1]$. If $n < P(l, \beta)$ for the given event, then we cut the event.

The cut described above treats the decay of the Λ in the Monte Carlo in a statistical way in that it generates a probability that a given Λ decayed outside of the start counter. This is satisfying as the same effect has already been imposed on the data by nature. More importantly, the cut depends only on the momentum resolution for the proton and π^- tracks. When we apply the cut, we find very good agreement with the *g1c* results. To lend creedence to this cut, we show a comparison of the integrated differential cross sections in Figure 7.6. Comparisons of the full differential cross section results are given in §6.2.3.

One final feature of this cut deserves comment. The cut described above imposes the effect of triggering on the Monte Carlo in a purely statistical way. By applying it, we are removing a fraction of events equal to the start counter's effect on the data. However, as we do not explicity take into account the actual location of the Λ decay vertex, the secondary vertex distributions of data and Monte Carlo do not display the same shape. As the Λ path length is still relatively small when compared to the scale of the CLAS detector, this mismatch does not seem to introduce any systematic discrepancies.

7.4 Comparison of Sector-wise $d\sigma/d\cos\theta^K_{CM}$

After general agreement with the *g1c* differential cross section results was achieved, we sought to check the *g11a* result for internal consistency. Fortunately, the nature of the CLAS detector allows comparisons of differential cross sections calculated from each sector. We have calculated differential cross sections treating each of the six sectors of CLAS as an independent detector, receiving one sixth of the flux associated with the whole detector. We find the agreement between differential cross sections resulting from sectors 1, 2, 3, 4, and 6 to be satisfactory. However, sector 5 displays a significant systematic discrepancy when compared to the average $d\sigma$ from the other sectors. In Figure 7.7, we provide plots of the ratio of the sector 5 $d\sigma/d\cos\theta$ to that of the other sectors combined. The dip in the sector 5 cross section is apparent in two 0.1-wide $\cos\theta^K_{CM}$ bins and over a nearly 400 MeV range in $\sqrt{s}$.

In the center-of-mass frame, it is difficult to ascertain whether this difference is due to a single detector element. For a more instructive comparison, we project these $d\sigma$ values onto their lab-frame

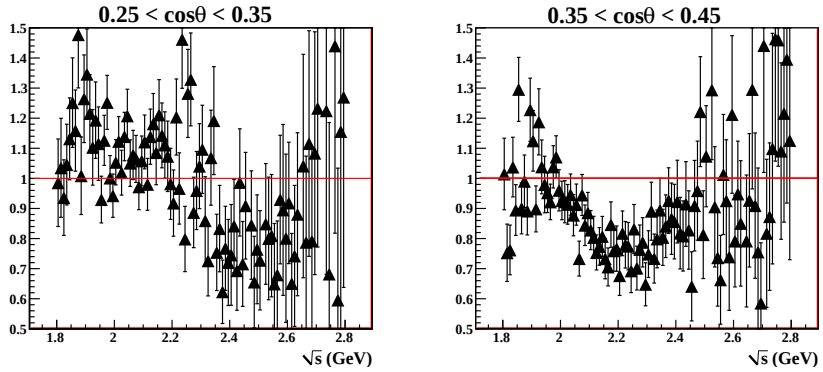

Figure 7.7: The plots above show the ratios of $d\sigma/d\cos\theta^K_{CM}$ values from sector 5 to those from sectors 1, 2, 3, 4, and 6 (combined). Shown are the $0.25 \leq \cos\theta^K_{CM} < 0.35$ (left) and $0.35 \leq \cos\theta^K_{CM} < 0.45$ (right) bins. The dip in the sector 5 cross section is apparent in both angular bins over a significant $\sqrt{s}$ range.

production angle ($\theta^{K^+}_{lab}$) and K^+ track momentum coordinates. We find that the declivity in the sector 5 measurements occurs at a fixed lab angle and is independent of track momentum. The effect is localized in the region $0.45 \leq \theta_{lab} < 0.55$. This effect is shown in Figure 7.8. Because the effect is independent of momentum, it must take place before tracks are bent by the magnetic field. Thus, we attribute the defect to an inefficiency in the Region 1 drift chamber in sector 5. This problem is clearly not modeled by the Monte Carlo, and we thus cut from our analysis all tracks (p, K^+, and π^-) that pass through sector 5 with $0.45 \leq \theta_{lab} < 0.55$. This cut restores consistency to the sector 5 cross section, though at the cost of statistics in this kinematic region. Though this subtle improvement of the sector 5 cross section does not have a significant effect on the total cross section, we count our ability to identify it as a tribute to the sensitivity of the detector.

7.5 Summary

The accuracy of this analysis benefits greatly from the existing analyses of the CLAS *g1c* dataset. By comparing to these previous analyses, we were able to identify several subtle issues, leading to much more accurate results. The most significant of these corrections was our simulation of the start counter's effect on triggering in *g11a*. After remedying the problems outlined in this chapter, we have found agreement between the results of this analysis and the CLAS *g1c* analyses to be quite good, as demonstrated in Chapter 6. Of all of the effects investigated in this chapter, only the start counter's effect on triggering and the resulting start counter simulation for Monte Carlo cause a systemaitc shift in differential cross section results.

We performed checks of *g11a*'s self-consistency by comparing acceptance-corrected yields from independent CLAS sectors. A slight dicrepancy between the acceptance-corrected yields of sector 5 was remedied by a cut on track polar angle in the lab frame. After this cut is applied, results from individual sectors agree quite well, indicating that our acceptance calculation is satisfactory.

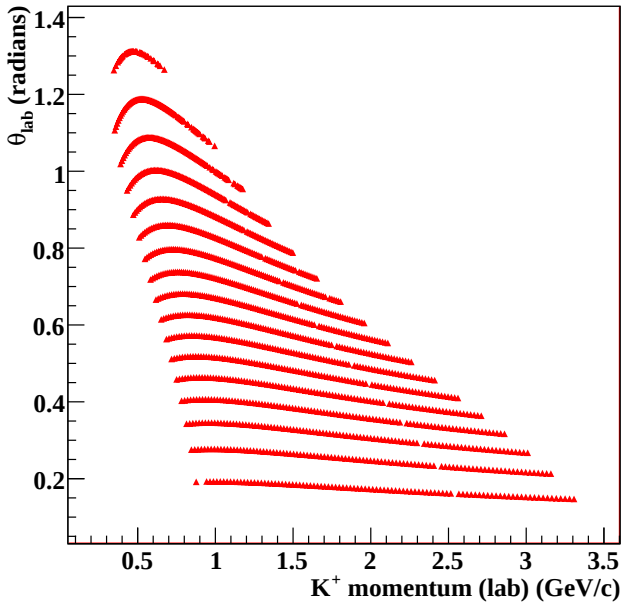

(a)

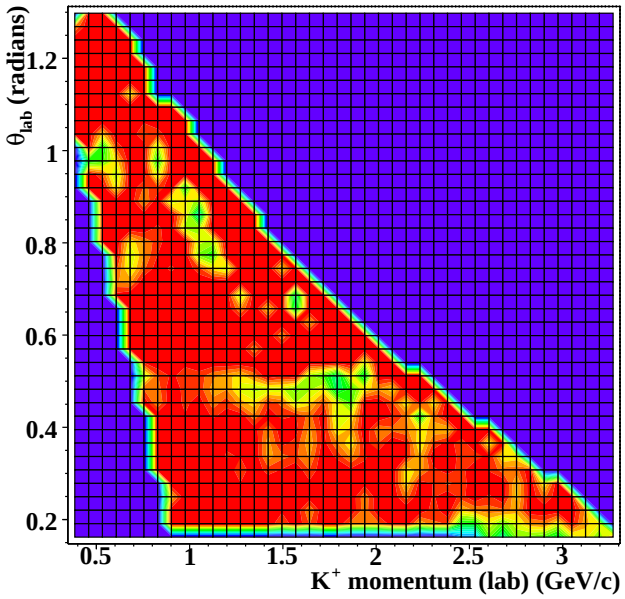

(b)

Figure 7.8: Shown above are differential cross section values versus K^+ production angle and track momentum in the lab frame. Figure (a) shows the location of differential cross section points. Figure (b) shows the ratio of the sector 5 cross section to the combined cross section from the other sectors. The scale of (b) shows a ratio of 1.0 in red and fades to a ratio of 0.4 in green.

Chapter 8

Partial Wave Analysis of $\gamma p \to K^+\Lambda$

.

In Chapter 6, we presented differential cross section and recoil polarization measurements for the $\gamma p \to K^+\Lambda$ reaction in the energy range 1.62 GeV $\leq \sqrt{s} <$ 2.84 GeV. By comparing these results with previous measurements, we have shown that the *g11a* results represent the most precise characterization of this reaction to date. In this chapter, we take our analysis a step further and investigate the physical processes by which the $K^+\Lambda$ system is photoproduced. We separate these production mechanisms into two types: non-resonant production (t- and u-channel processes) and resonant production (s-channel processes). In §8.2, we examine the non-resonant contributions to this reaction by developing our own t-channel model motivated by previous studies. In the sections that follow, we perform a partial wave analysis via binned χ^2 fits to *g11a* differential cross section and recoil polarization measurements and *g1c* beam-recoil polarization measurements. We have isolated two $\sqrt{s}$ regions in which we find interesting s-channel contributions. In this chapter, we present our in-depth studies of possible N^* states in these regions.

To investigate the presence of excited nucleon intermediate states in our reaction, we use the *mass-independent* partial wave analysis technique. In §5.6.4, we described the form of s-channel amplitudes used for this analysis. One factor in the calculation these amplitudes is the Feynman propagator which describes the transition amplitude for an intermediate particle to propagate between the two vertices in an s-channel diagram. To calculate the total probability for a given process, one must evaluate the propagator at all values of the exchanged momenta. By binning our data finely in $\sqrt{s}$, we are able to approximate the amplitudes in each bin by evaluating their propagator at the bin centroid. We then determine the contributions of the individual s-channel waves in each narrow $\sqrt{s}$ bin independently. No *a priori* assumptions need be made about the s-dependence (and thus the mass-dependence) of the partial waves. After analyzing all bins independently, s-channel contributions in neighboring bins can be compared, and s-dependence to may be noted.

All fits presented in this chapter are binned χ^2 fits. As discussed in Chapter 5, we employ binned fitting as a way of including other measurements in our partial wave analysis, namely the *g1c* double polarization observables C_x and C_z. In §8.1 of this chapter, we present our method of projecting these observables from our amplitudes. Recall that binned fitting differs from unbinned likelihood fitting in that its fewer number of degrees of freedom typically limits fit stability. For all fits we present in this chapter, this compromise of stability is mitigated by multiple fit iterations (at least twenty, unless otherwise noted) with randomized initial values for fit parameters.

8.1 Fitting to Double-Polarization Observables: C_x and C_z

In 2006, the CLAS Collaboration published measurements of $\gamma p \to K^+\Lambda$ beam-recoil polarization asymmetries, C_x and C_z, from the *g1c* dataset [83]. The use of circularly polarized photons (*i.e.*

polarization aligned or anti-aligned with the direction of photon momentum) for the *g1c* run period allowed for a net polarization of the Λ in the production plane. To add analysis power to our partial wave analysis, we use these data as well as our *g11a* results.

For what follows, we define a coordinate system in which $\hat{z}$ lies along the photon direction and $\hat{y}$ along $\vec{k}\times\vec{q}$, where $\vec{k}$ and $\vec{q}$ are the photon and K^+ momenta in the center-of-mass frame. Thus, $\hat{x}$ lies in the production plane, perpendicular to $\vec{k}$. C_x and C_z characterize the transfer of photon helicity to the Λ hyperon in the $\hat{x}$- and $\hat{z}$-directions, respectively. For a given circular beam polarization, $P_\odot \in [-1.0, +1.0]$, and Λ polarization vector, $\vec{P}_Y = (P_{Yx}, P_{Yy}, P_{Yz})$, C_x and C_z are defined by [84]

$$P_{Yx} = P_\odot C_x \tag{8.1a}$$

$$P_{Yz} = P_\odot C_z. \tag{8.1b}$$

The y-component of $\vec{P}_Y$ is simply the recoil polarization of the Λ discussed in §6.3. The *g1c* analysis produced C_x and C_z measurements at 160 $(\sqrt{s}, \cos\theta^K_{CM})$ values encompassing the energy range 1.652 GeV$\leq \sqrt{s} \leq$2.473 GeV.

Though we cannot measure C_x and C_z directly with *g11a* we want the results of our partial wave analysis to be consistent with these measurements. To include C_x and C_z in our PWA, we must calculate the double-polarization observables from our amplitudes in the same manner as we have P_Λ at all $(\sqrt{s}, \cos\theta^K_{CM})$ values for which there is a *g1c* result. Here we use the same technique put forth in §6.3.1 (see section for notation conventions). For a given $(\sqrt{s}, \cos\theta^K_{CM})$ value, we calculate the amplitudes $A^{m_\gamma, m_i, M}_{\gamma p\to K^+\Lambda}$, describing the $\gamma p \to K^+\Lambda$ process where m_γ ,m_i, and M are the spin-projections along the z-axis of the photon, target proton, and Λ, respectively. We construct the two-component wave-function for the process as

$$\psi(\sqrt{s}, \cos\theta^K_{CM}) = \begin{pmatrix} A^{m_\gamma, m_i, M=+}(\sqrt{s}, \cos\theta^K_{CM}) \\ A^{m_\gamma, m_i, M=-}(\sqrt{s}, \cos\theta^K_{CM}) \end{pmatrix}. \tag{8.2}$$

We then use the Pauli spin matrices, σ_x and σ_z, from eq. (5.3) to compute P_{Yx} and P_{Yz} for a given m_γ and m_i:

$$P_{Yx}(m_\gamma, m_i) = \frac{1}{\zeta}\psi^\dagger\sigma_x\psi \tag{8.3a}$$

$$P_{Yz}(m_\gamma, m_i) = \frac{1}{\zeta}\psi^\dagger\sigma_z\psi, \tag{8.3b}$$

where $\zeta = \psi^\dagger\psi$ is included for normalization. In extracting P_Λ, we summed over the initial target and photon spin polarizations. To project out C_x and C_z, we select a particular photon polarization, $m_\gamma = +$, and sum over the target polarization states. By selecting $m_\gamma = +$, we simulate a fully polarized photon beam, thus setting $P_\odot = +1.0$ in eq. (8.1). Including the sum over target polarizations gives the full expressions

$$P_{Yx} = C_x = \frac{1}{N}\sum_{m_i}\left(A^{*+,m_i,+}A^{+,m_i,-} + A^{*+,m_i,-}A^{+,m_i,+}\right) \tag{8.4a}$$

$$P_{Yz} = C_z = \frac{1}{N}\sum_{m_i}|A^{+,m_i,+}|^2 - |A^{+,m_i,-}|^2, \tag{8.4b}$$

where

$$N = \sum_{m_i}\sum_{M}|A^{+,m_i,M}(\sqrt{s}, \cos\theta^K_{CM})|^2. \tag{8.5}$$

To include C_x and C_z in binned χ^2 fits, we calculate amplitudes for all included production mechanisms (s-, t-, and u-channel) for each of $(\sqrt{s}, \cos\theta^K_{CM})$ for which there is a *g1c* measurement. We use the statistical errors associated with the points from the *g1c* C_x and C_z results to calculate the χ^2 from fit parameters as prescribed by eq. (5.24). We then combine the χ^2 values from differential cross section, recoil polarization, and double polarization points as described by eq. (5.31).

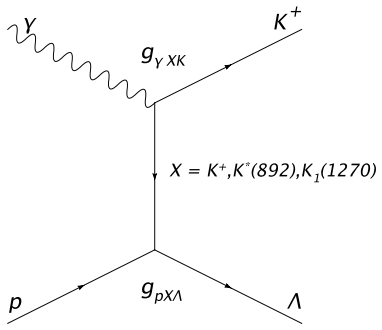

Figure 8.1: The diagram shown represents t-channel exchange of particle type $X = K, K^*(892), K_1(1270)$. The amplitudes could be parametrized by individual coupling factors, g, for each vertex. Each process considered in this analysis, however, has at least one experimentally undetermined vertex (see text). (Image produced by [77].)

8.2 Fitting Non-resonant Processes

To ensure a reliable treatment of resonant contributions to our channel, a refined understanding of the role of non-s-channel (*i.e.* t- and u-channel) production mechanisms is necessary. Several analyses have considered these non-resonant contributions to $K^+\Lambda$ photoproduction in the past. For the most part, these previous analyses have relied upon differential cross section measurements well-above ($\sqrt{s} \geq 4.0$ GeV [28]) or within ([25, 7]) the resonance region. Though these analyses have produced interesting results regarding N^* states coupling to $K^+\Lambda$, neither of these approaches is ideal. Furthermore, limited data on the Λ recoil polarization was available to these analyses. The differential cross section and recoil polarization measurements presented in Chapter 6 of this analysis allow us to study non-resonant contributions to the reaction in a $\sqrt{s}$ region that is dominated by t-channel processes (2.700 GeV $\leq \sqrt{s} <$ 2.840 GeV), yet not far-removed from the resonance region.

Motivated by previous theoretical work [25, 7], we seek to describe the non-resonant contributions to the $\gamma p \to K^+\Lambda$ differential cross section and polarization observables with a small set of t-channel diagrams. For t-channel processes, we choose the exchanges of the the three lowest-mass strange mesons for which a strangeness-conserving coupling to γK^+ is possible. These are the K^+, $K^*(895)$, and $K_1(1270)$ mesons with $J^P = 0^-$, 1^-, and 1^+, respectively. Full expressions for these amplitudes are given in §5.6.3. Here, we only comment that each t-channel amplitude has three free fit parameters: a coupling constant for the entire diagram and two form factor mass cut-offs, one associated with each vertex. We require these parameters to be the same across all values of $\sqrt{s}$. Furthermore, we require the mass cut-offs for corresponding vertices in the K^* exchange to be the same for electric and magnetic multipoles (*i.e.* $\Lambda^E_{\gamma K^* K} = \Lambda^M_{\gamma K^* K}$ and $\Lambda^E_{pK^*\Lambda} = \Lambda^M_{pK^*\Lambda}$), as the radius of the interaction should be mostly dependent only upon particle types. (Recall from §5.6.3 that for the K^* exchange, both electric and magnetic couplings are possible.) These constraints leave a total of ten free t-channel parameters. Unfortunately, none of these parameters has been measured experimentally. While measurements for coupling constants corresponding to particular vertices in the t-channel diagrams are known (*e.g.* the $K^* \to \gamma K^+$ decay width has been measured), none of the diagrams we consider has been fully characterized. Each of the diagrams contains (at least) one unknown vertex coupling (see Figure 8.1). As such, we fold both vertex factors into a single overall scale factor for each diagram and use this scale factor as a free fit parameter.

As was discussed in §6.2.3, the prominent peak in the $K^+\Lambda$ differential cross section at forward angles ($\cos\theta^K_{CM} > 0.4$) and high center-of-mass energies ($\sqrt{s} > 2.700$ GeV) suggests the dominance of t-channel exchange processes in this kinematic region. Our method for determining a suitable model

of non-resonant production is to perform a binned χ^2 fit to our *g11a* measurements of the differential cross section and recoil polarization in this range. Once the parameters of the t-channel amplitudes have been determined ("locked") in these high-$\sqrt{s}$ bins, we use the implicit $\sqrt{s}$-dependence of these amplitudes to extrapolate the non-resonant contributions into the resonance region.

We began by fitting the t-channel amplitudes described above to the *g11a* measurements in the range 2.700 GeV$\leq \sqrt{s} <$2.840 GeV and forward angles defined by $t > -2.1$ GeV$^2/c^2$. Here, the range in t assures that we consider only points in the forward peak in the differential cross section. The results of this fit produced a good description of our high-energy data; however, extrapolation into the resonance region showed questionable results. Calculating the differential cross section as prescribed by eq. (5.30) showed the non-resonant contribution to be larger than the measured differential cross section by a factor of ≈ 2 in the near-threshold bins ($\sqrt{s} < 1.7$ GeV). Though this effect could be mitigated by destructive interference between the t-channel diagrams and any s-channel diagrams present in this region, it is unlikely that this is an accurate description of the non-resonant production.

In light of this, we adapted our fitting technique to include the near-threshold differential cross section, recoil polarization and *g1c* double polarization measurements. In addition to the high-$\sqrt{s}$ data, we fit to measurements in the range 1.620 GeV$\leq \sqrt{s} <$1.680 GeV. In this low-$\sqrt{s}$ region, we cannot assume that production is dominated by t-channel mechanisms; we must add some s-channel contribution to fit the data reliably. Of the known N^* resonances, the PDG lists only the $S_{11}(1650)$ as having a "likely to certain" coupling to $K^+\Lambda$; experiments have shown convincing evidence of the $S_{11}(1650)$ decaying to $K^+\Lambda$ [5]. Furthermore, the PDG lists the $S_{11}(1650)$ as having been observed in several photoproduction experiments. We thus include the s-channel $J^P = \frac{1}{2}^-$ wave in our fit in the near-threshold bins. Inclusion of this wave adds a total of twelve parameters (one scale and one phase parameter for each of the six low-$\sqrt{s}$ bins) to the fit.

It should be noted that because we choose to fit only the forward peak of the high-energy data where we are certain t-channel is the dominant production mechanism, performing a reliable fit of any u-channel diagrams is difficult. u-channel production presents a characteristic backwards peak in the differential cross section. While there is such a peak in the backwards direction in the differential cross section for 2.60 GeV$\leq \sqrt{s} <$2.77 GeV, it is small in comparison to the forward peak. In this model of non-resonant production, we omit any u-channel processes.

Results of the non-resonant fit in a few characteristic bins are presented in Figure 8.2. Parameters returned by the fit are provided in Table 8.1. The fit describes the general trend in the differential cross section at high energies and forward angles. The t-channel amplitudes are not able to match the shape of the Λ recoil polarization data at high $\sqrt{s}$, although the magnitude of P_Λ is approximated by the fit. This suggests that our fit lacks some s-channel diagram with which the t-channel can interfere. In the low-$\sqrt{s}$ bins, addition of the $J^P = \frac{1}{2}^-$ resonance allows for a very good description of the differential cross sections. However, structures in the polarization observables C_x and C_z that are not reproduced by the fit again suggest that more waves are needed to describe the data in this region.

Though the non-resonant fit cannot reproduce some features of the data at high energies, it represents the best fit that can be made without making assumptions about s-channel states at high-$\sqrt{s}$. Unlike the low-$\sqrt{s}$ region, where experiment suggests the presence of a certain resonant state, there is no clear choice for the addition of s-channel waves in this region. Figure 6.23 shows that the recoil polarization for forward angles and $\sqrt{s} > 2.2$ GeV is approximately constant and of the magnitude given by the model. Thus, we accept the model for use in our scans for s-channel resonances. In §8.7, we show that the results of our partial wave analysis are robust by using a different t-channel model.

Finally, we show the intensities of the non-resonant model and individual t-channel mechanisms as they project to the lower-$\sqrt{s}$ region in Figure 8.3. These are compared to the total cross section in each bin. Note that inclusion of the near-threshold bins in the non-resonant fit has yielded a more reasonable magnitude for the non-resonant terms at threshold.

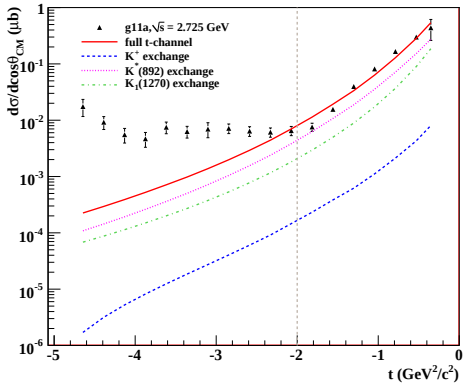

(a)

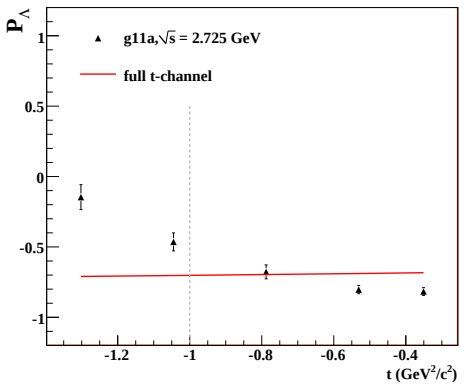

(b)

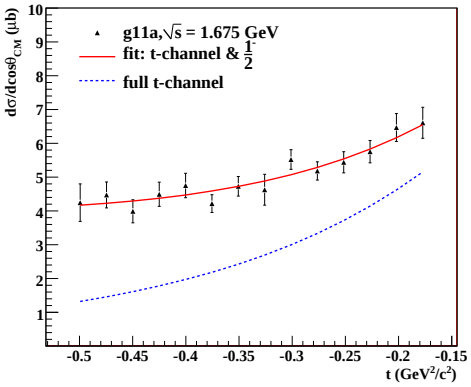

(c)

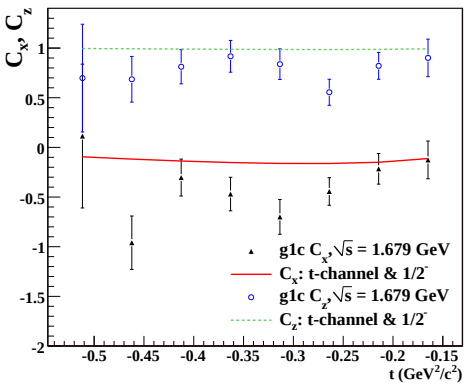

(d)

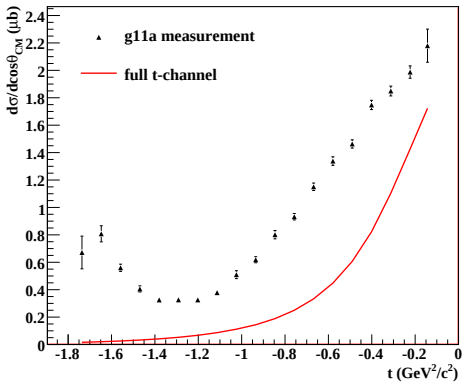

(e)

Figure 8.2: Results of the non-resonant model fits. Figure (a) shows the differential cross section data (black) and fit (solid red) for the $\sqrt{s} = 2.725$ GeV bin. The strengths of the individual t-channel diagrams are shown as well. Points included in the fit are those to the right of the dashed vertical line ($t > -2.0$). Figure (b) shows the P_Λ data (black) and fit result (red) in the $\sqrt{s} = 2.725$ GeV bin. Figure (c) shows the differential cross section data (black), total fit (red), and t-channel contribution in the $\sqrt{s} = 1.675$ GeV bin. Figure (d) shows the fit to C_x and C_z in the $\sqrt{s} = 1.675$ GeV bin. Differential cross section data (black) and t-channel contributions (red) projected into the $\sqrt{s} = 2.005$ GeV bin are shown in Figure (e).

Fit parameter	Description	Value
$\Lambda_{pK^+\Lambda}$	form factor cut-off for $pK^+\Lambda$ vertex	0.715
$\Lambda_{\gamma K^+K^+}$	form factor cut-off for γK^+K^+ vertex	0.713
g_{K^+}	coupling factor for K^+ exchange	325
$\Lambda_{pK^*\Lambda}$	form factor cut-off for $pK^*\Lambda$ vertex	0.690
$\Lambda_{\gamma K^*K^+}$	form factor cut-off for γK^*K^+ vertex	0.691
$g^E_{K^+}$	coupling factor for K^+ exchange (electric coupling)	77.4
$g^E_{K^+}$	coupling factor for K^+ exchange (magnetic coupling)	49.5
$\Lambda_{pK_1\Lambda}$	form factor cut-off for $pK_1\Lambda$ vertex	0.902
$\Lambda_{\gamma K_1K^+}$	form factor cut-off for γK_1K^+ vertex	0.902
g_{K_1}	coupling factor for K_1 exchange	20.7

Table 8.1: Table t-channel of fit parameters from non-resonant fit

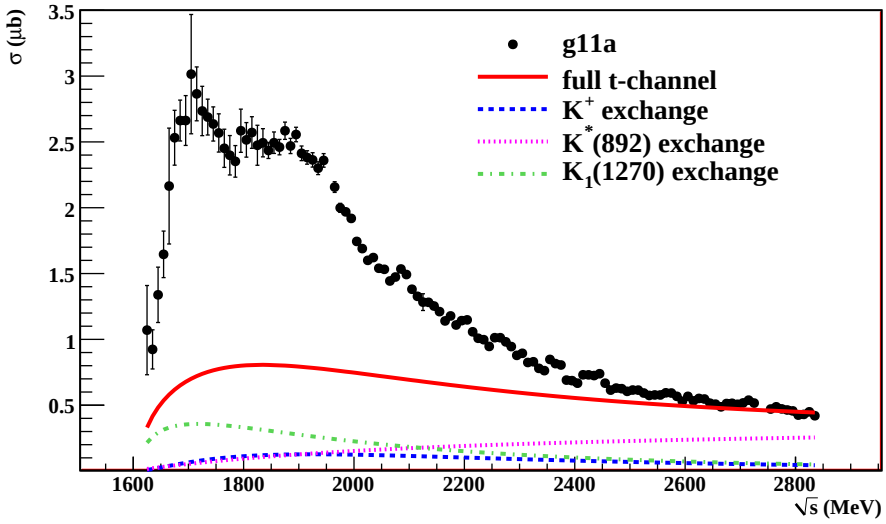

Figure 8.3: Shown above are comparisons of the total cross section (black) and projections of the full non-resonant model (red) and its component production mechanisms.

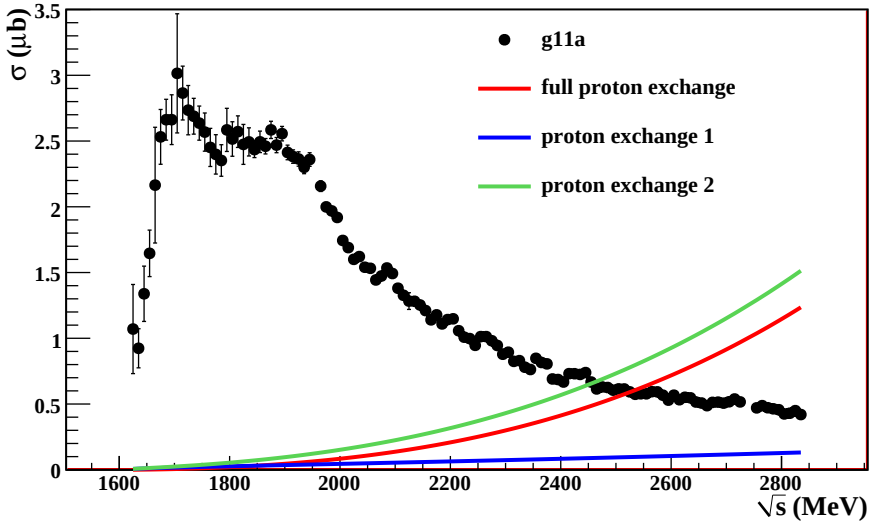

Figure 8.4: Shown above are intensities of the s-channel proton exchange amplitudes with $g_{K\Lambda N}$ =9.0. At low $\sqrt{s}$, the contribution to the cross section is negligible. At high $\sqrt{s}$, the contribution is roughly double the total cross section.

We also comment on the s-channel proton exchange amplitude described in eq. (5.66). Inclusion of this diagram in partial wave analyses has historical roots which reach back to initial theoretical studies of strangeness photoproduction in the 1960's [24]. Recall that this amplitude is dependent upon the coupling strength of the $K\Lambda N$ vertex expressed as the parameter $g_{K\Lambda N}$. Previous analyses have included this diagram in large-scale partial-wave fits treating $g_{K\Lambda N}$ as a free parameter. However, the resulting values of $g_{K\Lambda N}$ show a large dependence upon the resonant partial waves that are included in these fits; literature generally suggests values between $g_{K\Lambda N}$ =11.5 [78] and $g_{K\Lambda N}$ =3.65 [7]. To investigate the contribution of this process to our partial wave analysis, we used a conservative estimate for this coupling, $g_{K\Lambda N}$ =9.0 and calculated this amplitude at all values of $(\sqrt{s}, cos\theta^K_{CM})$ for which we have a differential cross section measurement. Figure 8.4 shows the total cross section resulting from this diagram as a function of $\sqrt{s}$. We see that at low $\sqrt{s}$, the total cross section from the proton exchange is negligible. At high $\sqrt{s}$, however, this diagram's intensity is a factor of two larger than the total cross section, placing this amplitude in doubt. The effect at high $\sqrt{s}$ could possibly be mitigated by the inclusion of a form factor in the proton exchange amplitude (as in eq. (5.53)). In the absence of a clear method for including this amplitude, we omit it in this study, noting that its contribution in the region of interest to our partial-wave analysis ($\sqrt{s}$ <2.1 GeV) is small.

8.3 Single Partial Wave Scans

The starting point of our Partial Wave Analysis is a scan across all $\sqrt{s}$ bins for single s-channel states. In each $\sqrt{s}$ bin, we performed a binned χ^2 fit to all available observables ($d\sigma$, P_Λ, and the $g1c$ C_x and C_z results) with our non-resonant model and one s-channel wave. Parameters of the s-channel amplitudes were left free, while the t-channel parameters were locked to the values presented in the last section. All s-channel amplitudes with $\frac{1}{2} \leq J \leq \frac{9}{2}$ (both parities) were investigated. Multiple fit iterations ($\geq$ 15 iterations) were run in each $\sqrt{s}$ bin with randomized initial values for free

parameters to ensure fit reliability (*i.e.* that fits are not simply in local minima).

Plots showing the χ^2 per number of degrees of freedom (ndf) in each $\sqrt{s}$ bin are provided in Figure 8.5. Here, the number of degrees of freedom is given as the number of measurement points included in the fit minus the number of free fit parameters. For bins in which we fit to all four measurements, the number of degrees of freedom is generally between 45 and 55. Recall that for binned χ^2 fits, a χ^2/ndf value of 1 signifies a suitable description of the data, whereas larger values indicate poorer fits.

Several overall features of single-wave χ^2's are worthy of comment. First, no single fit produces a χ^2/ndf that suggests that the data is described by the t-channel model and a single s-channel wave. Several waves show low χ^2's in specific $\sqrt{s}$ regions, such as the $\frac{3}{2}^+$ fit at $\sqrt{s} \approx 1.8$ GeV and the $\frac{1}{2}^-$ fit at threshold. Because the fits are not ideal, we do not assume that the single-wave description is correct in any $\sqrt{s}$ range. In light of this, we use the single-wave fit results as a suggestion of possible of possible s-channel contributions. Definite enhancements in the χ^2/ndf are apparent for the $J^P = \frac{1}{2}^-$ wave at threshold, $\sqrt{s} \approx 1.8$ GeV, and $\sqrt{s} \approx 1.92$ GeV. The $J^P = \frac{3}{2}^+$ wave displays the best χ^2/ndf over the range 1.82 GeV$\leq \sqrt{s} <$ 1.95 GeV. In the region above $\sqrt{s} = 2.0$ GeV, the $J^P = \frac{7}{2}^+$ shows the best χ^2/ndf.

8.4 Two Partial Wave Scans

In the last section, we showed that that no $\sqrt{s}$ region can be described by a single s-channel partial wave and our non-resonant model. We next performed χ^2 fits to $d\sigma$, P_Λ, and double-polarization observables with the non-resonant model and two s-channel partial waves. Fits using each of the 45 two-wave combinations (for $J \leq \frac{9}{2}$) were performed. Once again, multiple fit iterations were run with randomized initial values for s-channel fit parameters. Plots of the χ^2/ndf in each $\sqrt{s}$ bin in each fit are provided in Figures 8.6 and 8.7. For the two-wave scans, however, we find it instructive to also consider the individual intensity of each s-channel wave used. Figures 8.8 and 8.9 show the intensities of each wave given by fits with the waves indicated.

To determine whether a certain partial wave's contribution in a given $\sqrt{s}$ region is valid, we consider that wave's intensity when fit with all other waves. If the wave shows appreciable intensity regardless of what wave it is paired with, it is a good indication that the fit requires that partial wave. If, however, the wave's intensity is quenched when fit with any other wave, it's contribution to the reaction in that range is in doubt. As an example, we consider the $J^P = \frac{1}{2}^-$ wave in the range 1.8 GeV$\leq \sqrt{s} <$2.0 GeV. In this range, the intensity of the wave is sizable in all fits, suggesting that the presence of the $\frac{1}{2}^-$ wave is likely. Conversely, the $\frac{3}{2}^-$ partial wave shows a large intensity in the same range when fit with the $\frac{1}{2}^+$, $\frac{5}{2}^+$, or $\frac{7}{2}^-$ waves, but its intensity is quenched when fit with the $\frac{3}{2}^+$ or $\frac{1}{2}^-$ waves. The $\frac{1}{2}^+$ and $\frac{9}{2}^\pm$ (not shown) show no appreciable intensity at any $\sqrt{s}$ values in all fits.

From these results, we make several observations which will guide our Partial Wave Analysis and lead to more focused investigation in the following sections. In the near-threshold region ($\sqrt{s} <$1.8 GeV), the $\frac{1}{2}^-$ and $\frac{3}{2}^+$ partial waves show the most dominant intensities. This is consistent with previous analyses of the $\gamma p \to K^+\Lambda$ reaction. The PDG lists a four-star $J^P = \frac{1}{2}^-$ N^* resonance at 1.65 GeV, with a three-star rating for coupling to $K^+\Lambda$, as well as a four-star $\frac{3}{2}^+$ state at 1.72 GeV with a two-star coupling to $K^+\Lambda$. Also in this region, the $\frac{3}{2}^-$ partial wave shows intensity (albeit smaller) in all fits. It is encouraging that the PDG also lists coupling of $K^+\Lambda$ to the $D_{13}(1700)$ with a two-star rating. Though its intensities do not suggest a large contribution in these bins, we see that the presence of a $\frac{5}{2}^+$ partial wave is suggested by the χ^2/ndf from the two-wave scan with $\frac{5}{2}^+$ and $\frac{3}{2}^+$ waves. The PDG also lists a two-star coupling to $K^+\Lambda$ for the four-star $F_{15}(1680)$ state. In §8.5, we investigate this region with these four partial waves as primary candidates.

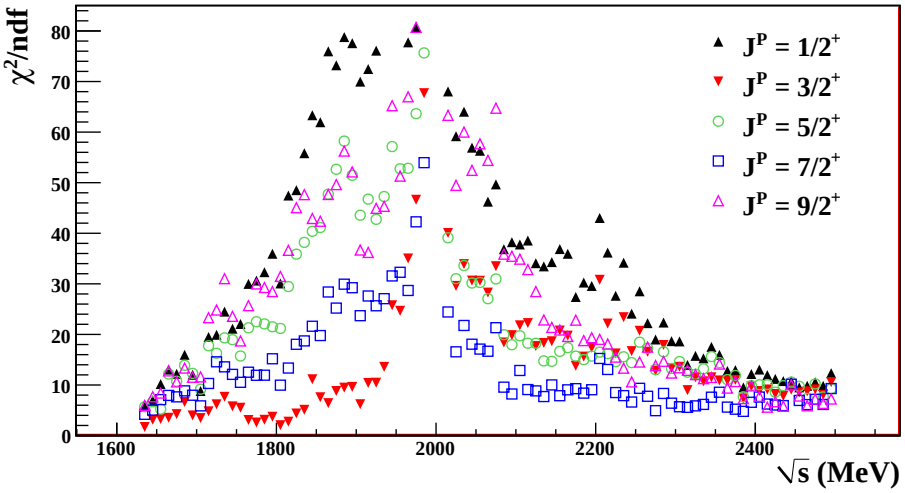

(a)

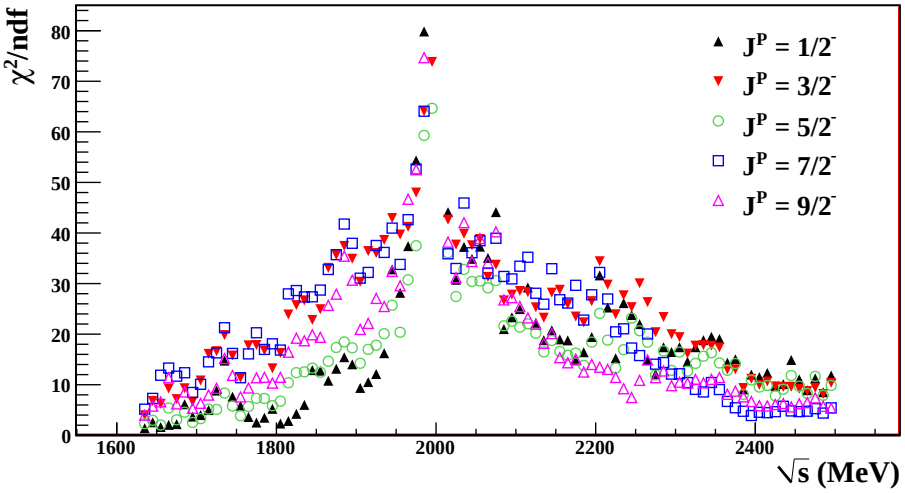

(b)

Figure 8.5: The plots above show the χ^2/ndf from fits of the non-resonant model and a single s-channel partial wave. Figures (a) and (b) show positive and negative parity waves, respectively. The vertical scale is the same in both plots.

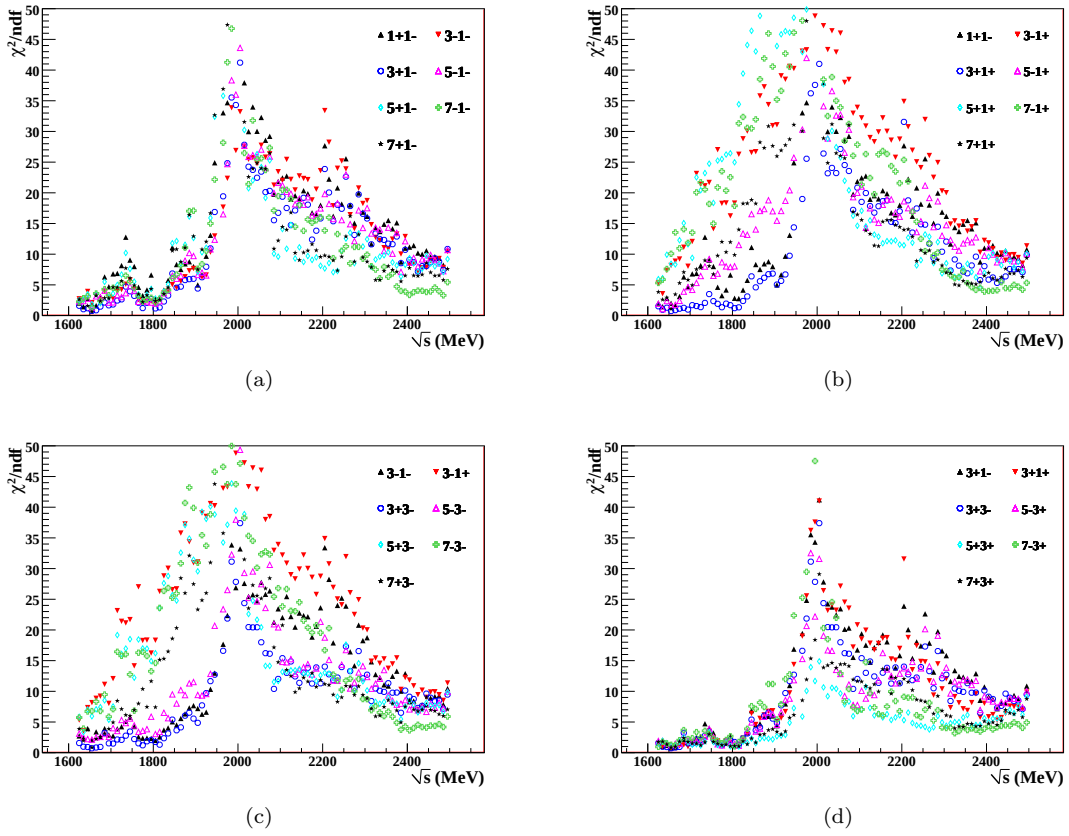

(a) (b)

(c) (d)

Figure 8.6: Shown above are the χ^2/ndf in each $\sqrt{s}$ bin for each two-wave scan. Each plot shows all fits involving a certain partial wave. Figures (a), (b), (c), and (d) show all fits which include the $\frac{1}{2}^-$, $\frac{1}{2}^+$, $\frac{3}{2}^-$, and $\frac{3}{2}^+$ waves, respectively.

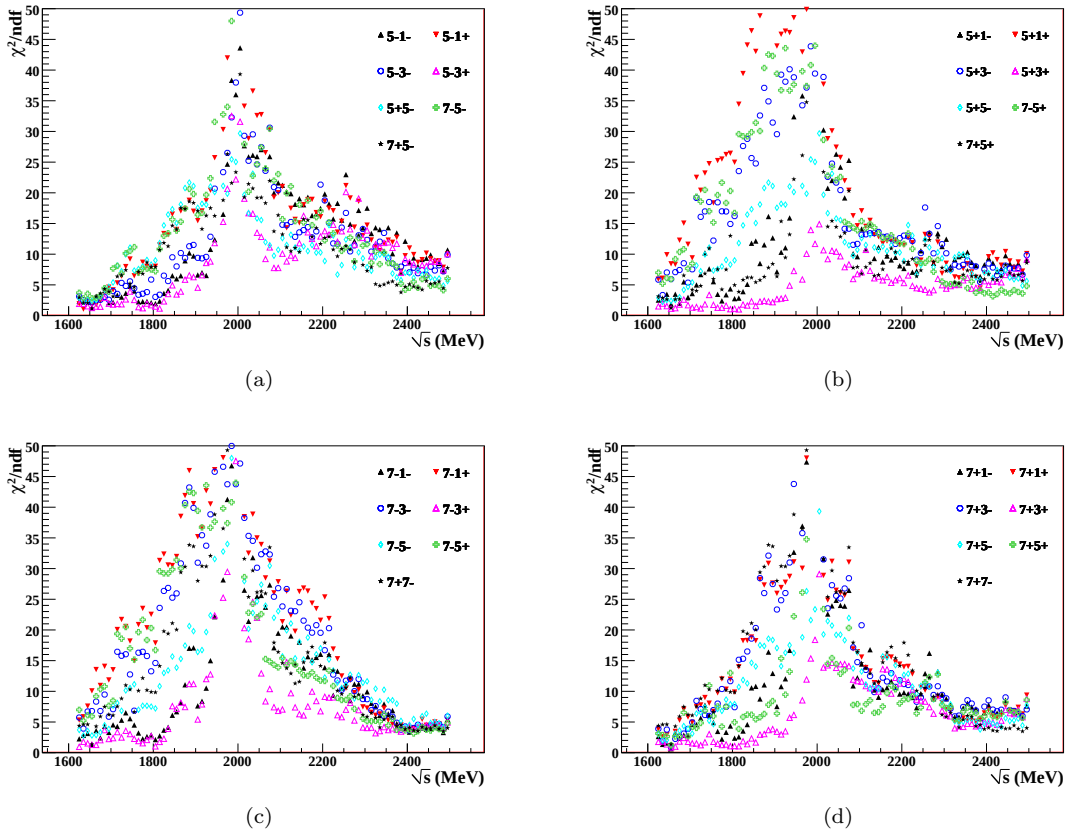

Figure 8.7: Shown above are the χ^2/ndf in each $\sqrt{s}$ bin for each two-wave scan. Each plot shows all fits involving a certain partial wave. Figures (a), (b), (c), and (d) show all fits which include the $\frac{5}{2}^-$, $\frac{5}{2}^+$, $\frac{7}{2}^-$, and $\frac{7}{2}^+$ waves, respectively.

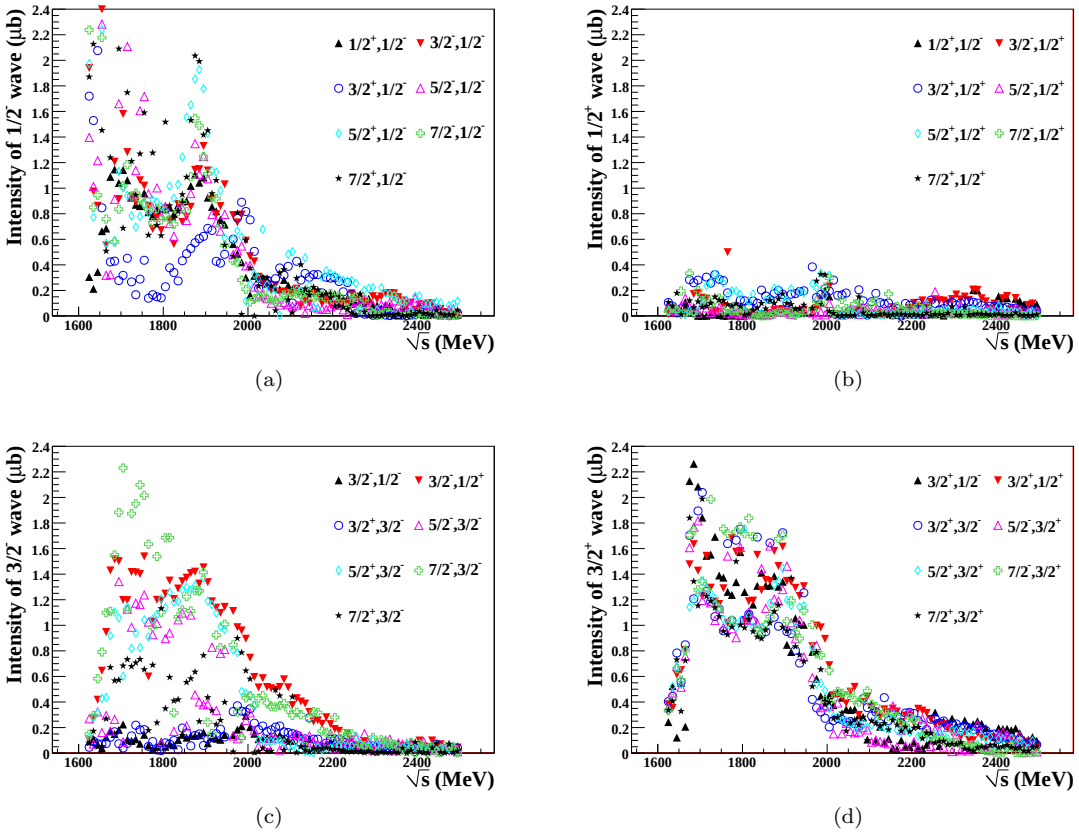

Figure 8.8: Shown above are the intensities of individual s-channel waves when fit with the wave combinations indicated. For example, plot (a) shows the intensity of the $\frac{1}{2}^-$ partial wave when fit with each of the other waves indicated. From this plot, we see that the $\frac{1}{2}^-$ wave has a sizable intensity at $\sqrt{s} = 1.9$ GeV in all fits, but its intensity is the least when paired with the $\frac{3}{2}^+$ partial wave. Shown are the $J^P = \frac{1}{2}^-$ (a), $\frac{1}{2}^+$ (b), $\frac{3}{2}^-$ (c), and $\frac{3}{2}^+$ (d) partial waves.

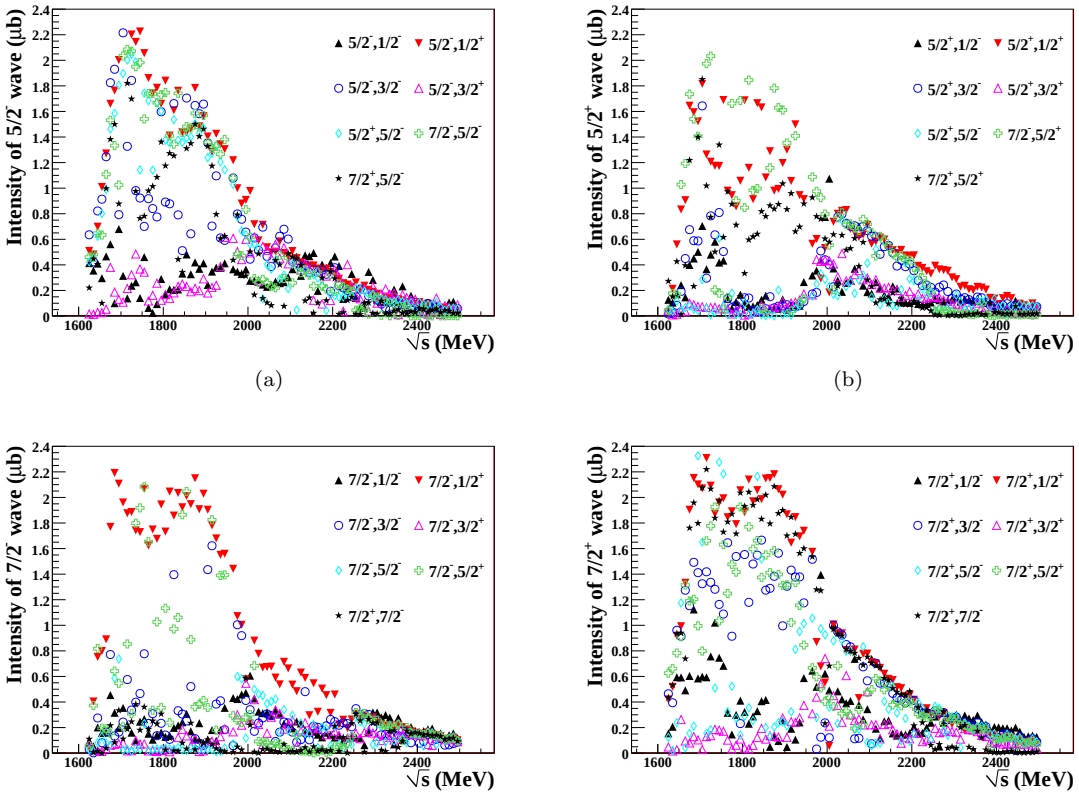

Figure 8.9: Shown above are the intensities of individual s-channel waves when fit with the wave combinations indicated. For example, plot (b) shows the intensity of the $\frac{5}{2}^+$ partial wave when fit with each of the other waves indicated. From this plot, we see that the $\frac{5}{2}^+$ wave displays a significant intensity at $\sqrt{s} = 2.0$ GeV in all fits, but its intensity is lowest when paired with the $\frac{5}{2}^-$ partial wave. Shown are the $J^P = \frac{5}{2}^-$ (a), $\frac{5}{2}^+$ (b), $\frac{7}{2}^-$ (c), and $\frac{7}{2}^+$ (d) partial waves.

In the region 1.8 GeV$\leq \sqrt{s} <$2.0 GeV, we see a large intensity in the $\frac{1}{2}^-$ partial wave. Though the PDG lists the one-star $S_{11}(2080)$ as the only known resonance in this region, Quark Model calculations predict a resonance with these quantum numbers at 1.945 GeV. Furthermore, the $\frac{3}{2}^+$ partial wave shows a very large intensity in this region. The PDG lists one two-star $\frac{3}{2}^+$ state at 1.9 GeV and Quark Model calculations predict four states in this range. We also observe intensities in the $\frac{5}{2}^\pm$ and partial waves. In §8.6, we investigate these waves' contributions to the reaction in this energy range.

8.5 Near-Threshold Bins: $\sqrt{s} < 1.8$ GeV

Guided by the two-wave scans in the last section, we began our investigation of the near-threshold bins ($\sqrt{s} <$1.8 GeV) with the $\frac{5}{2}^+$ and $\frac{3}{2}^+$ waves. Recall that this pair produced the best χ^2/ndf in the low-$\sqrt{s}$ range. In Figure 8.10(a), we present the cross section results from this fit. In the two-wave scans, all s-channel parameters were allowed to vary freely with no bin-to-bin constraints. This is encouraging when we consider the previously observed states in this region. The PDG lists the four-star $F_{15}(1680)$ and $P_{13}(1720)$ states in this region, both of which have a two-star-rated coupling to $K^+\Lambda$. Each of these observed states is associated with a state from Quark Model calculations [2].

8.5.1 Multipole Coupling Constraint

Following the work of [4], we may impose a further physical constraint on the s-channel waves via their multipole couplings. In §5.6.4, we discussed the role of the multipole couplings of γp to J^P states. Recall that in the $L-S$ basis, three Lorentz-invariant amplitudes ($A_1^{J^P}$, $A_2^{J^P}$, $A_3^{J^P}$) can be constructed describing $\gamma p \to J^P$, but that these amplitudes are not linearly-independent functions of production angle; two of the three amplitudes differ only by an energy factor and cannot be distinguished at a fixed value of s. In order to avoid this ambiguity, we construct our amplitudes in the multipole basis where the amplitudes $A_E^{J^P}$ and $A_M^{J^P}$ characterize the electric and magnetic couplings of the γp and J^P states. In §6.1.1, we presented our parametrization of s-channel amplitudes in terms of the angle θ_{J^P}, which dictates the ratio of electric and magnetic couplings (see eq. (6.4)). The $L-S$ and multipole bases are related by

$$\cos(\theta_{J^P}(s))A_E^{J^P} + \sin(\theta_{J^P}(s))A_M^{J^P} = \alpha A_1^{J^P} + \beta A_2^{J^P} + \gamma A_3^{J^P}, \tag{8.6}$$

where α, β, and γ are the (s-independent) couplings to the $L-S$ basis amplitudes. If the full J^P amplitude describes a single state, it is shown that the multipole production angle obeys the relationship [4]

$$\theta_{J^P}(s) = \tan^{-1}\frac{\gamma}{\alpha + \beta/E_{\gamma CM}^2} = \tan^{-1}\frac{1}{a + b/E_{\gamma CM}^2}, \tag{8.7}$$

where we have written $\alpha/\gamma = a$ and $\beta/\gamma = b$. We may constrain the multipole angles, $\theta_{\frac{5}{2}^+}$ and $\theta_{\frac{3}{2}^+}$, across all bins in our fit to the form of eq. (8.7), replacing each wave's 18 individual θ fit parameters (one in each $\sqrt{s}$ bin) with two fit parameters representing a and b in eq. (8.7).

We then fit all bins with $\sqrt{s} < 1.8$ GeV simultaneously enforcing the multipole constraint. Results of this fit are shown in Figure 8.10(b). Notice that the intensity profiles of both waves is changed dramatically from the previous fit. It is interesting to note that both waves now display intensity shapes that are suggestive of the mass and width parameters as listed in the PDG. Figure 8.11 shows the χ^2/ndf in each bin from the two fits. The added multipole constraint limits the fit's ability to describe the data, producting a much worse χ^2/ndf in these bins.

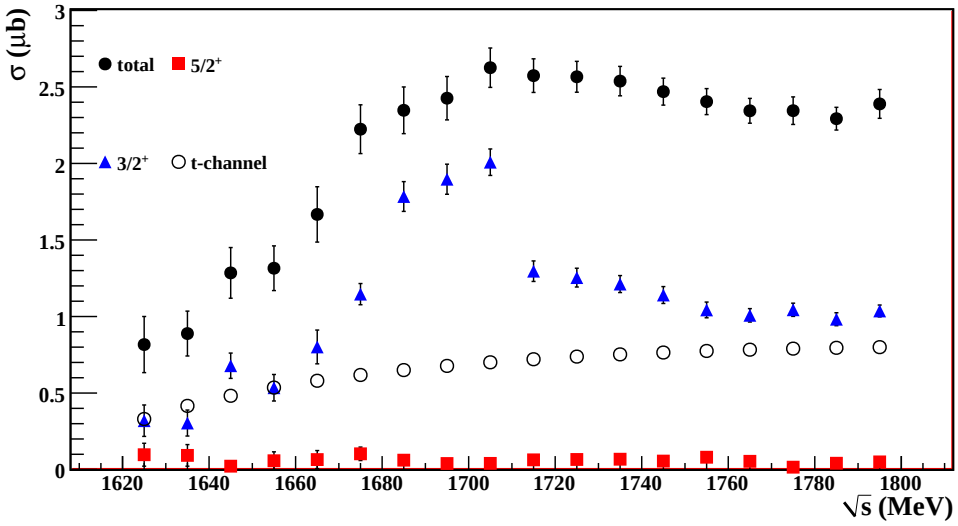

(a)

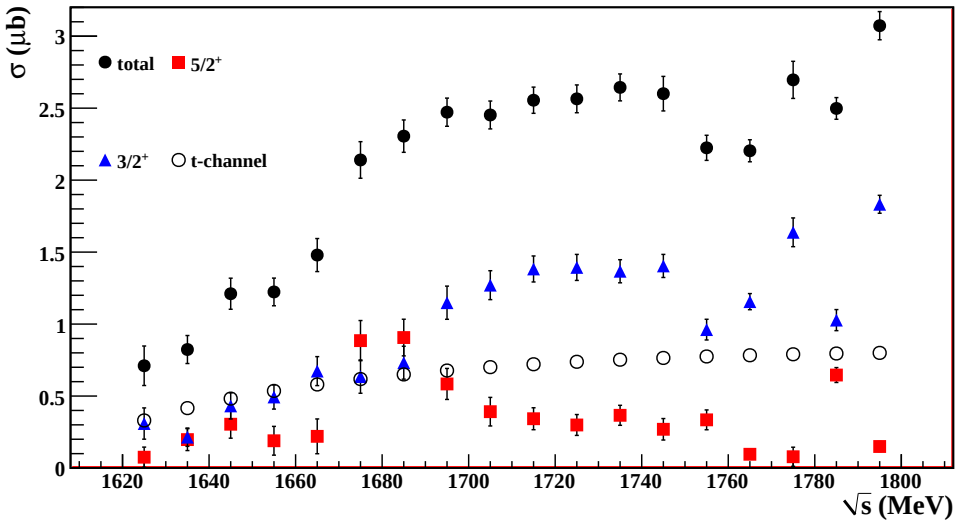

(b)

Figure 8.10: Shown above are results from fits of the non-resonant model and s-channel $J^P = \frac{5}{2}^+$ and $\frac{3}{2}^+$ waves in the $\sqrt{s}$ <1.8 GeV bins . Figure (a) shows intensities from a fit with the multipole coupling parameters of both waves free. Figure (b) shows intensities from a fit with multipole parameter constrained across all bins according to eq. (8.7). All error bars represent MINUIT errors.

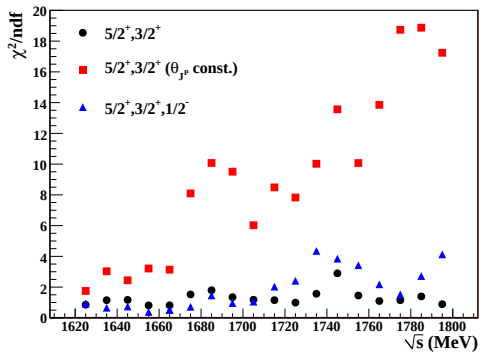

Figure 8.11: The plot above shows chi^2/ndf for each of the indicated fit schemes. The fit with $\frac{5}{2}^+$ and $\frac{3}{2}^+$ waves with multipole couplings free (black circles) produces a fair χ^2/ndf. Constraining the multipole parameter for both of these waves (red squares) reduces their ability to describe the data. Also shown is the fit with $\frac{5}{2}^+$, $\frac{3}{2}^+$, and $\frac{1}{2}^-$ waves with $\theta_{\frac{5}{2}^+}$ and $\theta_{\frac{3}{2}^+}$ constrained.

8.5.2 Fit with $J^P = \frac{5}{2}^+$, $\frac{3}{2}^+$, and $\frac{1}{2}^-$ Partial Waves

In light the inability of two waves to describe the data, we sought to add a third wave to the fit at threshold. By inspecting the intensities from the two-wave scans, we see that the $\frac{1}{2}^-$ partial wave is a good candidate; it shows sizable intensity in all two-wave scans in this energy range. Furthermore, the PDG lists a state with these quantum numbers, the four-star $S_{11}(1650)$, with a three-star-rated coupling to $K^+\Lambda$. We thus performed a fit with the $\frac{5}{2}^+$, $\frac{3}{2}^+$, and $\frac{1}{2}^-$ partial waves in bins with $\sqrt{s} < 1.8$ GeV. In this fit, we again imposed the multipole constraint of eq. (8.7) to $\theta_{\frac{5}{2}^+}$ and $\theta_{\frac{3}{2}^+}$. Recall from §5.6.4 that the $J = \frac{1}{2}$ amplitudes have only an electric or magnetic coupling. Thus, no further constraint is applied to the $\frac{1}{2}^-$ wave. The intensities resulting from this fit are displayed in Figure 8.12. We see that the $\frac{1}{2}^-$ is the dominant wave in this fit, and that its shape is suggestive of the four-star $S_{11}(1650)$ state. The $\frac{5}{2}^+$ and $\frac{3}{2}^+$ waves mainain the shapes that were seen in Figure 8.10(b), but their intensities are now decreased in magnitude. The χ^2/ndf from this fit is displayed in Figure 8.11. We see that addition of the $\frac{1}{2}^-$ wave has greatly improved the description of the data.

Further evidence of the presence of resonant states in this region is given by the difference in the phase parameters for pairs of partial waves. Figure 8.13 shows the phase differences, $\Delta\phi = \phi_{J_1^{P_1}} - \phi_{J_2^{P_2}}$, for each pair of waves. If we assume that each of the waves is describing a single resonant state, we can calculate the amplitude for each of the waves using a constant-width Breit-Wigner given by

$$BW(s) = \frac{m\Gamma}{s - m^2 + im\Gamma}, \tag{8.8}$$

where m and Γ are the mass and width of the resonance. The Breit-Wigner describes the s-dependence the of the propagator of each resonant amplitude. For each resonance, we can then calculate the Breit-Wigner phase, given by

$$\alpha(s) = \tan^{-1}\left(\frac{-m\Gamma}{s - m^2}\right). \tag{8.9}$$

For two overlapping resonant states, j and k, with different quantum numbers, the Breit-Wigner

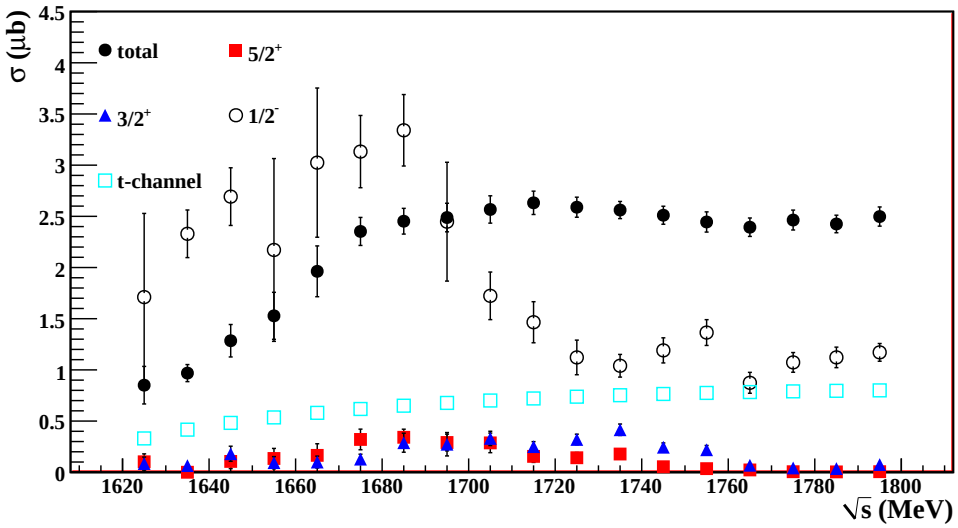

(a)

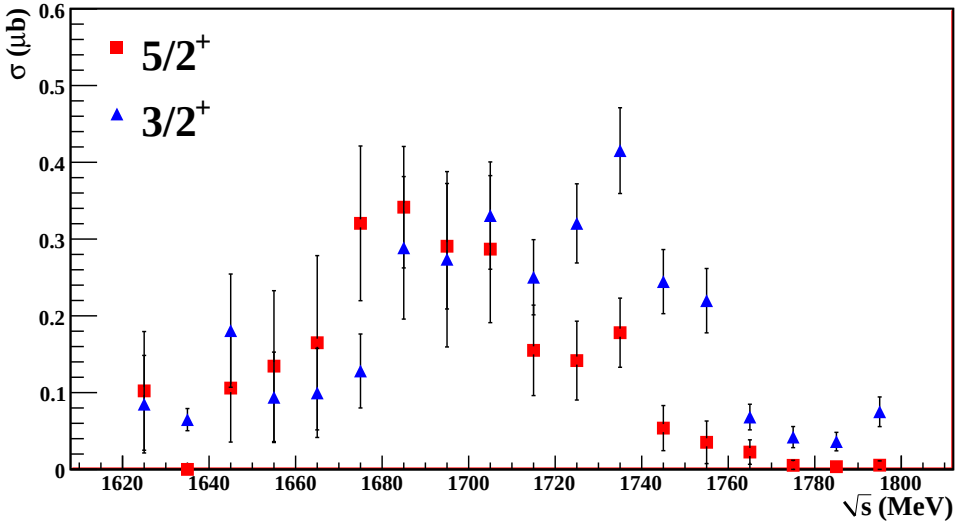

(b)

Figure 8.12: Shown in (a) and (b) are intensities from fits to $\sqrt{s}$ <1.8 GeV bins of the non-resonant model and s-channel $J^P = \frac{5}{2}^+$, $\frac{3}{2}^+$, and $\frac{1}{2}^-$ waves. The multipole coupling parameters of the $J^P = \frac{5}{2}^+$ and $\frac{3}{2}^+$ waves were constrianed in this fit. The scale is increased in Figure (b) to show the shape of the $J^P = \frac{5}{2}^+$ and $\frac{3}{2}^+$ waves' intensities.

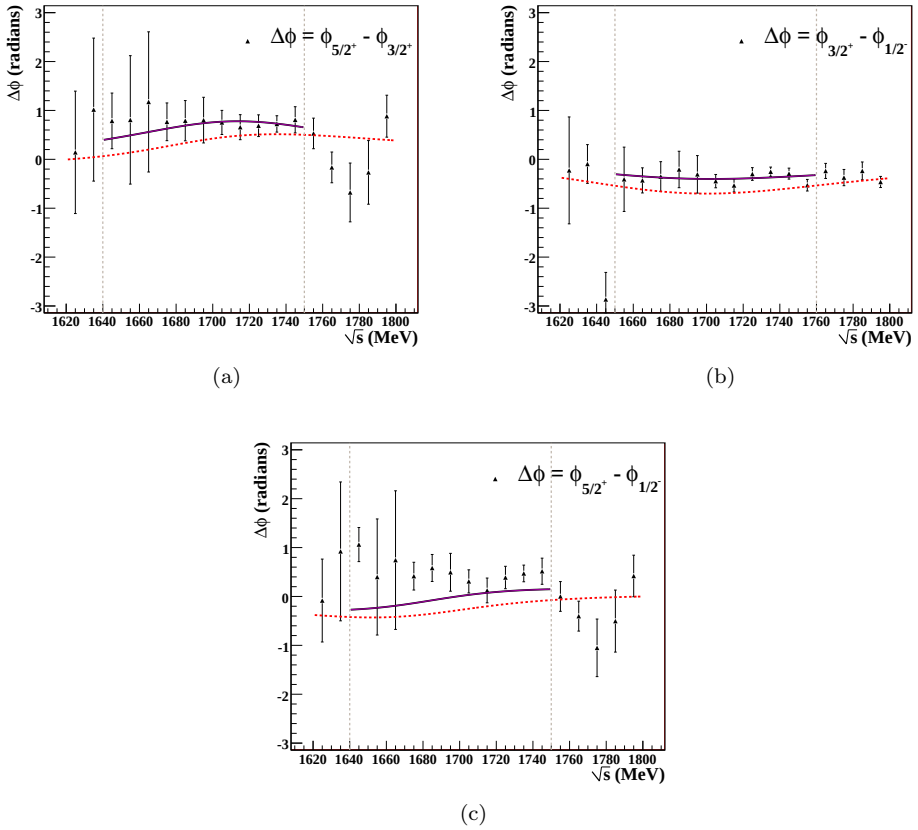

Figure 8.13: Shown above are the phase differences for each pair of s-channel waves in the fit with $\frac{5}{2}^+$, $\frac{3}{2}^+$, and $\frac{1}{2}^-$. The relevant waves are listed on each plot. Dashed red curves represent the theoretical phase motion using PDG average mass and width parameters. The solid magenta curves represent a fit of the theoretical phase motion allowing mass and width parameters within PDG limits.

phase difference is given by

$$\begin{aligned} \Delta\phi(s) &= \alpha_j - \alpha_k \\ &= \tan^{-1}\left(\frac{-m_j\Gamma_j}{s-m_j^2}\right) - \tan^{-1}\left(\frac{-m_k\Gamma_k}{s-m_k^2}\right). \end{aligned} \tag{8.10}$$

To apply this theoretical phase motion to a pair of waves, we must identify a $\sqrt{s}$ region in which both show appreciable intensity. For example, the phase difference between the $\frac{5}{2}^+$ and $\frac{3}{2}^+$ waves is given in Figure 8.13(a). We see that both of these waves display appreciable intensity in the $\sqrt{s}$ range 1.64 GeV to 1.75 GeV. The phase difference in this region shows a smooth trend similar in shape to the theoretical phase motion given by the PDG average mass and width values for the $F_{15}(1680)$ and $P_{13}(1720)$ states (shown by the dashed red curve). If we allow the mass and width values of both states to vary within the ranges listed by the PDG, we may fit eq. (8.10) to the observed phase differences. This fit (solid magenta curve) gives a mass of 1680 MeV and width of 140 MeV for the $\frac{5}{2}^+$ wave and a mass of 1739 MeV and width of 150 MeV for the $\frac{3}{2}^+$ wave with a

χ^2/ndf of 0.20. This match of phase difference and the shape of the intensities for both of the waves is consistent with the contribution of both the $F_{15}(1680)$ and $P_{13}(1720)$ in $K^+\Lambda$ photoproduction.

For the $\frac{3}{2}^+$ and $\frac{1}{2}^-$ waves, we identify sizable intensities in the $\sqrt{s}$ region from 1.65 GeV to 1.76 GeV. The phase difference for these two waves (Figure 8.13(b)) is smooth and shows a shape and magnitude similar to the theoretical phase motion for the $P_{13}(1720)$ and $S_{11}(1650)$ states. Once again, we allow the mass and width parameters to vary within the limits quoted by the PDG and fit eq. (8.10) to the measured phase difference. This fit gives masses and widths of 1700 MeV and 218 MeV for the $\frac{3}{2}^+$ wave and 1660 MeV and 185 MeV for the $\frac{1}{2}^-$ wave with a χ^2/ndf of 0.95. Once again, phase differences and intensity profiles are consistent with the contribution of the $P_{13}(1720)$ and $S_{11}(1650)$ N^* states to $K^+\Lambda$ photoproduction.

Finally, we consider the phase difference between the $\frac{5}{2}^+$ and $\frac{1}{2}^-$ waves shown in Figre 8.13(c). For these waves, we indentify the range 1.64 GeV$\leq \sqrt{s} <$1.75 GeV as having significant contributions from both waves. The phase motion is once again smooth in this region, however, its shape and scale differ from the Breit-Wigner description. The PDG mass and width ranges for the $F_{15}(1680)$ and $S_{11}(1650)$ states do not allow a good fit of eq. (8.10) to the observed phase differences. The inability of the Breit-Wigner phase difference to describe the data could be explained by multiple S_{11} states in this energy range. Previous analyses [36] have considered the contribution of the four-star $S_{11}(1535)$ state to the $K^+\Lambda$ channel. If this coupling is non-negligible in this region, the single-state Breit-Wigner hypothesis is inapplicable. Thus, we comment only that the phase differnce between these two waves displays interesting phase motion and warrants further study as more data becomes available.

Fianlly, we provide in Figure 8.14 plots of this fit's description of the differential cross section and polarization data in this region. We see that fits in most bins are very good (as demonstrated by the χ^2/ndf in Figure 8.11). As shown for the $\sqrt{s}$ =1.735 GeV and 1.765 bins, the fit has trouble reproducing the recoil polarization at backward angles. This could suggest the presence of u-channel contributions which our non-resonant model lacks. This mismatch could also suggest the presence of further N^* states in this energy regime. This is not surprising, as two other states have been observed to couple to $K^+\Lambda$ with two-star ratings. Motivated by this, we have attempted to add the $\frac{3}{2}^-$ and $\frac{5}{2}^-$ states to the fit, but results were inconclusive. Here, we simply comment that the three waves used do not provide a full description of the data and we do not rule out the possibility of other states.

8.6 $J^P = \frac{1}{2}^-$ and $\frac{3}{2}^+$ Partial Waves: 1.8 GeV$\leq \sqrt{s} <$2.0 GeV

The two-wave scans in §8.4 suggest the contribution of the $\frac{1}{2}^-$ and $\frac{3}{2}^+$ partial waves in the range 1.8 GeV$\leq \sqrt{s} <$2.0 GeV. We see from Figure 8.8 that both waves show sizable intensity in this range when fit with any other wave. The intensity of the $\frac{3}{2}^+$ wave is consistent in all fits; it displays wide contribution from threshold to $\sqrt{s} \approx$2.0 GeV. The $\frac{1}{2}^-$ intensity shows a very interesting shape; its intensity when fit with the $\frac{3}{2}^+$ wave has a smooth shape suggestive of a resonant state. It is important to note that in all of the two-wave scans involving the $\frac{1}{2}^-$ partial wave (excluding the fit with $\frac{3}{2}^+$), the $\frac{1}{2}^-$ wave has a larger intensity that the other partial wave for $\sqrt{s}$ in the range 1.88 GeV to 1.95 GeV. This is a strong indicator of the presence of a $\frac{1}{2}^-$ state in this range.

The fit with $\frac{3}{2}^+$ and $\frac{1}{2}^-$ together shows interesting structure in both waves' intensities. Figure 8.15 shows the intensities in this range from the fit with $\frac{3}{2}^+$ and $\frac{1}{2}^-$ partial waves and the non-resonant model. All s-channel fit parameters were left free in this fit. The $\frac{3}{2}^+$ contribution to the cross section is very wide. The $\frac{1}{2}^-$ partial wave shows two peaks in this range, one at $\sqrt{s} \approx$1.9 GeV and one at $\sqrt{s} \approx$2.0 GeV.

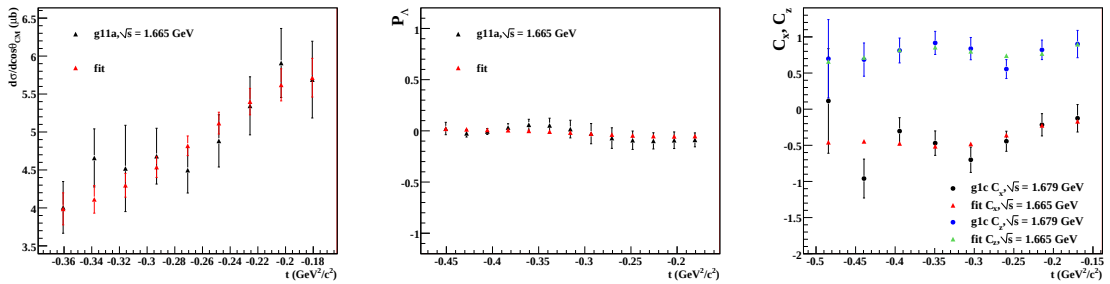

(a)

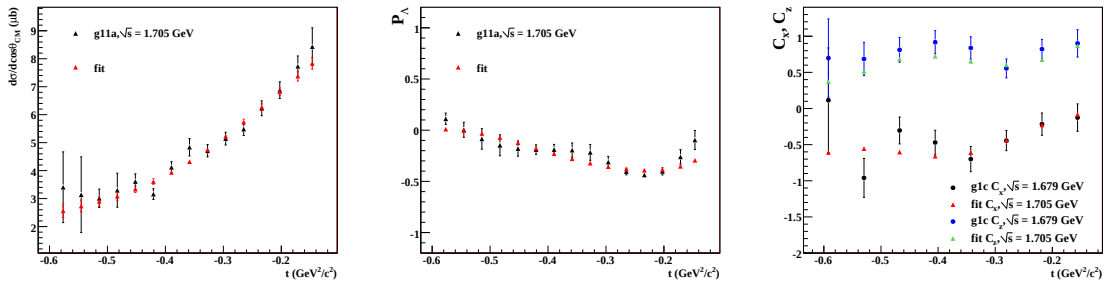

(b)

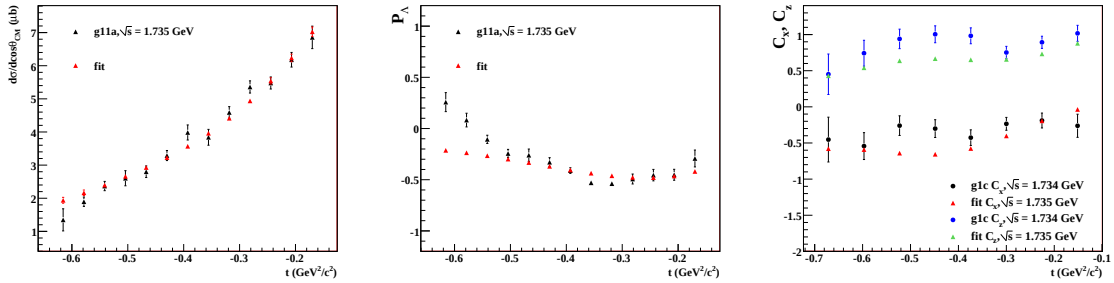

(c)

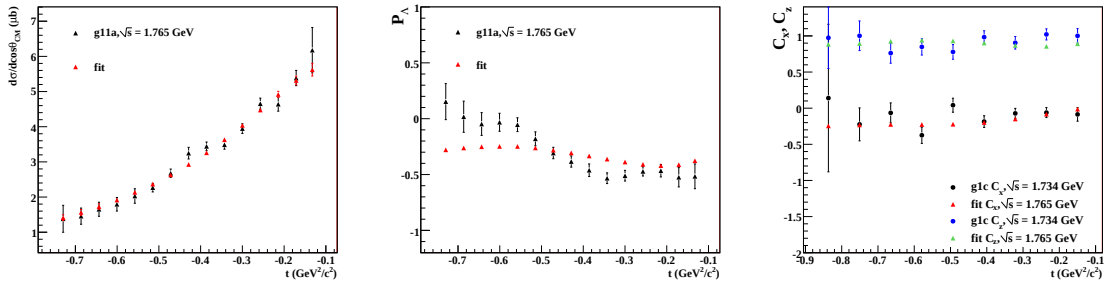

(d)

Figure 8.14: Shown above are comparisons of data and $\frac{5}{2}^+$, $\frac{3}{2}^+$, $\frac{1}{2}^-$ fit results in the $\sqrt{s}$ =1.665 GeV (a), 1.705 GeV (b), 1.735 GeV, and 1.765 GeV (d) bins. In each row, plots show $d\sigma$, P_Λ, and double-polarization observables from left to right.

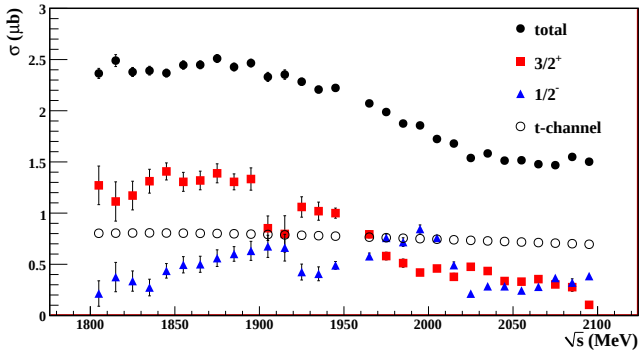

(a)

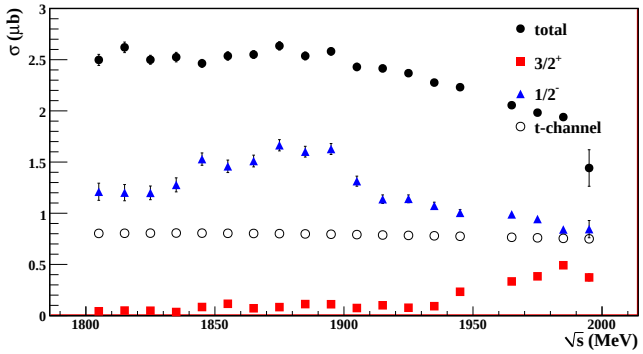

(b)

Figure 8.15: Shown in (a) are the intensities from the $\frac{3}{2}^+$ (red) and $\frac{1}{2}^-$ (blue) partial waves and the non-resonant model (open circles). All s-channel fit parameters were left free in this fit. The $\frac{3}{2}^+$ shows a broad contribution from 1.8 GeV to 2.05 GeV, while the $\frac{1}{2}^-$ wave shows a peak at 1.9 GeV and one at 2.0 GeV. Figure (b) shows the intensities from a fit of $\frac{3}{2}^+$,$\frac{1}{2}^-$ waves with $\theta_{\frac{3}{2}^+}$ constrained as in eq. (8.7).

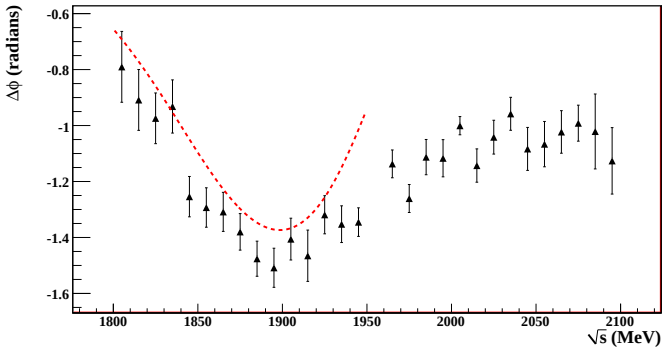

Figure 8.16: Shown above are the phase differences $\Delta\phi = \phi_{\frac{3}{2}^+} - \phi_{\frac{1}{2}^-}$ from fits with $\frac{3}{2}^+$ and $\frac{1}{2}^-$ s-channel waves and the non-resonant model. The points display interesting motion in the range 1.83 GeV to 1.92 GeV. The dashed red curve shows a theoretical phase difference for a $\frac{3}{2}^+$ state with a mass of 1850 MeV and width of 150 MeV and a $\frac{1}{2}^-$ state with mass 1950 MeV and width 100 MeV.

.

We then applied the single-state hypothesis by fitting the $\frac{3}{2}^+$ and $\frac{1}{2}^-$ waves in bins in the range 1.8 GeV$\leq \sqrt{s} <$2.0 GeV simultaneously with the $\frac{3}{2}^+$ wave's multipole parameter constrained as prescribed by eq. (8.7). We found that with this further constraint, the $\frac{3}{2}^+$ partial wave's intensity is greatly diminished in this range (see Figure 8.15(b)). This suggests that the $\frac{3}{2}^+$ contribution in this $\sqrt{s}$ range is not due to a single resonance. While the PDG lists only one such N^* state in this region, the two-star $P_{13}(1900)$, Quark Model calculations predict states at 1870 MeV, 1910 MeV, and 1950 MeV. Thus, for further fits in this region, we allow the $\frac{3}{2}^+$ multipole coupling to vary freely from bin to bin.

We now turn our attention to the peak in the $\frac{1}{2}^-$ intensity at $\sqrt{s} \approx 1.9$ GeV. We associate the $\frac{1}{2}^-$ strength for $\sqrt{s}$ in the range 1.83 GeV to 1.93 GeV with this structure. A plot of the phase differences $\Delta\phi = \phi_{\frac{3}{2}^+} - \phi_{\frac{1}{2}^-}$ is provided in Figure 8.16. The phase differences in this range display an interesting downward trend, as we would expect from $\frac{3}{2}^+$ states at $\sqrt{s} \approx 1.8$ GeV and a $\frac{1}{2}^-$ state at ≈ 1.92 GeV. For comparison, we have included in Figure 8.16 a theoretical phase difference (dashed red curve) generated assuming a $\frac{3}{2}^+$ state with a mass of 1850 MeV and width of 150 MeV and a $\frac{1}{2}^-$ state with mass 1950 MeV and width 100 MeV. The data displays a very similar trend to the curve. Because we believe there could be multiple $\frac{3}{2}^+$ states in this $\sqrt{s}$ range, however, we cannot apply the the Breit-Wigner description to interpret the phase differences between the $\frac{3}{2}^+$ and $\frac{1}{2}^-$ waves.

Figure 8.15(a) also shows a peak in the $\frac{1}{2}^-$ intensity at $\sqrt{s} \approx$2.0 GeV. However, this peak is suspicious as many of the two-wave scans show non-zero intensity at $\sqrt{s} = 2.0$ GeV. Furthermore, the single- and double-wave scans show a dramatic rise in χ^2/ndf at this $\sqrt{s}$ value. These lead us to believe that an adequate description of the data at $\sqrt{s}$ =2.0 GeV cannot be achieved with two s-channel waves alone. To investigate the validity of the $\frac{1}{2}^-$ contribution at this $\sqrt{s}$ value, we performed a series of three-wave fits in the range 1.8 GeV$\leq \sqrt{s} <$2.1 GeV. Motivated by the results of the two-wave scans, we chose the $J^P = \frac{5}{2}^\pm$ and $\frac{7}{2}^+$ waves as possible candidates. The results of a fit including $\frac{5}{2}^+$, $\frac{3}{2}^+$, and $\frac{1}{2}^-$ partial waves and the non-resonant model in the range 1.8 GeV$\leq \sqrt{s} <$2.1 GeV are

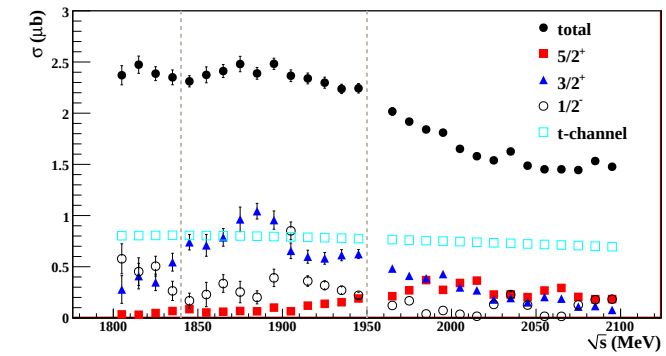

(a)

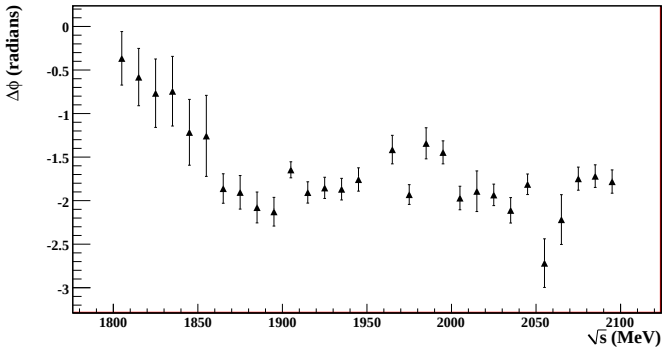

(b)

Figure 8.17: Intensities and phase differences from fit with $\frac{5}{2}^+$,$\frac{3}{2}^+$,$\frac{1}{2}^-$ waves: 1.80 GeV$\leq \sqrt{s} <$2.1 GeV. Figure (a) shows the intensities from each wave in the fit. The vertical dashed lines emphasize the shape of the $\frac{1}{2}^-$ at $\sqrt{s} \approx 1.9$ GeV. Figure (b) shows the phase difference between the $\frac{3}{2}^+$ and $\frac{1}{2}^-$ waves.

shown in Figure 8.17. We immediately see that the intensity of the $\frac{1}{2}^-$ wave at 2.0 GeV observed in Figure 8.15(a) has been replaced by the $\frac{5}{2}^+$ wave. The shape of the $\frac{1}{2}^-$ intensity at $\sqrt{s}$ =1.9 GeV remains. The shape of the $\frac{3}{2}^+$ intensity is largely unchanged. Most importantly, the addition of the third wave has not greatly affected the shape of the phase difference between the $\frac{3}{2}^+$ and $\frac{1}{2}^-$ waves in the region where the $\frac{1}{2}^-$ shows strength (1.85 GeV$\leq \sqrt{s} <$1.94 GeV).

Shown in Figure 8.17 are the results of fits with the $\frac{5}{2}^-$, $\frac{3}{2}^+$, and $\frac{1}{2}^-$ partial waves. In this fit, the $\frac{1}{2}^-$ partial wave displays a large contribution in the $\sqrt{s}$ range 1.8 GeV to 2.0 GeV. We see that the $\frac{3}{2}^+$ contribution has bee greatly reduced for $\sqrt{s} > 1.9$ GeV. In the range where the $\frac{3}{2}^+$ and $\frac{1}{2}^-$ intensities overlap, we see phase motion (Figure 8.17(b)) similar to that from previous fits.

We display the results of the fit with the $\frac{7}{2}^+$, $\frac{3}{2}^+$, and $\frac{1}{2}^-$ partial waves in this region in Figure 8.19. We find that the $\frac{1}{2}^-$ again shows a non-zero intensity at $\sqrt{s} \approx$1.9 GeV. The $\frac{3}{2}^+$ wave shows a smooth intensity in the large $\sqrt{s}$ range 1.8 GeV to 2.0 GeV, though its peak is now at roughly the same $\sqrt{s}$ value as that of the $\frac{1}{2}^-$ wave. Inspection of the phase difference between the $\frac{3}{2}^+$ and $\frac{1}{2}^-$

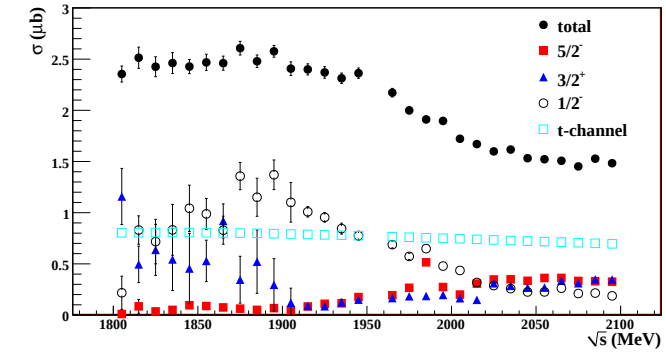

(a)

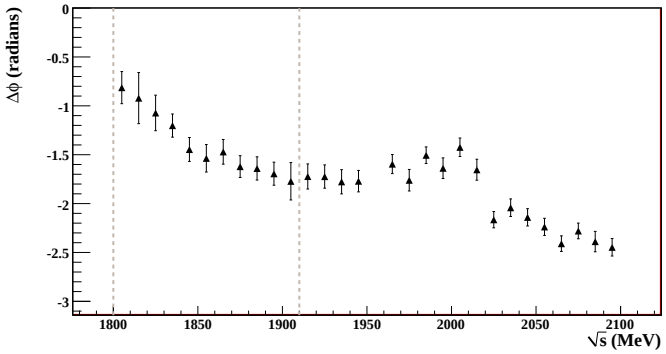

(b)

Figure 8.18: Intensities and phase differences from fit with $\frac{5}{2}^-$,$\frac{3}{2}^+$,$\frac{1}{2}^-$ waves: 1.80 GeV$\leq \sqrt{s} <$2.1 GeV. Figure (a) shows the intensities from each wave in the fit. Figure (b) shows the phase difference between the $\frac{3}{2}^+$ and $\frac{1}{2}^-$ waves. The vertical dashed lines show the region of overlap between $\frac{3}{2}^+$ and $\frac{1}{2}^-$ intensities.

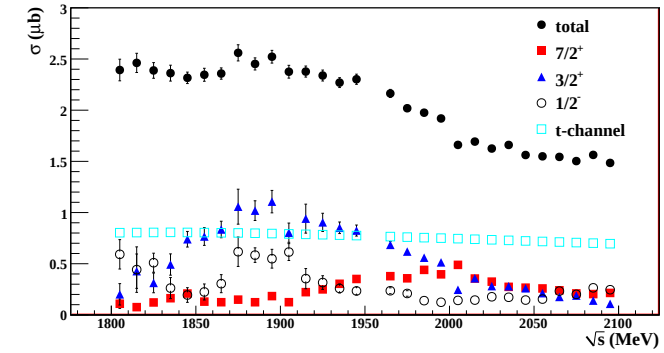

(a)

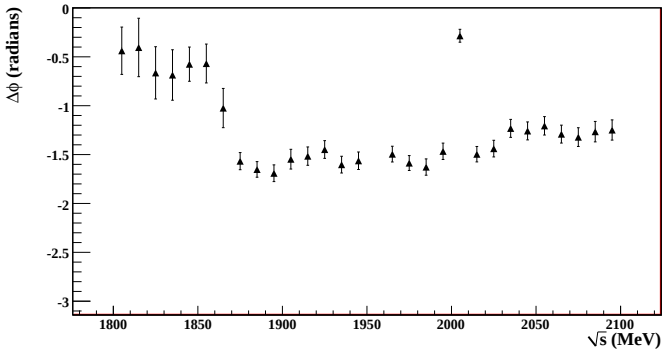

(b)

Figure 8.19: Intensities and phase differences from fit with $\frac{7}{2}^+$,$\frac{3}{2}^+$,$\frac{1}{2}^-$ waves: 1.80 GeV$\leq \sqrt{s} <$2.1 GeV. Figure (a) shows the intensities from each wave in the fit. Figure (b) shows the phase difference between the $\frac{3}{2}^+$ and $\frac{1}{2}^-$ waves.

waves in this region shows that the general trend displayed in the previous two fits is altered by the addition of the $\frac{7}{2}^+$ wave. For $\sqrt{s} >$1.87 GeV, the phase difference is relatively flat, as we expect for two Breit-Wigner resonances characterized by the same mass and width values. Once again, because of the possibility of multiple $\frac{3}{2}^+$ resonances, we cannot use the Breit-Wigner description to interpret these phase differences.

In summary, the contributions from $\frac{3}{2}^+$ and $\frac{1}{2}^-$ partial waves in the region 1.8 GeV$\leq \sqrt{s} <$2.0 GeV are difficult to observe conclusively. Both waves show sizable and consistent intensities in this region when fit with another wave. By constraining the multipole coupling of the $\frac{3}{2}^+$ partial wave and finding that its intensity in this region is greatly decreased, we ascertain that the $\frac{3}{2}^+$ partial wave does not describe a single state in this region; however, we cannot rule out the possibility of multiple resonances. The PDG lists one such state in this region, the $P_{13}(1900)$ (two-star rating), and the Constituent Quark Model predicts three states at 1870 MeV, 1910 MeV, and 1950 MeV. By investigating the presence of the $\frac{1}{2}^-$ partial wave in both two- and three-wave fits, we have shown that in all fit schemes, it displays appreciable intensity in the region 1.88 GeV$\leq \sqrt{s} <$1.95 GeV. We have observed some interesting motion in the phase difference between the $\frac{3}{2}^+$ and $\frac{1}{2}^-$ partial waves in this region, and shown that the motion is smooth and robust in reliable fits. The PDG lists

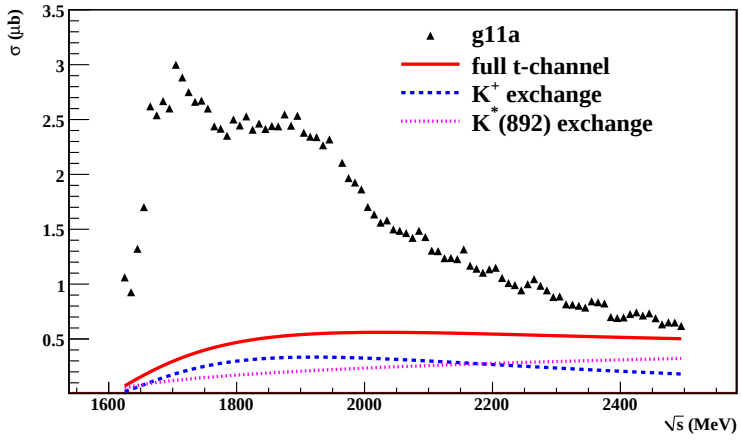

Figure 8.20: Shown above are comparisons of the total cross section (black) and projections of the alternate non-resonant model (red) and its component production mechanisms. Notice that this model has a very different contribution at low $\sqrt{s}$ than the previous non-resonant model.

the $S_{11}(2090)$ state as the only $\frac{1}{2}^-$ state observed near this region, although the Constituent Quark Model predicts a state at 1.945 GeV. Because multiple $\frac{3}{2}^+$ states may exist in this energy range, the phase motion cannot be studied with the Breit-Wigner phase difference from eq. (8.10). As such, we comment only that the observed phase motion is smooth, and that this warrants further study of these partial waves' contributions as more data becomes available.

8.7 Alternate t-channel Model

To investigate any systematic effects associated with our non-resonant model, we have tested the results of §8.5 with a second non-resonant mdoel. For this model, we used only the t-channel K and $K^*(892)$ exchange diagrams, repeating the procedure described in §8.2. The $\frac{1}{2}^-$ s-channel wave was again used in $\sqrt{s}$ bins in the range 1.62 GeV to 1.68 GeV. Figure 8.20 shows this new non-resonant model's contribution to the total cross section as a function of $\sqrt{s}$. Exclusion of the $K_1(1270)$ exchange diagram in this model yields a very different non-resonant contribution in the near-threshold bins than our primary non-resonant model.

With the alternate non-resonant model, we once again performed the three-wave fit described in §8.5.2. Figure 8.21 shows the results of this fit. We see that the intensity profile of the three s-channel waves has not been altered greatly by the alternate non-resonant model. The phase differences for all three two-wave combinations are very similar to those from the fit with the original non-resonant model, however Minuit errors on the phases are larger than in the previous fit. We thus consider our results to be robust againt variations in the non-resonant model.

8.8 Conclusions and Outlook

In this chapter, we have presented evidence for the contribution of several N^* states to the $\gamma p \to K^+\Lambda$ reaction. In the near-threshold region ($\sqrt{s}$ <1.8 GeV), we have found evidence of the previously-observed $S_{11}(1650)$, $P_{13}(1720)$, and $F_{15}(1680)$ states. Each of these states has a four-star existence rating as listed by the PDG. The PDG lists the $S_{11}(1650)$ coupling to $K^+\Lambda$ as a

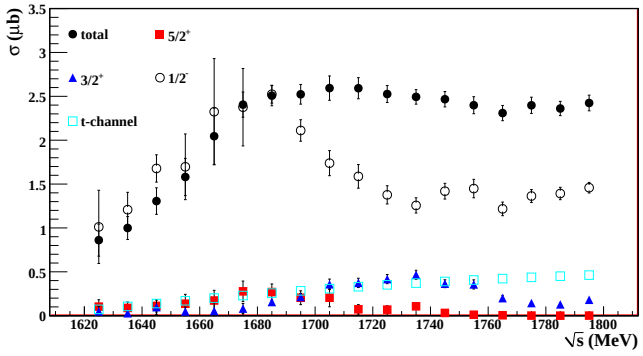

(a)

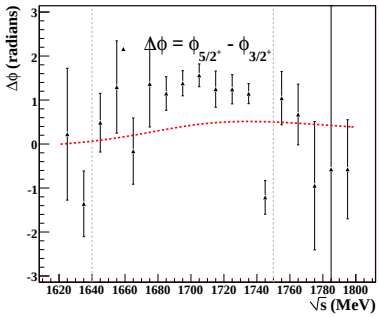

(b)

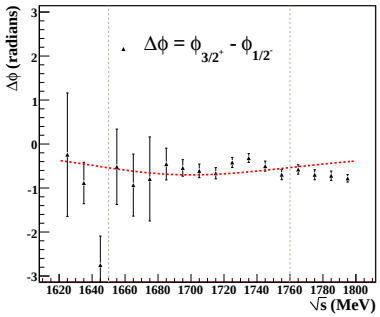

(c)

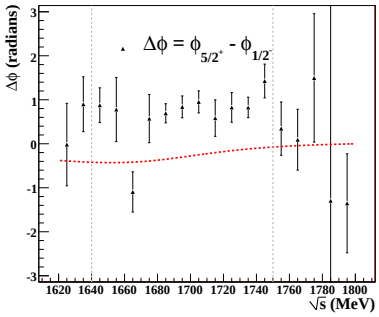

(d)

Figure 8.21: Shown above are the intensities (a) and phase differences (b-d) from the three-wave fit with alternate non-resonant model. In plots of phase differences, the vertical dashed lines indcate $\sqrt{s}$ regions considered in the previous fit. Dashed red curves indicate the theoretical phase motion given by PDG average values.

three-star phenomenon. The $P_{13}(1720)$ and $F_{15}(1680)$ couplings are both given two-star ratings. We further comment that our fit including these three partial waves does not provide a full description of the data in this $\sqrt{s}$ region. Thus, we cannot rule out further states such as the $D_{15}(1675)$ and $D_{13}(1700)$.

In the $\sqrt{s}$ region from 1.8 GeV to 2.0 GeV, we have found evidence for the existence of an S_{11} state at approximately 1.92 GeV. We ahve shown that the strength of this partial wave displays appreciable intensity in the range 1.85 GeV$\leq \sqrt{s} <$1.95 GeV in all two- and three-wave fits. We have also shown that the phase motion between this partial wave and the $\frac{3}{2}^+$ partial wave displays interesting shape in this region. This evidence is encouraging given the Quark Model prediction of an S_{11} state with mass of 1945 MeV. Previous experimental evidence for the S_{11} state in this region is dubious; the closest observed state is the one-star-rated $S_{11}(2090)$. Our investigation in this region also suggests the existence of multiple $\frac{3}{2}^+$ states in the 1.8 GeV$\leq \sqrt{s} <$1.95 GeV range. The PDG lists only one such state, the two-star $P_{13}(1900)$, whereas Quark Model calculations predict states at 1870, 1910, and 1950 MeV. Though the evidence for the S_{11} and P_{13} states presented in this chapter is not fully conclusive, it strongly suggests the presence of these states and warrants further study as more data becomes available.

Our technique for consistently combining results from different experiments into a signle partial wave analysis has proven useful. In the near future, several experiments will add previously unobserved quantities to our characterization of the $\gamma p \to K^+\Lambda$ reaction. Presently, Craig Patterson and David Ireland of Glasgow University are analyzing the photoproduction of the $K^+\Lambda$ system using the linear photon polarization data of the CLAS *g8b* dataset. This analysis will yield the measurements of O_x and O_z, the linear double-polarization observables. In late 2007, CLAS Collaboration performed the FROST (FROzen Spin Target) experiment. This experiment called for a linearly-polarized photon beam incident on a polarized hydorgen target and will allow measurement of a large number of the polarization observables which characterize this reaction. Our method allows for easy integration of these experiments' results as they become available. These added polarization measurements will provide a much more complete understanding of the $\gamma p \to K^+\Lambda$ reaction and add analyzing power to future partial analyses of this channel.

Bibliography

[1] K. Hagiwara, A. D. Martin, Daisuke Nomura, and T. Teubner. *Improved predictions for $g-2$ of the muon and $\alpha_{QED}(M_Z^2)$*. arXiv:hep-ph/0611102v3 (2007).

[2] S. Capstick and W. Roberts. *$N\pi$ decays of baryons in a relativised model*. Phys. Rev. D **47**, 1994-2010 (1993).

[3] N. Bohr. *On the Constitution of Atoms and Molecules*. Philosophical Magazine **6**, 26 (1913).

[4] M. Williams. *Measurement of Differential Cross Sections and Spin Density Matrix Elements along with a Partial Wave Analysis for $\gamma p \to p\omega$ using CLAS at Jefferson Lab*. Ph.D. Thesis, Carnegie Mellon University (2007).

[5] W.-M. Yao *et al. Review of Particle Physics*. J. Phys. G **33**, 1 (2006).

[6] S. Capstick and W. Roberts. *Strange decays of nonstrange baryons*. Phys. Rev. D **58**, 074011 (1998).

[7] R. A. Adelseck, C. Benhold, and L. E. Wright. *Kaon photoproduction operator for use in nuclear physics*. Phys. Rev. C **32**, 5 (1985).

[8] M. Bockhorst *et al. Measurement of $\gamma p \to K + \Lambda$ and $\gamma p \to K + \Sigma^0$ at photon energies up to 1.47 GeV*. Z. Phys. C **63**, 37 (1994).

[9] M. Q. Tran, *et al. Measurement of $\gamma p \to K^+\Lambda$ and $\gamma p \to K^+\Sigma^0$ at photon energies up to 2 GeV*. Phys. Lett. B **445**, 20 (1998).

[10] K. H. Glander, *et al. Measurement of $\gamma p \to K^+\Lambda$ and $\gamma p \to K^+\Sigma^0$ at photon energies up to 2.6 GeV*. Eur. Phys. J. A 19, 2 (2004).

[11] R. Bradford, *et al. Differential cross sections for $\gamma p \to K^+Y$ for Λ and Σ^0 hyperons*. Phys. Rev. C **73**, 035202 (2006).

[12] J. McNabb. *Photoproduction of Λ and Σ^0 Hyperons off Protons in the Nucleon Resonance Region using CLAS at Jefferson Lab*. Ph.D. Thesis, Carnegie Mellon University (2004).

[13] R. Bradford. *Measurement of Differential Cross Sections and C_x and C_z for $\gamma p \to K^+\Lambda$ and $\gamma p \to K^+\Sigma^0$ Using CLAS at Jefferson Lab*. Ph.D. Thesis, Carnegie Mellon University (2004).

[14] M. Sumihama, *et al. The $\gamma p \to K^+\Lambda$ and $\gamma p \to K^+\Sigma^0$ reactions at forward angles with photon energies from 1.5 to 2.4 GeV*. Phys. Rev. C **73**, 035214 (2006).

[15] K. Hicks, *et al. Measurement of the $\gamma p \to K^+\Lambda$ Reaction at Backward Angles*. Phys. Rev. C **76**, 042201 (2007).

[16] H. Thom, E. Gabathuler, D. Jones, B. D. McDaniel, and W. M. Woodward. *Polarization of Λ Hyperons from Photoproduction in Hydrogen*. Phys. Rev. Lett. **11**, 433 - 435 (1963).

[17] B. Borgia, *et al.* Nuovo Cimento **32**, 218 (1964).

[18] M. Grilli, *et al.* Nuovo Cimento **38**, 1467 (1965).

[19] D. E. Groom and J. H. Marshall. Λ *Polarization at* 90° *in* $K^+\Lambda$ *Photoproduction.* Phys. Rev. **159**, 1213-1219 (1967).

[20] T. Fujii, *et al. Photoproduction of* K^+ *Mesons and Polarization of* Λ^0 *Hyperons in the 1 GeV Range.* Phys. Rev. D **2**, 439 (1970).

[21] R. Haas, T. Miczaika, U. Opara, K. Quabach and W. J. Schwille. *Measurement of the polarization of the* Λ^0 *in the reaction* $\gamma p \to K^+\Lambda^0$ *in the resonance region.* Nucl. Phys. B137, 261-268 (1978).

[22] J. W. C McNabb, *et al. Hyperon photoproduction in the nucleon resonance region.* Phys. Rev. C 69, 042201 (2004).

[23] A. Lleres, *et al. Polarization observable measurements for* $\gamma p \to K^+\Lambda$ *and* $\gamma p \to K^+\Sigma^0$ *for energies up to 1.5 GeV.* Eur. Phys. J. A 31, 79 (2007).

[24] H. Thom. *Phenomenological Analysis of* $K^+\Lambda$ *Photoproduction.* Phys. Rev. **151**, 1322 (1966).

[25] T. Mart and C. Bennhold. *Evidence for a missing nucleon resonance in kaon photoproduction.* Phys. Rev. C **61**, 012201 (1999).

[26] C. Bennhold, H. Haberzettl, and T. Mart. *A new resonance in K+Lambda electroproduction: the* $D_{13}(1895)$ *and its electromagnetic form factors.* arXiv:nucl-th/9909022v1 (1999).

[27] S. Janssen, J. Ryckebusch, W. Van Nespen, D. Debruyne and T. Van Cauteren. *The role of hyperon resonances in* $p(\gamma, K^+)\Lambda$ *processes.* Eur. Phys. J. A**11**, 105-111 (2001).

[28] T. Corthals, J. Ryckebusch, and T. Van Cauteren. *Forward-angle* $K^+\Lambda$ *photoproduction in a Regge-plus-resonance approach.* Phys. Rev. C **73**, 045207 (2006).

[29] M. Guidal, J.-M. Laget, and M. Vanderhaeghen. *Exclusive electromagnetic production of strangeness on the nucleon: review of recent data in a Regge approach.* Phys. Rev. C **68**, 058201 (2003).

[30] D. J. Quinn, *et al. A Study Of Charged Pseudoscalar Meson Photoproduction From Hydrogen And Deuterium With 16 Gev Linearly Polarized Photons.* Phys. Rev. D **20**,1553 (1979).

[31] T. Mart, C. Bennhold, T. Haberzettl, and L. Tiator. "Kaon-MAID 2000" at http://www.kph.uni-mainz.de/MAID/kaon/.

[32] B. Saghai. *From known to undiscovered resonances.* arXiv:nucl-th/0105001 (2001).

[33] S. Janssen, J. Ryckebusch, D. Debruyne, and T. Van Cauteren. *Kaon photoproduction: Background contributions, form factors, and missing resonances.* Phys. Rev. C **65**, 015201 (2001).

[34] V. Shklyar, H. Lenske, U. Mosel. *A coupled-channel analysis of* $K\Lambda$ *production in the nucleon resonance region.* Phys.Rev. C **72**, 015210 (2005).

[35] B Juliá-Díaz, B Saghai, F. Tabakin, W.-T. Chiang, T.-S. H. Lee, and Z. Li. *Dynamical coupled-channel analysis of* $K^+\Lambda$ *photoproduction.* Nucl.Phys. A**755**, 463-466 (2005).

[36] A. V. Sarantsev, V. A. Nikonov, A. V. Anisovich, E. Klempt, and U. Thoma. *Decays of Baryon Resonances into* ΛK^+, $\Sigma^0 K^+$ *and* $\Sigma^+ K^0$. Eur. Phys. J. A **25**, 441-453 (2005).

[37] M. Battaglieri et al. *Spectroscopy of Exotic Baryons with CLAS: Search for ground and first excited states*. CLAS Analysis Proposal PR04-021, (2004).

[38] Jefferson Laboratory. *The JLab Picture Exchange*. `http://www1.jlab.org/ul/jpix`.

[39] B.M. Dunham. *Jefferson Lab, A Status Report*. Thomas Jefferson National Accelerator Facility (1996).

[40] Jefferson Laboratory. `http://www1.jlab.org/`.

[41] N.W. Ashcroft and N. D. Mermin. *Solid State Physics*. Brooks Cole, 1976.

[42] D.I. Sober et al. *The bremsstrahlung tagged photon beam in Hall B at JLab*. Nucl Inst Meth A **440**, 263 (2000).

[43] G. Adams et al. *The CLAS Cherenkov Detector*. Nucl Inst Meth A **465**, 414 (2001).

[44] M. Amarian et al. *The CLAS Forward Electromagnetic Calorimeter*. Nucl Inst Meth A **460**, 239 (2001).

[45] S. Christo. *The g11a Target Cell*, `http://www.jlab.org/ christo/g11a_target.html`.

[46] Y.G. Sharabian et al. *A new highly segmented start counter for the CLAS detector*. Nucl Inst Meth A **556**, 246 (2006).

[47] Alan J. Street et al. *Final Site Assembly and Testing of the Superconducting Toroidal Magnet for the CEBAF Large Acceptance Spectrometer (CLAS)*. IEEE Trans. Mag. **32**, No. 4, 2074 (1996).

[48] M.D. Mestayer et al. *The CLAS drift chamber system*. Nucl Inst Meth A **449**, 81 (2000).

[49] D.S. Carman et al. *The Region 1 drift chamber for the CLAS spectrometer*. Nucl Inst Meth A **419**, 315 (1998).

[50] Y.M. Qin et al. *Prototype studies and design considerations for the CLAS Region 2 drift chambers*. Nucl Inst Meth A **367**, 316 (1995).

[51] F.J. Barbosa et al. *A drift chamber system for a toroidal detector*. Nucl Inst Meth A **323**, 19 (1992).

[52] E.S. Smith et al. *The time of flight system for CLAS*. Nucl Inst Meth A **432**, 265 (1999).

[53] R. Ursik et al. *1 nA beam position monitoring system*. Proceeding of the 1997 Particle Accelerator Conference, 2131 (1999) .

[54] M. Battaglieri and R. De Vita. *The g11a Triggers efficiency*. ????????

[55] M. Ungaro, R. De Vita, and L. Elouadrhiri. *g11a data processing*. CLAS Analysis Note 2005-014 (2005).

[56] C. Meyer and M. Williams. *Kinematic Fitting the Reaction* $\gamma d \to K^+K^-p(n)$. CLAS Analysis Note 2004-109 (2004).

[57] Siegmund Brandt. *Statistical and Computational Methods in Data Analysis*. North Holland Publishing Company, 1970.

[58] R. Frühwirth, M. Regler, R. K. Bock, and H. Grote. *Data Analysis Techniques for High-Energy Physics*. Cambridge University Press, 2000.

[59] E. Pasyuk. *The CLAS ELOSS Package*. Software available via the CLAS CVS repository under `clas/utilities/packages/eloss`.

[60] M. Williams, D. Applegate, and C. A. Meyer. *Determining Momentum and Energy Corrections for g1c Using Kinematic Fitting*. CLAS Analysis Note 2004-017 (2004).

[61] D. Sober, H. Crannell, and F. Klein. *The Tagger Energy Scale: Interpreting the CMU Kinematic Fit Results* CLAS Analysis Note 2004-019 (2004)

[62] D. Applegate, M. Bellis, Z. Krahn, C. Meyer, and M. Williams. *A Detailed Study of the Sources of Systematic Errors in the CLAS g11 Data*. CLAS Analysis Note 2006-017 (2006).

[63] G. Feldman and R. Cousins. *Unified approach to the classical statistical analysis of small signals*. Phys. Rev. D **57**, 3873-3889 (1998).

[64] M. Bellis. *Reliability and Limitations of GSIM*. CLAS Analysis Note 2002-016 (2002).

[65] M. Williams, *et al. Photoproduction of $p\eta$ using CLAS*. submitted to Phys. Rev. C (2008).

[66] M. Williams, M. Bellis, and C. Meyer. *Background Fitting method*. submitted to NIM (2008).

[67] M. Holtrop. *GSIM: CLAS GEANT Simulation*. `http://www.physics.unh.edu/maurik/Gsim/gsim_current_code_dev.shtml`

[68] M. McCracken. *Systematic studies of $\gamma p \to K^+\Lambda$ in the g11a dataset*. CLAS note...

[69] J. Ball and E. Pasyuk. *Photon Flux Determination Through Sampling of "out-of-time" Hits with the Hall B Photon Tagger*. CLAS Analysis Note 2005-002 (2005).

[70] M. E. Peskin and D. V. Schroeder. *An Introduction to Quantum Field Theory*. Westview Press, 1995.

[71] S. U. Chung. *Formulas for Partial Wave Analysis, Version II*. Brookhaven National Laboratory Preprint BNL-QGS-93-05, (1993).

[72] F. James. *MINUIT: Function Minimization and Error Analysis, v. 94.1*. CERN Program Library D506.

[73] W. Rarita and J. Schwinger. *On a Theory of Particles with Half-Integral Spin*. Phys. Rev. **60**, 61 (1941).

[74] M. Williams. *Object Oriented Quantum Field Theory Calculations*. ???.

[75] S. U. Chung. *Spin Formalisms*. BNL Preprint BNL-QGS-02-0900 (2004).

[76] E. D. Commins and P. H. Bucksbaum. *Weak interactions of leptons and quarks*. Cambridge University Press, 1983.

[77] D. Binosi and L. Thesßel. *JaxoDraw: A graphical user interface for drawing Feynman diagrams*. Comp. Phys. Comm. **106**, 1-2 (2004).

[78] M. Guidal, J.-M. Laget, and M. Vanderhaeghen. *Electroproduction of strangeness above the resonance region*. Phys. Rev. C **61**, 025204 (2000).

[79] R. A. Adelseck and B. Saghai. *Kaon photoproduction: Data consistency, coupling constants, and polarization variables*. Phys. Rev. C **42**, 1 (1990).

[80] R. Schumacher. Private Communications (2007).

[81] M. Williams, et al. *Differential Cross Sections and Spin Density Matrix Elements for $\gamma p \to p\omega$.* submitted to Phys. Rev. C, (2008).

[82] R. H. Dalitz. *Strange Particles and Strong Interactions.* Oxford University Press, 1962.

[83] R. Bradford, *et al. First measurement of beam-recoil observables C_x and C_z in hyperon photoproduction.* Phys. Rev. C **75**, 035205 (2007).

[84] R. Schumacher. *Polarization of Hyperons in Elementary Photoproduction.* arXiv:nucl-ex/0611035.

[85] S. U. Chung and E. Klempt. *A Primer of K-matrix Formalism.* BNL Preprint (1995).